View metadata, citation and similar papers at core.ac.uk

brought to you by CORE

provided by ScholarBank@NUS

# MODEL ORDER REDUCTION TECHNIQUES IN MICROELECTROMECHANICS

LIN WU ZHONG

(*M.Eng. NUS*)

A THESIS SUBMITTED

FOR THE DEGREE OF DOCTOR OF PHILOSOPHY

DEPARTMENT OF MECHANICAL ENGINEERING

NATIONAL UNIVERSITY OF SINGAPORE

2004

## ACKNOWLEGEMENTS

First and foremost, I would like to express my most sincere gratitude to my two supervisors, Professor Lim Siak Piang and the late Professor Lee Kwok Hong, for introducing me to the microelectromechanics field, for their invaluable advice and support, and for being instrumental in my academic development. I have benefited greatly from their intellectually stimulating and enlightening comments. Their constant enthusiasm, encouragement, kindness, patience and humor are much appreciated and will always be gratefully remembered.

I would like to thank Professor Liang Yanchun for many fruitful discussions and assistance, Drs Lu Pin, Shan Xuechuan and Wang Zhenfeng for their support and friendship.

My thanks are also due to the staff of the Dynamics Lab for their help and support in various ways.

Finally, I would like to thank my wife, Xu Xiaofei, for her understanding, patience and encouragement. Her love is always the inspiration for me. I dedicate this thesis to her and my sons George and Austin.

# TABLE OF CONTENTS


| | | | |
|---|---|---|---|
| Acknowledgements | | | i |
| Table of contents | | | ii |
| Summary | | | vi |
| Nomenclature | | | viii |
| List of Figures | | | xii |
| List of Tables | | | xviii |
| Chapter | 1 | Introduction | 1 |
| Chapter | 2 | Macromodels for quasi-static analysis of MEMS | 14 |
| | 2.1 | Actuator modelling | 17 |
| | 2.2 | No contact | 19 |
| | 2.2.1 | Global admissible trial functions and macromodel | 19 |
| | 2.2.2 | Numerical results and discussion | 23 |
| | 2.3 | Contact over a finite length | 27 |
| | 2.3.1 | Global admissible trial functions and macromodel | 27 |
| | 2.3.2 | Numerical results and discussion | 29 |
| | 2.4 | Conclusion | 31 |
| Chapter | 3 | Macromodels for dynamic simulation of MEMS using Karhunen-Loève decomposition | 32 |
| | 3.1 | Theory of Karhunen-Loève decomposition | 34 |
| | 3.2 | Galerkin procedure | 39 |
| | 3.3 | The relationship between Karhunen-Loève modes and the vibration modes of the distributed parameter system | 41 |

| | | | |
|---|---|---|---|
| | 3.3.1 | Free vibration of the conservative distributed parameter system | 42 |
| | 3.3.2 | Numerical results and discussion | 43 |
| | 3.3.3 | Conclusion | 48 |
| | 3.4 | A MEMS device and governing equations | 49 |
| | 3.5 | Snapshot generation | 51 |
| | 3.6 | Macromodel generation | 53 |
| | 3.7 | Numerical results and discussion | 56 |
| | 3.7.1 | Macromodel accuracy | 56 |
| | 3.7.2 | Change of the input voltage spectrum | 61 |
| | 3.7.3 | Time intervals and number of the snapshots | 65 |
| | 3.7.4 | The effect of the large deformation | 67 |
| | 3.8 | Conclusion | 70 |
| Chapter | 4 | Macromodels for dynamic simulation of MEMS using neural network-based generalized Hebbian algorithm | 72 |
| | 4.1 | Theory of principal component analysis | 73 |
| | 4.2 | Generalized Hebbian algorithm | 76 |
| | 4.3 | Macromodel generation | 80 |
| | 4.3.1 | Numerical results | 82 |
| | 4.3.2 | Conclusion | 88 |
| | 4.4 | Robust generalized Hebbian algorithm | 90 |
| | 4.4.1 | Macromodel generation | 92 |
| | 4.4.2 | Numerical results | 92 |
| | 4.4.3 | Conclusion | 104 |
| Chapter | 5 | Relationship between Karhunen-Loève decomposition, | 105 |

| | | | |
|---|---|---|---|
| | | principal component analysis and singular value decomposition | |
| | 5.1 | Three proper orthogonal decomposition methods | 106 |
| | 5.2 | Principal component analysis | 107 |
| | 5.3 | Discrete Karhunen-Loève decomposition | 114 |
| | 5.4 | Singular value decomposition | 118 |
| | 5.5 | The equivalence of three proper orthogonal decomposition methods | 124 |
| | 5.5.1 | The equivalence of principal component analysis and Karhunen-Loève decomposition | 126 |
| | 5.5.2 | The equivalence of principal component analysis (Karhunen-Loève decomposition) and singular value decomposition | 128 |
| | 5.6 | Conclusion | 132 |
| Chapter | 6 | Computation improvement in the macromodel dynamic simulation | 133 |
| | 6.1 | Macromodel | 134 |
| | 6.2 | Pre-computation | 137 |
| | 6.3 | Cubic splines approximation and Gaussian quadrature | 139 |
| | 6.4 | Numerical results | 141 |
| | 6.5 | Conclusion | 145 |
| Chapter | 7 | Macromodel generation and simulation for complex MEMS devices | 146 |
| | 7.1 | Macromodel for a micro-optical device | 147 |
| | 7.1.1 | Model description | 147 |
| | 7.1.2 | Karhunen-Loève modes for components | 149 |
| | 7.1.3 | Component mode synthesis and macromodel generation | 153 |

| | | | |
|---|---|---|---|
| | 7.1.4 | Numerical results and discussion | 158 |
| | 7.2 | Macromodel for a micro-mirror device | 167 |
| | 7.2.1 | Model description | 167 |
| | 7.2.2 | Karhunen-Loève modes for components | 173 |
| | 7.2.3 | Component mode synthesis and macromodel generation | 174 |
| | 7.2.4 | Numerical results and discussion | 178 |
| | 7.3 | Conclusion | 190 |
| Chapter | 8 | Conclusions | 191 |
| | 8.1 | Conclusions | 191 |
| | 8.2 | Scope for future research | 194 |
| References | | | 195 |

# SUMMARY

The modelling and simulation of the microelectromechanical systems (MEMS) and devices are usually presented with nonlinear partial differential equations (PDEs) due to the multiple coupled energy domains and media involved in the MEMS devices, the existence of inherent nonlinearity of electrostatic actuation forces and the geometric nonlinearities caused by large deformation. Traditional fully meshed models, such as finite element method (FEM) or finite difference method (FDM), can be used for explicit dynamic simulation of nonlinear PDEs. However, time-dependent FEM or FDM is usually computationally very intensive and time consuming for device and system designers to use when a large number of simulations are needed, especially when multiple devices are present in the system. In order to perform rapid design verification and optimisation of MEMS devices, it is essential to generate low-order dynamic models that permit fast simulation while retaining most of the accuracy and flexibility of the fully meshed FEM or FDM model simulations. These low-order models are called macromodels or reduced-order models.

Macromodel generation using the global admissible trial functions and the principle of minimum potential energy has been developed for quasi-static simulation of the MEMS devices and systems. The accuracy of the macromodels and their suitability for use in MEMS analysis is examined by applying them to a MEMS device idealized as doubly-clamped microbeam. Numerical results for the static pull-in phenomenon and the hysteresis characteristics from the macromodels are shown to be in good agreement with those computed from finite element method/boundary element method-based commercial code CoSolver-EM, meshless method and shooting method.

For dynamic simulation of MEMS devices and systems, methods based on the principle of proper orthogonal decomposition (POD), including Karhunen-Loève decomposition (KLD), principal component analysis (PCA), and the Galerkin procedure for macromodel generation have been presented. The dynamic pull-in responses of a doubly-clamped microbeam, actuated by the electrostatic forces with squeezed gas-film damping effect, from the macromodel simulations are found to be much faster, flexible and accurate compared with the full model solutions based on FEM and FDM.

A novel approach of model order reduction by a combination of KLD and classical component mode synthesis (CMS) for the dynamic simulation of the structurally complex MEMS device has also been developed. Numerical studies demonstrate that it is efficient to divide the structurally complex MEMS device into substructures or components to obtain the Karhunen-Loève modes (KLMs) as "component modes" for each individual component in the modal decomposition process. Using the CMS technique, the original nonlinear PDEs can be represented by a macromodel with a small number of degrees-of-freedom. Numerical results obtained from the simulation of pull-in dynamics of a non-uniform microbeam and a micro-mirror MEMS device subjected to electrostatic actuation force with squeezed gas-film damping effect show that the macromodel generated this way can dramatically reduce the computation time while capturing the device behaviour faithfully.

# NOMENCLATURE

| | |
|---|---|
| $a$ | Generalized coordinate vector |
| $a_i$ | Coefficient premultiplying the $i-$th empirical eigenfunction or Karhunen-Loève mode |
| | The $i-$th principal component |
| $a_i^w$ | Coefficient premultiplying the $i-$th Karhunen-Loève mode for deflection |
| | Coefficient premultiplying the $i-$th principapl eigenvector for deflection |
| $a_i^p$ | Coefficient premultiplying the $i-$th Karhunen-Loève mode for back pressure |
| | Coefficient premultiplying the $i-$th principapl eigenvector for back pressure |
| $b$ | Width of the microbeam |
| $C$ | Transformation matrix |
| $d_i$ | Thickness of dielectric layer |
| $E$ | Young's modulus |
| $E[\bullet]$ | Statistical expectation operator |
| $h$ | Thickness of the microbeam |
| $I$ | Number of basis for deflection in Galerkin procedure |
| $I_{XX}$, $I_{YY}$ | Second moment of area about $X-$ and $X-$ axes, respectively |
| $J$ | Number of basis for back pressure in Galerkin procedure |
| $k$ | Number of constraint equations |
| $K$ | Two-points correlation function of the Karhunen-Loève decomposition |
| $K_n$ | Knudsen number |
| $L$ | Length of the microbeam |
| $m$ | Number of elements in generalized coordinate vector $a$ |

| | |
|---|---|
| | Mass of the mirror plate |
| $M$ | Number of inner grid in $x-$ direction |
| $n$ | Number of elements in the independent generalized coordinate vector $q$ |
| $N$ | Number of inner grid in $y-$ direction |
| | Number of snapshots |
| $p_a$ | Ambient pressure |
| $p$ | Back pressure force acting on the microbeam due to the squeezed gas-film damping |
| $q$ | Uniformly distributed force |
| | Principal eigenvector |
| | Independent generalized coordinate vector |
| $q_i$ | The $i-$th principal eigenvector |
| $q_i^w$ | The $i-$th principal eigenvector for deflection |
| $q_i^p$ | The $i-$th principal eigenvector for back pressure |
| $R$ | Transfer matrix after a sequence of rotations |
| $R_x$ | Correlation matrix of the random vector $x$ |
| $R_X$ | Transfer matrix about $X-$ axis |
| $R_Y$ | Transfer matrix about $Y-$ axis |
| $R^m$ | $m-$ dimensinal real Euclidean space, the element of which are vectors $x=(x_1, x_2, \dots, x_m)$, with each $x_i$ a real number |
| $t_r$ | Residual stress |
| $t_b$ | Bending induced stress |
| $t$ | Time |
| $T$ | Axial force |
| $u_n$ | Member of the ensemble, snapshot |
| $U_b$, $U_r$, $U_t$ | Strain energy due to bending, residual stress and bending induced stress, respectively |

| | |
|---|---|
| $U_e$ | Electrostatic potential energy |
| $v_n$ | Global admissible trial functions |
| $V$ | Input voltage |
| $V_{\mathrm{PI}}$ | Static pull-in voltage |
| $V_{\mathrm{R}}$ | Static release voltage |
| $w$ | Flextural deflection of the microbeam |
| $w_0$ | Initial gap between microbeam and substrate |
| $w_i$ | The wight vector of $i-\text{th}$ neuron |
| $\hat{w}$ | Approximation of flextural deflection |
| $W$ | The synaptic weight matrix |
| $W_i$ | The $i-\text{th}$ vibration mode |
| $x, y, z$ | Cartesian co-ordinates with $z-$axis in thickness direction of measured from the reference surface |
| $X, Y, Z$ | Global Cartesian co-ordinates |
| $Z_C$ | Tanslational movement of the center of mass |
| $\alpha$ | Eigenvector |
| $\alpha_i$ | Coefficient premultiplying the $i-\text{th}$ global admissible trial function |
| | Coefficient premultiplying the $i-\text{th}$ snapshot |
| $\alpha_{\mathrm{PI}}$ | Coefficient at pull-in |
| $\beta$ | Learning-rate parameter |
| $\delta_{ij}$ | Kronecker delta |
| $\varepsilon_0$, $\varepsilon_r$ | Permittivity of free space and relative permittivity, respectively |
| $\theta_X$, $\theta_Y$ | Angle of rotation about global $X-$ and $Y-$ axes, respectively |
| $\lambda$ | Eigenvalue |
| | Mean-free path of the air |
| | Lagrangian multiplier |
| $\lambda_i$ | The $i-\text{th}$ eigenvalue or Karhunen-Loève value |

| | |
|---|---|
| $\overline{\lambda}_i$ | The $i-\text{th}$ normalized eigenvalue or normalized Karhunen-Loève value |
| $\mu$ | Air viscosity |
| $\xi_i$ | The phase of the $i-\text{th}$ vibration mode |
| $\Pi$ | Total potential energy |
| $\rho$ | Length of contact |
| | Mass per unit length |
| $\phi_i$ | The $i-\text{th}$ empirical eigenfunction or Karhunen-Loève mode |
| | The $i-\text{th}$ orthonormal basis vector |
| $\phi_i^w$ | The $i-\text{th}$ Karhunen-Loève mode for deflection |
| $\phi_i^p$ | The $i-\text{th}$ Karhunen-Loève mode for back pressure |
| $\omega_i$ | The natural frequency of the $i-\text{th}$ vibration mode |
| $\Omega$ | System domain |
| $\langle f \rangle$ | An average of the quantity or function $f$ |
| $(f, g)$ | Inner product in the function space |
| $\in$ | An element of |

# LIST OF FIGURES


| | | |
|---|---|---|
| Figure 1.1 | A parallal-plate transverse electrostatic transducer and its equivalent circuit representation. | 4 |
| Figure 2.1 | A voltage-controlled parallel-plate electrostatic actuator. | 14 |
| Figure 2.2 | A doubly-clamped microbeam. | 17 |
| Figure 2.3 | Schematic view of a doubly-clamped microbeam subjected to a uniformly distributed force in region of no contact. | 20 |
| Figure 2.4 | Deflection profiles of microbeam for a series of applied voltages. | 24 |
| Figure 2.5 | Schematic view a doubly-clamped microbeam subjected to a uniformly distributed force in region of contact. | 27 |
| Figure 2.6 | Contact length of microbeam $\rho$ with respect to applied voltage. | 30 |
| Figure 2.7 | Deflection profiles of microbeam for a series of applied voltages. | 30 |
| Figure 3.1 | The first KLM and the first mode of the vibration. | 44 |
| Figure 3.2 | The second KLM and the second mode of the vibration. | 45 |
| Figure 3.3 | The $10-\mathrm{th}$ KLM and $10-\mathrm{th}$ mode of the vibration. | 45 |
| Figure 3.4 | The $20-\mathrm{th}$ KLM and $20-\mathrm{th}$ mode of the vibration. | 46 |
| Figure 3.5 | The mean square error between KLMs and the corresponding modes of the vibration. | 46 |
| Figure 3.6 | The $10-\mathrm{th}$ KLM and $10-\mathrm{th}$ mode of the vibration with various sampling rate and the length of time period. | 47 |
| Figure 3.7 | The mean square error between the $10-\mathrm{th}$ KLM and $10-\mathrm{th}$ mode of the vibration with various sampling rate and the length of time period. | 48 |
| Figure 3.8 | Doubly-clamped microbeam. | 50 |
| Figure 3.9 | Finite difference mesh of the microbeam. | 52 |
| Figure 3.10 | Comparison of the microbeam pull-in dynamics for an input step voltage of 10.25 V. | 59 |
| Figure 3.11 | The error of macromodel simulation with respect to FDM solution for an input step voltage of 10.25 V. | 59 |

| | | |
|---|---|---|
| Figure 3.12 | Comparison of the microbeam pull-in dynamics for an input sinusoidal voltage of 14 V at a frequency of 10 kHz. | 61 |
| Figure 3.13 | The error of macromodel simulation with respect to FDM solution for an input sinusoidal voltage of 14 V at a frequency of 10 kHz. | 62 |
| Figure 3.14 | Comparison of the first two deflection KLMs with different input voltage spectrum. | 63 |
| Figure 3.15 | Comparison of the first two pressure KLMs with different input voltage spectrum. | 63 |
| Figure 3.16 | Comparison of the microbeam pull-in dynamics for a set of input sinusoidal voltages of 14 V at different frequency at 10 kHz and 100 kHz. | 74 |
| Figure 3.17 | Comparison of the microbeam pull-in dynamics for an input ramp voltage $V = Rt,\ R = 0.4$ V $\mu$s$^{-1}$. | 65 |
| Figure 3.18 | The error of macromodel simulation with respect to FDM solution for an input ramp input voltage $V = Rt,\ R = 0.4$ V $\mu$s$^{-1}$. | 65 |
| Figure 3.19 | The first two deflection KLMs for different number of snapshots. | 66 |
| Figure 3.20 | The first two KLMs along the centre of the microbeam for different number of snapshots. | 67 |
| Figure 3.21 | The error of simulations from macromodel based on three different numbers of snapshots with respect to FDM solution for input step voltage of 10.25 V. | 67 |
| Figure 3.22 | Comparison of the first two deflection KLMs with and without consideration of bending induced tension (BIT) effect. | 68 |
| Figure 3.23 | Comparison of the first two back pressure KLMs with and without consideration of bending induced tension (BIT) effect. | 69 |
| Figure 3.24 | Comparison of macromodel simulations for an input step voltage of 14 V with and without consideration of bending induced tension (BIT) effect. | 69 |
| Figure 3.25 | The error of macromodel simulation with respect to FDM solution for an input step voltage of 14 V. | 70 |
| Figure 4.1 | The first two deflection basis functions obtained by KLD and GHA. | 82 |
| Figure 4.2 | The first back pressure basis function obtained by KLD and GHA. | 83 |

| | | |
|---|---|---|
| Figure 4.3 | The second back pressure basis function obtained by KLD and GHA. | 84 |
| Figure 4.4 | Comparison of the microbeam pull-in dynamics for an input step voltage of 10.25 V. | 84 |
| Figure 4.5 | The error of macromodel simulation with respect to FDM solution for an input step voltage of 10.25 V. | 85 |
| Figure 4.6 | Comparison of the microbeam pull-in dynamics for input step voltages of 20 V and 30 V. | 85 |
| Figure 4.7 | The errors of macromodel simulation with respect to FDM solution for input step voltages of 20V and 30 V. | 86 |
| Figure 4.8 | Comparison of the microbeam pull-in dynamics for an input sinusoidal voltage of 14 at a frequency of 10 kHz. | 87 |
| Figure 4.9 | The error of macromodel simulation with respect to FDM solution for an input sinusoidal voltage of 14 V at a frequency of 10 kHz. | 87 |
| Figure 4.10 | Comparison of the microbeam pull-in dynamics for an input ramp voltage $V = Rt$, $R = 0.4$ V$\mu$s$^{-1}$. | 88 |
| Figure 4.11 | The error of macromodel simulation with respect to FDM solution for an input ramp voltage $V = Rt$, $R = 0.4$ V$\mu$s$^{-1}$. | 88 |
| Figure 4.12 | The first two eigenvectors obtained by GHA for noise-free and noise-injected snapshots. | 93 |
| Figure 4.13 | Comparison of errors using GHA and RGHA for sigmoid function. | 97 |
| Figure 4.14 | Comparison of errors using GHA and RGHA during learning steps between 0–00. | 98 |
| Figure 4.15 | Comparison of errors using GHA and RGHA during learning steps between 100–1 000. | 99 |
| Figure 4.16 | Comparison of errors using GHA and RGHA during learning steps between 1 000–2 000. | 99 |
| Figure 4.17 | Comparison of errors using GHA and RGHA during learning steps between 2 000–3 000. | 100 |
| Figure 4.18 | Comparison of errors using GHA and RGHA during learning steps between 3 000–5 000. | 100 |
| Figure 4.19 | Comparison of errors using GHA and RGHA during learning steps between 5 000–10 000. | 101 |

Figure 4.20 Comparison of errors using GHA and RGHA during learning steps between 10 000–25 000. 101

Figure 4.21 Comparison of the microbeam pull-in dynamics for an input step voltage of 10.25 V. 102

Figure 4.22 The mean square error of macromodel simulation with respect to FDM solution for an input step voltage of 10.25 V. 103

Figure 4.23 Comparison of the microbeam pull-in dynamics for an input sinusoidal voltage of 14 V at a frequency of 10 kHz. 103

Figure 4.24 The mean square error of macromodel simulation with respect to FDM solution for an input sinusoidal voltage of 14 V at a frequency of 10 kHz. 104

Figure 6.1 Comparison of the microbeam pull-in dynamics for an input step voltage of 8 V. 142

Figure 6.2 Comparison of the microbeam pull-in dynamics for an input step voltage of 10.25 V. 144

Figure 7.1 An idealized micro-optical switch device. 148

Figure 7.2 The first KLM for deflection of microbeams. 150

Figure 7.3 The second KLM for deflection of microbeams. 152

Figure 7.4 First three KLMs for back pressure of microbeam 2. 152

Figure 7.5 Comparison of the pull-in dynamics for an input step voltage of 30 V . 158

Figure 7.6 Comparison of the pull-in dynamics for an input step voltage of 50 V . 159

Figure 7.7 Error in midpoint deflection of microbeam 2 from macromodel simulations with respect to FDM results for input step voltages of 30 V and 50 V . 160

Figure 7.8 Comparison of pull-in dynamics for an input sinusoidal voltage of 30 V at a frequency of 20 kHz . 161

Figure 7.9 Error in midpoint deflection of microbeam 2 from macromodel simulation with respect to FDM result for an input sinusoidal voltage of 30 V at a frequency of 20 kHz . 161

Figure 7.10 Comparison of the first KLM for deflection of microbeams with different input voltage spectrum and length of microbeam 3. 163

Figure 7.11 Comparison of the second KLM for deflection of microbeams 163

with different input voltage spectrum and length of microbeam 3.

Figure 7.12 Comparison of first three KLMs for back pressure of microbeam 2 with different input voltage spectrum and length of microbeam 3. 164

Figure 7.13 Comparison of the pull-in dynamics for an input step voltage of $30\,\text{V}$ when treating the system as a single structure. 166

Figure 7.14 Error in midpoint deflection of microbeam 2 from macromodel simulation with respect to FDM results for an input step voltage of $30\,\text{V}$ when treating the system as a single structure. 167

Figure 7.15 A micro-mirror structure. 168

Figure 7.16 Mirror plate rotations. 169

Figure 7.17 Mirror plate position after vertical translational movement and two rotations. 170

Figure 7.18 First three KLMs for deflection of microbeams 1, 2, 3 and 4. 179

Figure 7.19 The first KLM for back pressure of mirror plate. 180

Figure 7.20 The second KLM for back pressure of mirror plate. 180

Figure 7.21 The third KLM for back pressure of mirror plate. 181

Figure 7.22 Comparison of pull-in dynamics of microbeams 1-4 for input step voltages of $V_1 = V_2 = V_3 = V_4 = V_p = 50\,\text{V}$. 182

Figure 7.23 Error in end point deflection of microbeams 1-4 from macromodel simulation with respect to FDM results for input step voltages of $V_1 = V_2 = V_3 = V_4 = V_p = 50\,\text{V}$. 183

Figure 7.24 First three KLMs for deflection of microbeams 1 and 2. 185

Figure 7.25 First three KLMs for deflection of microbeams 3 and 4. 185

Figure 7.26 The first KLM for back pressure of mirror plate. 186

Figure 7.27 The second KLM for back pressure of mirror plate. 187

Figure 7.28 The third KLM for back pressure of mirror plate. 187

Figure 7.29 Comparison of pull-in dynamics of microbeams 1 and 2 for the combination of input step voltages of $V_1 = V_2 = 80\,\text{V}$, $V_3 = V_4 = V_p = 60\,\text{V}$. 188

Figure 7.30 Comparison of pull-in dynamics of microbeams 3 and 4 for the combination of input step voltages of $V_1 = V_2 = 80\,\text{V}$, 188

$V_3 = V_4 = V_p = 60$ V .

Figure 7.31 Comparison of angle of rotation of mirror plate for the combination of input step voltages of $V_1 = V_2 = 80$ V, $V_3 = V_4 = V_p = 60$ V . 189

Figure 7.32 Error in angle of rotation of mirror plate from macromodel simulation with respect to FDM results for the combination of input step voltages of $V_1 = V_2 = 80$ V, $V_3 = V_4 = V_p = 60$ V . 189

# LIST OF TABLES


| | | |
|---|---|---|
| Table 2.1 | Material properties and geometric dimensions of microbeam for example 1. | 24 |
| Table 2.2 | Pull-in voltage $V_{\mathrm{PI}}$ and the constant $\alpha_{\mathrm{PI}}$ for example 1. | 25 |
| Table 2.3 | Constant $\alpha$ with respect to the applied voltage $V$ . | 25 |
| Table 2.4 | Material properties and geometric dimensions of microbeam for example 2. | 26 |
| Table 2.5 | Pull-in Voltage $V_{\mathrm{PI}}$ and the constant $\alpha_{\mathrm{PI}}$ at pull-in for example 2. | 26 |
| Table 2.6 | Material properties and geometric dimensions of microbeam. | 30 |
| Table 3.1 | The first three KLVs versus the number of snapshots. | 46 |
| Table 3.2 | Material properties and geometric dimension of the microbeam. | 57 |
| Table 3.3 | Accumulative normalized KLVs corresponding to the number of deflection KLMs. | 57 |
| Table 3.4 | Accumulative normalized KLVs corresponding to the number of back pressure KLMs. | 58 |
| Table 4.1 | Comparison of square errors using GHA with those using RGHA versus noise (%). | 96 |
| Table 6.1 | Performance of macromodels with respect to FDM simulation for an input step voltage of 8 V. | 143 |
| Table 6.2 | Performance of macromodels with respect to FDM simulation for an input step voltage of 10.25 V. | 144 |
| Table 7.1 | Material properties and geometric dimensions of microbeams. | 150 |
| Table 7.2 | Normalized accumulative KLVs corresponding to the number of deflection KLMs. | 151 |
| Table 7.3 | Normalized accumulative KLVs corresponding to the number of back pressure KLMs. | 152 |
| Table 7.4 | Material properties and geometric dimensions of microbeams. | 174 |
| Table 7.5 | Normalized accumulative KLVs corresponding to the number of deflection KLMs. | 179 |
| Table 7.6 | Normalized accumulative KLVs corresponding to the number of | 179 |

back pressure KLMs.

Table 7.7 Normalized accumulative KLVs corresponding to the number of deflection KLMs. 184

Table 7.8 Normalized accumulative KLVs corresponding to the number of back pressure KLMs. 184

# CHAPTER 1

# INTRODUCTION

Microelectromechanical systems (MEMS), also known as Microsystems in Europe or Micromachines in Japan is the integration of micromechanical parts which can perform functions of signal acquisition (sensor) and some action (actuator), through electronic parts which can perform signal process, control and display etc. Usually the sensors and actuators are fabricated on a common silicon substrate through lithography-based microfabrication technology. The sensors acquire the signals through detecting and measuring mechanical, electrical, fluidic, thermal, biological, chemical, optical, and electromagnetic phenomena. The electronics process the information derived from the sensors then direct the actuators to respond with some desired outcome or purpose.

Computer-aided design (CAD) tools enable the simulation and computational prototyping of MEMS devices that may not have been constructed. The ultimate requirements of these tools are that they can provide accurate, easy-to-use behavioural models that capture all of the essential behaviour and permit predictable design modification and optimisation to be carried (Senturia, 1998).

The modelling and simulation of the MEMS devices are usually resulted in nonlinear partial differential equations (PDEs) due to the multiple coupled energy domains and media involved in the MEMS devices and the existence of inherent nonlinearity of electrostatic actuation forces as well as the geometric nonlinearities caused by large deformation. Traditional fully meshed models, such as finite element method (FEM) or finite difference method (FDM), can be used for explicit dynamic simulation of

nonlinear PDEs. The first generation of CAD tools for the simulation of multiple coupled physical phenomena was the OYSTER program (Koppelman, 1989) which concentrated on creating a three-dimensional solid geometric model from an integrated-circuit process description and mask data, and CAEMEMS (Crary and Zhang, 1990) which focused on constructing a FEM tool with the capability of simulating the mechanical behaviours of specific MEMS devices. In the MEMCAD software developed by Massachusetts Institute of Technology (Senturia et al., 1992), the mechanical analysis was performed using commercially available FEM-based ABAQUS whereas the electrostatic analysis was performed using FASTCAP (Nanors and White, 1991, 1992a, 1992b) which combined boundary element techniques, fast multipole methods and pre-corrected-FFT methods (Philips and White, 1994) for capacitance extraction and electrostatic force computation. The coupled electromechanical domain analysis was solved self-consistently using CoSolve-EM (Gilbert et al., 1995) by iteration to determine the electrostatic force and the structure deformation. These works had been refined and implemented in some commercial packages, such as CoventorWare™ (formally known as MEMCAD) from Coventor Inc and IntelliSuite™ (formally known as IntelliCAD) from Corning IntelliSense. Korvink et al. (1994) developed SESES program which provided external compatibility, including commercially available FEM code ANSYS and FASTCAP for flexible coupling of electrical, thermal and mechanical deformation phenomena in uniform and consistent environment. Another three-dimensional FEM-based SOLIDIS (Funk et al., 1997) provided similar self-consistent analysis for actuation forces, especially for a large class of coupled electrothermomechanical interactions.

However, it was soon realized in the MEMS computer-aided design community that explicit dynamical simulations of nonlinear PDEs using the time-dependent FEM or

FDM were usually computationally very intensive and time consuming when a large number of simulations were needed, especially when multiple devices were present in the system. In order to perform rapid design verification and optimization of MEMS devices, it is essential to have low-order dynamic models that permit fast simulation while retaining most of the accuracy and flexibility of the fully meshed FEM or FDM model simulations of the original system. These low-order models generated through model order reduction techniques are called macromodels or reduced-order models which can then be embedded in system-level MEMS simulators (Senturia, 1998).

Generally and ideally, a macromodel for MEMS simulation has the following attributes (Senturia, 1998 and Romanowicz, 1998)

i) It is preferably analytical, rather than numerical, permitting the designer to performance the parametric study to assess the effect of the parameter changes in design choices.

ii) It exhibits correct dependencies on device geometry and material constitutive properties.

iii) It reveals correct explicit energy conservation and dissipation behaviours.

iv) It covers both quasi-static and dynamic behaviours of the device.

v) It is expressible in a simple-to-use form, either an equation, a network analogy, or a small set of coupled ordinary differential equations (ODEs).

vi) It is easy to be connected to system level simulators.

vii) It agrees with three-dimensional multiple coupled physical phenomena simulations.

Lumped-parameter modelling technique was an equivalent circuit approach and the most common form of macromodel for linear sensor and actuator MEMS devices (Tilmans, 1993; Tilmans and Legtenberg, 1994; Tilmans, 1996; Veijola, 1995). In this

system engineering technique, the elements in the lumped-element electric circuit were physically representatives of a MEMS device's properties such as its mass, stiffness, capacitance, inductance and damping. Exchange of energy of a MEMS device and the external environment was achieved through port that was defined by a pair of conjugate pairs called effort and flow, with the product of the effort and flow being power. The development of equivalent circuit representations was based on the analogy in the mathematical description that exists between electric and mechanical phenomena.

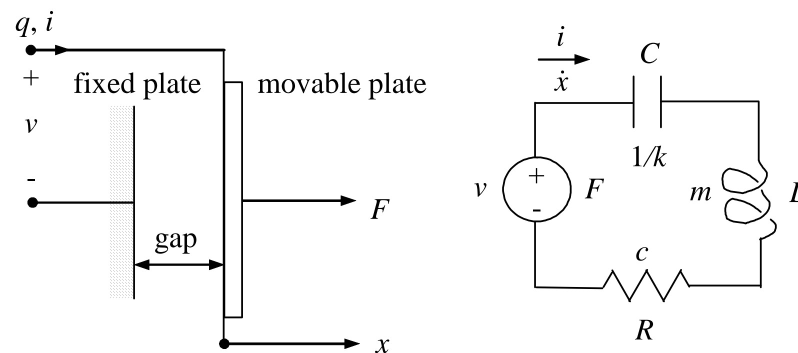


Figure 1.1 A parallal-plate transverse electrostatic transducer and its equivalent circuit representation.

For instance, Figure 1.1 shows a MEMS device that includes a movable parallel plate as the transverse electrostatic transducer, the force $F$ acted on the plate is mathematically analogous to and represented by the voltage $v$, the velocity $u$ by the current $i$, the plate inertial proof mass $m$ by the inductance $L$, the displacement of plate $x$ by the charge $q$, the compliance of a linear spring supporting the mass $1/k$, where $k$ is the spring constant, by capacitance $C$ and the viscous damping $c$ by resistance $R$. The applications of lumped-parameter technique are extensive and theirs use is strongly supported by modern electric network theory which provides powerful mathematical techniques and commercially available circuit simulators, such as SPICE. Equivalent circuits are particularly useful for the analysis of systems

consisting of complex structural members and coupled subsystem with several electrical and mechanical ports. The major problems in constructing accurate lumped-parameter macromodels are the partition of the continuum device into a network of lumped elements, especially when arbitrary geometries are involved, and determination of the parameter values for each element. Macromodels based on lumped-parameter techniques and element library with parameterised behavioural models for some structurally complex MEMS devices, such as crab-leg resonator and O-shaped coupling spring which were designed as netlist of general purpose micromechanical beams, plates, electrostaticgaps, joints and anchors, were also developed in NODAS program (Febber, 1994; Vandemeer et al., 1997).

Swart et al. (1998) and Zaman et al. (1999) developed a code, called AutoMM, for the automatic generation of lumped macromodels for a broad class of MEMS devices charaterized as plate-tethered structures. AutoMM used the concept of lumped modelling for mechanical components and assumed that the tethers which provided mechanical compliance were electrostatically inert and massless, and the proof mass was electronically driven and moved as a rigid body. The lumped spring behaviours originated from mechanical reaction forces and the moments produced by tethers supporting the proof mass. Damping forces were calculated mainly by gas viscosity. The electrostatic forces were obtained by calculating the spatial derivatives of the electrostatic co-energy. The basic techniques used in AutoMM also included exploring the device operation space, modelling of data through multi-degree polynomial curve fitting, and using the polynomial coefficients and other simulation data in dynamic equations of motion.

Anathasuresh et al. (1996), Gabby (1998) and Gabby et al. (2000) developed model order reduction technique based on linear modal analysis to generate the macromodels

for dynamic simulation of conservative MEMS system, such as electrostatic actuation of a suspended beam and an elastically supported plate with an eccentric electrode and unequal springs. In this technique, the linear normal mode was used to represent the deformed shape of the structure in both the three-dimensional finite element meshed models and lumped models where mechanical structure was modelled appropriately using masses and springs. The dynamic behaviours of a conservative system with $m$ degrees-of-freedom can be represented as

$$M\ddot{x} + Kx + f = 0 \tag{1.1}$$

where $M$ is the global mass matrix, $K$ is the global stiffness matrix, $x$ is the vector of states, such as displacement, and $f$ is the vector of nonlinear force which is the function of state $x$, inputs and time $t$. Using the linear normal mode summation method (Thomson and Dahleh, 1998), the original coordinates $x$ is transformed to the nodal coordinates $q$

$$x = P\,q \tag{1.2}$$

where $P$ is a matrix whose columes are the normal mode of the system, the dynamic equation becomes

$$P^T MP\,\ddot{q} + P^T KP\,q + P^T f = 0 \tag{1.3}$$

where both $P^T MP$ and $P^T KP$ are diagonal matrices. There are $m$ normal modes for a system with $m$ degrees-of-freedom. Generally, only a few lower modes are excited and become significant. Higher modes which have negligible effects on the system can be truncated without significant loss of accuracy. Truncated expression of Equation (1.2) can be used to reduce the order of system expressed by Equation (1.3) from $m$ degrees-of-freedom to a much lower $n$ degrees-of-freedom in the most cases. Anathasuresh et al. (1996) proved that only five or fewer modes were sufficient, therefore the dynamic simulation of the system can be computed much faster. The

limits to this approach are the convertion from modal coordinates back to the original state $x$ at each time step in order to re-compute the nonlinear force $f$ for the item $P^T f$ in Equation (1.3), and the difficulty in calculating accurately the stress stiffening of an elastic body undergoing large deformation. To overcome the first shortcoming, Gabby (1998) and Gabby et al. (2000) developed a method to directly express the term $P^T f$ in terms of modal coordinates through energy method. It however requires many tedious simulations plus fitting to analytical functions and the designer must decide on the number of modes and the range of modal amplitude to be included in the simulation. The method also faces difficulty with the problem invloving nonlinear dissipation which is common in fluid-structure interactions, for instance the squeezed gas-film damping. In such case, the fluid does not have any normal modes of its own that can be used in normal mode summation method in combination with the structure normal mode of the system.

Using Arnoldi process for computing orthonormal basis of Krylov subspaces (Saad and Schultz, 1986), Wang and White (1998) demonstrated that an accurate macromodel could be generated for linear systems in coupled domain simulation of MEMS devices with single input-single output (SISO) characteristics. If the original linear system is given in the form of

$$\begin{aligned} \dot{x}(t) &= Ax(t) + b\,u(t) \\ y(t) &= c^T x(t) \end{aligned} \tag{1.4}$$

where $b$ and $c$ are $m-$dimentional constant vectors, $x$ is $m-$dimentioanl viarable vector, $A$ is an $m \times m$ constant matrix, $u$ is the input and $y$ is the output, with the transfer function

$$G(s) = c^T (sI - A)^{-1} b = -c^T A^{-1} \left(I - sA^{-1}\right)^{-1} b = -\sum_{i=0}^{\infty} c^T A^{-(i+1)} b s^i \tag{1.5}$$

a much smaller $n-$th order reduced model for the original system of Equation (1.4) is given as

$$A_n \dot{z}(t) = z(t) + b_n\ u(t)$$
$$y_n(t) = c_n^T z(t) \tag{1.6}$$

whose transfer function

$$G_n(s) = c_n^T (sI - A_n)^{-1} b_n \tag{1.7}$$

approximates the original transfer function $G(s)$ in Equation (1.5). Making use of the Arnoldi algorithm, an $m \times n$ column-orthonormal matrix $V$, an $n \times n$ matrix $H$ and an $n \times 1$ vector $v_{n+1}$ are generated, and the following relationship holds

$$AV = VH + hv_{n+1}e_n^T \tag{1.8}$$

where $h$ is a scalar and $e_n^T$ is the $n-$th standard unit vector. The $n$ coulumns in matrix $V$ form a set of orthonormal vectors that spans the same Krylov subspace defined as

$$K_n(A^{-1}, b) = span\{b, A^{-1}b, A^{-2}b, \cdots, A^{-(n-1)}b\} \tag{1.9}$$

This approach works satisfactorily for linear and some nonlinear systems which are actually closed to linear systems or operating within or near its linear regime. For most of nonlinear systems, such as MEMS devices, a nonlinear extension needs to be explored. Chen (1999) developed a quadratic reduction method for nonlinear systems and Rewienski and White (2001a) applied it to generate macromodels for MEMS simulation. The quadratic reduction is based on the startegy that approximates the original nonlinear system by its quadratic approximation firstly

$$\dot{x}(t) = Ax(t) + x^T Dx + b\,u(t)$$
$$y(t) = c^T x(t) \tag{1.10}$$

where $D$ is the quadratic tensor of the system, and then reduces the quadratic approximation system which has the same size as the original nonlinear system to a much smaller quadratic system. This reduced quadratic system can approximate the original nonliear system with good accuracy but the computation of vector-quadratic tensor in this approach is usaully intensive and complicated in the integration of the reduced quadratic system. The method becomes computationally ineffective if higher order nonlinearities are required in the macromodel, such as cubic or quartic terms.

Rewienski and White (2001b) porposed a model order reduction method based on representing the entire nonlinear system with piecewise-linear sub-systems and then reducing each of pieces with Krylov subspace projection method. Although the algorithm works satisfactorily for dynamic simulation of MEMS devices, such as the device modelled as doubly-clamped microbeam, the issues remain open in the selection of linearization points, merging of the linearized models and the proper training of the system.

Similar to the lumped-parameter modelling and linear modal analysis which result in a set of coulped ordinary defferential equations (ODEs), Hung and Senturia (1999) proposed a global basis function technique to construct a macromodel for MEMS dynamic simulation in the form of a set of much fewer nonlinear ODEs. Selecting a set of basis functions $\phi_k(x)$ not only for mechanical domain but also for fludic domain and projecting the state solution $u(x,t)$ of the following original nonlinear PDEs

$$L[u(x,t)] - f = 0 \tag{1.11}$$

onto a set of truncated complete basis functions

$$\hat{u}(x,t) \approx \sum_{k=1}^{n} a_k(t)\phi_k(x) \tag{1.12}$$

and making use of Galerkin procedure lead to a set of nonlinear ODEs in terms of the amplitudes of the basis funtions

$$\left(\phi_k, L[\hat{u}(x,t)] - f\right) = 0, \quad (k = 1,2,\cdots,n) \tag{1.13}$$

Because the introduction of a set of basis functions $\phi_k(x)$ introduces a coordinatization $(a_1, a_2, \cdots, a_n)$ of the original PDEs, the selection of an optimal basis, i.e., one for which the number $n$ of basis functions (hence, the number of ODEs) needed in Equations (1.12) and (1.13) to represent the dynamic behaviours of the original PDEs as small as possible, becomes the main issue in this technique. In Hung and Senturia (1999), the basis functions were obtained based on singular value decomposition of some numerical simulation results. The simulation of the pull-in dynamics of a doubly-clamped microbeam subjected to time dependent input voltage demonstrated that this approach could achieve several orders of magnitude computation speed without loss of accuracy. However, the selection of sufficient number of basis functions remains open in this approach.

The main goal and innovative contribution of this thesis is to develop some novel model order reduction techniques for simulation and anaysis of the microelectromechanical behaviors in MEMS devices and systems that involve multiple coupled energy domains.

Macromodel generated by using the global admissible trial functions, variational principle and Rayleigh-Ritz method are developed in Chapter 2 for simulation of the quasi-static instability, contact electromechanics and hysteresis characteristics of a single MEMS device modelled as doubly-clamped microbeam. Where possible, the

results are compared with those from FEM/BEM based commercial code CoSolver-EM, meshless method and shooting method.

Similar to the method developed in Hung and Senturia (1999), Chapter 3 presents a relatively new method by making use of the Karhunen-Loève modes (KLMs) extracted from ensemble of signals through Karhunen-Loève decomposition (KLD) process and the Galerkin procedure which employs these KLMs as the basis functions to convert the original high-dimensional system to low-dimensional macromodels with reduced number of degrees-of-freedom. The macromodels can be used for subsequent dynamic simulations of the original nonlinear system. Numerical studies on macromodel accuracy, efficiency and flexibility compared with the full model finite difference method (FDM) are carried out for the doubly-clamped microbeam subjected to electrostatic actuation forces with squeezed gas-film damping effect.

In Chapter 4, a neural-network-based method of model order reduction that combines the generalized Hebbian algorithm (GHA) for principal component analysis (PCA) and Galerkin procedure to generate the reduced order macromodels is presented. The principle eigenvectors extracted by PCA is equivalent to the KLMs of KLD and the procedure of macromodel generation is similar to that in Chapter 3. The key advantage of the GHA is that it does not need to compute the input correlation matrix in advance so that it commands higher computation efficiency in creating the basis for macromodel generation. A stable and robust GHA algorithm, which is able to process noise-injected data and has faster convergence of iterations in the network training, is also developed for macromodel generation. The effect of the noise level on the accuracy of the macromodel simulations is investigated.

Chapter 5 focuses on the derivation of the relationship among three of the proper orthogonal decomposition (POD) methods, i.e., KLD, PCA and singular value

decomposition (SVD), which are popular in the applications for model order reduction in science and engineering fields. It is the first time to provide a clear description of the relationship and equivalence among these three formulations for discrete random vectors.

The techniques to enhance the computation efficiency of the macromodels based on POD methods, developed in the Chapters 3 and 4, are proposed in Chapter 6 to overcome the unproductive re-computation of the time-dependant nonlinear items at every time step during the numerical integration. Numerical experiments demonstrate that the techniques of the pre-computation prior to numerical time integration, and the cubic splines approximation of the basis functions in combination of Gaussian quadrature can improve the macromodel simulation efficiency significantly.

In Chapter 7, a novel method for macromodel generation for the dynamic simulation and analysis of structurally complex MEMS device is developed by making use of KLD and classical component mode synthesis (CMS). The complex MEMS device is modelled as an assemblage of interacting components. KLD is used to extract KLMs and their corresponding KLVs for each component from an ensemble of data obtained by selective computations of the full model simulation. These KLMs for each component are similar to “components modes” and used as basis functions in Galerkin projection to formulate the equations of motion for each component expressed in terms of a set of component generalized coordinates. When the continuity conditions at the interfaces are imposed, a set of constraint equations is obtained which relates the component generalized coordinates to the system generalized coordinates through a transformation matrix. Finally, a macromodel, represented by a set of equations of motion expressed in terms of a set of system generalized coordinates, is formulated to determine the system dynamic responses. The accuracy, effectiveness and flexibility

of the proposed model order reduction methodology are demonstrated with the simulations of the pull-in dynamics of a complex micro-optical device modelled as non-uniform microbeam and a micro-mirror device modelled as rigid square mirror plate with four clamped-guided parallel microbeams along each side of the plate subjected to electrostatic actuation force with squeezed gas-film damping effect.

Finally, the present work ends with its main conclusions and some future research direction in model order reduction in Chapter 8.

# CHAPTER 2

# MACROMODELS FOR QUASI-STATIC ANALYSIS OF MEMS

The voltage-controlled parallel-plate electrostatic actuation is widely used in MEMS actuators in which a movable conductor touches down or makes contact with a fixed plane in the course of the device operation. Electrostatic actuators are attractive not only because of their high energy density and larger actuation force in microscale, but also relatively simple in design, fabrication and system integration. By applying a quasi-static bias voltage across the movable conductor and fixed plane, an electrostatic force is generated and tends to pull the movable conductor onto the fixed plane as shown in Figure 2.1.

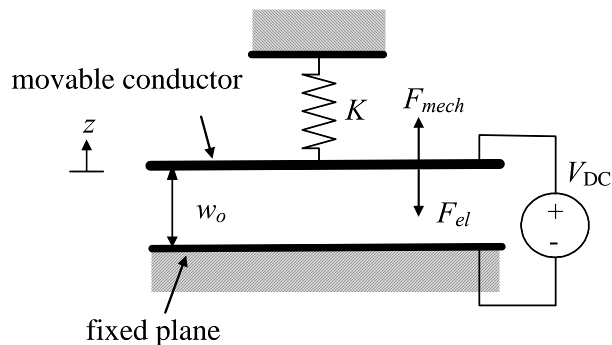


Figure 2.1 A voltage-controlled parallel-plate electrostatic actuator.

In static equilibrium, this electrostatic force is balanced by the spring restoring force when the applied bias voltage is low. As the voltage is increased, the electrostatic force increases. When the voltage attains a value equal to the pull-in voltage $V_{\mathrm{PI}}$ (Osterberg and Senturia, 1997), the electrostatic force is larger than the spring restoring force. As the result, the movable conductor becomes unstable and spontaneously pulls in onto the fixed plane. If the voltage is then reduced after pull-in,

at its release voltage $V_R$ the movable conductor will be spontaneously released (Gilbert et al., 1996). These devices exhibit electromechanical hysteresis manifested by a finite difference in the pull-in and release voltages (Anathasuresh et al., 1996, Gilbert et al., 1996). In some voltage–controlled electrostatic actuation MEMS devices, the inclusion or avoidance of this hysteresis depends on the application of the devices. Electrostatic actuators are applied in wide range of MEMS devices including micromechanical switch (McCarthy el al., 2002), microswitch for optical communications (Min and Kim, 1999; Hung and Senturia, 1999), radio frequency oscillator for wireless communication (Young and Boser, 1997; Nguyen et al., 1998), test device for material property measurement (Osterberg and Senturia, 1997), microresonator for resonant strain gauge (Tilmans and Legtenberg, 1994), accelerometer (Veijola et al., 1995; 1998), and pressure sensor (Gupta and Senturia, 1997). Accurate and efficient simulation and prediction of the applied quasi-static bias voltage at which the conductors of actuators deform, pull in, contact with the fixed plane and release are important in the design of these voltage-controlled electrostatically actuated MEMS devices. The CoSolve-EM code, based on coupled three-dimensional finite element method (FEM) and boundary element method (BEM) modelling tools to iteratively approaching the pull-in voltage with decreasing voltage increments was developed in Gilbert et al. (1995) and implemented in commercially available codes CoventorWare™ and IntelliSuite™. The release voltage, quasi-static contact electromechanics and the electromechanical hysteresis for doubly-clamped microbeam were also computed using this method in Gilbert et al. (1996). Aluru (1999) presented a reproducing kernel particle method and meshless method for pull-in voltage calculation. Ngiam (2000) developed a shooting method to obtain the pull-in and release voltages with consideration of the bending induced tension or axially

stretching effect which is found to have significant influence on the electromechanical resposnes of the MEMS devces, especially in the case of large deformation (Choi and Lovell, 1997). In Osterberg and Senturia (1997), a qualitative closed-form model derived through empirical fit to the simulated data using a theoretically derived form for the pull-in voltage $V_{\text{PI}}$ of structures as functions of their geometry and material properties was presented. Anathasuresh et al. (1996) used the normal mode summation method to generate a macromodel to compute the pull-in voltage. Tilemans and Legtenberg (1994), and Legtenberg et al. (1997) proposed to compute the pull-in voltage using a simplified semi-analytical model based on energy method. Bochobza-Degani et al. (2002) developed an algorithm to extract the pull-in voltage based on iterating the displacement of a pre-chosen degree of freedom node of the actuator instead of the iterating of applied bias voltage. Recently Pamidighantam et al. (2002) reported a refined method based on the lumped model for pull-in voltage analysis of doubly-clamped microbeam and cantilever microbeam.

In this chapter, a semi-analytical low-order model based on global admissible trial functions and the principle of minimum potential energy (Washizu, 1982) is presented to simulate the quasi-static pull-in instability and contact electromechanical behaviour of MEMS devices modelled as doubly-clamped microbeam. The comparison of some numerical results from present method, finite element and boundary element based CoSolve-EM module of CoventorWare™ (Gilbert et al., 1996), meshless method (Aluru, 1999) and shooting method (Ngiam, 2000) are presented to validate and demonstrate the present method.

## 2.1 ACTUATOR MODELLING

Doubly-clamped microbeam actuated by electrostatic force has become a classical design for wide range of MEMS devices. Osterberg and Senturia (1997) applied this structure in their M-Test chip for MEMS material property measurement and process monitoring at the wafer level during process development and manufacturing. This structure was designed as resonator by Tilmans and Legtenberg (1994) for application as resonant strain gauges to replace the conventional piezoresistors, and as pressure sensor by Gupta and Senturia (1997). The schematic drawing of this device is shown in Figure 2.2. Parallel-plate approximation is assumed for this MEMS device when the gap to length ratio is small hence the electrostatic field lines are assumed to be transversal to the deformed microbeam. When a quasi-static bias voltage is applied across the top and bottom electrodes, the top deformable microbeam is pulled downwards due to electrostatic actuation force that is inversely proportional to the square of the gap spacing.

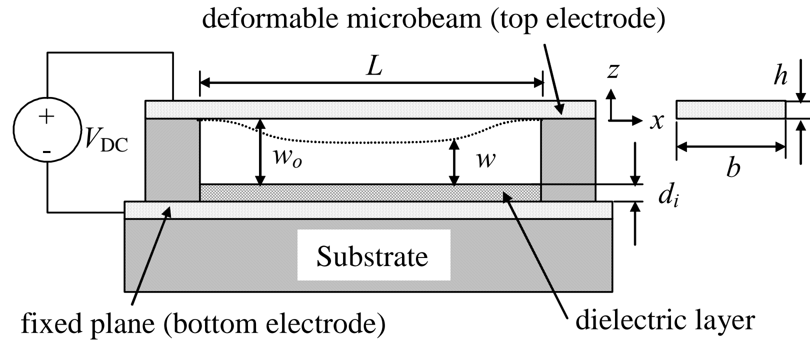


Figure 2.2 A doubly-clamped microbeam.

In general, the microbeam can be modelled as a classical Euler-Bernoulli beam subjected to electrostatic force

$$EI\frac{\partial^4 w}{\partial x^4} - T\frac{\partial^2 w}{\partial x^2} = -\frac{\varepsilon_0 b V^2}{2w^2} \tag{2.1}$$

where $E$ is Young's modulus, $I = bh^3/12$ is the second moment of area where $b$ is the width and $h$ is the thickness of the microbeam, $V$ is the applied quasi-static bias voltage, $\varepsilon_0$ is the permittivity of free space and equals to $8.854\times10^{-12}$ Farad • m$^{-1}$, $T/(bh)$ is the sum of residual stress $t_r$ and the bending induced stress (axially stretching effect) $t_b$ due to large deflection which can be expressed as

$$\frac{T}{bh} = t_r + t_b = t_r + E\frac{\Delta L}{L} \approx t_r + \frac{E}{2L}\int_L \left(\frac{dw}{dx}\right)^2 dx \tag{2.2}$$

where $L$ is the length of the microbeam.

Equation (2.1) is a nonlinear differential equation and its analytical closed-form solution cannot be found. Hence the approximate numerical solutions have to be sought. It has been shown in elasticity that Rayleigh-Ritz method is an efficient and simpler technique for obtaining approximate solutions of the problem defined by differential equations and boundary conditions through the use of the variational method (Washizu, 1982). For the problem described in Equation (2.1), an approximate solution is assumed as the linear combination of a set of global admissible trial functions

$$\hat{w}(x) = \sum_{n=1}^{N} \alpha_n v_n(x) \tag{2.3}$$

where $v_n(x)$ are the global admissible trial functions and $\alpha_n$ are coefficients to be determined by the Rayleigh-Rize method.

To solve this elastic beam problem in the presence of a rigid horizontal bottom surface which is assumed in the present study, Westbrook (1982) proposed a solution that was divided into four basic types or regions depending on whether or not the beam was in contact with the bottom surface. Following Westbrook's (1982) idea and using deflection profile function of the beam when subjected to the uniformly distributed

force $q$ as the truncated global admissible trial function together with the principle of minimum potential energy, semi-analytical macromodels are derived in the following sections to analyse the electromechanical behaviours of a MEMS device as shown in Figure 2.2 in the regions of no contact and contact with finite length with the bottom surface. It is noted that the global admissible trial functions defined in this chapter are a kind of semi-comparison functions that satisfy some geometric and natural boundary conditions (Meirovitch, 1997) so that fewer number of truncated admissible trial functions are needed to achieve better approximate accuracy. Also some global trial functions need not satisfy the geometric and force conditions at each boundary as long as their combined sum allows these conditions to be satisfied. In other words, the approximate solutions in terms of the linear combination of truncated global admissible trial functions must satisfy the boundary conditions. This approach is commonly used in mode summation or component mode synthesis procedure (Thomson and Dahleh, 1998).

## 2.2 NO CONTACT

### 2.2.1 GLOBAL ADMISSIBLE TRIAL FUNCTIONS AND MACROMODEL

In this region as shown in Figure 2.3, there is no contact between the deformable microbeam and the bottom surface.

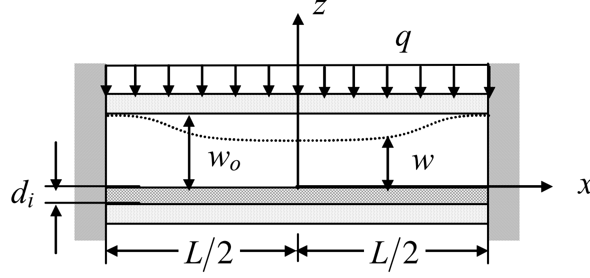


Figure 2.3 Schematic view of a doubly-clamped microbeam subjected to a uniformly distributed force in region of no contact.

The deflection function $w$ of a doubly-clamped microbeam subjected to a uniformly distributed force $q$ is obtained as

$$EIw(x) = -\frac{1}{24}qx^4 + \frac{1}{6}a_1x^3 + \frac{1}{2}a_2x^2 + a_3x + a_4 \tag{2.4}$$

where $a_1$, $a_2$, $a_3$ and $a_4$ are constants to be determined by boundary conditions. After imposing the boundary conditions

$$w'(0) = w'''(0) = 0$$
$$w\left(\frac{L}{2}\right) = w_0,\ w'\left(\frac{L}{2}\right) = 0 \tag{2.5}$$

Equation (2.4) becomes

$$EIw(x) = -\frac{1}{24}q\left(x^2 - \frac{L^2}{4}\right)^2 + EIw_0 \tag{2.6}$$

The deflection profile function of the microbeam is then used as the truncated admissible trial function. Thus the deflection function $w$ of microbeam subjected to electrostatic force is approximated as

$$\hat{w}(x) = \alpha\left(x^2 - \frac{L^2}{4}\right)^2 + w_0 = \alpha v(x) + w_0 \tag{2.7}$$

where $\alpha$ is a constant to be determined through the Rayleigh-Ritz method.

For the problem described in Equation (2.1), the microbeam strain energy due to bending is defined as

$$U_b = EI\int_0^{L/2}\left(\frac{d^2w}{dx^2}\right)^2 dx \tag{2.8}$$

the microbeam strain energies due to the axial deformation of the residual stress and bending induced stress are given by

$$U_r = bht_r\int_0^{L/2}\left(\frac{dw}{dx}\right)^2 dx \tag{2.9}$$

and

$$U_t = bht_b\int_0^{L/2}\left(\frac{dw}{dx}\right)^2 dx = \frac{Ebh}{L}\left[\int_0^{L/2}\left(\frac{dw}{dx}\right)^2 dx\right]^2 \tag{2.10}$$

respectively. And the electrostatic potential energy is

$$U_e = -\int_0^{L/2}\frac{\varepsilon_0 bV^2}{w + d_i/\varepsilon_r}dx \tag{2.11}$$

where $b$ is the width, $h$ is the thickness of the microbeam, $d_i$ is the thickness of dielectric layer and $\varepsilon_r$ is the relative permittivity. Hence, the total potential energy of the structure can be expressed as

$$\Pi = U_b + U_r + U_t + U_e \tag{2.12}$$

Introducing Equations (2.7)-(2.11) into Equation (2.12), the following expression for the approximate total potential energy is obtained

$$\begin{aligned}\Pi &= EI\int_0^{L/2}\left(\alpha\frac{d^2v}{dx^2}\right)^2 dx + bhT_r\int_0^{L/2}\left(\alpha\frac{dv}{dx}\right)^2 dx \\ &+\frac{Ebh}{L}\left[\int_0^{L/2}\left(\alpha\frac{dv}{dx}\right)^2 dx\right]^2 - \int_0^{L/2}\frac{\varepsilon_0 bV^2}{\alpha v + w_0 + d_i/\varepsilon_r}dx\end{aligned} \tag{2.13}$$

The principle of minimum potential energy states that the potential energy has a stationary value at an equilibrium point. In other words, the system is in equilibrium when the first variation of the total potential energy is zero ($\delta\Pi = 0$), which in the present case, in terms of Rayleigh-Ritz method, becomes

$$\frac{\partial \Pi}{\partial \alpha} = 0 \tag{2.14}$$

hence

$$C_t \alpha^3 + \left(C_b + C_r\right) \alpha + \varepsilon_0 V^2 \int_0^{L/2} \frac{v(x)}{\left[\alpha v(x) + w_0 + d_i / \varepsilon_r\right]^2} dx = 0 \tag{2.15}$$

where $C_t$, $C_b$ and $C_r$ are defined as follows

$$C_t = 4 \frac{Eh}{L} \left[ \int_0^{L/2} \left( \frac{dv}{dx} \right)^2 dx \right]^2 \tag{2.16}$$

$$C_b = \frac{Eh^3}{6} \int_0^{L/2} \left( \frac{d^2 v}{dx^2} \right)^2 dx \tag{2.17}$$

$$C_r = 2hT_r \int_0^{L/2} \left( \frac{dv}{dx} \right)^2 dx \tag{2.18}$$

At this equilibrium point, the electrostatic force is balanced by the microbeam elastic restoring force as described by Equation (2.1). Given a set of quasi-static voltages $V$, Equation (2.15) determines the corresponding constants $\alpha$, and the Equation (2.7) gives the deflection profiles of the microbeam. The increase of quasi-static voltage will increase the electrostatic force and decrease the gap spacing between the deformable microbeam and bottom surface. As the electrostatic force is inversely proportional to the square of the gap spacing, the decrease of gap spacing results in an increase of electrostatic force. When the applied quasi-static voltage increases and reaches a value equal to the pull-in voltage $V_{\mathrm{PI}}$, the electrostatic force becomes larger than the microbeam elastic restoring force for any deformation and the system exhibits sharp instability resulting in the collapse of microbeam and the gap spacing becomes to zero. The stability of the system is determined by the second variation of the total potential energy. If the total potential energy has a minimum at an equilibrium point and the second variation is said to be positive definite ($\delta^2 \Pi \geq 0$), then the equilibrium

point is stable. Otherwise, if $\delta^2 \Pi \leq 0$, the equilibrium point is unstable (Meirovitch, 1997). The pull-in voltage is a critical value at which the equilibrium point changes from stable to unstable and the second variation of the total potential energy is equal to zero ($\delta^2 \Pi = 0$). In the present case, this criterion can be written as

$$\frac{\partial^2 \Pi}{\partial \alpha^2} = 0 \qquad (2.19)$$

Finally, at the pull-in point, Equations (2.15) and (2.19) can be expressed explicitly in terms of pull-in voltage $V_{\mathrm{PI}}$ and constant $\alpha_{\mathrm{PI}}$ (the value of $\alpha$ at pull-in) as follows

$$C_t \alpha_{\mathrm{PI}}^3 + \left(C_b + C_r\right)\alpha_{\mathrm{PI}} + \varepsilon_0 V_{\mathrm{PI}}^2 \int_0^{L/2} \frac{v(x)}{\left[\alpha_{\mathrm{PI}} v(x) + w_0 + d_i/\varepsilon_r\right]^2} dx = 0 \qquad (2.20)$$

$$3C_t \alpha_{\mathrm{PI}}^2 + \left(C_b + C_r\right) - 2\varepsilon_0 V_{\mathrm{PI}}^2 \int_0^{L/2} \frac{v^2(x)}{\left[\alpha_{\mathrm{PI}} v(x) + w_0 + d_i/\varepsilon_r\right]^3} dx = 0 \qquad (2.21)$$

Equations (2.20) and (2.21) constitute a macromodel to determine the pull-in voltage $V_{\mathrm{PI}}$ and the constant $\alpha_{\mathrm{PI}}$ at pull-in. It is noted from the equations that the pull-in voltage is independent of the width of the microbeam.

### 2.2.2 NUMERICAL RESULTS AND DISCUSSION

To validate the present method, example 1 considers a structure with material properties and geometric dimensions listed in Table 2.1. The same device had been studied by Gilbert et al., (1996) using finite element method (FEM) and boundary element method (BEM) based CoSolve-EM module of CoventorWare™. This device was also studied by Anathasuresh et al. (1996) using macromodel generated by normal mode summation method and Aluru (1999) using meshless method when dielectric layer, residual stress and bending induced tension effect were ignored. Without considering these factors, Equations (2.15), (2.20) and (2.21) become

$$C_b\alpha \ + \varepsilon_0 V^2 \int_0^{L/2} \frac{v(x)}{[\alpha v(x) + w_0]^2} dx = 0 \tag{2.22}$$

and

$$C_b\alpha_{\text{PI}} + \varepsilon_0 V_{\text{PI}}^2 \int_0^{L/2} \frac{v(x)}{[\alpha_{\text{PI}} v(x) + w_0]^2} dx = 0 \tag{2.23}$$

$$C_b - 2\varepsilon_0 V_{\text{PI}}^2 \int_0^{L/2} \frac{v^2(x)}{[\alpha_{\text{PI}} v(x) + w_0]^3} dx = 0 \tag{2.24}$$

Table 2.1 Material properties and geometric dimensions of microbeam for example 1.

| Young's modulus $E$ (GPa) | Initial gap $w_0$ ($\mu$m) | Dielectric layer $d_i$ ($\mu$m) | Thickness $h$ ($\mu$m) | Length $L$ ($\mu$m) | Width $b$ ($\mu$m) |
|---|---|---|---|---|---|
| 169 | 0.7 | 0 | 0.5 | 80 | 10 |

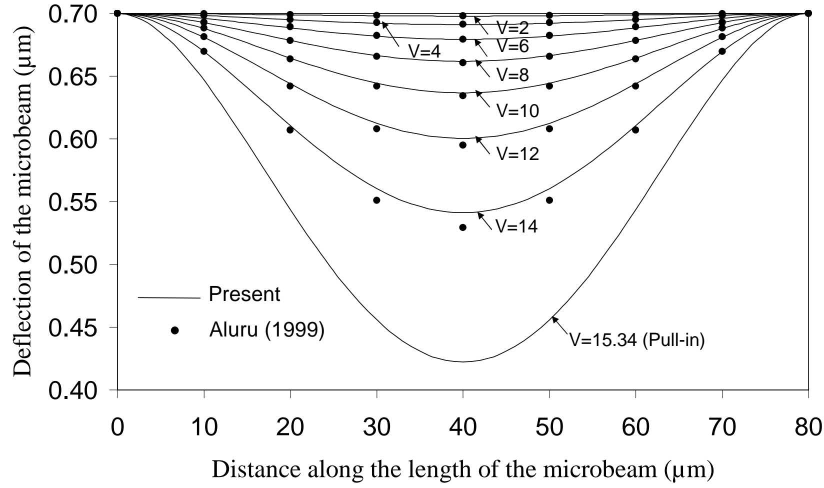


Figure 2.4 Deflection profiles of microbeam for a series of applied voltages.

Substituting Equation (2.7) and the data listed in Table 2.1 into Equations (2.23) and (2.24), the constant $\alpha_{\text{PI}}$ at the pull-in and the pull-in voltage $V_{\text{PI}}$ are obtained. The comparison of the numerical results from the present method with the FEM/BEM

based method CoSolve-EM (Anathasuresh et al. 1996) and meshless method (Aluru, 1999) is listed in Table 2.2.

Table 2.2 Pull-in voltage $V_{\mathrm{PI}}$ and the constant $\alpha_{\mathrm{PI}}$ for example 1.

| Constant $\alpha_{\mathrm{PI}}$ ($\mu\mathrm{m}^{-3}$) | $V_{\mathrm{PI}}$ (V) | | | |
|---|---|---|---|---|
| | Present | CoSolve-EM (Gilbert et al.,1996) | Meshless (Aluru, 1999) | Normal mode summation (Anathasuresh et al., 1996) |
| $-0.1085\times10^{-6}$ | 15.34 | 15 | 15.07 | 15.17 |

Table 2.3 Constant $\alpha$ with respect to the applied voltage $V$.

| Applied quasi-static voltage $V$ (V) | Constant $\alpha$ ($\mu\mathrm{m}^{-3}$) |
|---|---|
| 2 | $-0.8595\times10^{-9}$ |
| 4 | $-0.3489\times10^{-8}$ |
| 6 | $-0.8057\times10^{-8}$ |
| 8 | $-0.1491\times10^{-7}$ |
| 10 | $-0.2470\times10^{-7}$ |
| 12 | $-0.3890\times10^{-7}$ |
| 14 | $-0.6201\times10^{-7}$ |
| 15.34 (Pull-in) | $-0.1085\times10^{-6}$ |

It is noted that the reason for the present relative larger value of $V_{\mathrm{PI}}$ compared with the other simulation results is because that the energy method generally gives upper bound result and the fringe-filed correction that softens the microbeam is not considered here but in Anathasuresh's and Aluru's. Nevertheless, the agreement between the present method and the CoSolve-EM is good with 2.3% difference when only one global admissible trial function is used in the present simulation. When the applied voltage is less than $V_{\mathrm{PI}}$=15.34V, Table 2.3 gives a series of constants $\alpha$ corresponding to a set of applied quasi-static voltages, the microbeam deflection profiles obtained by the present method and Aluru's meshless method are plotted in Figure 2.4, respectively.

The second example considers a structure with material properties and geometric dimensions listed in Table 2.4. Considering the bending induced tension effect due to larger deformation, Equations (2.20) and (2.21) become

$$C_t\alpha_{\mathrm{PI}}^3 + C_b\alpha_{\mathrm{PI}} + \varepsilon_0 V_{\mathrm{PI}}^2 \int_0^{L/2} \frac{v(x)}{\left[\alpha_{\mathrm{PI}} v(x) + w_0\right]^2} dx = 0 \tag{2.25}$$

$$3C_t\alpha_{\mathrm{PI}}^2 + C_b - 2\varepsilon_0 V_{\mathrm{PI}}^2 \int_0^{L/2} \frac{v^2(x)}{\left[\alpha_{\mathrm{PI}} v(x) + w_0\right]^3} dx = 0 \tag{2.26}$$

Solving the above two equations simultaneously yields the pull-in voltage $V_{\mathrm{PI}}$ and the constant $\alpha_{\mathrm{PI}}$ at pull-in. Comparison of the simulation results from present resolution with and without considering the bending induced tension against the shooting method (Ngiam, 2000) and CoSolve-EM of CoventorWare™ is listed in Table 2.5. The result of present solution agrees well with the CoSolve-EM with around 0.2% difference. In this case, it is noted that pull-in voltage is less by 3% if bending induced tension effect is not considered.

Table 2.4 Material properties and geometric dimensions of microbeam for example 2.

| Young's modulus $E$ (GPa) | Initial gap $w_0$ ($\mu$m) | Dielectric layer $d_i$ ($\mu$m) | Thickness $h$ ($\mu$m) | Length $L$ ($\mu$m) | Width $b$ ($\mu$m) |
|---|---|---|---|---|---|
| 165 | 1 | 0 | 2 | 400 | 45 |

Table 2.5 Pull-in Voltage $V_{\mathrm{PI}}$ and the constant $\alpha_{\mathrm{PI}}$ at pull-in for example 2.

| Constant $\alpha_{\mathrm{PI}}$ ($\mu\mathrm{m}^{-3}$) | $V_{\mathrm{PI}}$ (V) | | |
|---|---|---|---|
| | Present | CoSolve-EM | Shooting method (Ngiam, 2000) |
| -0.2650$\times 10^{-9}$ | 8.518 | 8.5 | 8.38 |
| -0.2481$\times 10^{-9}$ * | 8.28* | - | - |

* The bending induced tension effect is ignored.

## 2.3 CONTACT OVER A FINITE LENGTH

### 2.3.1 GLOBAL ADMISSIBLE TRIAL FUNCTIONS AND MACROMODEL

In this region, the finite length of microbeam in contact with the bottom dielectric layer surface is assumed to be over $x = \rho$ as shown in Figure 2.5.

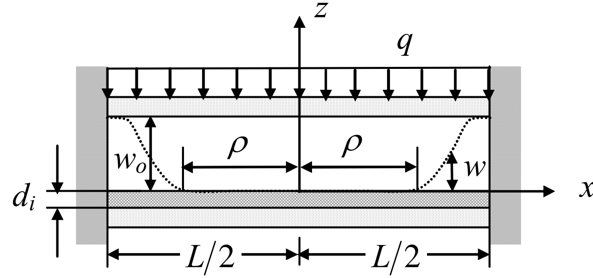


Figure 2.5 Schematic view a doubly-clamped microbeam subjected to a uniformly distributed force in region of contact.

For $0 \le x \le \rho$, $w = 0$. For $\rho \le x \le L/2$, considering the bending momonet and curvature vanish at the point of contact (Timoshenko, 1956), the microbeam satisfies the following bounday conditions

$$w(\rho) = w''(\rho) = 0$$
$$w\left(\frac{L}{2}\right) = w_0,\; w'\left(\frac{L}{2}\right) = 0 \tag{2.27}$$

Hence the beam deflection for a constant load $q$ is obtained as

$$EIw(x) = -\frac{q}{24}(x-\rho)\left[(x-\rho)^3 - \frac{3}{2}\left(\frac{L}{2}-\rho\right)(x-\rho)^2 + \frac{1}{2}\left(\frac{L}{2}-\rho\right)^3\right]$$
$$+\frac{EIw_0}{2\left(\frac{L}{2}-\rho\right)}(x-\rho)\left[3 - \frac{(x-\rho)^2}{\left(\frac{L}{2}-\rho\right)^2}\right] \tag{2.28}$$

If the microbeam is subjected to the electrostatic force loading after pull-in, the beam deflection profile in this region is then assumed as the linear combination of the truncated global admissible trial functions as follows

$$\hat{w}(x) = \alpha(x-\rho)\left[(x-\rho)^3 - \frac{3}{2}\left(\frac{L}{2}-\rho\right)(x-\rho)^2 + \frac{1}{2}\left(\frac{L}{2}-\rho\right)^3\right]$$
$$+\frac{w_0}{2\left(\frac{L}{2}-\rho\right)}(x-\rho)\left[3-\frac{(x-\rho)^2}{\left(\frac{L}{2}-\rho\right)^2}\right] = \alpha v_1 + v_2 \tag{2.29}$$

where the coefficient $\alpha$ and the value of $\rho$ are to be determined.

If the residual stress and the bending induced tension are ignored in this region, the total potential energy can be expressed as

$$\Pi = U_b + U_e \tag{2.30}$$

Using Equations (2.8) and (2.11), and substituting the approximate solutions of the deflection, Equation (2.29), into Equation (2.30), the approximate total potential energy of the system in this region can be expressed as

$$\Pi = EI\int_{\rho}^{L/2}\left(\alpha\frac{d^2v_1}{dx^2}+\frac{d^2v_2}{dx^2}\right)^2 dx - \int_0^{\rho}\frac{\varepsilon_0 bV^2}{d_i/\varepsilon_r}dx - \int_{\rho}^{L/2}\frac{\varepsilon_0 bV^2}{\alpha v_1 + v_2 + d_i/\varepsilon_r}dx \tag{2.31}$$

The Rayleigh-Ritz method asserts that the stationary property of the solution of the above equation can be satisfied approximately by requiring $\delta\Pi = 0$, which in the present case, becomes

$$\frac{\partial\Pi}{\partial\alpha} = 0, \quad \left[\frac{Eh^3}{6}\int_{\rho}^{L/2}\left(\frac{d^2v_1}{dx^2}\right)^2 dx\right]\alpha + \frac{Eh^3}{6}\int_{\rho}^{L/2}\frac{d^2v_1}{dx^2}\frac{d^2v_2}{dx^2}dx$$
$$+\varepsilon_0 V^2\int_{\rho}^{L/2}\frac{v_1(x)}{[\alpha v_1(x)+v_2(x)+d_i/\varepsilon_r]^2}dx = 0 \tag{2.32}$$

and

$$\frac{\partial \Pi}{\partial \rho} = 0, \quad \frac{E}{12} h^3 \left[ \int_{\rho}^{L/2} \frac{\partial}{\partial \rho} \left( \alpha \frac{d^2 v_1}{dx^2} + \frac{d^2 v_2}{dx^2} \right)^2 dx - \left( \alpha \frac{d^2 v_1}{dx^2} + \frac{d^2 v_2}{dx^2} \right)^2_{x=\rho} \right]$$

$$- \varepsilon_0 V^2 \left\{ \frac{1}{d_i / \varepsilon_r} + \int_{\rho}^{L/2} \frac{\partial}{\partial \rho} \left( \frac{1}{[\alpha v_1(x) + v_2(x) + d_i / \varepsilon_r]} \right) dx \right. \tag{2.33}$$

$$\left. - \frac{1}{[\alpha v_1(x) + v_2(x) + d_i / \varepsilon_r]_{x=\rho}} \right\} = 0$$

The above Equations (2.32) and (2.33) constitue a macromodel which determine the values of $\alpha$ and $\rho$, which, when substituted into Equation (2.29) provide the approximate solutions for the microbeam deflection profile when it comes in contact with the bottom dielectric layer surface.

### 2.3.2 NUMERICAL RESULTS AND DISCUSSION

A system with the material properties and geometric dimension listed in Table 2.6 is examined to validate the present method. Figure 2.6 shows the contact length with respect to the applied quasi-static voltage. The release voltage $V_{\mathrm{R}}$ is defined as a voltage corresponding to the zero contact length, or point contact of the microbeam with bottom surface (Jacobson et al., 1995), which is around 10.4V computated by the present method while it is calculated at around 11V by the three dimentional CoSolve-EM (Gilbert et al.,1996). Since $V_{\mathrm{R}}$ =10.4 is less than pull-in voltage $V_{\mathrm{PI}}$ =15.34, some length of microbeam will be remaining in contact with the bottom surface even when the applied voltage is quasistatically decreased from $V_{\mathrm{PI}}$ after pull-in. The presence of this difference exhibits the system electromechanical hysteresis as shown in Figure 2.6. This hysteresis effect is important as it allows a voltage gap between the actuation

voltage and the de-actuation voltage for some MEMS device designs. The microbeam deflection profiles and the contact lengths corresponds to a series applied volages are plotted in Figure 2.7.

Table 2.6 Material properties and geometric dimensions of microbeam.

| Young's modulus $E$ (GPa) | Initial gap $w_0$ ($\mu$m) | Dielectric layer $d_i$ ($\mu$m) | Relative permittivity $\varepsilon_r$ | Thickness $h$ ($\mu$m) | Length $L$ ($\mu$m) | Width $b$ ($\mu$m) |
|---|---|---|---|---|---|---|
| 169 | 0.6 | 0.1 | 1 | 0.5 | 80 | 10 |

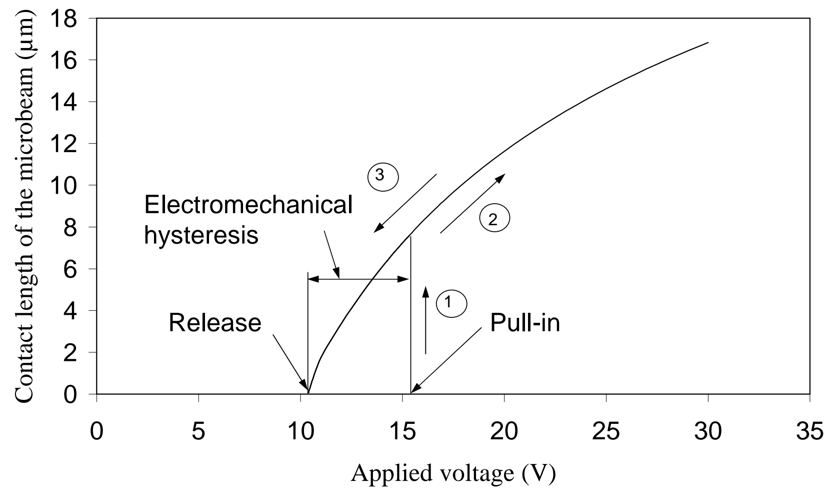


Figure 2.6 Contact length of microbeam $\rho$ with respect to applied voltage.

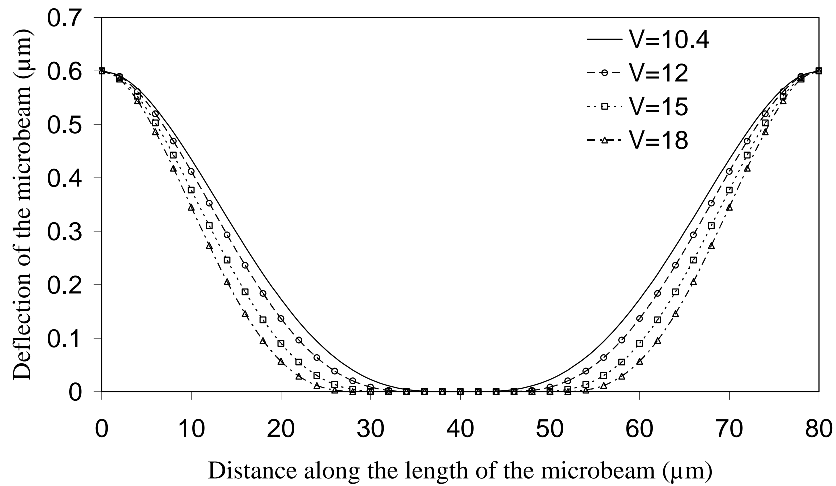


Figure 2.7 Deflection profiles of microbeam for a series of applied voltages.

## 2.4 CONCLUSION

Approximate solution for the nonlinear differential equation with boundary conditions through the use of variational principle and Rayleigh-Ritz method can provide an accurate and efficient tool for electrostatic actuators simulation and analysis. It has demonstrated in this chapter that, for MEMS devices modelled as doubly-clamped microbeam, the global admissible trial functions obtained from the deflection profile of a doubly-clamed beam with uniformly distributed load can be used in the macromodel generation to yield accurate results in pull-in voltage and the electromechanical hysteresis compared with those obtained from FEM/BEM based commercial CoSolve-EM package and other numerical techniques, such as meshless and shooting methods.

# CHAPTER 3

# MACROMODELS FOR DYNAMIC SIMULATION OF MEMS USING KARHUNEN-LOÈVE DECOMPOSITION

A model order reduction technique based on Karhunen-Loève decomposition (KLD) and Galerkin procedure to generate macromodels for dynamic simulation and analysis of nonlinear microelectromechanical systems and devices is presented in this chapter. KLD, also known as proper orthogonal decomposition (POD) has emerged as an important model order reduction technique for fast and accurate simulation of continuous systems with infinite degrees-of-freedom. KLD, in essence, is a method of representing a stochastic system with a minimum number of degrees-of-freedom (Loève, 1955). It is a procedure for extracting a basis for modal decomposition from an ensemble of signals or data obtained in the course of experiments or numerical simulations. This basis is a set of orthogonal empirical eigenfunctions of KLD, which are called as Karhunen-Loève modes (KLMs) in this thesis, are also known as proper orthogonal modes (POMs). Their corresponding empirical eigenvalues, which are called as Karhunen-Loève values (KLVs) here, are also named as proper orthogonal values (POVs). The KLVs provide a measure of the importance of each of the KLMs, that is the KLMs can be ranked in descending order of signal power by using the corresponding descending order of the KLVs. The KLMs can be used to obtain low-dimensional approximate description of a high-dimensional system. The most striking feature of KLD is its optimality: it provides the most efficient way of capturing the dominant components of an infinite-dimensional system with only a finite number of "modes", and often surprisingly fewer "modes" than the first few functions of any

other basis (Holmes et al., 1996; Kirby, 2001). Another key feature of KLD lies in the fact that it is a robust method for the nonlinear system. Although it is a linear procedure of superposition by a finite or an infinite sum of modal functions multiplied by appropriate coefficients, KLD makes no assumptions about the linearity of the system to which it is applied. In other words, this linear representation in terms of basis functions chosen a priori or by KLD are blind to the origin of the functions they are called upon to represent, which may derive from nonlinear dynamical process. It is also noted that the KLMs obtained from KLD procedure for a certain set of system parameters can, in most cases, be used to reconstruct the response of a system whose parameters are slightly different from the original system. This is a distinctive advantage in a sense that KLMs need not to be regenerated with the changes of the system parameters so long as the changes do not affect the system behaviours. KLD has been applied successfully in many science and engineering fields, including image processing (Kirby, 2001), data compression (Reed, 1994), pattern recognition (Fukunaga, 1990), damage detection (Banks et al., 2000; Feldmann et al., 2000), process identification and control in chemical engineering (Baker et al., 2000) and etc. In the bulk of these applications, KLD is used to analyse experimental data with the objective of extracting dominant features of the systems. In its applications as a model order reduction technique, KLD has been used to obtain approximate, low dimensional descriptions of vibration analysis (Azeez and Vakakis, 2001), structure mechanics (Ma and Vakakis, 1999; Ma et al, 2001), fluid dynamics (Sirovich, 1987a, 1987b, 1987c; Park and Cho 1996), and more recently MEMS (Hung and Senturia, 1999; Lin et al., 2001; Liang et al., 2001). In this chapter, KLD method is applied to develop low dimensional macromodels to simulate pull-in dynamics of MEMS devices modelled as doubly-clamped microbeam with squeezed gas-film damping effect. The numerical

results show that the macromodels can significantly reduce the computation time and achieve close agreement with those obtained by fully meshed finite difference method (FDM).

### 3.1 THEORY OF KARHUNEN-LOÈVE DECOMPOSITION

Suppose that there is an ensemble of scalar fields $\{u_n\}$, each member of the ensemble is a continuous function $u_n = u_n(x)$ defined on some spatial domain $\Omega$ taken at various snapshots in time instant of $n = 1, 2, \cdots, N$. The objective of KLD is to find a deterministic function $\phi(x)$ that is the most representative to the members of $u_n(x)$ on average. The mathematical statement of for this is that a function $\phi(x)$ to be chosen maximizes the averaged projection of $u_n$ onto $\phi$ , i.e.

$$\text{Maximize } \left\langle (\phi, u_n)^2 \right\rangle \tag{3.1}$$

where $\langle \bullet \rangle$ is the averaging operator that may be a time, space or ensemble average and $(\phi, u_n) = \int_\Omega \phi(x)\, u_n(x)\, d\Omega$ is the inner product defined in the function space $\Omega$. Equation (3.1) is expressed as

$$\begin{aligned} \text{Maximize } \left\langle (\phi, u_n)^2 \right\rangle &= \left\langle \int_\Omega \phi(x) u_n(x) dx \int_\Omega \phi(x') u_n(x')\, dx' \right\rangle \\ &= \int_\Omega \left[ \int_\Omega \langle u_n(x) u_n(x') \rangle\, \phi(x) dx \right] \phi(x')\, dx' \end{aligned} \tag{3.2}$$

Several solutions to $\phi$ for the above equation can exist, in order to make the solution unique, the following normalization condition is imposed

$$(\phi, \phi) = \int_\Omega \phi^2(x)\, dx = 1 \tag{3.3}$$

Using the technique of the Lagrange multiplier, the corresponding functional for the constrained variational problem of Equation (3.2) subject to the constraint (3.3) is obtained

$$J[\phi] = \left\langle (\phi, u_n)^2 \right\rangle - \lambda[(\phi,\phi) - 1] \tag{3.4}$$

The necessary condition for extrema is that the first variation of functional vanishes

$$\delta J[\phi] = \frac{d}{d\varepsilon} J[\phi + \varepsilon\eta] \,|_{\varepsilon=0} = 0 \tag{3.5}$$

where $\eta(x)$ is an arbitrary function and $\varepsilon$ is a small real number. From Equation (3.4), the above condition becomes

$$\begin{aligned}
\frac{d}{d\varepsilon} J[\phi + \varepsilon\eta] \,|_{\varepsilon=0} &= \frac{d}{d\varepsilon}\left\{ \left\langle (\phi + \varepsilon\eta,\ u_n)^2 \right\rangle - \lambda[(\phi + \varepsilon\eta,\ \phi + \varepsilon\eta) - 1] \right\} |_{\varepsilon=0} \\
&= \frac{d}{d\varepsilon}\left\{ \left\langle \int_\Omega [\phi(x) + \varepsilon\eta(x)]\, u_n(x)\, dx \int_\Omega [\phi(x') + \varepsilon\eta(x')]\, u_n(x')\, dx' \right\rangle \right. \\
&\qquad \left. - \lambda\left[ \int_\Omega [\phi(x) + \varepsilon\eta(x)]^2\, dx - 1 \right] \right\} |_{\varepsilon=0} \\
&= \frac{d}{d\varepsilon}\left\{ \int_\Omega \left[ \int_\Omega \langle u_n(x) u_n(x') \rangle [\phi(x') + \varepsilon\eta(x')]\, dx' \right] [\phi(x) + \varepsilon\eta(x)]\, dx \right. \\
&\qquad \left. - \lambda\left[ \int_\Omega [\phi(x) + \varepsilon\eta(x)]^2\, dx - 1 \right] \right\} |_{\varepsilon=0} \\
&= 2\left\{ \int_\Omega \left[ \int_\Omega \langle u_n(x) u_n(x') \rangle \phi(x')\, dx' \right] \eta(x)\, dx - \lambda \int_\Omega \phi(x)\, \eta(x)\, dx \right\} \\
&= 2\int_\Omega \left[ \int_\Omega \langle u_n(x) u_n(x') \rangle \phi(x')\, dx' - \lambda\phi(x) \right] \eta(x)\, dx = 0
\end{aligned} \tag{3.6}$$

Since $\eta(x)$ is an arbitrary function, the above condition is finally reduced to

$$\int_\Omega \langle u_n(x) u_n(x') \rangle\, \phi(x')\, dx' - \lambda\phi(x) = 0 \tag{3.7}$$

Introducing an averaged two-points correlation function

$$K(x,x') = \langle u_n(x)\, u_n(x') \rangle = \frac{1}{N}\sum_{n=1}^{N} u_n(x)\, u_n(x') \tag{3.8}$$

and denoting an operator

$$R(\bullet) \equiv \int_{\Omega} K(x,x')(\bullet)dx' \tag{3.9}$$

as well as moving the second item on the left-hand side of Equation (3.7) to the right-hand side, it is revealed that the condition for maximizing Equation (3.1) subjected to the constraint of Equation (3.3) is finally reduced to the following integral eigenvalue problem

$$R\,\phi = \lambda\phi \tag{3.10}$$

It is noted that $K(x,x')$ is non-negative definite that implies that the integral operator $R(\bullet)$ is non-negative definite. Hence the eigenvalue in Equation (3.10) is also assured to be non-negative, i.e. $\lambda_i \geq 0$. Schmidt-Hilbert theory assures that there are $N$ number of eigenvalues $\lambda_i$ and eigenfunctions $\phi_i(x)$ which are mutually orthogonal for eigenvalue problem of Equation (3.10) and two-points correlation function of Equation (3.8) can be decomposed as

$$K(x,x') = \langle u_n(x)\, u_n(x') \rangle = \sum_{n=1}^{N} \lambda_n \phi_n(x)\, \phi_n(x') \tag{3.11}$$

Equation (3.10) can be solved by direct method or method of snapshots (Sirovitch, 1987a; 1987b; 1987c). The method of snapshots is a numerical procedure in solving the eigenvalue problem of Equation (3.10), in which the eigenfunction $\phi(x)$ can be represented as the linear combination of snapshots $\{u_n\}$ as follows

$$\phi(x) = \sum_{k=1}^{N} \alpha_k u_k(x) \tag{3.12}$$

where the coefficients $\alpha_k$ remain to be determined. It is customary to mean-subtract each member in the ensemble of snapshots $\{u_n\}$. Substituting Equation (3.12) into (3.10) yields the following $N-$dimensional eigenfunction problem

$$\int_{\Omega} \frac{1}{N} \sum_{n=1}^{N} u_n(x)\, u_n(x') \sum_{k=1}^{N} \alpha_k u_k(x')\, dx' = \lambda \sum_{k=1}^{N} \alpha_k u_k(x) \tag{3.13}$$

The left-hand side of the above equation can be rearranged to give

$$\sum_{n=1}^{N} \left\{ \sum_{k=1}^{N} \left[ \frac{1}{N} \int_{\Omega} u_n(x')\, u_k(x')\, dx' \right] \alpha_k \right\} u_n(x) = \lambda \sum_{k=1}^{N} \alpha_k u_k(x) \tag{3.14}$$

Hence a sufficient condition for the solution of Equation (3.14) will result in the following matrix eigenvalue problem for determination of the coefficient $\alpha_k$

$$\sum_{k=1}^{N} \left[ \frac{1}{N} \int_{\Omega} u_n(x')\, u_k(x')\, dx' \right] \alpha_k = \lambda \alpha_n, \quad n = 1, 2, \ldots, N \tag{3.15}$$

or

$$C\alpha = \lambda \alpha \tag{3.16}$$

where the element in matrix $C$ is defined as

$$C_{nk} = \frac{1}{N}(u_n, u_k) = \frac{1}{N} \int_{\Omega} u_n(x')\, u_k(x')\, dx', \quad n,k = 1, 2, \ldots, N \tag{3.17}$$

and the set of eigenvectors is given as

$$\alpha = (\alpha_1, \alpha_2, \ldots, \alpha_N) \tag{3.18}$$

It is noted that the above matrix $C$ has dimensions $N \times N$ and is symmetric and positive definite, $\alpha$ is the set of eigenvectors containing the unknown coefficient $\alpha_k$. Solving for eigenvalues $\lambda$ and eigenvectors $\alpha$ in Equation (3.16) and substituting $\alpha$ into Equation (3.12) yield the empirical eigenfunctions $\phi_n(x)$ which satisfy the following orthogonality relation

$$(\phi_j, \phi_k) = \begin{cases} 1 & (j = k) \\ 0 & (j \neq k) \end{cases} \tag{3.19}$$

Finally, every member of the original ensemble could be reconstructed by a modal decomposition in terms of the linear combination of eigenfunctions $\phi(x)$

$$u_n(x) = \sum_{k}^{N} a_k \phi_k(x) \tag{3.20}$$

Substituting the above Equation (3.20) into Equation (3.8), the following is obtained

$$K(x,x') = \langle u_n(x)\, u_n(x') \rangle = \left\langle \sum_{j}^{N} a_j \phi_j(x) \sum_{k}^{N} a_k \phi_k(x') \right\rangle = \sum_{jk}^{N} \left\langle a_j a_k \right\rangle \phi_j(x) \phi_k(x') \tag{3.21}$$

Comparing Equation (3.21) with Equation (3.11) and taking consideration of the orthogonality of the eigenfunctions $\phi_k(x)$ leads to

$$\left\langle a_j a_k \right\rangle = \delta_{jk} \lambda_j \tag{3.22}$$

The first eigenfunction is found by requiring that it maximizes

$$\left\langle (\phi_1, u_n)^2 \right\rangle \tag{3.23}$$

or, equivalently, by requiring that it maximizes

$$\left\langle (\phi_1, u_n)^2 \right\rangle = \left\langle \int_{\Omega} \phi_1(x) \left[ \sum_{n=1}^{N} a_n \phi_n(x) \right] dx \int_{\Omega} \phi_1(x') \left[ \sum_{n=1}^{N} a_n \phi_n(x') \right] dx' \right\rangle \tag{3.24}$$

subjected to the orthonormal condition of eigenfunctions. Using the Equation (3.22), the following result is found

$$\text{Maximum} \quad \left\langle (\phi_1, u_n)^2 \right\rangle = \left\langle a_1^2 \right\rangle = \lambda_1 \tag{3.25}$$

Following this procedure, the second eigenvalue is defined by requiring that

$$\text{Maximum} \quad \left\langle (\phi_2, u_n)^2 \right\rangle = \left\langle a_2^2 \right\rangle = \lambda_2 \tag{3.26}$$

and so on for the remaining eigenfunctions and eigenvalues. Hence the order of eigenfunctions $\phi_1(x),\ \phi_2(x),\ldots,\phi_N(x)$ can be arranged corresponding to the order of the

magnitude of the eigenvalues $\lambda_1 > \lambda_2 > ... > \lambda_N$. And the eigenfunction $\phi_1(x)$ corresponding to the largest eigenvalue $\lambda_1$ is the most representative to the members of the ensemble snapshots $\{u_n\}$ followed by the eigenfunction $\phi_2(x)$ and so forth, i.e. the most of the structural information, or energy, is captured by the subspace associated with the first few eigenfunctions (Sirovitch, 1987a; 1987b; 1987c).

Equation (3.20) is called Karhunen-Loève decomposition. The eigenvalues $\{\lambda_i\}$ are also called empirical eigenvalues or Karhunen-Loève values (KLVs), and the corresponding eigenfunctions $\{\phi_i\}$ are also referred to as empirical eigenfunctions, empirical basis functions, or Karhunen-Loève modes (KLMs) which can represent the system in the most efficient and optimal way. In other words, the first $m$ KLMs capture more energy on average than the first $m$ functions of any other basis. When the first few KLMs are employed as basis functions in the Galerkin procedure, the original high-dimensional system can be represented by a low-dimensional model with minimum number of degrees-of-freedom.

## 3.2 GALERKIN PROCEDURE

The Galerkin procedure, or Galerkin projection, is a well-known method that converts an infinite-dimensional evolution equation or partial differential equation (PDE) into a finite set of ordinary differential equations (ODEs). In this procedure the functions defining the original equation are projected onto a finite-dimensional subspace of the full phase space. The finite-dimensional subspace is spanned by small sets of basis functions. Considering the PDE described as follows

$$\frac{du(x,t)}{dt} - L[u(x,t)] = 0 \tag{3.27}$$

where $u(x,t)$ is a function defined on a spatial domain $\Omega$ and $L[\bullet]$ is a nonlinear partial differential operator that may involve spatial derivatives and/or integrals. Given a basis $\{\phi_n(x)\}$ for the solutions to the PDE, $u(x,t)$ can be expressed as sum of time-dependant model coefficients multiplied by elements of the basis

$$u(x,t) = \sum_{i}^{\infty} a_i(t)\phi_i(x) \tag{3.28}$$

This solution is then approximated by a $N$ term truncated basis functions as

$$u(x,t) \approx \sum_{i}^{N} a_i(t)\phi_i(x) \tag{3.29}$$

Substituting Equation (3.29) into the left-hand side of Equation (3.27) and taking the inner product of this with each member of the $N$ term truncated basis functions $\{\phi_n(x)\}$, $n = 1, 2, \ldots, N$ in turn and equating each expression to zero, the following expression is obtained

$$\left(\phi_k, \frac{du(x,t)}{dt} - L[u(x,t)]\right) = 0, \quad k = 1, 2, \ldots, N \tag{3.30}$$

Noting that

$$\left(\phi_k, \frac{du(x,t)}{dt}\right) = \left(\phi_k, \frac{d}{dt}\sum_{n}^{N} a_n(t)\phi_n(x)\right) = \sum_{n}^{N} \frac{da_n(t)}{dt}(\phi_k, \phi_n) = \frac{da_k(t)}{dt} \tag{3.31}$$

a set of $N$ ordinary defferential equations (ODEs) to determine the coefficients $a_k(t)$ is then derived from Equation (3.30)

$$\frac{da_k(t)}{dt} = f_k[a_1(t), a_2(t), \cdots, a_N(t)], \quad k = 1, 2, \ldots, N \tag{3.32}$$

A suitable choice of truncation order $N$ will depend upon the properties of the original equations and the basis functions.

## 3.3 THE RELATIONSHIP BETWEEN KARHUNEN-LOÈVE MODES AND THE VIBRATION MODES OF THE DISTRIBUTED PARAMETER SYSTEM

In the area of the structural dynamic analysis and system identification, many researchers from different groups have demonstrated that KLD can be used to obtain accurate low-dimensional dynamic models (Ma et al., 2000; Georgiou and Schwartz, 1999; Cusumano et al., 1994). The modes derived by KLD are optimal in the sense that fewer modes could capture the same amount of energy among modes compared with modes resulting from the traditional Galerkin or Rayleigh-Ritz procedure (Sirovich et al., 1990). However, there is lack of clear description given to show the relationship between the KLMs and the normal modes of the vibration. With the increasing applications of KLD method in structural dynamics, it is worthwhile to find this relationship. It had been pointed out in (Feeny and Kappagantu, 1998) that in discrete vibration systems, the eigenvectors extracted from numerical simulation data by KLD converged to the normal modes of vibration if the number of the data in the ensemble was large enough, and the eigenvalues were related to the principal moments of inertia. This section extends this finding from the discrete vibration system to the conservative distributed parameter vibration system, and shows that, for the distributed parameter vibration system, the KLMs derived from an ensemble of numerical simulation data converge to the mode shape of the vibration of the system.

### 3.3.1 FREE VIBRATION OF THE CONSERVATIVE DISTRIBUTED PARAMETER SYSTEM

Assume a distributed parameter vibration system executes synchronous harmonic motion in the following form

$$u(x) = \sum_{n}^{\infty} C_n \cos(\omega_n t - \xi_n) W_n(x) \tag{3.33}$$

where $W_n$ is the $n-$th mode, $\omega_n$ and $\xi_n$ are the corresponding natural frequency and phase of the $n-$th mode. In order to demonstrate whether the KLMs converge to the modes of the vibration, the following approximation needs to be verified whether it is valid

$$\int_{\Omega} K(x,x')\, W_j(x')\, dx' \equiv \int_{\Omega} \frac{1}{N} \sum_{n=1}^{N} u_n(x)\, u_n(x')\, W_j(x')\, dx' \quad \text{approaches } \lambda W_j(x) \tag{3.34}$$

where $N$ is the total number of the snapshots. Using Equation (3.33), the left-hand side of Equation (3.34) may be rewritten as

$$\frac{1}{N} \sum_{n=1}^{N} \sum_{k} C_k \cos(\omega_k t_n - \xi_k) W_k(x) \int_{\Omega} \sum_{k} C_k \cos(\omega_k t_n - \xi_k) W_k(x') W_j(x') dx' \tag{3.35}$$

Considering the orthogonal property of the vibration modes

$$\int_{\Omega} W_k(x)\, W_j(x)\, dx = A_j\, \delta_{jk} \tag{3.36}$$

Equation (3.35) becomes

$$\frac{1}{N} \sum_{n=1}^{N} \left\{ \sum_{k} C_k \cos(\omega_k t_n - \xi_k) W_k(x) \right\} A_j C_j \cos(\omega_j t_n - \xi_j) \tag{3.37}$$

If the frequencies and phases of the vibration modes are distinct, and the total number of the snapshots $N$ approaches infinite, then Equation (3.37) becomes

$$\lim_{N \to \infty} \frac{1}{N} \sum_{n=1}^{N} \left\{ \sum_{k} C_k \cos(\omega_k t_n - \phi_k) W_k(x) \right\} A_j C_j \cos(\omega_j t_n - \phi_j) = A_j C_j^2 W_j(x) \tag{3.38}$$

Hence, it is proved that $W_j(x)$ is an eigenfunction of the following eigenvalue problem

$$\lim_{N\to\infty}\int_{\Omega} K(x,x')\, W_j(x)\, dx' = A_j C_j^2\ W_j(x) = \lambda\ W_j(x) \tag{3.39}$$

In other words, the KLMs converge to the modes of vibration of a distributed parameter system when the total size of the snapshots is large enough.

### 3.3.2 NUMERICAL RESULTS AND DISCUSSION

A problem for consideration in vibration is that of a string fixed at both ends. Considering a flexible string of mass $\rho$ per unit length which is stretched under tension $T$ and assuming that the lateral deflection $u(x,t)$ of the string is small, the equation for the lateral deflection in the general case of free vibration initiated in any manner can be obtained as follows (Thomson and Dahleh, 1998)

$$u(x,t) = \sum_{n=1}^{\infty}(C_n \sin\omega_n t + D_n \cos\omega_n t)W_n(x) \tag{3.40}$$

where the normal mode $W_n(x)$ is sinusoidal with the distribution $\sin(n\pi x/L)$ where $L$ is the length of the string, $\omega_n = n\pi\sqrt{T/(\rho L^2)}$ is the natural frequency of the $n-$th mode, $C_n$ and $D_n$ are constants determined by the initial and the boundary conditions. Assume the string is displaced into a shape

$$u(x,0) = -\frac{x}{L}(L-x)e^{-x/L} \tag{3.41}$$

and released, thus the $C_n$ and $D_n$ in Equation (3.40) become

$$C_n = 0$$

$$D_n = -\frac{2L}{\left(1+n^2\pi^2\right)^3}\left[-8e^{-1}\cos(n\pi)n\pi + 4n\pi - 4n^3\pi^3\right], \quad (n = 1, 2, \ldots) \tag{3.42}$$

In the following numerical computation tests to demonstrate the relationship between the KLMs and vibration modes, snapshots are obtained from the numerical solution of Equation (3.40) with the number of vibration modes taken as $n = 20$. The KLMs and KLVs for various ensembles of snapshots are obtained by making use of the Equations (3.12) and (3.16). In the first computation test, KLMs and KLVs are obtained by applying KLD to a number of ensembles of snapshots which are evenly taken at fixed time interval within one fundamental period of time $t_1 = 2\pi / \omega_1 = 2\sqrt{\rho L^2 / T}$. Figure 3.1 to Figure 3.4 show the first, second, $10-\text{th}$ and $20-\text{th}$ orthonormal KLMs corresponding to the order of magnitude of the respective KLVs $\lambda_1, \lambda_2, \lambda_{10}$ and $\lambda_{20}$ when the number of the snapshots is 30 and 50, respectively.

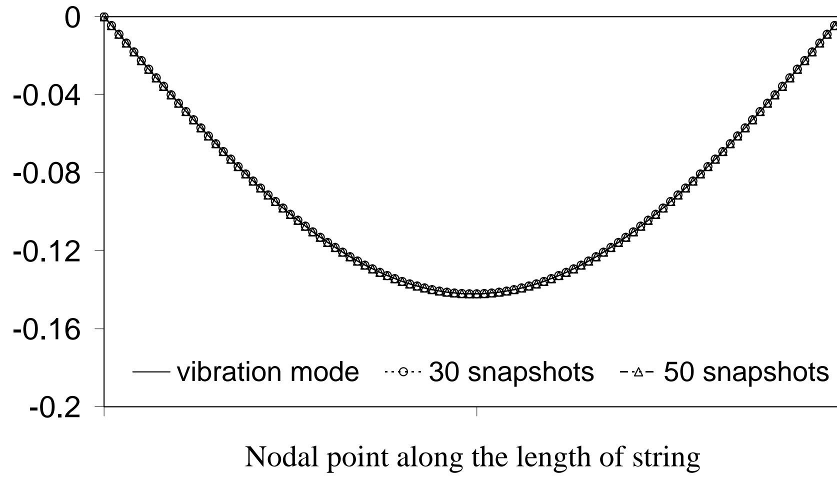


Figure 3.1 The first KLM and the first mode of the vibration.

The mean square error between the KLM and the corresponding vibration mode is defined as

$$MSE = \frac{1}{L}\int_L (\phi_i - W_i)^2 dx \tag{3.43}$$

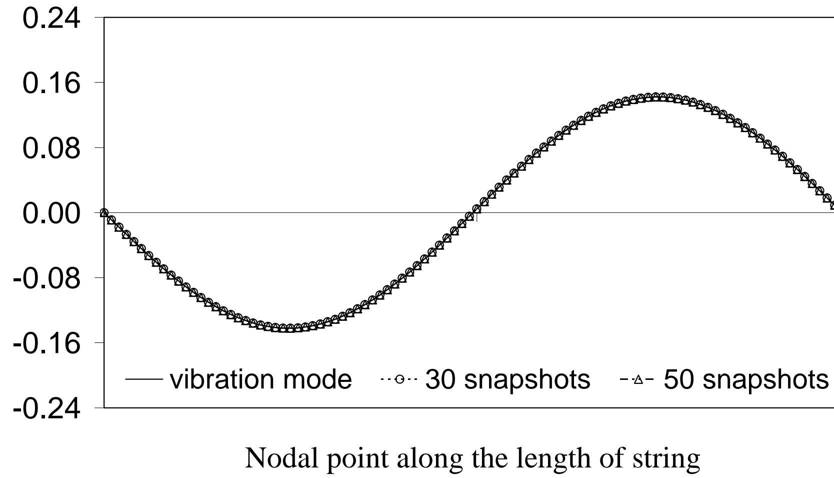


Figure 3.2 The second KLM and the second mode of the vibration.

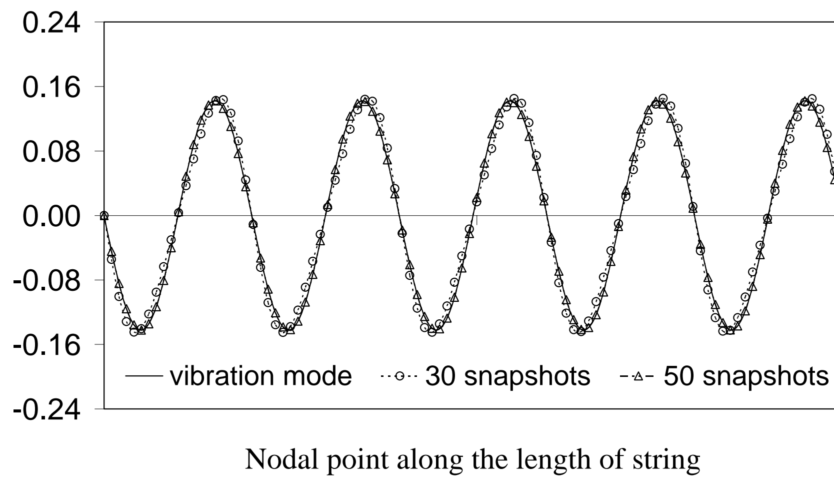


Figure 3.3 The $10-\text{th}$ KLM and $10-\text{th}$ mode of the vibration.

Figure 3.5 shows the MSE for the first, second, $10-\text{th}$ and $20-\text{th}$ orthonormal KLMs compared with the corresponding order of the vibration modes. The error decreases with increasing number of snapshots for higher $10-\text{th}$ and $20-\text{th}$ modes. It is also noted in Figure 3.4 and Figure 3.5 that the $20-\text{th}$ KLM does not converge to the corresponding $20-\text{th}$ vibration mode when the number of the snapshots is taken as 30. However, all the KLMs can converge to the corresponding modes of vibration almost exactly when the number of the snapshots is 50. Table 3.1 shows that the first,

second and third KLVs converge quite well as the number of the snapshot increases from 5 to 50.

Table 3.1 The first three KLVs versus the number of snapshots.

| Number of snapshots | $\lambda_1$ | $\lambda_2$ | $\lambda_3$ |
|---|---|---|---|
| 5 | 0.0063402695 | 0.0002400612 | 0.0000022490 |
| 10 | 0.0063265951 | 0.0002197678 | 0.0000217581 |
| 20 | 0.0063347454 | 0.0002208136 | 0.0000205208 |
| 30 | 0.0063347450 | 0.0002208131 | 0.0000205201 |
| 50 | 0.0063347450 | 0.0002208131 | 0.0000205201 |

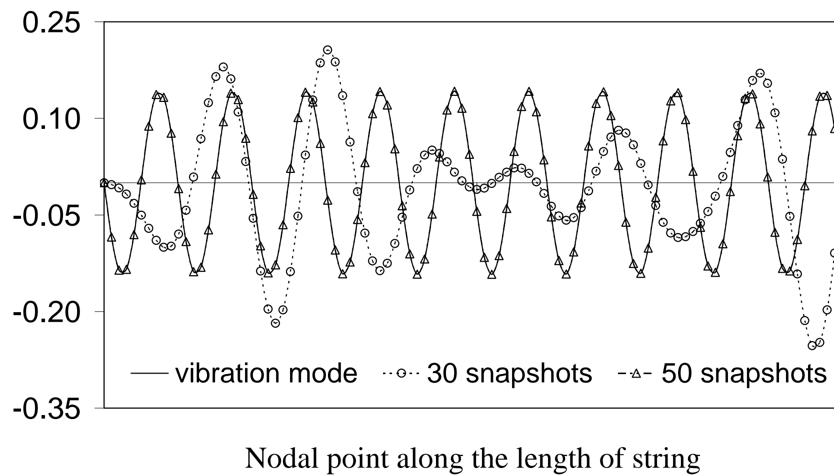


Figure 3.4 The $20-\text{th}$ KLM and $20-\text{th}$ mode of the vibration.

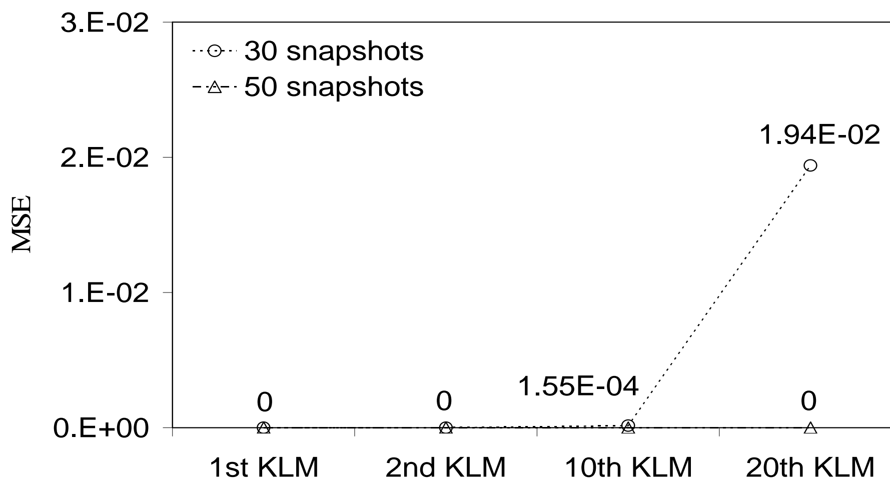


Figure 3.5 The mean square error between KLMs and the corresponding modes of the vibration.

In the second computation test, KLMs are obtained from four sets of ensemble of snapshots, each set has the same number of snapshots $N = 50$ but the sampling rate and the length of time period for sampling are different. The snapshots in the first set of ensemble are taken at fixed time interval within the time period of one fundamental period $t = t_1$ (sampling rate $\delta = t_1/50$), the snapshots in the second set are taken at fixed time interval within 1.6 times of the fundamental period $t = 1.6t_1$ (sampling rate $\delta = 1.6t_1/50$), the snapshots in the third set are taken at fixed time interval within 2 times of the fundamental period $t = 2t_1$ (sampling rate $\delta = 2t_1/50$) and the snapshots in the fourth set are taken at various time interval within the fundamental period $t = t_1$, i.e. in the first half of $t_1$, 30 snapshots are taken at one fixed time interval while in the second half of $t_1$, 20 snapshots are taken at another fixed time interval (sampling rate $\delta = (t_1/2)/30$ and $\delta = (t_1/2)/20$, respectively).

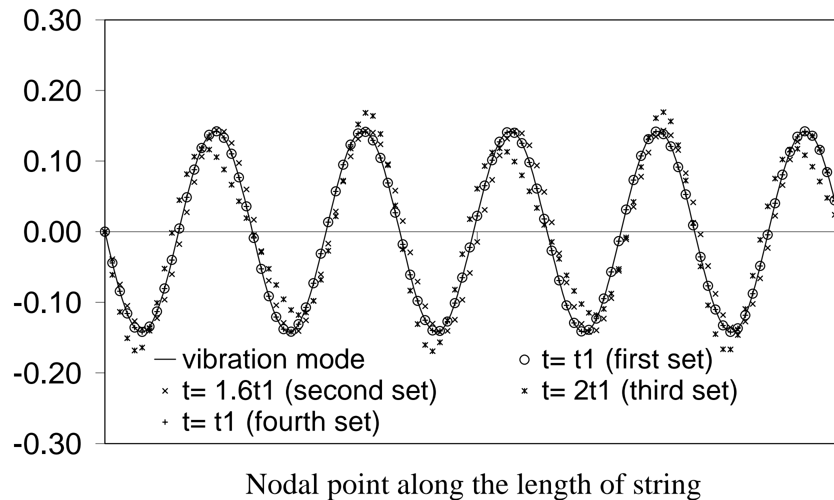


Figure 3.6 The $10-\text{th}$ KLM and $10-\text{th}$ mode of the vibration with various sampling rate and the length of time period.

Figure 3.6 shows the $10-\text{th}$ KLM obtained by KLD from these four sets of ensemble and the corresponding $10-\text{th}$ mode of the vibration. The respective MSE is shown in Figure 3.7. Again, the second computation results shown in Figure 3.6 and Figure 3.7

indicate that the KLM agree well with the system vibration mode, the error increases with increasing sampling rate or increasing length of time period if the number of the sampling (snapshots) is the same. It is also noted from these results that there is no significant difference between the KLMs obtained from the first set and fourth set of ensemble, i.e. the results do not show a significant difference by the evenly or unevenly sampling provided it is sampled within the same length of time period and with same number of the sampling. This is probably due to the fact that the ensemble of the numerical data is obtained from the steady-state response rather than the transient response of the system.

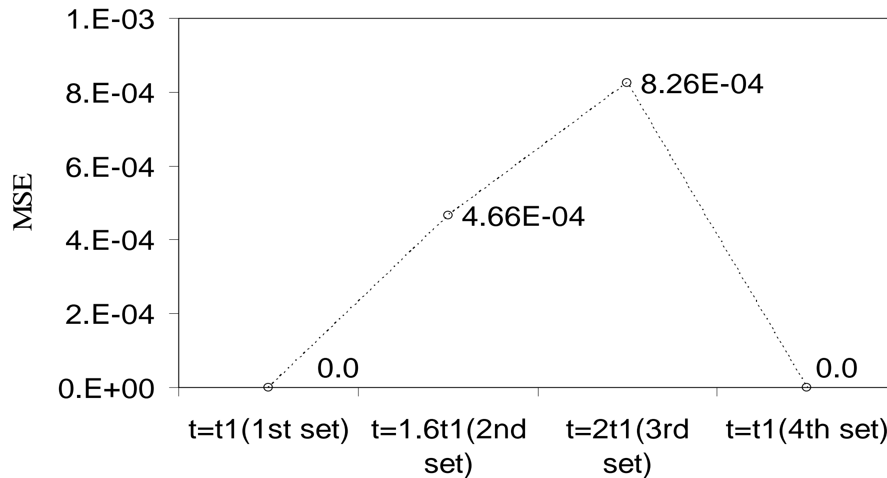


Figure 3.7 The mean square error between the $10-\text{th}$ KLM and $10-\text{th}$ mode of the vibration with various sampling rate and the length of time period.

### 3.3.3 CONCLUSION

The relationship between the KLMs extracted by KLD from an ensemble of numerical simulation data and the corresponding modes of the vibration of the distributed parameter system has been established. The KLMs agree well with modes of vibration if the number of sampling or snapshots is large enough. This property can be used to

obtain the modes of the vibration when the numerical simulation or experiment data are obtained from a distributed parameter system. Future research would be to use KLD for the signals with noise-injected data, the nonlinear distributed parameter vibration system, and the system with generalized damping.

### 3.4 A MEMS DEVICE AND GOVERNING EQUATIONS

To demonstrate the model reduction technique for the generation of the macromodel for dynamic simulation of MEMS systems and devices based on Karhunen-Loève decomposition procedure, a doubly-clamped microbeam pulled in by the electrostatic actuation force with squeezed gas-film damping effect is examined in this section. Figure 3.8 shows a schematic cross section of this device (Gupta and Senturia, 1997). When a voltage $V$ is applied between the top and bottom electrodes, the top deformable microbeam is pulled downwards due to the electrostatic force. At the same time, the narrow air gap between the moving microbeam and the substrate will generate back pressure force on the microbeam due to squeezed gas-film damping effect. The top microbeam will be pulled onto the bottom substrate when the applied voltage reaches the dynamic pull-in voltage. The pull-in dynamics is sensitive to the ambient pressure of the air thus this structure can be used as pressure sensor (Gupta and Senturia, 1997). Accurate and efficient simulation of squeezed gas-film damping problems are important for the applications of the MEMS devices in order to control moving microstructures and to determine the time needed for microstructures when moving in air.

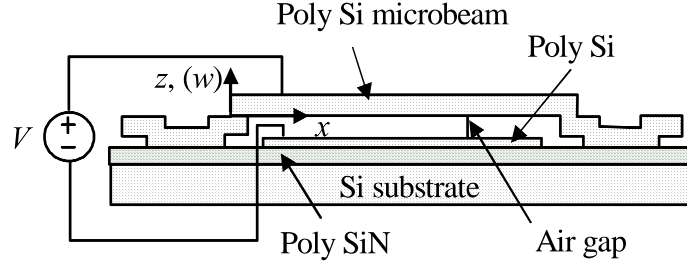


Figure 3.8 Doubly-clamped microbeam.

This MEMS device is a coupled domain system. In general, the microbeam can be modelled by one-dimensional Euler beam with electrostatic actuation force, and the back pressure force can be obtained from the two-dimensional nonlinear Reynold's squeezed gas-film damping equation (Hamrock, 1994) which yield the following nonlinear partial differential equations (PDEs) (Hung and Senturia, 1999)

$$EI\frac{\partial^4 w}{\partial x^4} - T\frac{\partial^2 w}{\partial x^2} = -\frac{\varepsilon_0 b V^2}{2w^2} + \int_0^b (p - p_a)dy - \rho\frac{\partial^2 w}{\partial t^2} \tag{3.44}$$

$$\nabla \cdot (w^3 p \nabla p) = \frac{12\mu}{1 + 6K_n}\frac{\partial (pw)}{\partial t} \tag{3.45}$$

where $E$ is Young's modulus, $I = bh^3/12$ is the second moment of area where $b$ is the width and $h$ is the thickness of the microbeam, $\rho$ is the microbeam density; $\mu$ is the air viscosity and equals to $1.82\times10^{-5}$ $\text{kg}(\text{m}\bullet\text{s})^{-1}$, $w(x,t)$ is the height of the microbeam above the substrate, $K_n(x,t) = \lambda/w$ is the Knudsen number where $\lambda$ is the mean-free path of the air and equals to $0.064\,\mu\text{m}$, $-\varepsilon_0 bV^2/(2w^2)$ is the electrostatic actuation force where $V$ is the applied voltage, $\varepsilon_0$ is the permittivity of free space and equals to $8.854\times10^{-12}$ $\text{Farad}\bullet\text{m}^{-1}$, $p(x,y,t)$ is the back pressure force acting on the microbeam due to the squeezed gas-film damping in which isothermal process is assumed, $p_a$ is the ambient pressure and equals to $1.013\times10^5$ Pa, and $T/(bh)$ is the

sum of residual stress $t_r$ and the bending induced stress $t_b$ due to large deflection which can be expressed as

$$\frac{T}{bh} = t_r + t_b = t_r + E\frac{\Delta L}{L} \approx t_r + \frac{E}{2L}\int_L \left(\frac{dw}{dx}\right)^2 dx \tag{3.46}$$

where $L$ is the length of the deformable microbeam.

Traditional finite element methods (FEMs) or finite difference methods (FDMs) can be used for explicit dynamical simulations of coupled nonlinear system, but the resulting number of degrees-of-freedom is usually too large so that it is usually computationally very intensive and time-consuming for practical problem, especially when a large number of simulations are needed or the system is structurally complex. It will be demonstrated in the following sections that the Galerkin procedure employing the KLMs obtained from KLD procedure as basis functions can convert the original coupled nonlinear system with infinite number of degrees-of-freedom to low-order macromodels with small number of degrees-of-freedom while capturing all the essential behaviours of the original system faithfully and efficiently.

## 3.5 SNAPSHOT GENERATION

In order to obtain the ensemble of signals for KLD, the time-dependant deflection $w(x,t)$ and pressure $p(x,y,t)$ distribution of Equations (3.44) and (3.45) will be simulated by using finite difference method (FDM) for an ensemble of applied voltage. These time-dependant parameters are used as the snapshots $\{u_n\}$ for KLD to generate the sets of KLMs $\{\phi_k\}$ and KLVs $\{\lambda_k\}$. The ensemble of snapshots must be representative of the dynamical characteristics of the system under consideration. For the system shown in Figure 3.8, the pull-in dynamics of the microbeam at a series of

different time are simulated using FDM for an ensemble of applied step voltages to obtain beam deflection $\{u_n^w\}$ and the back air pressure $\{u_n^P\}$ ensembles. Each vector in $\{u_n^w\}$ and $\{u_n^P\}$ corresponds to the microbeam flexural deflection $w_n(x_i, t_s)$ and back pressure $p_n(x_i, y_j, t_s)$ distribution at time $t_s$, and the entries in each vector $u_n^w(x_i)$ and $u_n^p(x_i, y_j)$ correspond to the deflection and back pressure at different node of the finite difference mesh as shown in Figure 3.9. These deflection and back pressure ensembles $\{u_n^w\}$ and $\{u_n^P\}$ are then used as snapshots i.e. the ensemble of signals in Equations (3.12) and (3.16) to extract the KLMs and KLVs. The ensemble of applied step voltages is taken to be that of the operating range of the systems.

To simulate the systems shown in Figure 3.8 using FDM, the Euler beam equation (3.44) and the nonlinear Reynold equation (3.45) are discretized in space to generate an $(M+1)\times(N+1)$ mesh with $M \times N$ inner grids and $2M + 2N + 4$ boundary grids as shown in Figure 3.9.

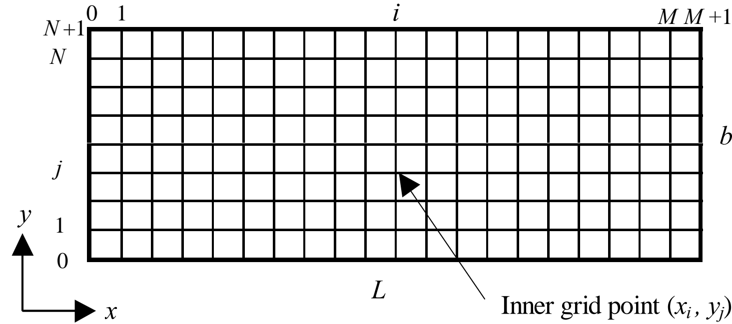


Figure 3.9 Finite difference mesh of the microbeam.

Central difference scheme is used to approximate the spatial partial derivative operators in Equations (3.44) and (3.45) and the trapezoidal rule is adopted to discretize the integral operator. The state of the three unknowns $w(x,t)$, $\partial w(x,t)/\partial t$ and $p(x, y, t)$ are projected onto each grid point. This discretizatioin will transform the

Equations (3.44) and (3.45) into a set of $M \times N + 2M$ nonlinear ODEs. The following state space can be used to represent the unknowns on the grids as

$$\dot{x} = \left( \frac{\partial w_1}{\partial t} \cdots \frac{\partial w_M}{\partial t} \ \frac{\partial^2 w_1}{\partial t^2} \cdots \frac{\partial^2 w_M}{\partial t^2} \ \frac{\partial p_{11}}{\partial t} \cdots \frac{\partial p_{MN}}{\partial t} \right)^T \tag{3.47}$$

and integrated numerically by using the fifth-order Runge-Kutta method (Press et al., 1992) with the following boundary conditions

$$\begin{aligned} & w = w_0, \quad \frac{\partial w}{\partial x} = 0, \quad \frac{\partial p}{\partial n} = 0, \quad (\text{at } x = 0,\ L) \\ & p = p_a, \qquad\qquad\qquad\qquad (\text{at } y = 0,\ b) \end{aligned} \tag{3.48}$$

and initial conditions

$$w = w_0, \quad \frac{\partial w}{\partial t} = 0, \quad p = p_a, \quad (\text{at } t = 0) \tag{3.49}$$

The snapshots can be taken at varied or fixed time interval during pull-in dynamics. Since there is no distinct difference between transient and steady-state for the system shown in Figure 3.8, snapshots at fixed time interval are taken in the study.

### 3.6 MACROMODEL GENERATION

Using the above-mentioned ensembles of snapshots and following the method of snapshots in KLD procedure described in the Section 3.1, a set of KLMs and the corresponding KLVs are obtained. The Galerkin procedure employing these KLMs as basis functions is then applied to the original nonlinear governing PDEs (3.44) and (3.45) to convert them to a macromodel with a small number of ordinary differential equations (ODEs). Because independent deflection and pressure basis functions make the Galerkin procedure simpler and also make clear of the physics of the problem, the independent KLMs for deflection and back pressure are extracted respectively.

Denoting the KLMs with respect to the deflection as $\phi_i^w(x)$ and those with respect to the back pressure as $\phi_j^p(x, y)$, the deflection $w(x,t)$ and pressure $p(x,y,t)$ can be represented as a linear combination in terms of these KLMs as follows

$$w(x,t) = w_0 + \sum_{i=1}^{I} a_i^w(t)\phi_i^w(x) \tag{3.50}$$

$$p(x,y,t) = p_a + \sum_{j=1}^{J} a_j^p(t)\phi_j^p(x,y) \tag{3.51}$$

where $w_0$ is the initial gap between the deformable microbeam and the substrate, $p_a$ is the gap air ambient pressure, the coefficients $a_i^w$ and $a_j^p$ are the amplitudes of the basis functions or the modal coordinates in modal decomposition, and $I$ and $J$ are the numbers of KLMs for deflection and back pressure respectively. Using Equation (3.12) in the method of snapshots for solving the eigenvalue problem of Equation (3.10), $\phi_i^w(x)$ and $\phi_j^p(x,y)$ can be represented as the linear combination of snapshots $\{w_n(x)\}$ and $\{p_n(x,y)\}$ as follows

$$\phi^w(x) = \sum_{n=1}^{N} \alpha_n^w [w_n(x) - w_0] \tag{3.52}$$

$$\phi^p(x,y) = \sum_{n=1}^{N} \alpha_n^p [p_n(x,y) - p_a] \tag{3.53}$$

where $N$ is the total number of snapshots, $\alpha_n^w$ and $\alpha_n^p$ are the entries of eigenvectors obtained in matrix eigenvalue problem of (3.16). Substituting Equations (3.50) and (3.51) into Equations (3.44) and (3.45), and applying the KLMs as basis functions in the Galerkin procedure, the following reduced coupled nonlinear ODEs in terms of the basis functions are derived

$$M_j \frac{\mathrm{d}^2 a_j^w}{\mathrm{d}t^2} + \sum_{i=1}^{I} K_{ji} a_i^w + f_j = 0, \quad (j = 1, 2, \cdots, I) \tag{3.54}$$

$$\sum_{i=1}^{J} H_{ji} \frac{\mathrm{d}a_i^p}{\mathrm{d}t} + \sum_{i=1}^{J} S_{ji} a_i^p + c_j = 0, \quad (j = 1, 2, \cdots, J) \tag{3.55}$$

where the elements in matrix $M_j$ can be obtained once the basis functions are known, the elements in matrixes $K_{ji}$, $H_{ji}$ and $S_{ji}$, and vectors $c_j$ and $f_i$ are expressed as follows

$$M_j = \int_L \rho \left(\phi_j^w\right)^2 dx \tag{3.56}$$

$$K_{ji} = K_{ij} = \int_L \left( EI \frac{\partial^2 \phi_j^w}{\partial x^2} \frac{\partial^2 \phi_i^w}{\partial x^2} + T \frac{\partial \phi_j^w}{\partial x} \frac{\partial \phi_i^w}{\partial x} \right) dx \tag{3.57}$$

$$f_j = \int_L \left( \frac{\varepsilon_0 b V^2}{2w^2} - \int_0^b (p - p_a)\, dy \right) \phi_j^w \, dx \tag{3.58}$$

$$H_{ji} = H_{ij} = \int_A \frac{12\mu}{1 + 6K_n} w \phi_j^p \phi_i^p \, dxdy \tag{3.59}$$

$$S_{ji} = S_{ij} = \int_A \left[ w^3 p \left( \frac{\partial \phi_j^p}{\partial x} \frac{\partial \phi_i^p}{\partial x} + \frac{\partial \phi_j^p}{\partial y} \frac{\partial \phi_i^p}{\partial y} \right) + \frac{12\mu}{1 + 6K_n} \phi_j^p \phi_i^p \frac{\partial w}{\partial t} \right] dxdy \tag{3.60}$$

$$c_j = \int_A \frac{12\mu}{1 + 6K_n} p_a \phi_j^p \frac{\partial w}{\partial t} \, dxdy \tag{3.61}$$

where $\int_L$ indicates the integration along the length of the microbeam and $\int_A$ indicates the integration along the microbeam area.

The small set of coupled nonlinear ODEs (3.54) and (3.55) constitutes the dynamic macromodel which represents the original nonlinear PDEs (3.44) and (3.45) with low-order model in terms of global basis functions. Since this dynamic macromodel is generated by the Galerkin procedure employing the KLMs extracted from KLD as the basis functions, the resulting number of degrees-of-freedom is usually small compared with full model simulation by FEM or FDM which contains a large number of degrees-of-freedom.

It is noted that the elements $K_{ji}$, $H_{ji}$, $S_{ji}$, $c_j$ and $f_i$ in Equations (3.57)-(3.61) are corresponding to the nonlinear terms related to the microbeam flexural deflection, electrostatic force, squeezed gas-film damping and bending induced stress in the original PDEs (3.44) and (3.45), and cannot be expressed directly in the generalized coordinates or modal coordinates. Since $w$, $p$ and $T$ in these equations are time-dependent, much of the computation time is thus spent on re-computation these elements at every time step during the numerical integration of Equations (3.54) and (3.55). Some techniques to handle this shortcoming and improve the computational efficiency will be discussed in Chapter 6.

The macromodel expressed by the coupled nonlinear ODEs (3.54) and (3.55) is integrated numerically in time by a fifth-order Runge-Kutta method to simulate the dynamics of the system. The initial values for the system are obtained as follows

$$a_j^w\big|_{t=0} = \frac{\int_L \left(w - w_0\right)\big|_{t=0} \phi_j^w \, dx}{\int_L \left(\phi_j^w\right)^2 dx} \tag{3.62}$$

$$a_j^p\big|_{t=0} = \frac{\int_A \left(p - p_a\right)\big|_{t=0} \phi_j^p \, dxdy}{\int_A \left(\phi_j^p\right)^2 dxdy} \tag{3.63}$$

## 3.7 NUMERICAL RESULTS AND DISCUSSION

### 3.7.1 MACROMODEL ACCURACY

In order to validate the present macromodel for MEMS device dynamic simulation, the pull-in dynamics simulation of the MEMS device shown in Figure 3.8 is carried out. For the purpose of simplicity but not to harm the methodology in this section, the

bending induced stress $t_b$ is ignored in the numerical experiments. The material properties and geometric dimensions of the microbeam are given in Table 3.2.

Table 3.2 Material properties and geometric dimension of the microbeam.

| Young's modulus $E$ (GPa) | Density $\rho/(bh)$ (kg/m$^3$) | Residual stress $t_r$ (MPa) | Knudsen's number $K_n = \lambda/w$ | Initial gap $w_0$ ($\mu$m) | Thickness $h$ ($\mu$m) | Length $L$ ($\mu$m) | Width $b$ ($\mu$m) |
|---|---|---|---|---|---|---|---|
| 149 | 2330 | -3.7 | ≈0.028 | 2.3 | 2.2 | 610 | 40 |

Table 3.3 Accumulative normalized KLVs corresponding to the number of deflection KLMs.

| Number of KLMs $I$ | Normalized KLVs $\bar{\lambda}_I = \lambda_I \Big/ \sum_{i=1}^{N} \lambda_i$ | Accumulative normalized KLVs $S_n = \sum_{i=1}^{I} \bar{\lambda}_i$ |
|---|---|---|
| 1 | $\bar{\lambda}_1 = 0.9998892100$ | $S_1 = 0.9998892100$ |
| 2 | $\bar{\lambda}_2 = 0.0001097713$ | $S_2 = 0.9999989813$ |
| 3 | $\bar{\lambda}_3 = 0.0000009954$ | $S_3 = 0.9999999768$ |
| 4 | $\bar{\lambda}_4 = 0.0000000195$ | $S_4 = 0.9999999963$ |

The snapshots are obtained from the solution of Equations (3.44) and (3.45) by using central FDM mentioned above for an ensemble of two different input step voltages of $V_1$ =10 V and $V_2$ =16 V which are assumed to be the device operating range under consideration. Each 25 snapshots are taken at the fixed time interval from the moment when each step voltage is applied till the pull-in occurs. These snapshots are then used as signal for KLD to generate KLMs and KLVs. The Galerkin procedure uses these KLMs as the basis functions to generate the macromodel to represent and simulate the pull-in dynamics. Based on numerical experiments, the mesh size $40 \times 20$ for the finite difference simulation of the original nonlinear PDEs (3.44) and (3.45) is able to give sufficient accuracy. The minimum pull-in step voltage for this device is calculated at 8.87 V by FDM code, which matches the experimental data measured at 8.76 V (Osterberg and Senturia, 1997).

Table 3.4 Accumulative normalized KLVs corresponding to the number of back pressure KLMs.

| Number of KLMs $J$ | Normalized KLVs $\bar{\lambda}_J = \lambda_J \Big/ \sum_{j=1}^{N} \lambda_j$ | Accumulative normalized KLVs $S_n = \sum_{j=1}^{J} \bar{\lambda}_j$ |
|---|---|---|
| 1 | $\bar{\lambda}_1 = 0.9813929100$ | $S_1 = 0.9813929100$ |
| 2 | $\bar{\lambda}_2 = 0.0178970820$ | $S_2 = 0.9992899920$ |
| 3 | $\bar{\lambda}_3 = 0.0005202848$ | $S_3 = 0.9998102768$ |
| 4 | $\bar{\lambda}_4 = 0.0001617258$ | $S_4 = 0.9999720025$ |
| 5 | $\bar{\lambda}_5 = 0.0000258564$ | $S_5 = 0.9999978589$ |

Table 3.3 and Table 3.4 show the normalized KLVs and accumulative normalized KLVs with respect to the number of deflection and back pressure KLMs employed as basis functions in macromodel simulations where the total sum of the KLVs is normalized to one. Recalling Equations (3.25) and (3.26), this accumulative normalized KLVs represents the total percentage of the system informaiton, or energy captured by the corresponding number of the KLMs. It is found in Table 3.3 that the first deflection KLM, which is corresponding to the first KLV, can capture 99.99% energy of the system while it takes at least four back pressure KLMs to capture the same level of system energy as listed in Table 3.4. This indicates that the value of the accumulative normalized KLVs can be used as a guideline for the optimal selection of the number of basis functions employed in the Galerkin procedure for macromodel generation and system simulation. Following this guideline, it is found that macromodel can achieve sufficient accuracy for dynamical simulation of the MEMS device of Figure 3.8 if the accumulative normalized KLVs corresponding to the first few $n$-dominant KLMs satisfies the following criteria

$$S_n = \sum_{i=1}^{n} \bar{\lambda}_i = \frac{\sum_{i=1}^{n} \lambda_i}{\sum_{i=1}^{N} \lambda_i} \times 100\% \geq 99.99\% \tag{3.64}$$

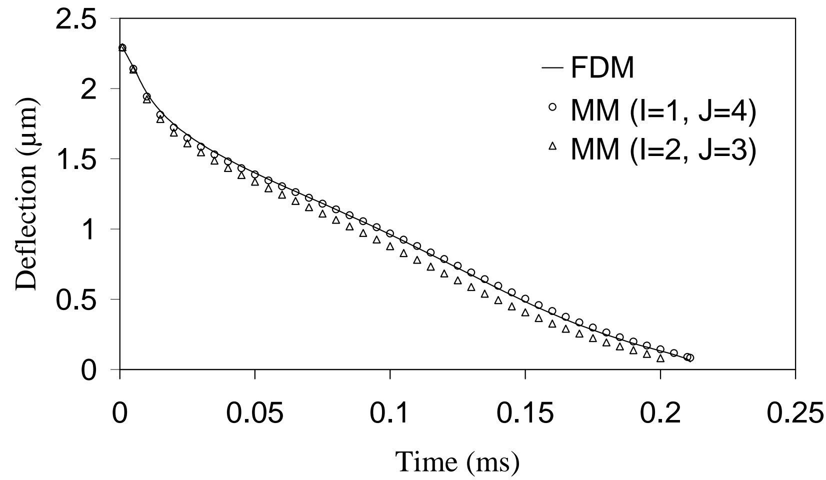


Figure 3.10 Comparison of the microbeam pull-in dynamics for an input step voltage of 10.25 V.

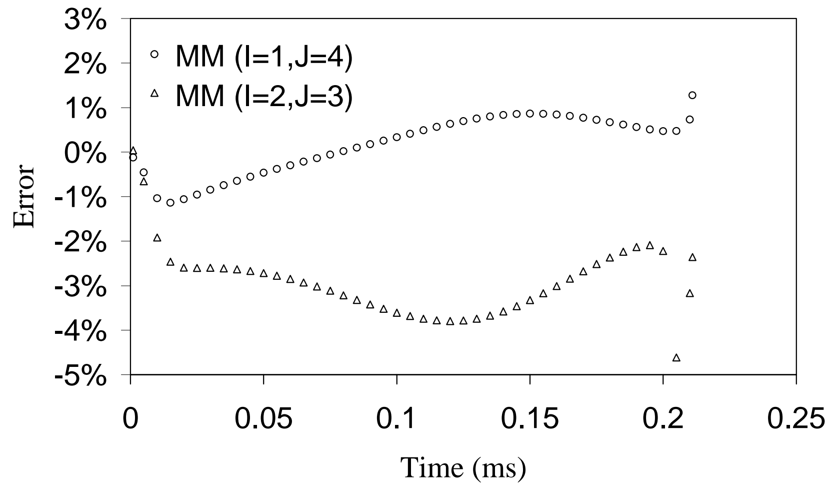


Figure 3.11 The error of macromodel simulation with respect to FDM solution for an input step voltage of 10.25 V.

Figure 3.10 shows a comparison of the deflection of the midpoint of the microbeam between FDM approximation of the original nonlinear PDEs (3.44) and (3.45) and macromodel representation when the system is applied with an input step voltage of 10.25 V, where FDM denotes the FDM simulation results and MM stands for the macromodel simulation results, $I$ denotes the number of deflection KLMs and $J$

denotes the number of back pressure KLMs. Figure 3.11 shows the error between the macromodel and FDM simulations, where the error is defined as

$$\text{error} = \frac{w_{\text{MM}}(x_c, t) - w_{\text{FDM}}(x_c, t)}{w_0} \times 100\% \tag{3.65}$$

here $w_{\text{MM}}$ denotes the midpoint deflection of the microbeam from the macromodel simulation and $w_{\text{FDM}}$ is the FDM solutions of the original nonlinear PDEs (3.44) and (3.45). Figure 3.11 shows the error is very small $(\leq 1.2\%)$ when $I \geq 1$ and $J \geq 4$. It appears in Figure 3.11 that the error is oscillatory but tends to increase with time due to the stronger nonlinearity in electrostatic force and squeezed gas-film damping near pull-in. This means that there is less macromodel simulation accuracy compared to the area away from pull-in where macromodel simulation should have better approximation. It is also noted in Figure 3.10 and Figure 3.11 that macromodel employing two deflection KLMs $(I = 2)$ and three back pressure KLMs $(J = 3)$ as basis functions in Galerkin procedure has less accuracy compared with macromodel employing one deflection KLM $(I = 1)$ and four back pressure KLMs $(J = 4)$. This is because three back pressure KLMs can only capture 99.98% energy even though two deflection KLMs can capture up to 99.9999% energy as indicated in Table 3.3 and Table 3.4, despite the total number of basis functions is the same $(I + J = 5)$ for both macromodels. If it is not otherwise stated, one deflection KLM and four back pressure KLMs $(I = 1, J = 4)$ are assumed to be the number of basis functions employed in the macromodel in the following simulations.

### 3.7.2 CHANGE OF THE INPUT VOLTAGE SPECTRUM

It is noted that the macromodel generated by the above ensemble of two different input step voltages could also be used to simulate the system when the applied input voltage spectrum is changed. Figure 3.12 shows the simulation from the same macromodel using KLMs generated from input step voltages for the dynamic response of system to an input sinusoidal voltage with magnitude of 14 V at a frequency of 10 kHz. The error of the macromodel simulation compared with the finite difference solution is plotted in Figure 3.13. It shows that the macromodel simulation can capture the system dynamics accurately with less than 1.6% error when the number of basis functions $I = 1$ for deflection and $J = 4$ for back pressure are chosen in the macromodel without re-generating the macromodel.

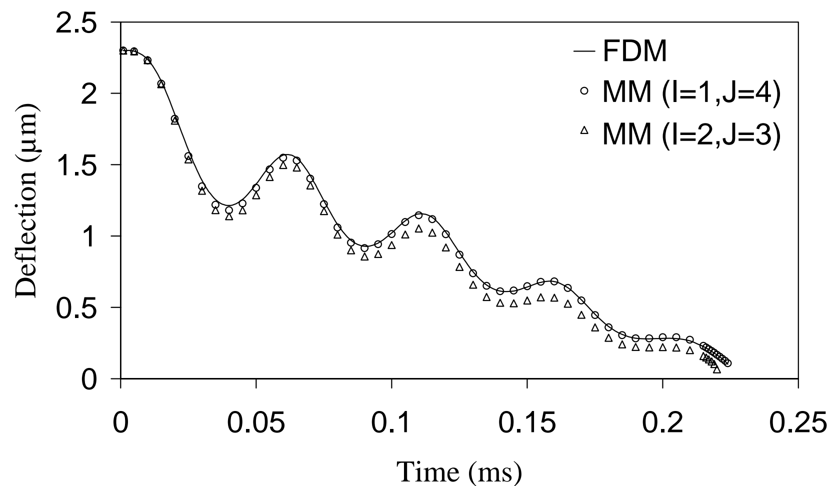


Figure 3.12 Comparison of the microbeam pull-in dynamics for an input sinusoidal voltage of 14 V at a frequency of 10 kHz.

In order to understand this macromdel flexibility characteristics qualitatively, the deflection and back pressure KLMs for the system with this input sinusoidal voltage are extracted independently following KLD procedure, and compared with the KLMs extracted for the original system with the ensemble of input step voltages as described

above. The comparisons of the first and the second deflection KLMs plotted in Figure 3.14 shows that the first KLM shape difference between these two different input voltages is neglegible but there is some slightly difference between the second KLM which however does not harm the simulation accuracy simply because that only the first deflection KLM, which captures more than 99.99% of the system energy, is employed in the macromodel.

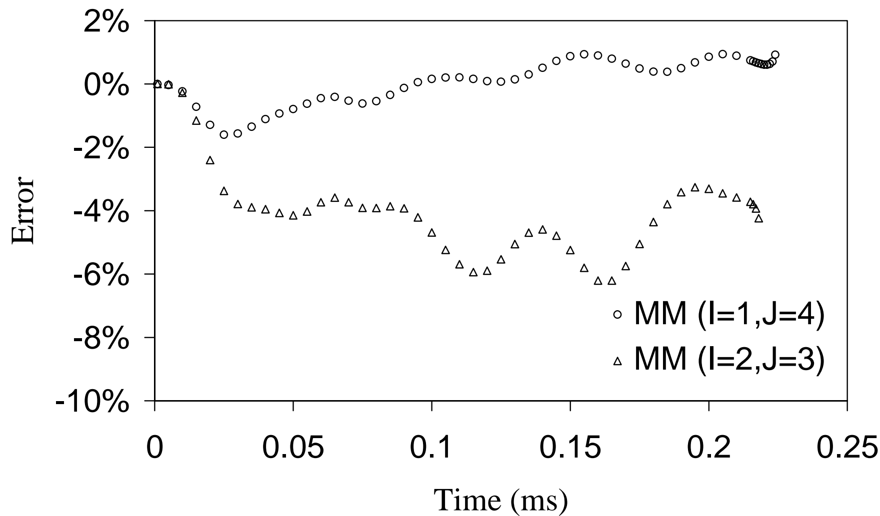


Figure 3.13 The error of macromodel simulation with respect to FDM solution for an input sinusoidal voltage of 14 V at a frequency of 10 kHz.

Figure 3.15 shows the comparison for the first two back pressure KLMs along the centre of microbeam between these two input voltages. It is obeserved in Figure 3.15 that the first back pressure KLM is almost identical while there is some noticeable difference betweem the second KLM, but this difference does not cause significant accuracy drop in the macromodel simulation as indicated in Figure 3.12 and Figure 3.13 due to the system energy lever captured by the second KLM (1.79% as indicated in Table 3.4) is much lower than that captured by the first KLM (98.14%) which is obviously the dominant mode. However, the above observations are based on the qualitatively numerical experimental results, the accuracy limits on quantitatively

measure or scaling of parameter changes over the parameter space in which the KLMs can still be used as basis functions without re-generation needs to be studied further.

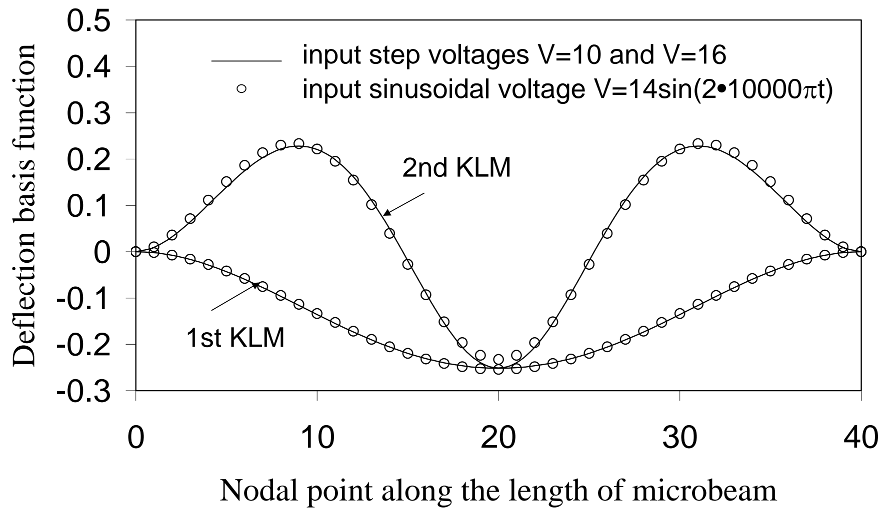


Figure 3.14 Comparison of the first two deflection KLMs with different input voltage spectrum.

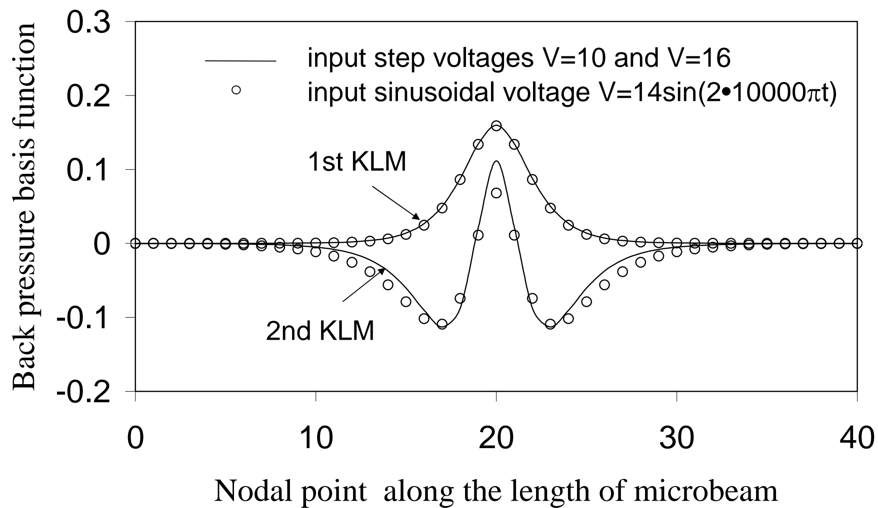


Figure 3.15 Comparison of the first two pressure KLMs with different input voltage spectrum.

Figure 3.16 shows the macromodel simulation for microbeam deflection when the frequency of the input sinusoidal voltage varies from 10 kHz to 2000 kHz. It is found that the system has the similar pull-in dynamics characteristics compared with the

system response from the input step voltage when the frequency is larger than 100 kHz. Due to this similarity, the pull-in dynamics simulated by macromodel and finite difference for the frequency larger than 100 kHz are not plotted in Figure 3.16.

To further demonstrate the flexibility of the macromodel generated by the above ensemble of the input step voltages to simulate the system applied with different input voltage spectrum, the macromodel simulation is carried out for an input ramp voltage of $V = Rt$ with ramp rate at $R = 0.4$ V $\mu$s$^{-1}$ and the microbeam midpoint deflection is plotted in Figure 3.17. It is noted that the macromodel simulation has a very good result with error less than 2.1% compared with FDM solutions with $I = 1, J = 4$ as shown in Figure 3.18. The results demonstrate again that the macromodel can well simulate the system with different input voltage spectra without re-generation of the macromodel.

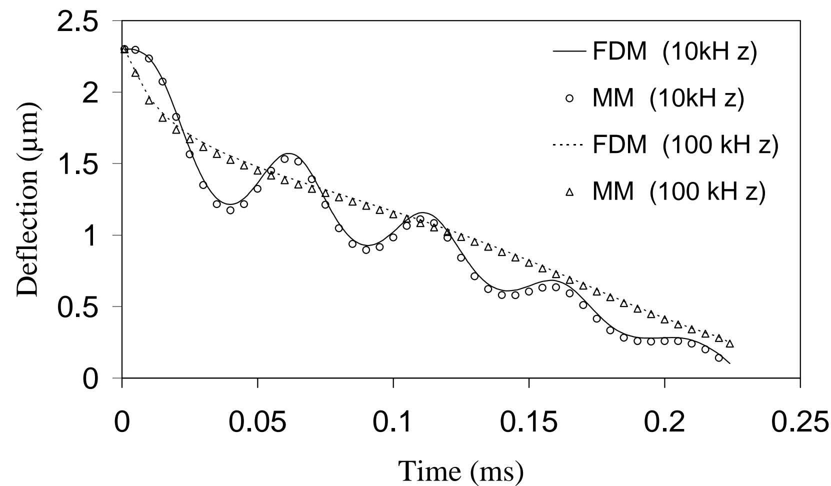


Figure 3.16 Comparison of the microbeam pull-in dynamics for a set of input sinusoidal voltages of 14 V at different frequency at 10 kHz and 100 kHz.

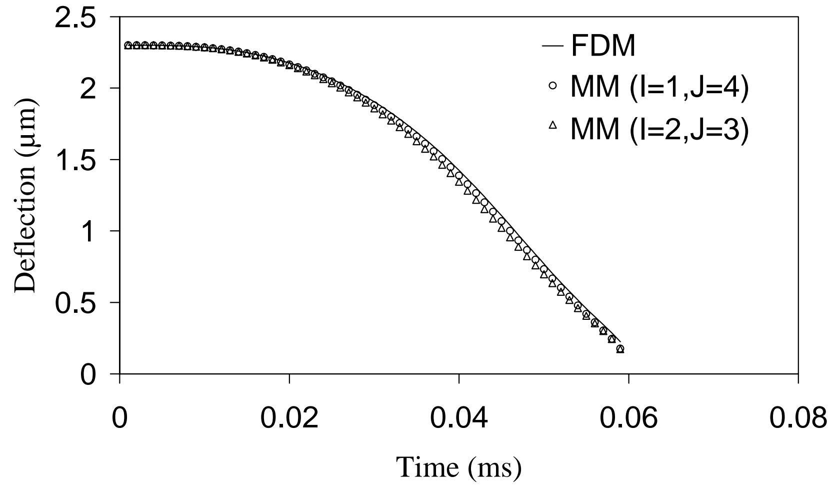


Figure 3.17 Comparison of the microbeam pull-in dynamics for an input ramp voltage $V = Rt,\ R = 0.4\,\mathrm{V}\ \mu\mathrm{s}^{-1}$.

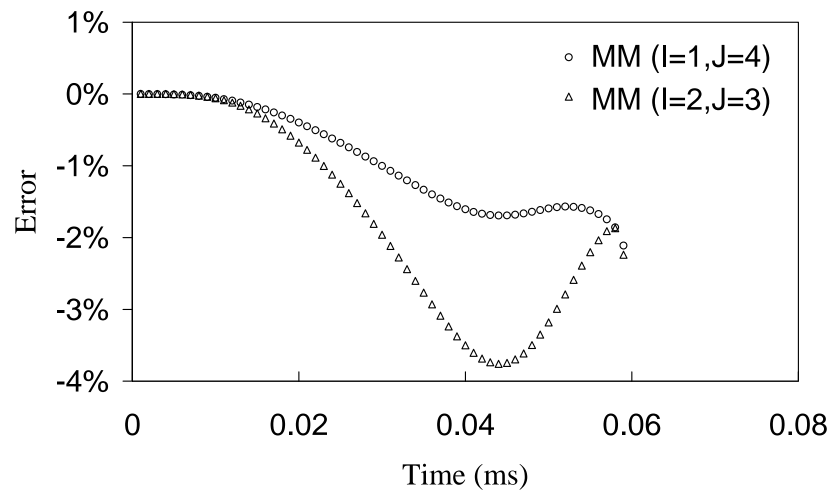


Figure 3.18 The error of macromodel simulation with respect to FDM solution for an input ramp input voltage $V = Rt,\ R = 0.4\,\mathrm{V}\ \mu\mathrm{s}^{-1}$.

### 3.7.3 TIME INTERVALS AND NUMBER OF THE SNAPSHOTS

Study on the influence of the time interval and the number of snapshots on the convergence of the KLMs and the accuracy of the macromodel simulation is carried out. Three ensembles of snapshots obtained from the same ensemble of input two step

voltages of 10 V and 16 V are used for study. The first ensemble consists of 20 snapshots at the fixed time interval from the moment when each input step voltage is applied till the pull-in occurs, the second ensemble is composed of 25 snapshots and the third ensemble has 50 snapshots. It is noted that time interval decreases when more snapshots are taken. KLD is applied to each set of snapshots to generate three sets of KLMs and three corresponding macromodels are created through the Galerkin procedure by employing each set of the KLMs as basis functions.

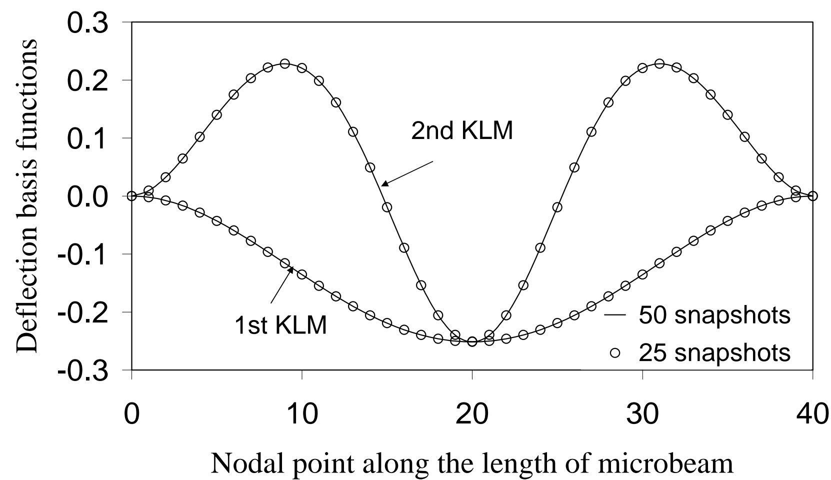


Figure 3.19 The first two deflection KLMs for different number of snapshots.

Figure 3.19 shows the first and second deflection KLMs obtained from the ensemble of 25 snapshots are almost identical to those obtained from the ensemble of 50 snapshots. Same observation for the first and second back pressure KLMs along the centre of the microbeam is plotted in Figure 3.20. Figure 3.21 shows the errors of the deflection of the midpoint of the microbeam simulated by these three macromodels compared with the FDM solutions when the system is applied with an input step voltage 10.25 V. Generally, the error of the dynamic macromodel simulation will decrease as the number of snapshots increases from 20 to 25 but the accuracy could not be improved significantly when the number of snapshots increases from 25 to 50.

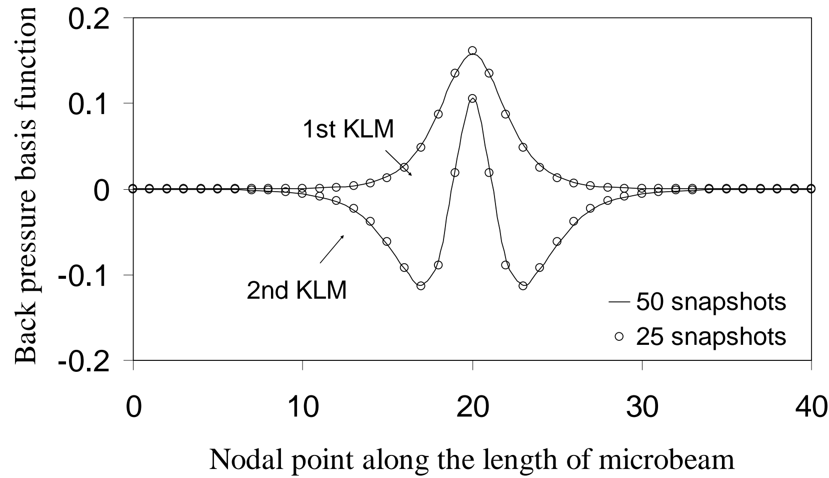


Figure 3.20 The first two KLMs along the centre of the microbeam for different number of snapshots.

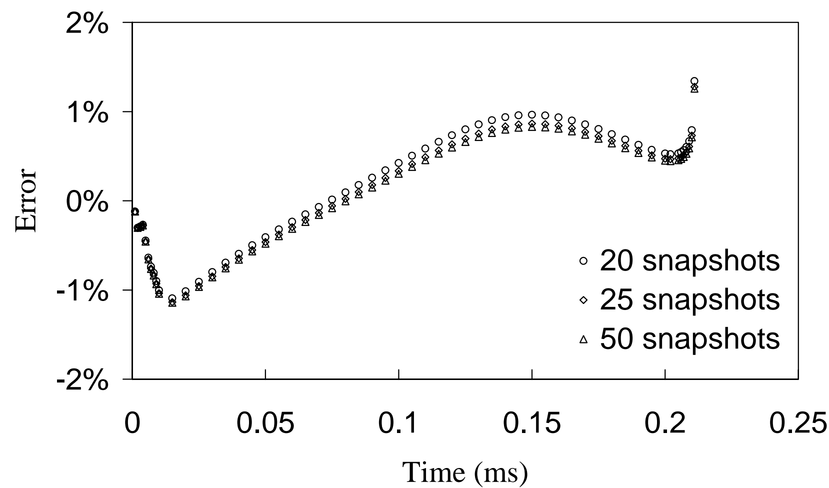


Figure 3.21 The error of simulations from macromodel based on three different numbers of snapshots with respect to FDM solution for input step voltage of 10.25 V.

### 3.7.4 THE EFFECT OF THE LARGE DEFORMATION

The influence of bending induced tension due to large deformation as described by Equation (3.46) on dynamic response of the system is investigated. Two macromodels based on the KLMs extracted from two sets of ensembles of snapshots obtained when

the system is applied with an ensemble of step voltage of 12 V and 16 V, respectively, are created. The bending induced tension effect is considered in the first ensemble of snapshots but neglected in the second ensemble of snapshots.

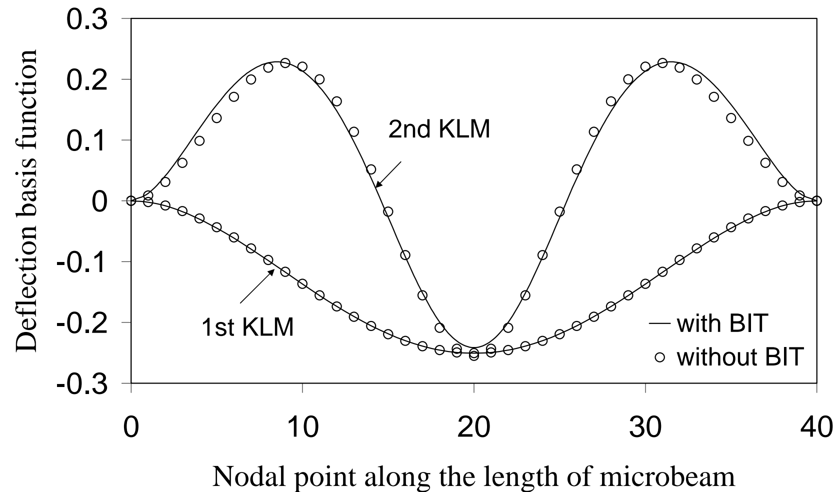


Figure 3.22 Comparison of the first two deflection KLMs with and without consideration of bending induced tension (BIT) effect.

The first two deflection KLMs are plotted in Figure 3.22, and the first two back pressure KLMs are plotted in Figure 3.23. Again, it is observed that the mode shape difference of the first deflection KLM is negligible and the differences between first two back pressure KLMs are also insignificant. The results of midpoint deflection of microbeam in pull-in dynamics simulation when the system is applied with input step voltage of 14 V by the two macromodels compared with FDM solutions are plotted in Figure 3.24. The error of macromodel simulation results with respect to the FDM results is plotted in Figure 3.25. It is observed from Figure 3.24 and Figure 3.25 that the macromodel using the KLMs obtained from the first set of ensemble of snapshots can well represent the system without consideration of bending induced tension, while the macromodel using the KLMs obtained from the second ensemble of snapshots can also reproduce enough accurate results for the system with consideration of bending induced tension. This demonstrates the flexibility of macromodel for system dynamic

simulation when the axial stress in the microbeam is changed. It is noted from Figure 3.24 that the pull-in time is 23% longer when the bending induced tension effect is considered.

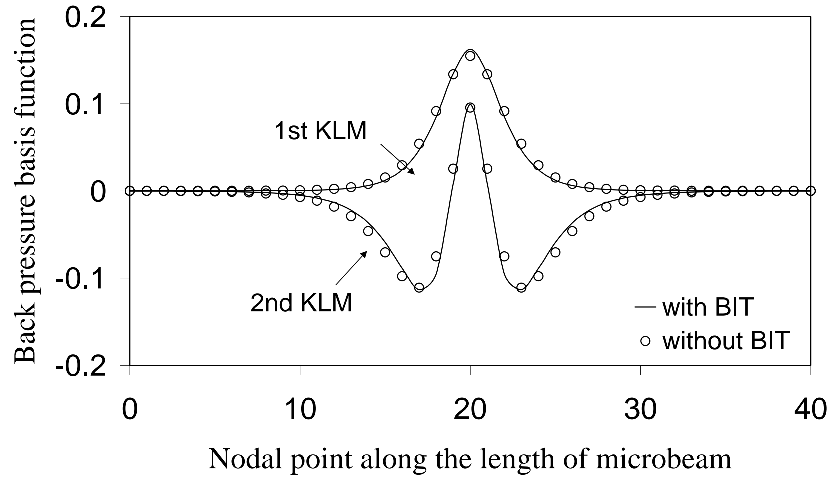


Figure 3.23 Comparison of the first two back pressure KLMs with and without consideration of bending induced tension (BIT) effect.

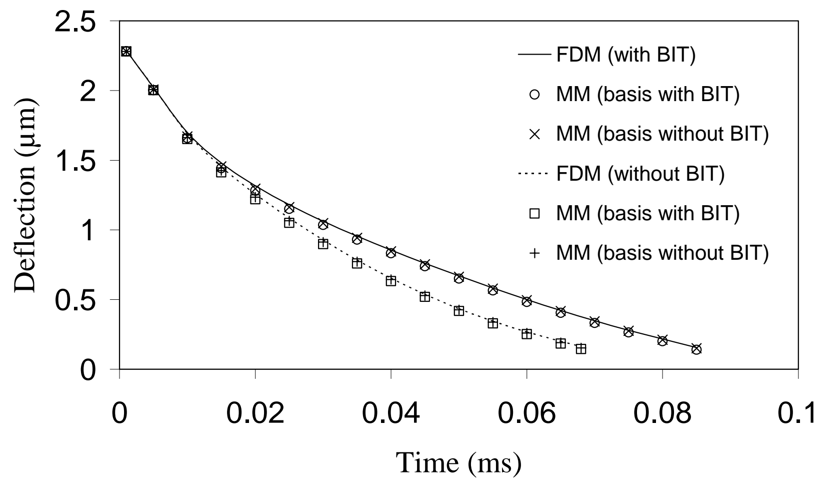


Figure 3.24 Comparison of macromodel simulations for an input step voltage of 14 V with and without consideration of bending induced tension (BIT) effect.

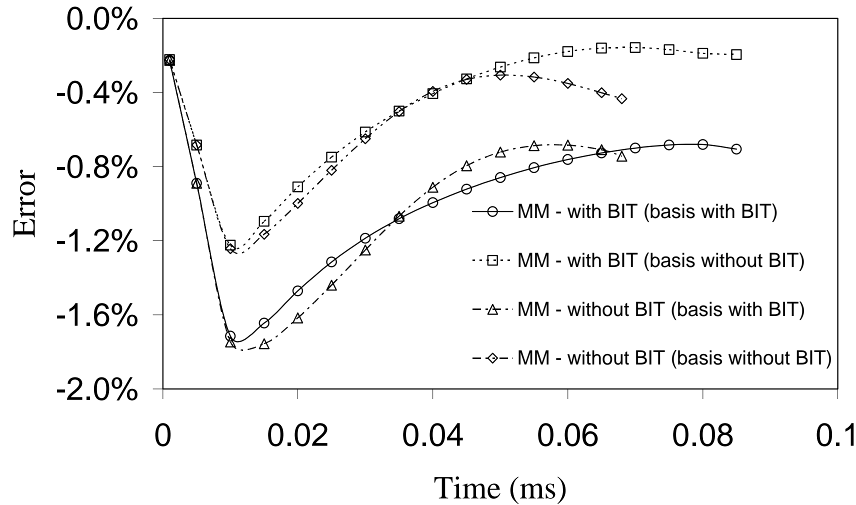


Figure 3.25 The error of macromodel simulation with respect to FDM solution for an input step voltage of 14 V.

## 3.8 CONCLUSION

The model reduction technique based on KLD to create macromodel for the dynamic simulation of the nonlinear dynamics of MEMS systems has been developed in this chapter. The macromodel generated by employing the KLMs extracted from KLD procedure as the basis functions in the Galerkin projection has shown its accuracy, flexibility and efficiency in the representation of the original system. Although it needs an initial process of 48.9 min by using the FDM to simulate the original nonlinear PDEs to obtain the snapshots and KLD procedure to extract the KLMs and KLVs, it has been demonstrated that macromodels are very flexible to simulate the system. As for the computation time efficiency, when Silicon Graphics Origin 2000 is used, it takes 32.53 min to obtain the pull-in time by using FDM when the input step voltage is 10.25 V. In comparison, it requires only 3.03 min to simulate the pull-in dynamics by macromodel with less than 1.2% error. The effects of the number of

snapshots, input voltage spectrum and bending induced tension on the KLMs extraction and the accuracy of macromodel simulation have also been investigated. In conclusion, KLD and the Galerkin procedure that employs the KLMs as the basis functions can reduce the original nonlinear PDEs to low-dimensional macromodel with small number of degrees-of-freedom, and the macromodel can well represent and simulate the original systems. The model reduction technique developed in this chapter provides a tool for system designer to design and optimize the MEMS system efficiently and effectively.

# CHAPTER 4

# MACROMODELS FOR DYNAMIC SIMULATION OF MEMS USING NEURAL NETWORK-BASED GENERALIZED HEBBIAN ALGORITHM

A neural network-based method of model order reduction that combines the generalized Hebbian algorithm (GHA) and Galerkin procedure to perform the dynamic simulation and analysis of MEMS systems and devices is presented in this chapter. The GHA is an unsupervised neural network model used to perform principal component analysis (PCA) of the correlation matrix of the input signals (Sanger, 1989). It has been investigated and applied in image coding and texture segmentation problems, finding the principal eigenvectors of a correlation matrix in different kinds of seismograms, and handling sensor array signal processing in the complex domain (Diamantaras and Kung, 1996; Zhang and Ma, 1997; Huang, 1999; Fiori, 2000). In this chapter, the extensive computer results of PCA using the neural network-based GHA are used to extract empirical basis functions from an ensemble of numerical or experimental data. The basis can then be employed in the Galerkin procedure to convert the original system into a low-dimensional macromodel that can be used to carry out dynamic simulations of the original system resulting in dramatic reduction of computation time while not losing flexibility and accuracy. Compared with model reduction method based on KLD described in the preceding chapter, the key advantage of the present method is that it does not need to compute the input correlation matrix in advance (Equation (3.8) or (3.17)). It needs only to find very few required basis functions that can be learned directly from the input data. This feature spares much

computation time, especially when the measured data set is large. The method is evaluated based on the simulation of the pull-in dynamics of a doubly-clamped microbeam subjected to different input voltages. The accuracy, efficiency and the flexibility of the proposed method are examined by comparing the simulation results with the fully meshed FDM solutions.

## 4.1 THEORY OF PRINCIPAL COMPONENT ANALYSIS

Principal component analysis (PCA) is a statistical technique and the idea behind PCA is quite old. The earliest descriptions of the technique are given by Pearson (1901) and Hotelling (1933). The purpose of PCA is to identify the dependence structure behind a multivariate stochastic observation in order to obtain a compact description of it. PCA can be seen equivalently as either a variance maximization technique or a least-mean-squares technique. Through PCA, many variables can be represented by a few principal components, so it can be considered as a feature extraction technique. Performing PCA on a set of multivariate random data means computing the eigenvectors of its correlation matrix corresponding to the largest eigenvalues, and the projection of the data over the eigenvectors to obtain a number of principal components.

Let $x$ denote a $m-$dimensional random vector with zero mean and $q$ a $m-$dimensional unit vector onto which the vector $x$ is to be projected. This projection is defined as the inner product of $x$ and $q$ as

$$S = (x, q) = x^T q = q^T x \tag{4.1}$$

subject to the constraint

$$\|q\|^2 = (q^T q) = 1 \tag{4.2}$$

Since the random vector $x$ has zero mean value, the mean value of the projection $S$ is zero too. Thus the variance of $S$ is the same as its mean square value

$$\sigma^2 = E\left[S^2\right] = E\left[q^T x x^T q\right] = q^T E\left[x x^T\right] q = q^T R\, q \tag{4.3}$$

where $E[\bullet]$ is the statistical expectation operator and $R$ is the $m \times m$ symmetric correlation matrix of the random vector $x$.

PCA is to find the unit vector $q$ so that the variance $S$ has extremal value subjected to the constraint (4.2)

$$\text{Maximize } \sigma^2 = E\left[S^2\right] = q^T R\, q$$
$$\text{subject to } \|q\|^2 = \left(q^T q\right) = 1 \tag{4.4}$$

Introducing the Lagrangian multiplier $\lambda$, the conditional extreme value problem becomes

$$J(q,\lambda) = q^T R\, q - \lambda\left(q^T q - 1\right) \tag{4.5}$$

Differentiating the above with respect to $q$ yields

$$\frac{\partial J(q,\lambda)}{\partial q} = 2(R - \lambda I)\, q \tag{4.6}$$

The necessary and sufficient conditions for extrema are for the right hand side of Equation (4.6) to be zero. Hence it implies

$$Rq = \lambda\, q \tag{4.7}$$

It reveals that the solution of $\lambda$ and the unit vectors $q$ for the extreme value problem are the eigenvalue and the corresponding eigenvector of the correlation matrix $R$, respectively. The symmetric and positive definite properties of correlation matrix ensure the solutions are real, positive eigenvalues and mutual orthonormal eigenvectors. The order of eigenvectors $q_1, q_2, \ldots, q_m$, which are also known as

principal eigenvectors in PCA, can be arranged corresponding to the magnitude of the eigenvalues $\lambda_1 > \lambda_2 > \ldots > \lambda_m$.

According to the spectral theorem, the correlation matrix $R$ can be expressed in terms of its eigenvalues and eigenvectors as

$$R = \sum_{i=1}^{m} \lambda_i q_i q_i^T \tag{4.8}$$

Considering Equation (4.3) and the orthonormality condition of eigenvectors, it is obvious that variances are equal to eigenvalues

$$\sigma_j^2 = \lambda_j, \quad j = 1, 2, \ldots, m \tag{4.9}$$

Hence the first eigenvector $q_1$ corresponding the the largest eigenvalue $\lambda_1$ represents most of the system feature, followed by the second eigenvector $q_2$ and so forth. The principal component $a_j$ is defined as the projection of data vector $x$ onto the pricipal eigenvector $q_i$ as

$$a_j = q_j^T x, \quad j = 1, 2, \ldots, m \tag{4.10}$$

The original data vector $x$ can then be reconstruced as

$$x = \sum_{j=1}^{m} a_j q_j \tag{4.11}$$

The advantage of PCA is that it provides an effective technique for dimensionality reduction. In particular, the number of features needed for effective data representation can be reduced by discarding those linear combinations in Equation (4.11) that have small variances and retaining those terms that have large variance. Let $\lambda_1 > \lambda_2 > \ldots > \lambda_l$ denote the first $l$ largest eigenvalues of the correlation matrix $R$, the data vector $x$ can be approximated by truncating the expansion of Equation (4.11) after $l$ terms as

$$x \approx \sum_{j=1}^{l} a_j q_j , \quad l \leq m \tag{4.12}$$

## 4.2 GENERALIZED HEBBIAN ALGORITHM

Since the pioneering work of Oja (1982) in which a single linear neuron with a Hebbian type adaptation rule for its synaptic weights can evolve into a filter for the first principal component of the input distribution, the neural networks-based PCA and its extensions have become an important research field both for the interesting implications on unsupervised learning theory and fruitful applications to neural information processing (Fiori, 2000). In recent years, several neural network architectures and learning rules for performing PCA have been proposed in scientific literature. Among them, the generalized Hebbian algorithm (GHA) presented by Sanger (1989) to extract the principal eigenvectors of the correlation matrix from an ensemble of signals is well received and will be used in this section.

The GHA is closely related to classical Hebbian learning algorithms. Hebbian learning rules modify the connection between two units by an amount proportional to the product of the activation of those units. If $x$ is the activation of the input nodes and $W$ is the synaptic weight matrix, then $y = Wx$ is the activation at the outputs. Hebbian algorithms modify $W$ by using

$$W(t+1) = W(t) + \beta(t) y(t) x(t)^T \tag{4.13}$$

where $\beta(t)$ is a sequence of small step-size parameter, or learning-rate parameter, which determines the rate of change of the weights.

Oja (1982) showed that if the diagonal elements of $WW^T$ was maintained as unity so that the norm of each row was one, then a Hebbian learning rule would cause the rows

of $W$ to converge to the principal eigenvectors of the correlation matrix $R = E[xx^T]$, and a network learning algorithm was proposed as

$$w_i(t+1) = w_i(t) + \beta(t)\left(y_i(t)x(t) - y_i^2(t)w_i(t)\right) \tag{4.14}$$

where $w_i$ was a column of $W$, and $y_i = w_i^T x$. Oja showed that Equation (4.14) could be approximated under conditions imposed on $x$ and $\beta(t)$ by a differential equation

$$\dot{w}(t) = Rw_i(t) - \left[w_i(t)^T R w_i(t)\right] w_i(t) \tag{4.15}$$

Oja then proved that for an arbitrary choice of initial weights, $w_i$ would converge to the principal eigenvector $q_1$ so long as $w_i(0)^T q_1 \neq 0$ at time zero.

The Oja algorithm only finds the first eigenvector, whereas the GHA presented by Sanger (1989) would find the other eigenvectors, which was effected through combining Oja learning rule (4.14) and a Gram-Schmidt orthogonalization process. The GHA derived by Sanger is as follows.

Let the inputs to a single-layer neural network be a $n-$dimensional column vector $x$, the weights be a $m \times n$ matrix $W$, and the outputs be a $m-$dimensional column vector $y = Wx$ where $m < n$. The values of $x$ are generated by a stationary white random vector stochastic process with a correlation matrix $R = E[xx^T]$. Assume $x$ and $y$ are both time-varying, therefore $W$ will be time-varying as a result of adaptation through the training algorithm.

The GHA is expressed as

$$w_{ij}(t+1) = w_{ij}(t) + \beta(t)\left[y_i(t)x_j(t) - y_i(t)\sum_{k \le i} w_{kj}(t)y_k(t)\right] \tag{4.16}$$

where $w_{ij}$ is the element of the weight matrix $W$ which is the connection strength between the $j-$th input neuron and the $i-$th output neuron ($w_{ij}$ is initially assigned

random weights), $x_j$ is the $j-\text{th}$ component of the input vector $x$, $y_i$ is the $i-\text{th}$ component of the output vector $y$, and $\beta(t)$ is the learning parameter that decreases with time in such way that

$$\lim_{t\to\infty}\beta(t)=0 \quad \text{and} \quad \sum_{t=0}^{\infty}\beta(t)=\infty \tag{4.17}$$

Equation (4.16) can be rewritten in matrix form as

$$\Delta W(t)=\beta(t)\left\{y(t)x^T(t)-\mathrm{LT}\left[y(t)y^T(t)\right]W(t)\right\} \tag{4.18}$$

where the lower triangular operator $\mathrm{LT}[\bullet]$ sets all elements above the diagonal of its matrix argument to zero, thereby making it 'lower triangular'. The second term on the GHA of Equation (4.16) is the Hebbian term, and the third term ensures that the algorithm learns successive eigenvectors of the correlation matrix of the input vectors ordered by decreasing eigenvalues. Under conditions (4.17), Sanger (1989) proved the following

Theorem 1: If $W$ is assigned random weights at time zero, then with probability 1, Equation (4.16) will converge, and $W$ will approach the matrix whose rows are the first $l$ eigenvectors of the input correlation matrix $R$, ordered by decreasing eigenvalues.

The significance of this theorem is that it is a procedure that guarantees the GHA to find the first $l$ eigenvectors of the correlation matrix $R$, assuming that the associated eigenvalues are distinct. The implementation network for the GHA possesses the following features

i) No need to compute the correlation matrix $R$ explicitly in advance. This is because the eigenvectors are derived (learned) directly from the input vector. It is an important feature, particularly if the number of inputs is large such that computation and manipulation of $R$ are not feasible or economical. For instance,

if a network has 4 000 inputs, then $R$ has 16 million elements, and it may be difficult to find the eigenvectors using traditional PCA methods. However, the GHA requires only the computation of the outer products $yx^T$ and $yy^T$, so that if the number of outputs is small, the computational and storage requirements can be correspondingly decreased. If there are 5 outputs, for example, $yx^T$ will have only 20 000 elements, and $yy^T$ will have only 25 elements. The GHA takes advantage of this network structure. Generally, for the problem with large number of inputs and required small number of outputs, GHA provides a practical and useful procedure for finding the required first few dominant principal eigenvectors.

ii) Implementation with local operation. This feature is favourable for parallel computations and parallel hardware.

iii) Good expandability. Updating of the $j-\text{th}$ neuron is affected only by those neurons with number less than $j$. Hence, if the first $k$ principal eigenvectors have been obtained, then the learning of the $(k+1)-\text{th}$ neuron will leave the preceding $k$ neuron weight vectors intact.

In the present model reduction method for dynamic simulation of MEMS device as shown in Figure 3.8, GHA is used to obtain the eigenvectors by iteratively training the neural network, where the input vector $x$ is the snapshot of the flexural deflection of the deformable microbeam or the back pressure data at one temporal sampling as described in the preceding Section 3.5, and the rows of the weight matrix $W$ are the eigenvectors which need to be found by the algorithm. It should be pointed out that, from numerous experience, the choice of the learning parameter $\beta(t)$ in Equation (4.16) has a profound impact in the convergence speed of the GHA. $\beta(t)$ is chosen

empirically at a value fixed between 0.1 and 0.01 which provides good convergence as shown in Sanger (1989). However, the fixed value of $\beta(t)$ in the present study of the above-mentioned MEMS device does not ensure good convergence. An adaptive choice of $\beta(t)$ described in Diamantaras and Kung (1996) is adopted in the present study, in which $\beta(t)$ is calculated iteratively by

$$\beta(t) = \frac{\beta(t-1)}{\gamma + y^2(t)\beta(t-1)} \tag{4.19}$$

where $0 < \gamma \leq 1$ is a factor chosen by the user. Simulation results show that good convergence can be obtained if $\gamma$ is chosen to be closer to one. One problem to be studied further in the learning algorithm is how to balance the convergence speed and the convergence effectiveness.

## 4.3 MACROMODEL GENERATION

Similar to the procedure described in Section 3.5, for the MEMS system as shown in Figure 3.8, the pull-in dynamics of the microbeam at different time steps are simulated using FDM for an ensemble of applied input step voltages to obtain the ensembles of microbeam deflection $w_n(x_i, t_s)$ and the back air pressure $p_n(x_i, y_j, t_s)$. These ensembles of deflection and back pressure are then used as snapshots, i.e., the ensemble of input signals for the GHA network to generate the eigenvectors of the input correlation matrix. After the eigenvectors are obtained, the Galerkin procedure which employs these eigenvectors as basis functions is applied to the original nonlinear governing PDEs (3.44) and (3.45) to convert them to a macromodel with smaller number of ODEs. Considering Equation (4.12) and denoting the eigenvectors (The rows of weight matrix $W$) with respect to the deflection as $q_i^w(x)$ and those with

respect to the back pressure as $q_j^p(x,y)$, the deflection $w(x,t)$ and pressure $p(x,y,t)$ can be approximated as a linear combination of the eigenvectors as follows

$$w(x,t) = w_0 + \sum_{i=1}^{I} a_i^w(t) q_i^w(x) \tag{4.20}$$

$$p(x,y,t) = p_a + \sum_{j=1}^{J} a_j^p(t) q_j^p(x,y) \tag{4.21}$$

Substituting Equations (4.20) and (4.21) into governing equations (3.44) and (3.45) and applying the Galerkin procedure, a macromodel in terms of a set of nonlinear ODEs in analogy to Equations (3.54) and (3.55) is derived

$$M_j \frac{d^2 a_j^w}{dt^2} + \sum_{i=1}^{I} K_{ji} a_i^w + f_j = 0, \quad (j = 1, 2, \cdots, I) \tag{4.22}$$

$$\sum_{i=1}^{J} H_{ji} \frac{da_i^p}{dt} + \sum_{i=1}^{J} S_{ji} a_i^p + c_j = 0, \quad (j = 1, 2, \cdots, J) \tag{4.23}$$

where the coefficients $a_i^w$ and $a_i^p$ are to be determined and the elements in the matrices $M_j$, $K_{ji}$, $H_{ji}$ and $S_{ji}$, and vectors $c_j$ and $f_i$ are analogoue to Equations (3.56)-(3.61) and expressed as follows

$$M_j = \int_L \rho \left(q_j^w\right)^2 dx \tag{4.24}$$

$$K_{ji} = K_{ij} = \int_L \left( EI \frac{\partial^2 q_j^w}{\partial x^2} \frac{\partial^2 q_i^w}{\partial x^2} + T \frac{\partial q_j^w}{\partial x} \frac{\partial q_i^w}{\partial x} \right) dx \tag{4.25}$$

$$f_j = \int_L \left( \frac{\varepsilon_0 b V^2}{2w^2} - \int_0^b (p - p_a)\, dy \right) q_j^w \, dx \tag{4.26}$$

$$H_{ji} = H_{ij} = \int_A \frac{12\mu}{1 + 6K_n} w q_j^p q_i^p dxdy \tag{4.27}$$

$$S_{ji} = S_{ij} = \int_A \left[ w^3 p \left( \frac{\partial q_j^p}{\partial x} \frac{\partial q_i^p}{\partial x} + \frac{\partial q_j^p}{\partial y} \frac{\partial q_i^p}{\partial y} \right) + \frac{12\mu}{1 + 6K_n} q_j^p q_i^p \frac{\partial w}{\partial t} \right] dxdy \tag{4.28}$$

$$c_j = \int_A \frac{12\mu}{1+6K_n} p_a q_j^p \frac{\partial w}{\partial t} dxdy \qquad (4.29)$$

The ODEs (4.22) and (4.23) can be integrated numerically in time for the coefficients $a_i^w$ and $a_i^p$. Substituting them into Equations (4.20) and (4.21) yield the system dynamical response when subjected to an input voltage.

### 4.3.1 NUMERICAL RESULTS

In order to demonstrate the efficiency and accuracy of the present model reduction technique using the GHA network, simulated experiments on the MEMS device shown in Figure 3.8 are implemented. The physical features and dimension of the microbeam are listed in Table 3.1.

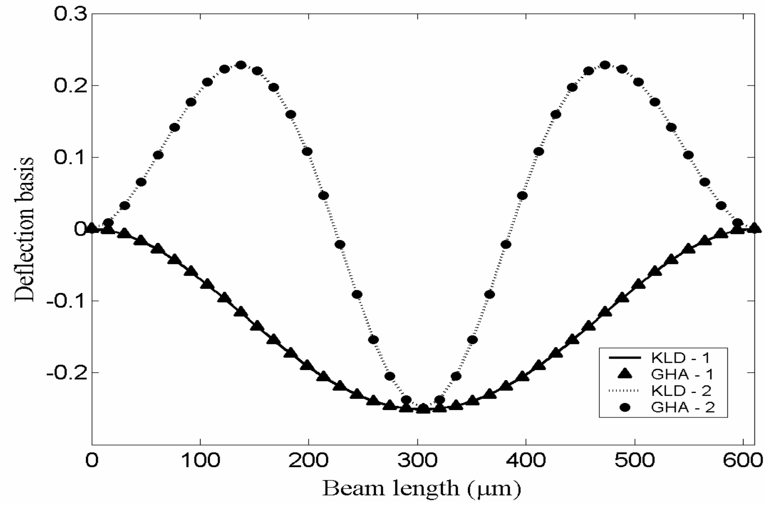


Figure 4.1 The first two deflection basis functions obtained by KLD and GHA.

Following the procedure described in Section 3.5, the snapshots are obtained from the solutions of governing equations of (3.44) and (3.45) by using FDM with mesh size of $40\times20$ for an ensemble of two different step voltages of $V_1 = 10$ V and $V_1 = 16$ V. Each of the 25 snapshots is taken at the fixed time interval from the moment when

each step voltage is applied till pull-in. These snapshots are then used as the inputs of the GHA neural network to generate the principal eigenvectors. In order to demonstrate the validity and suitability of the eigenvectors obtained using GHA as the proper shape functions, the eigenvectors given by GHA and the KLMs obtained by KLD are examined and compared. The first two eigenvectors corresponding to the deflection are plotted in Figure 4.1.

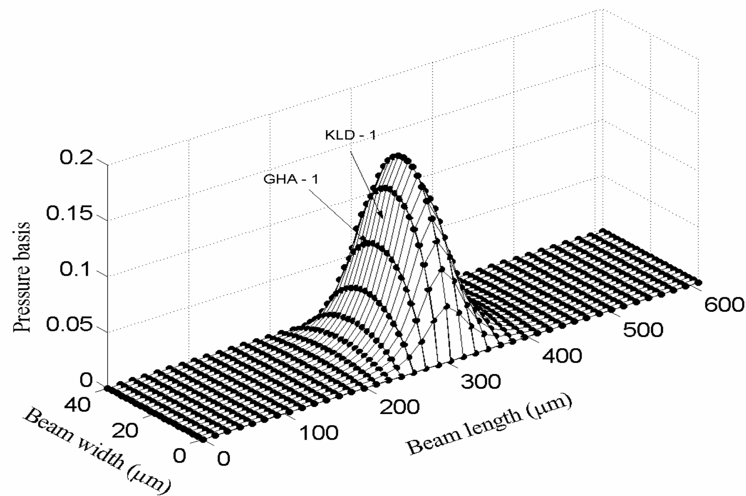


Figure 4.2 The first back pressure basis function obtained by KLD and GHA.

Figure 4.2 and Figure 4.3 show the first and second eigenvectors for back pressure, respectively, where KLD-1 and KLD-2 stand for the first and second KLMs and GHA-1 and GHA-2 denote the first and second principal eigenvectors obtained by GHA. It is observed that the eigenvectors extracted from GHA are identical to KLMs. The higher-order eigenvectors also possess such agreements. The relationship between the discrete KLD and PCA will be addressed in Chapter 5 to understand this similarity. Macromodel is created by the Galerkin procedure using these principal eigenvectors as the basis functions to represent and simulate the pull-in dynamics of the original system.

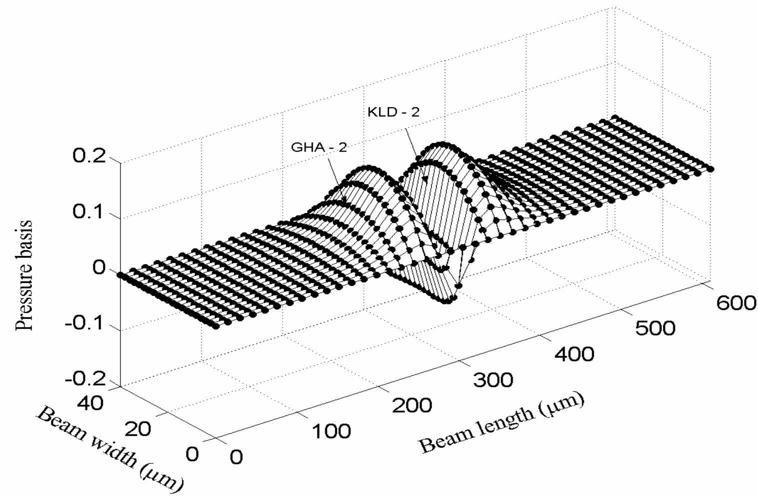


Figure 4.3 The second back pressure basis function obtained by KLD and GHA.

It has been shown in the Tables 3.2 and 3.3 that for the deflection simulation the first eigenvector $q_1^w(x)$ can capture 99.99% of the system feature while it takes at least four first eigenvectors for the back pressure $q_i^p(x,y)$ to capture the same level of feature accuracy in the back pressure simulation. For this reason, only one deflection basis vector but four back pressure basis vectors are chosen in the macromodel simulation to ensure the original system can be properly represented.

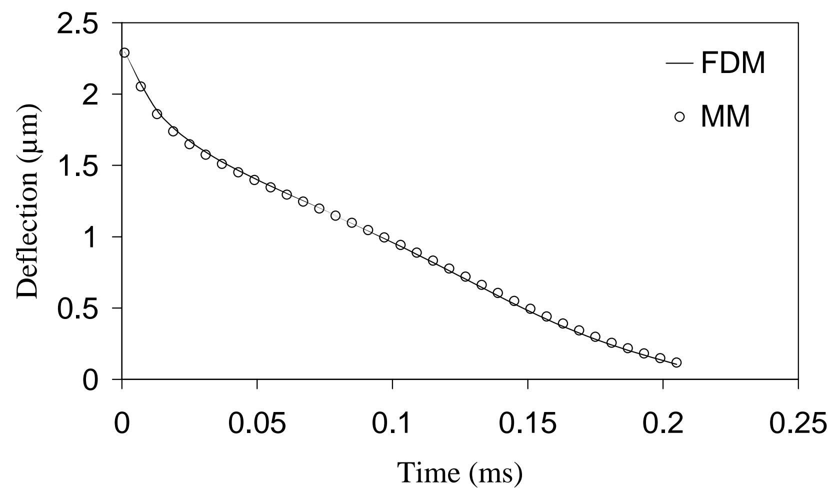


Figure 4.4 Comparison of the microbeam pull-in dynamics for an input step voltage of 10.25 V.

Figure 4.4 shows a comparison of the deflection of the midpoint of the microbeam between the FDM solutions of the original nonlinear PDEs (3.44) and (3.45) and the macromodel (MM) approximation when the system is applied with an input step voltage of 10.25 V. Figure 4.5 shows that the error defined by Equation (3.65) is very small $(\leq 1.2\%)$ when $I = 1$ and $J = 4$ are selected in macromodel.

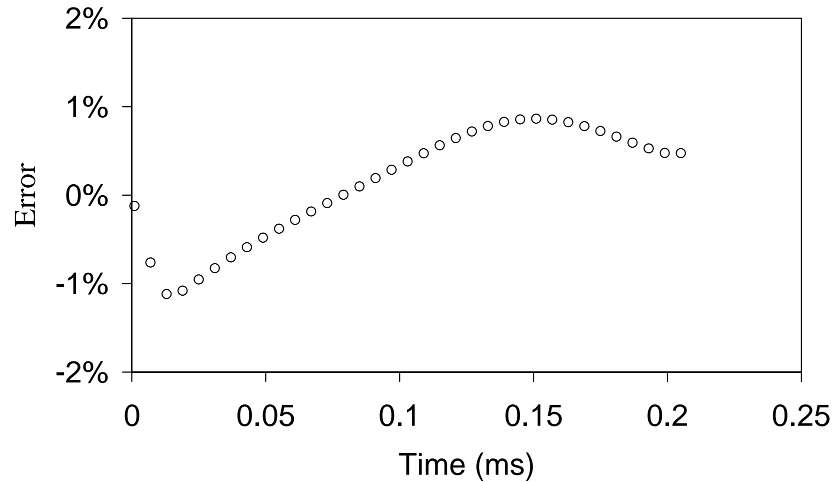


Figure 4.5 The error of macromodel simulation with respect to FDM solution for an input step voltage of 10.25 V.

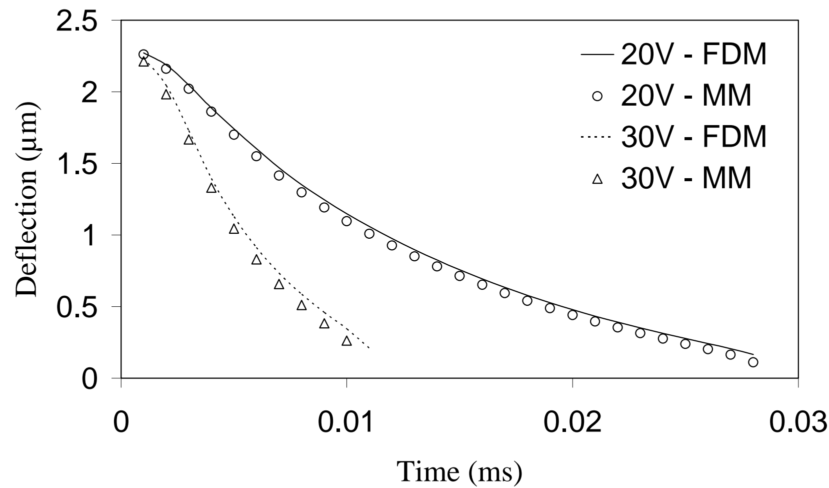


Figure 4.6 Comparison of the microbeam pull-in dynamics for input step voltages of 20 V and 30 V.

In order to examine the flexibility of the macromodel, simulations with voltages that are far from the voltages used to create the basis functions are performed. The input step voltages of 20 V and 30 V are used to simulate the pull-in dynamics by the same macromodel. It shows that good accuracy can also be obtained when the input voltage are changed without re-generating the macromodel. Figure 4.6 and Figure 4.7 show that the macromodel simulations are accurate and the errors are small, less than 2.5% and 3.7% with respect to full mode FDM solutions, respectively.

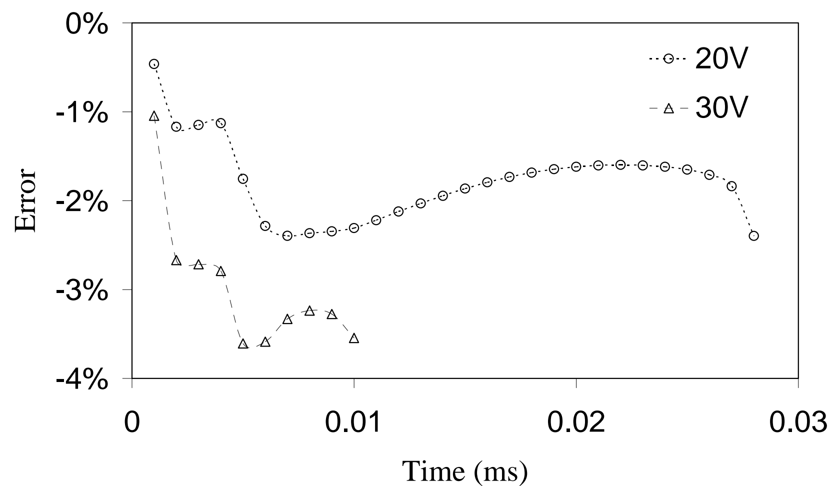


Figure 4.7 The errors of macromodel simulation with respect to FDM solution for input step voltages of 20V and 30 V.

It is noted that the macromodel generated by the above ensemble of two different input step voltages can also be used to simulate the system when the input voltage wave spectrum is changed. Similar to the numerical experiments carried out in Chapter 3, Figure 4.8 shows the macromodel simulation for an input sinusoidal voltage with magnitude of 14 volt at a frequency of 10kHz. Figure 4.9 plots the error of the macromodel simulation compared with the FDM solution. It shows that the macromodel simulation can capture the system dynamics accurately with error less than 1.7% without re-generating the macromodel.

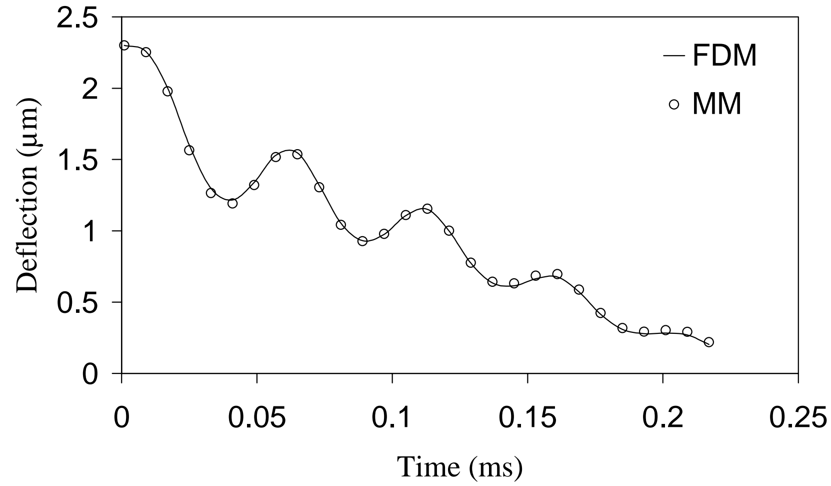


Figure 4.8 Comparison of the microbeam pull-in dynamics for an input sinusoidal voltage of 14 at a frequency of 10 kHz.

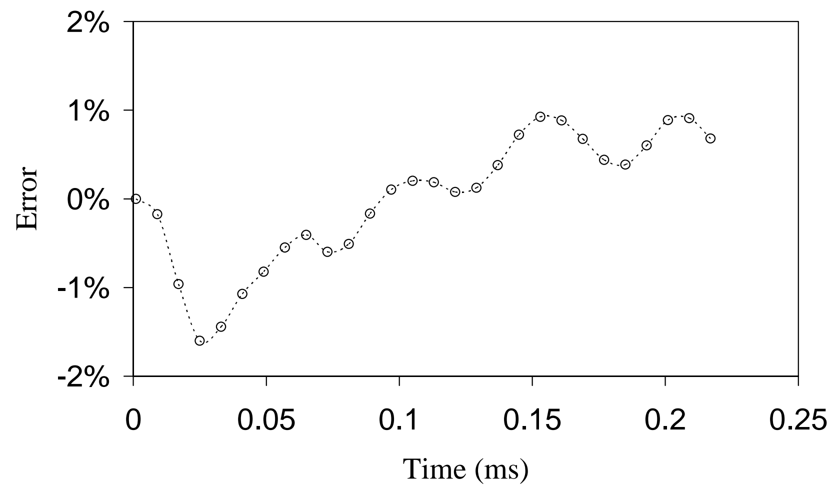


Figure 4.9 The error of macromodel simulation with respect to FDM solution for an input sinusoidal voltage of 14 V at a frequency of 10 kHz.

Figure 4.10 shows the simulation of an input ramp voltage of $V = Rt$ with ramp rate of $R = 0.4\ \mathrm{V}\mu\mathrm{s}^{-1}$. It is noted from Figure 4.11 that the simulation has a very good result with error less than 2.1% with respect to FDM solution. The results demonstrate again that the same macromodel can simulate the system with different input voltage spectra.

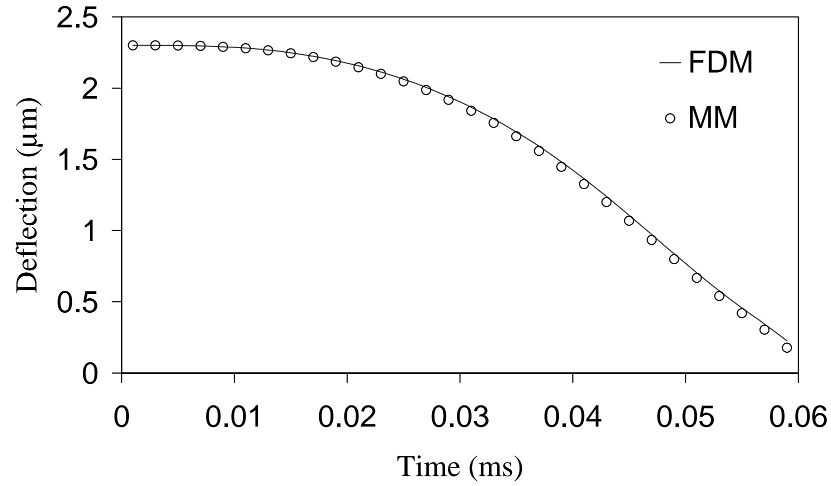


Figure 4.10 Comparison of the microbeam pull-in dynamics for an input ramp voltage $V = Rt$, $R = 0.4\ \mathrm{V}\mu\mathrm{s}^{-1}$.

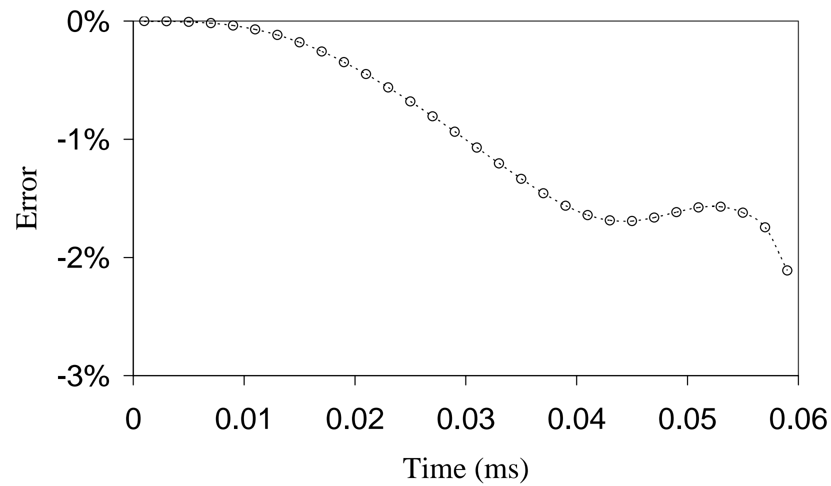


Figure 4.11 The error of macromodel simulation with respect to FDM solution for an input ramp voltage $V = Rt$, $R = 0.4\ \mathrm{V}\mu\mathrm{s}^{-1}$.

### 4.3.2 CONCLUSION

A model reduction approach is presented for the simulation of the nonlinear dynamics of MEMS based on the neural network-based GHA. The macromodel generated by

employing the eigenvectors extracted from the GHA network as basis functions in the Galerkin procedure has shown its flexibility and efficiency in the representation and simulation of the original nonlinear PDEs. The potential applicability of the proposed neural network method on other MEMS structures is worth mentioning. In general, this methodology can be used to simulate the dynamic behaviours of MEMS, however, for different MEMS devices or systems, the basis functions would be different. The method is useful for designing and simulating MEMS devices and systems, especially if different types of coupled devices are involved in the system. In conclusion, it has demonstrated that the proposed method reduces original nonlinear PDEs to a macromodel with smaller number of degrees-of-freedom, and the macromodel can represent and simulate the original systems faithfully. Besides these, this method does not need to compute the input correlation matrix explicitly, it needs only to find very few required basis functions compared with other existing model reduction methods for dynamic simulation of MEMS. This method has the computational advantages when the measured data as input signals are large. For the input vector with dimension $n$, the existing traditional methods use memory space of order $n^2$ in computation because of the correlation matrix, but the neural network based on the GHA learning rule only uses a memory space of order $n$ to find the eigenvectors. Successful simulation results show that the present model reduction technique provides another feasible way for system designers to design and optimize MEMS systems and devices efficiently and effectively.

## 4.4 ROBUST GENERALIZED HEBBIAN ALGORITHM

Robustness theory is concerned about solving problems subject to model perturbation or added noise. A robust algorithm could not only perform well under the assumed model, but also produce a satisfactory result when the assumed model is deviated. Compared with the standard neural network-based PCA model, the robust neural network-based PCA model has a number of numerical advantages such as stability, robustness to noise-injected data, and faster convergence of iterations in the network training stages. The ability of processing noisy data ensures that the robust neural network-based PCA method as an ideal choice in the model reduction of MEMS in practical applications. The robust neural network-based PCA algorithm proposed by Karhunen and Joutsensalo (1995) to extract the principal eigenvectors of the correlation matrix from an ensemble of signals is applied in this section. The algorithm is derived from the representation error minimization, which is given by

$$\begin{cases} w_{k+1}(i) = w_k(i) + \beta_k y_k(i) f(e_k(i)) \\ e_k(i) = x_k - \sum_{j=1}^{I(i)} y_k(j) w_k(j) \\ y_k(i) = x_k^T w_k(i), \qquad (i = 1, 2, \ldots, M) \end{cases} \tag{4.30}$$

where $w_k(i)$ is the weight vector of the $i-$th neuron, $e_k(i)$ is the instantaneous representation error vector, $y_k(i)$ is the output of the $i-$th neuron, $\beta_k$ is the gain parameter, $M$ is the number of the neurons in the output layer of the network, $x_k$ is the input data vector, and $f(\xi)$ is a nonlinear function. In general, $f(\xi)$ needs to satisfy to the following requirements

i) $f(\xi)$ is a monotonically growing function of $\xi$.

ii) $f(\xi) \le 0$ for $\xi < 0$ and $f(\xi) \ge 0$ for $\xi > 0$, i.e., it is required that the growing of $f(\xi)$ should be less than the linear growing for stability reasons.

The upper bound of the summation index $I(i)$ represents the two different cases of the network models. $I(i) = M$ where $i = 1, 2, \ldots, M$, for the standard symmetric case; $I(i) = i$ for the standard hierarchic case. The optimal weight vector of the $i-$th neuron defines the robust counterpart of the $i-$th principal eigenvector. In the standard hierarchic case and linear special case $f(\xi) = \xi$, Equation (4.30) coincides exactly with standard GHA of Equation (4.16) so that it defines a generalization of the GHA algorithm. Considering that the algorithm using Equation (4.30) possesses the robustness for noise-injected data, it is called the robust GHA (RGHA).

In the present model reduction algorithm, Equation (4.30) is used to obtain the principal eigenvectors of the correlation matrix of the input signals by iteratively train the neural network. The input vector $x_k$ is the ensemble of snapshots described in the preceding sections and the weight vectors $w_k(i)$ is the eigenvector sought for. It should be pointed out that the choice of the gain parameter $\beta_k$ has a profound impact in the convergence speed of the RGHA. In general, $\beta_k$ should decrease with time as described in Equation (4.17). For the purpose of comparing the simulation results from this section with those obtained using the GHA model, the adaptive choice for $\beta_k$ of Equation (4.19) is adopted in the present RGHA algorithm, which is expressed as

$$\beta_k = \frac{\beta_{k-1}}{\gamma + y_k^2 \beta_{k-1}} \tag{4.31}$$

### 4.4.1 MACROMODEL GENERATION

Following the same procedure as described in Section 4.3, for the system shown in Figure 3.8, the pull-in dynamics of the microbeam at a series of different time steps are simulated using FDM for an ensemble of applied step voltage to obtain the microbeam deflection $w_n(x_i, t_s)$ and the back air pressure $p_n(x_i, y_j, t_s)$ ensembles. These deflection and back pressure ensembles are then used as snapshots, i.e., the ensemble of signals for the RGHA network to generate the principal eigenvectors from the correlation matrix of the input signals. The Galerkin procedure which employs these eigenvectors as basis functions is applied to the governing equations (3 .44) and (3.45) to convert them to a macromodel in the same form of Equations (4.22) and (4.23).

### 4.4.2 NUMERICAL RESULTS

The device shown in Figure 3.8 with its properties and dimension listed in Table 3.1 is used to demonstrate the efficiency and accuracy of the present model reduction technique based on the RGHA neural network. It has also been demonstrated that the macromodel is flexible and efficient to simulate the system without re-generation of the macromodel when the input voltage wave spectrum is changed and the input voltages are far from the voltages which are used to create the basis functions. However, all these results are obtained based on the assumption that the data used to generate the eigenvectors have not been corrupted by noise. Currently, little attention has been paid to this problem in the MEMS model reduction literature, although it is essentially important for real applications. In practice, real data often contain some noise, and usually it is not easy to separate it from the signal sought. One way to

examine the influence of the noise on the data processing techniques based on the neural network-based PCA methods is to analyse the effect of the noise on the principal eigenvectors obtained using the GHA and RGHA models, respectively. Figure 4.12 shows the comparisons of the first two deflection eigenvectors, where GHA-1 and GHA-2 represent the first and second deflection eigenvectors obtained by using the GHA model based on the noise-free input data, and GHA-N1 and GHA-N2 represent the first and second deflection eigenvectors obtained using the GHA model based on the noise-injected input data with noise level of 0.5%. The eigenvector mode shape deterioration caused by the noise signals can be observed from the figure. For example, the deviation from the true values and the destruction of the symmetry of the mode shape in the second eigenvector obtained based on the noise-injected data are obvious. Since the PCA algorithms have to process information from real world, they should have the ability to cope with the noisy data or have the robustness when noise exists. How to decrease the influence of the noise on feature extraction by choosing a suitable data processing technique is an important problem.

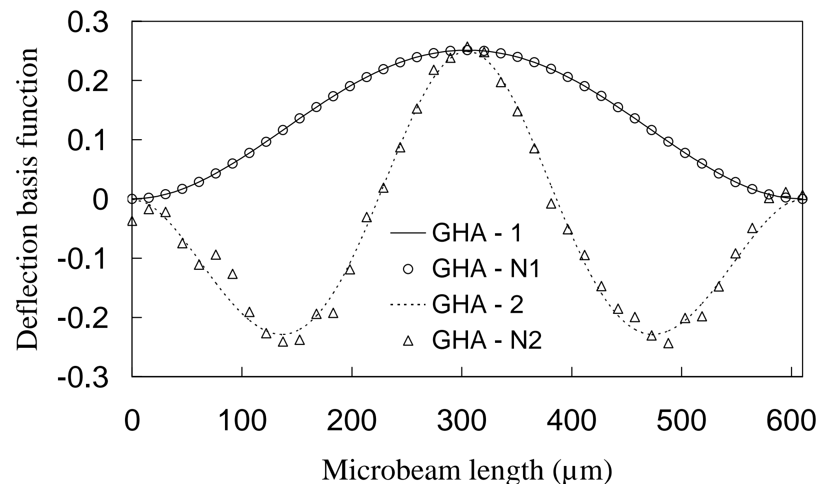


Figure 4.12 The first two eigenvectors obtained by GHA for noise-free and noise-injected snapshots.

The robustness of the RGHA approach to noise corrupted data is examined in the following. Comparative studies are made between the GHA and RGHA techniques. The noise is added to the snapshots obtained using the FDM where the noise array with uniform distribution is scaled in the range of $[-1, 1]$. The noise scale is controlled within 0 to the magnitude of $10^{-3}$ in numerical experiments so that the noise-injected displacement data do not cause serious distortion to the original data.

In order to compare the results obtained from the noise-free data and the noise-injected data, the following square error function is defined as a criterion for comparison

$$\text{error} = \begin{cases} \sum_{i=1}^{l} (N_i - S_i)^2 \Big/ \sum_{k=1}^{l} S_k^2, & (N_j S_j > 0) \\ \sum_{i=1}^{l} (-N_i - S_i)^2 \Big/ \sum_{k=1}^{l} S_k^2, & (N_j S_j < 0) \end{cases} \tag{4.32}$$

where $l$ is the number of the components of the eigenvector, $N_i$ is the component of the eigenvector obtained using the neural network method based on noise-injected snapshots, $S_i$ is the component of the eigenvector obtained using the GHA based on noise-free snapshots, and $N_j$ and $S_j$ are two selected typical values from the above $N_i$ and $S_i$ $(i = 1, 2, \ldots, l)$, respectively. In the above definition, it is considered that the eigenvectors obtained using the two different methods may have different signs.

The comparative experiments are implemented in two different ways as shown in the following sections.

i) Comparisons using different nonlinear functions

In order to examine the effectiveness of applying nonlinear functions in Equation (4.30) to the noise-injected data, besides the sigmoid function which is used frequently in a number of neural network models, several other nonlinear functions listed in Luo

and Unbehauen (1997) are also used in the comparative experiments. The nonlinear functions employed in this section are as follows

$$f_1(\xi) = \frac{1 - e^{-\alpha\xi}}{1 + e^{-\alpha\xi}} \tag{4.33}$$

$$f_2(\xi) = \begin{cases} \xi, & |\xi| \le \beta \\ \beta \operatorname{sgn}(\xi), & |\xi| > \beta \end{cases} \tag{4.34}$$

$$f_3(\xi) = \begin{cases} \xi, & |\xi| \le \beta \\ 0, & |\xi| > \beta \end{cases} \tag{4.35}$$

$$f_4(\xi) = \begin{cases} \beta \sin\left(\dfrac{\xi}{\beta}\right), & |\xi| \le \pi\beta \\ 0, & |\xi| > \pi\beta \end{cases} \tag{4.36}$$

$$f_5(\xi) = \operatorname{sgn}(\xi) \tag{4.37}$$

$$f_6(\xi) = \log(1 + 5\xi) \tag{4.38}$$

where $f_1(\xi)$ is the sigmoid function, $\alpha$ is a real coefficient, $\beta$ is a parameter with its value taken as 1 in the simulations and $\operatorname{sgn}(\xi)$ is the signum function, that is

$$\operatorname{sgn}(\xi) = \begin{cases} 1, & \xi > 0 \\ 0, & \xi = 0 \\ -1, & \xi < 0 \end{cases} \tag{4.39}$$

The square errors defined in Equation (4.32) for the first eigenvector obtained using the GHA and the RGHA based on different nonlinear functions, are calculated according to different noise levels of the noise-injected deflection snapshots. Considering the randomness of the noise-injected data, each nonlinear function and each noise level are calculated ten times. The comparisons of the square errors in statistic mean value obtained using the GHA against those using RGHA employing different nonlinear functions versus noise level are shown in Table 4.1.

Table 4.1 Comparison of square errors using GHA with those using RGHA versus noise (%).

| Noise (%) | GHA | RGHA-1 | RGHA-2 | RGHA-3 | RGHA-4 | RGHA-5 | RGHA-6 |
|---|---|---|---|---|---|---|---|
| 0.00 | 3.06E-14 | 6.63E-15 | 3.06E-14 | 3.06E-14 | 1.50E-14 | 1.50E-14 | 1.17E-14 |
| 0.05 | 8.41E-09 | 8.38E-09 | 8.00E-09 | 8.36E-09 | 9.70E-09 | 9.70E-09 | 8.51E-09 |
| 0.10 | 3.11E-08 | 3.73E-08 | 3.26E-08 | 3.83E-08 | 3.78E-08 | 3.78E-08 | 3.41E-08 |
| 0.15 | 7.34E-08 | 7.03E-08 | 6.47E-08 | 8.23E-08 | 8.60E-08 | 8.60E-08 | 9.02E-08 |
| 0.20 | 1.41E-07 | 1.39E-07 | 1.51E-07 | 1.34E-07 | 1.38E-07 | 1.38E-07 | 1.37E-07 |
| 0.25 | 2.42E-07 | 2.18E-07 | 2.24E-07 | 1.93E-07 | 2.32E-07 | 2.32E-07 | 2.32E-07 |
| 0.30 | 3.25E-07 | 3.11E-07 | 3.19E-07 | 3.67E-07 | 3.61E-07 | 3.61E-07 | 3.61E-07 |
| 0.35 | 4.63E-07 | 4.28E-07 | 4.31E-07 | 5.04E-07 | 5.06E-07 | 5.06E-07 | 4.81E-07 |
| 0.40 | 5.46E-07 | 5.35E-07 | 5.64E-07 | 5.51E-07 | 6.44E-07 | 6.44E-07 | 6.71E-07 |
| 0.45 | 7.01E-07 | 6.46E-07 | 7.40E-07 | 7.01E-07 | 8.28E-07 | 8.28E-07 | 6.48E-07 |
| 0.50 | 8.70E-07 | 8.56E-07 | 9.22E-07 | 1.04E-06 | 1.00E-06 | 1.00E-06 | 9.13E-07 |

In this Table RGHA-$i$ represents the nonlinear function $f(\bullet)$, $(i = 1, 2, \ldots, 6)$ of Equations (4.33)-(4.38) used in the RGHA model. In the simulations, 25 000 iteration steps are performed in the training of the GHA and RGHA neural network and the coefficient $\alpha$ in the sigmoid function is taken as 1.5. The comparative experiments show that the same results are obtained using the GHA and RGHA models based on the noise-free data, which are not listed in the table. However, the results for noise corrupted data are different. From the table it can be seen that the results based on RGHA employing sigmoid function are better than those using GHA; whereas the results using RGHA employing other nonlinear functions are not better and sometimes even worse than those using GHA. From these simulation results, it is shows that RGHA approach does not possess the robustness to noise for all kinds of nonlinear functions in Equation (4.30), but the RGHA algorithm using the sigmoid function has the ability of decreasing the influence of the injected noise.

ii) Comparisons using sigmoid function

Because of the robustness of the RGHA using the sigmoid function to the injected noise, only the sigmoid function is then used in the RGHA model in the following

comparative experiments. The effectiveness of using the sigmoid function to the noisy data is firstly examined. Numerical experiments for the MEMS model reduction using the GHA neural network method have shown that the steps of training to the network have significant influence to the accuracy of the results. Simulations on the RGHA network using sigmoid function show that the RGHA model is superior to the GHA model in dealing with the noisy data when the learning steps are changed. Figure 4.13 shows the comparison of the errors defined in Equation (4.32) multiplied by $\sum_{k=1}^{l} S_k^2$ where the errors are the statistical mean values from ten times calculations for each noise level. The coefficient of the sigmoid function is taken as 1.5 and the number of learning steps is 25 000. From a number of numerical simulations it reveals that the RGHA method has relative robust to noisy data when compared with the GHA model after the noise level is larger than 0.25%. The training convergence examined for the GHA and RGHA models to different noise level shows that the RGHA approach is superior to the GHA in robustness.

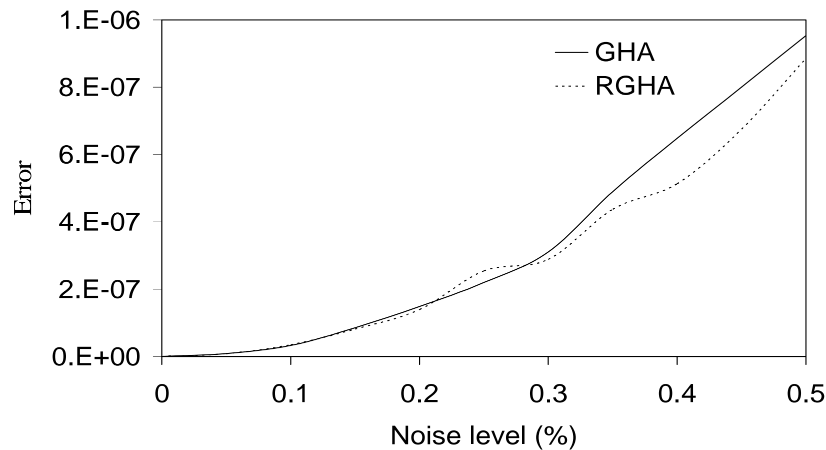


Figure 4.13 Comparison of errors using GHA and RGHA for sigmoid function.

Figure 4.14-Figure 4.20 show the errors defined by Equation (4.32) multiplied by $\sum_{k=1}^{l} S_k^2$ versus the learning steps of the GHA and RGHA used to extract the first

deflection eigenvector from the noise-injected snapshots with noise level of 0.3%. The segmented plotting and the local enlargement of the figures enable one to observe clearly the change of the errors versus the learning steps. From these figures, it is clear that the speed of convergence of the RGHA is obviously superior to that of the GHA. This feature is more prominent during the initial stages of the training. For example, the square error reaches the order of $10^{-6}$ when 300 iteration steps are completed using the RGHA, whereas it needs 1 600 iteration steps for the GHA to reach the same order in square error. It shows that for the same accuracy of convergence, the RGHA needs fewer iteration steps than the GHA. Therefore, the RGHA possesses the feature of fast convergence. From the simulations, it can also be seen that in the middle and later learning stages, the error curve of the GHA fluctuates, whereas the error curve of the RGHA are relatively smooth. It shows that the RGHA model is superior in the stability of convergence compared to the GHA model.

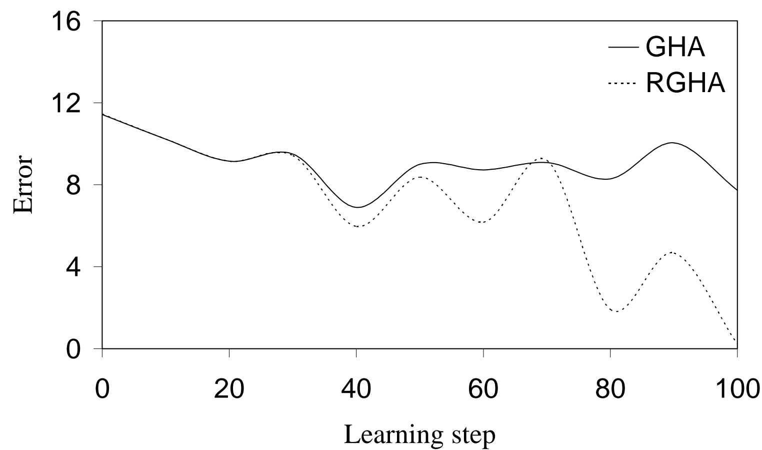


Figure 4.14 Comparison of errors using GHA and RGHA during learning steps between 0–100.

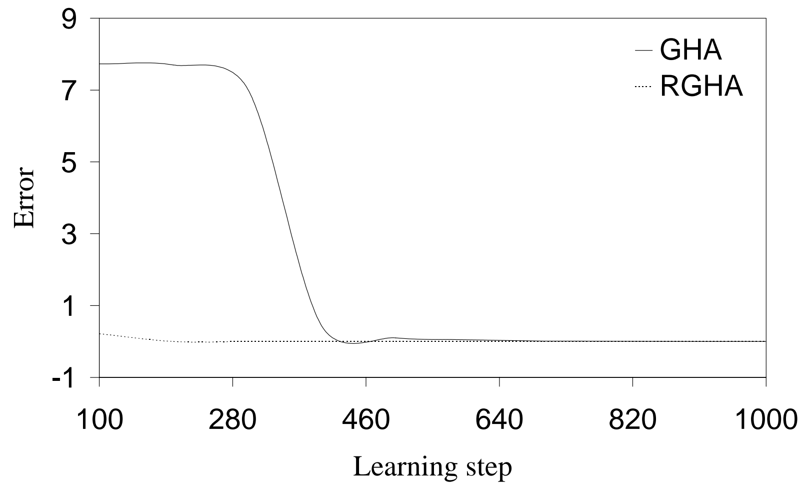


Figure 4.15 Comparison of errors using GHA and RGHA during learning steps between 100–1 000.

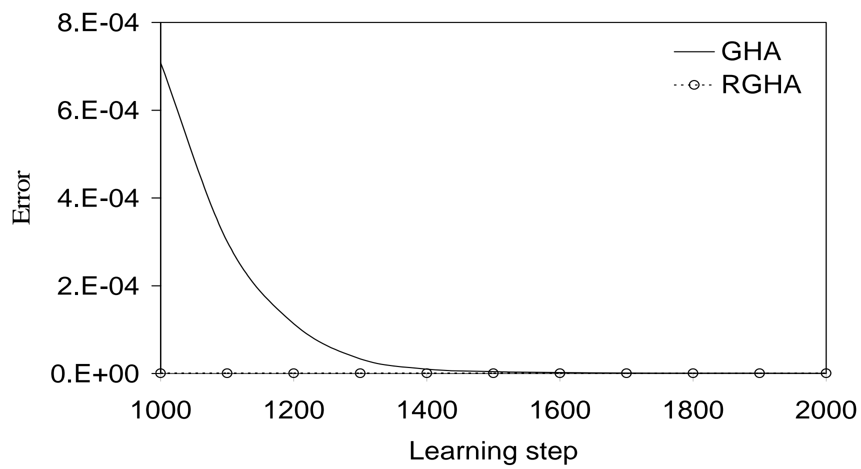


Figure 4.16 Comparison of errors using GHA and RGHA during learning steps between 1 000–2 000.

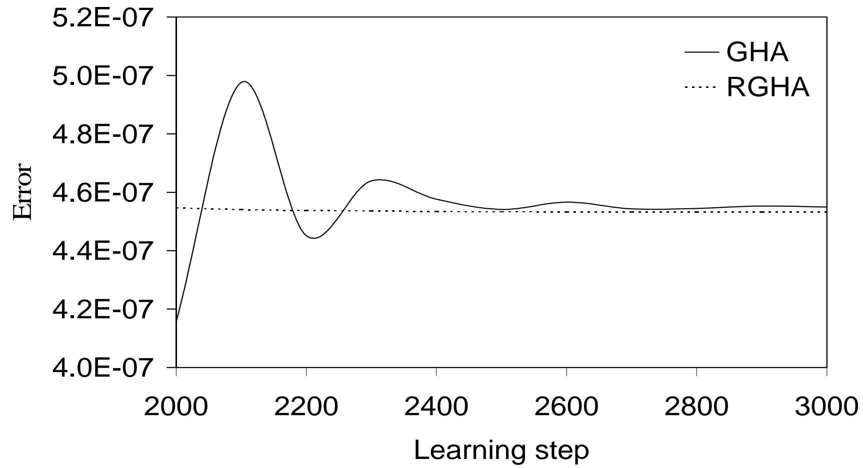


Figure 4.17 Comparison of errors using GHA and RGHA during learning steps between 2 000–3 000.

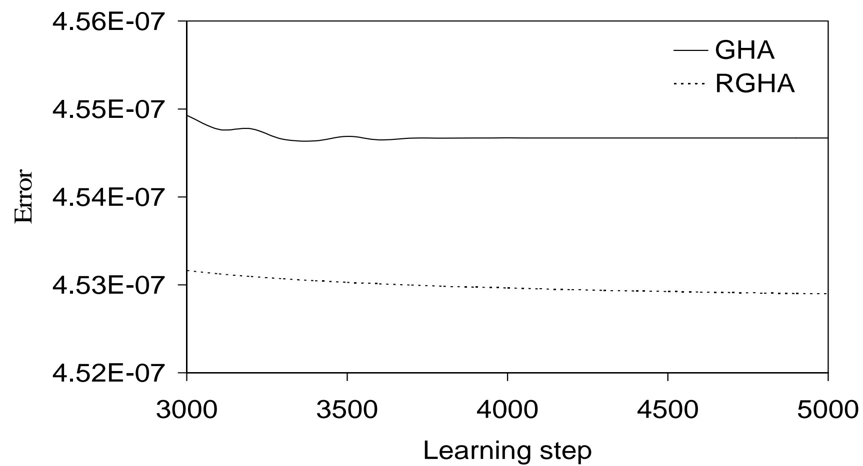


Figure 4.18 Comparison of errors using GHA and RGHA during learning steps between 3 000–5 000.

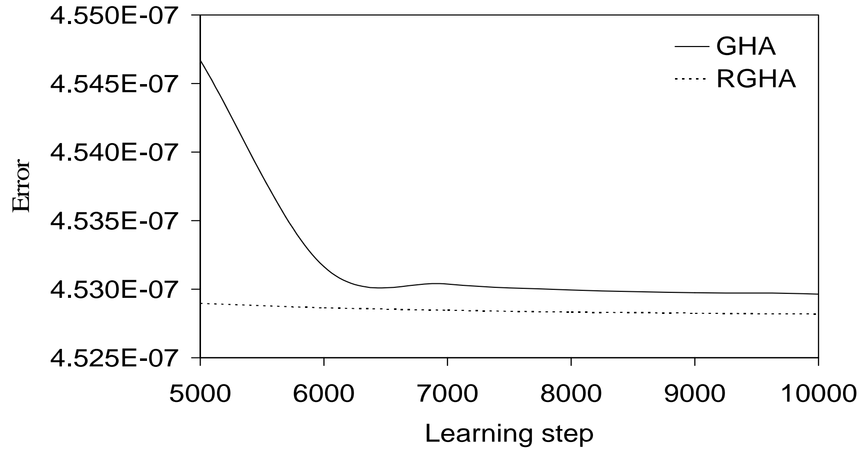


Figure 4.19 Comparison of errors using GHA and RGHA during learning steps between 5 000–10 000.

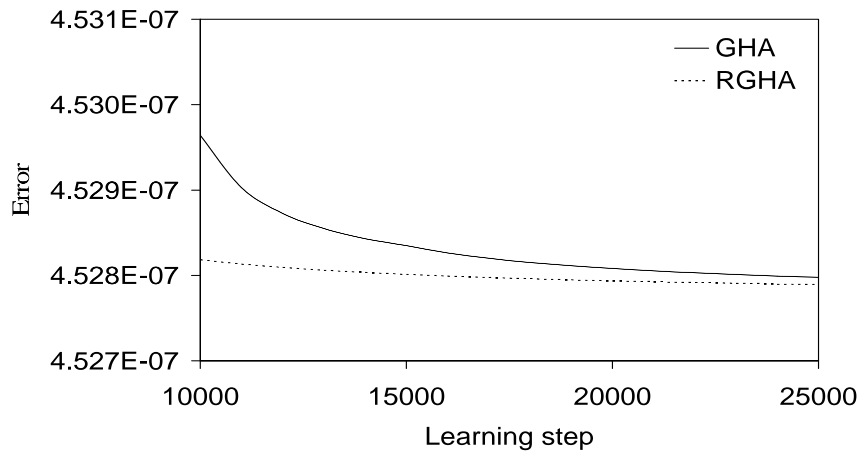


Figure 4.20 Comparison of errors using GHA and RGHA during learning steps between 10 000–25 000.

In order to demonstrate the flexibility and efficiency of the macromodel based on RGHA in the representation and simulation of the original nonlinear PDEs, a number of simulations by macromodel generated by RGHA to the noise-injected data are performed. One deflection eigenvector and four back pressure eigenvectors are selected in the macromodel. Figure 4.21 shows a comparison of the deflection of the midpoint of the microbeam between the FDM solution of the original nonlinear PDEs and the macromodel approximation when a step voltage of 10.25 V is applied to the

system with noise level ranging from 0 to 0.3%. Numerical data of deflection simulated by FDM is considered as noise-free signal snapshots, RGHA is used to extract the principal eigenvectors from the noise-injected snapshots. Figure 4.22 shows that the mean square error of the macromodel simulation is small compared with the FDM solution when noise level is assumed to be at 0.3%, here the mean square error between the results using the macromodel and that using the FDM is defined as

$$\mathrm{MSE} = \frac{1}{m}\sum_{i=1}^{m}\left[w_{\mathrm{MM}}(x_c, t_i) - w_{\mathrm{FDM}}(x_c, t_i)\right]^2 \tag{4.40}$$

where $x_c$ denotes the midpoint of the microbeam, $t_i$ is the sampled time instant, $w_{\mathrm{MM}}$ is the simulation result from macromodel, $w_{\mathrm{FDM}}$ is the FDM solution of the original nonlinear PDEs (3.44) and (3.45), and $m$ is the number of the sampled time series.

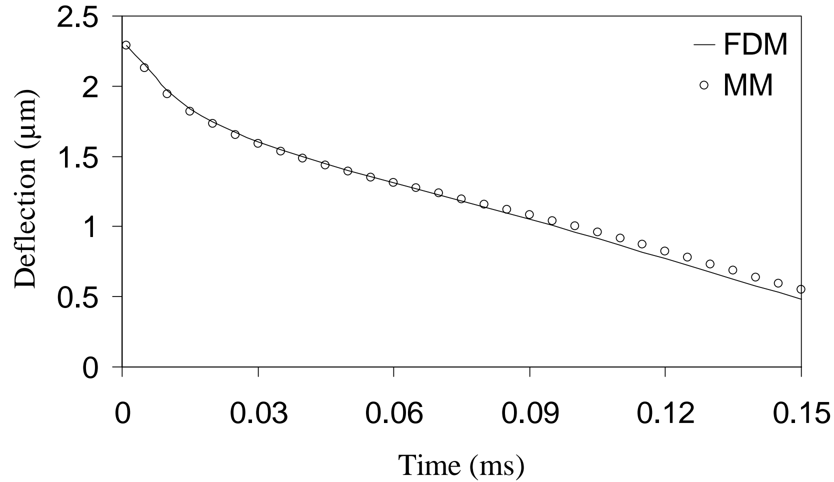


Figure 4.21 Comparison of the microbeam pull-in dynamics for an input step voltage of 10.25 V.

Figure 4.23 plots the simulation by the same macromodel for an input sinusoidal voltage with magnitude of 14 V at frequency of 10 kHz compared with FDM solution and Figure 4.24 shows the mean square error of macromodel simulation result with respect to the FDM solution. It is shown in the figures that good simulation accuracy

can still be given by the same macromodel. From both Figure 4.22 and Figure 4.24, it is noted that the MSE increases noticeably after the noise level exceeds 0.1%, however, good results can still be obtained when the noise level is up to 0.3%.

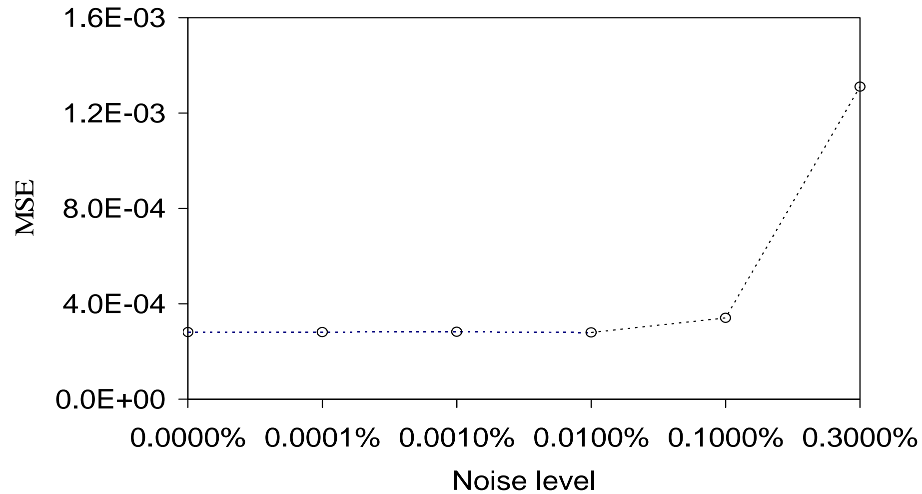


Figure 4.22 The mean square error of macromodel simulation with respect to FDM solution for an input step voltage of 10.25 V.

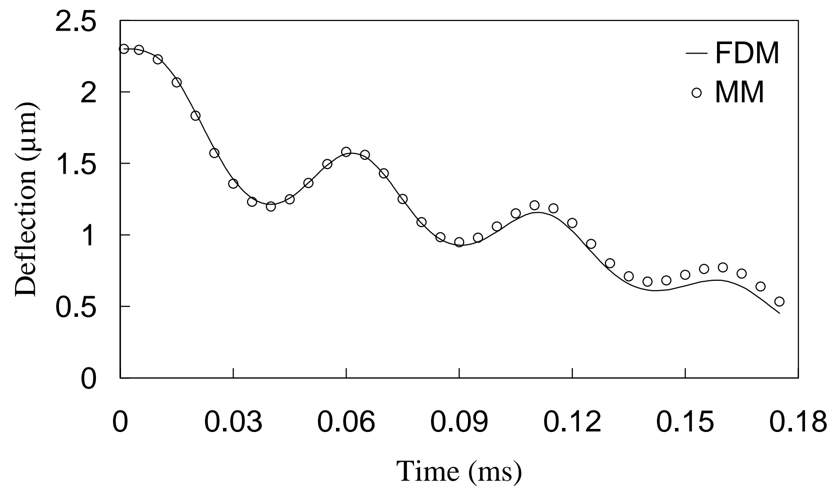


Figure 4.23 Comparison of the microbeam pull-in dynamics for an input sinusoidal voltage of 14 V at a frequency of 10 kHz.

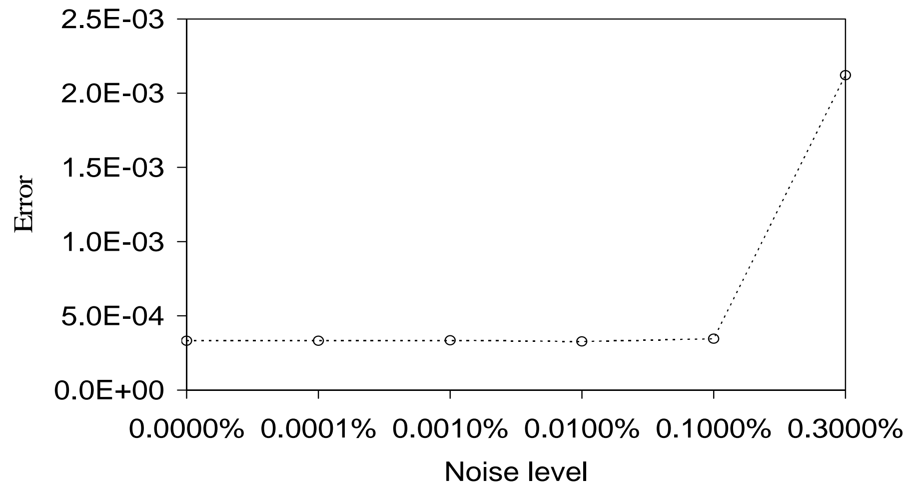


Figure 4.24 The mean square error of macromodel simulation with respect to FDM solution for an input sinusoidal voltage of 14 V at a frequency of 10 kHz.

### 4.4.3 CONCLUSION

The applications of a robust PCA neural network model, RGHA, as a technique for model order reduction is developed. The macromodel generated by using the principal eigenvectors extracted from the RGHA neural network, when noise is presented in the input signals, as basis functions in the Galerkin procedure has shown its flexibility and efficiency in the representation and simulation of the original nonlinear PDEs. Comparative numerical experiments show that the proposed RGHA neural network model using the sigmoid function has a number of numerical advantages compared with the GHA model in the model stability and robustness when dealing with noise-injected data and the fast convergence of iterations in the network training stages. The simulation results show that the model reduction technique based on RGHA provides another feasible tool for system designers to design and optimize MEMS accurately and effectively.

# CHAPTER 5

# RELATIONSHIP BETWEEN KARHUNEN-LOÈVE DECOMPOSITION, PRINCIPAL COMPONENT ANALYSIS AND SIGULAR VALUE DECOPOSITION

The applications of Karhunen-Loève decomposition (KLD), principal component analysis (PCA), and singular value decomposition (SVD) in science and engineering fields for the purpose of system features extraction and model order reduction are getting popular. In general, these three mathematical techniques can be categorized as the method of the proper orthogonal decomposition (POD). There is, however, no clear description of the relationship among these three techniques in the literature to date other than vaguely regarding the POD either as a method that is equivalent to KLD, or a method that includes KLD, PCA and SVD. The former interpretation appears in many engineering literatures while the later is more general and accepted as the interpretation of the POD in this thesis. This chapter is to give a summary of the POD method and to show the relationship among KLD, PCA and SVD techniques for discrete random vectors. Firstly, the derivation and performance of KLD, PCA and SVD are summarized, the equivalence among them is discussed through the theoretical comparison among these three techniques. Secondly, the equivalence in matrices for processing, the objective functions for finding the optimal basis vectors and the expression of mean square errors is described. Finally the asymptotic connections of these three techniques are derived.

## 5.1 THREE PROPER ORTHOGONAL DECOMPOSITION METHODS

The POD is developed by several researchers. Holmes et al. (1996) traces the idea of the POD back to the independent investigations by Kosambi (1943), Loève (1955), Karhunen (1946), Pougachev (1953) and Obukhov (1954). From the physical applications point of view, only the discrete version of the POD is investigated in this chapter.

The main idea of the POD is to find a set of ordered orthonormal basis vectors in a subspace (without loss of generality, denoting the subspace as $R^m$) where a random vector takes its values, so that the samples in the sample space can be expressed optimally using the selected $l$ basis vectors. Selection is normally based on the relative importance of the basis vectors. The mean square error can be used as a measure for the optimal problem, i.e.

$$E\left[\|x - x(l)\|^2\right] \le E\left[\|x - \tilde{x}(l)\|^2\right] \tag{5.1}$$

where $E[\bullet]$ is the statistical expectation operator, $x(l)$ is the approximate expression of a random vector $x$ using the $l$ basis vectors of the undetermined set of orthonormal basis vectors, and $\tilde{x}(l)$ is the approximate expression of $x$ using arbitrary $l$ basis vectors in $R^m$.

Assuming that $x \in R^m$ is a random vector and $\{\phi_i\}_{i=1}^m$ is a set of arbitrary orthonormal basis vectors, $x$ can then be expressed in terms of $\phi_i$ as

$$x = \sum_{i=1}^{m} y_i \phi_i = \Phi\, y \tag{5.2}$$

where

$$y_i = \phi_i^T x, \quad (i = 1, 2, \ldots, m) \tag{5.3}$$

$$y = (y_1, y_2, \ldots, y_m)^T \tag{5.4}$$

$$\Phi = (\phi_1, \phi_2, \ldots, \phi_m) \tag{5.5}$$

The objective of the POD is to find a set of basis vectors that satisfies the following extreme value problem

$$\min_{\phi_i} \varepsilon^2(l) = E\left[\|x - x(l)\|^2\right]$$

$$\text{subject to } \phi_i^T \phi_j = \delta_{ij}, \quad i, j = 1,2,\ldots,m \tag{5.6}$$

where $x(l) = \sum_{i=1}^{l} y_i \phi_i$, $(l \leq m)$. In order to obtain the same form of expressions for the mean square errors using the three different POD methods, the centralization on the sample data is preformed, i.e., the expectation of the random vector $x$ is zero.

The three POD methods are introduced in the following three sections, respectively.

## 5.2 PRINCIPAL COMPONENT ANALYSIS

The brief description of PCA has been given in the Section 4.1. There exist different versions on the description of PCA in the literatures (Jolliffe 1986; Dunteman, 1989; Diamantaras and Kung, 1996). In order to have the same approaches to describe the three POD methods in this chapter, the theory of PCA is re-visited here and given as follows.

Supposing that $x \in R^m$ is a random vector, and $y_1, y_2, \ldots, y_m \in R$ are the 1st, 2nd,…, $m-$th principal components accordingly, according to the principle of PCA, the first principal component $y_1$ is defined as a linear combination of each element of the original random vectors

$$y_1 = \sum_{i=1}^{m} \alpha_{i1} x_i = \alpha_1^T x \tag{5.7}$$

where $\alpha_1 = (\alpha_{11}, \alpha_{21}, \ldots, \alpha_{m1})^T$ is a constant vector. The variance of $y_1$ is given as

$$\begin{aligned}\sigma_{y_1}^2 &= \mathrm{Var}(y_1) = E\left[(y_1 - E[y_1])^2\right] = E\left[\left(\alpha_1^T x - E\left[\alpha_1^T x\right]\right)\left(\alpha_1^T x - E\left[\alpha_1^T x\right]\right)^T\right] \\ &= \alpha_1^T E\left[(x - E[x])(x - E[x])^T\right]\alpha_1\end{aligned} \tag{5.8}$$

A $m \times m$ covariance, or correlation matrix $R_x$ corresponding to the random vector $x$ is defined as

$$R_x = E\left[(x - E[x])(x - E[x])^T\right] \tag{5.9}$$

where $E[x]$ is the expectation of $x$. From the knowledge of linear algebra, $R_x \in R^{m \times m}$ is a semi-definite matrix (Murdoch, 1970). Let

$$\alpha_1^0 = \alpha_1 / \|\alpha_1\| \tag{5.10}$$

Thus

$$\sigma_{y_1}^2 = \|\alpha_1\|^2 \alpha_1^{0T} R_x \alpha_1^0 \tag{5.11}$$

It is apparent that the maximum of $\sigma_{y_1}^2$ will not be achieved for a finite $\alpha_1$, so a normalization constraint needs to be imposed and the most convenient constraint is $\alpha_1^T \alpha_1 = 1$. Hence, the problem of finding the first principal component is transformed to a conditional extreme value problem

$$\begin{aligned}&\max_{\alpha_1} \quad \sigma_{y_1}^2 = \alpha_1^T R_x \alpha_1 \\ &\text{subject to} \quad \alpha_1^T \alpha_1 = 1\end{aligned} \tag{5.12}$$

Introducing the Lagrangian multiplier $\lambda_1$, the corresponding functional for this constrained extreme problem becomes

$$L(\alpha_1, \lambda_1) = \alpha_1^T R_x \alpha_1 + \lambda_1 \left(\alpha_1^T \alpha_1 - 1\right) \tag{5.13}$$

Differentiating the above functional with respect to $\alpha_1$ yields

$$\frac{\partial L(\alpha_1, \lambda_1)}{\partial \alpha_1} = 2(R_x - \lambda_1 I)\alpha_1 \tag{5.14}$$

The necessary condition for extreme is to let the right hand side of the above equation equal to zero. Thus the following is obtained

$$R_x \alpha_1 = \lambda_1 \alpha_1 \tag{5.15}$$

It is noted that Equation (5.15) is a matrix eigenvalue problem. Thus the solutions of $\lambda_1$ and $\alpha_1$ of the extreme value problem are the eigenvalue and the corresponding eigenvector of the covariance matrix $R_x$, respectively. Since $\sigma_{y_1}^2 = \alpha_1^T R_x \alpha_1 = \lambda_1$, $\lambda_1$ must be as large as possible to maximize $\sigma_{y_1}^2$, it is selected as the largest eigenvalue of $R_x$.

Similarly, the second principal component is expressed by the following linear combination

$$y_2 = \sum_{i=1}^{m} \alpha_{i2} x_i = \alpha_2^T x \tag{5.16}$$

where $\alpha_2 = (\alpha_{12}, \alpha_{22}, \ldots, \alpha_{m2})^T$. The variance of $y_2$ is given as

$$\begin{aligned} \sigma_{y_2}^2 &= \mathrm{Var}(y_2) = E\left[ (y_2 - E[y_2])^2 \right] = E\left[ \left(\alpha_2^T x - E[\alpha_2^T x]\right)\left(\alpha_2^T x - E[\alpha_2^T x]\right)^T \right] \\ &= \alpha_2^T E\left[ (x - E[x])(x - E[x])^T \right] \alpha_2 \end{aligned} \tag{5.17}$$

Again a normalization constraint $\alpha_2^T \alpha_2 = 1$ is necessary for a unique $\alpha_2$ which enables the maximum $\sigma_{y_2}^2$ to be attained.

The second principal component $y_2$ must be uncorrelated with the first principal component $y_1$, thus

$$\mathrm{Cov}(y_1, y_2) = E\left[\left(\alpha_1^T x - E[\alpha_1^T x]\right)\left(\alpha_2^T x - E[\alpha_2^T x]\right)^T\right] = \alpha_1^T R_x \alpha_2 = 0 \tag{5.18}$$

Using the above equation and the symmetry of $R_x$ gives

$$\alpha_2^T R_x \alpha_1 = 0 \tag{5.19}$$

Since $\alpha_1$ is an eigenvector of $R_x$

$$\lambda_1 \alpha_2^T \alpha_1 = 0 \tag{5.20}$$

If $\lambda_1 = 0$, because of the fact that $\lambda_1 \geq \lambda_2 \geq \ldots \geq \lambda_m \geq 0$, therefore $\lambda_1 = \lambda_2 = \ldots = \lambda_m = 0$, i.e., all the eigenvalues are the same. As $R_x$ is a real symmetry matrix, there exists an orthogonal matrix $P \in R^{m \times m}$ (Murdoch, 1970) such that

$$P^T R_x P = \begin{pmatrix} \lambda_1 & 0 & 0 & \cdots & 0 \\ 0 & \lambda_2 & 0 & \cdots & 0 \\ 0 & 0 & \lambda_3 & \cdots & 0 \\ \vdots & \vdots & \vdots & \ddots & 0 \\ 0 & 0 & 0 & \cdots & \lambda_m \end{pmatrix} = 0_{m \times m} \tag{5.21}$$

Premultiplying the above equation by $P$ and postmultiplying the result by $P^T$ gives

$$R_x = 0_{m \times m} \tag{5.22}$$

Thus

$$\mathrm{Cov}(x_i, x_j) = 0, \quad (i, j = 1, 2, \ldots, m) \tag{5.23}$$

and

$$\mathrm{Cov}(x_i, x_i) = \mathrm{Var}(x_i) = E\left[(x_i - E[x_i])^2\right] = 0 \tag{5.24}$$

The above equation means that the value of each random variable $x_i$, $(i = 1, 2, \ldots, m)$ is centralized at its expectation, so it can be considered as a constant but not a random variable. The values of $x_i$, $(i = 1, 2, \ldots, m)$ can be replaced completely by their expectations.

If $\lambda_1 > 0$, then $\alpha_2^T \alpha_1 = 0$, i.e., $\alpha_2$ is orthogonal to $\alpha_1$. Thus, the problem of finding the second component can be transformed into the following constrained extreme value problem

$$\max_{\alpha_2} \ \sigma_{y_2}^2 = \alpha_2^T R_x \alpha_2 \qquad \text{subject to} \quad \alpha_2^T \alpha_2 = 1 \quad \text{and} \quad \alpha_1^T \alpha_2 = 0 \tag{5.25}$$

To solve the above problem, Lagrangian multipliers $\lambda_2$ and $u$ are introduced and the Lagrangian functional is written as

$$L(\alpha_2, \lambda_2, u) = \alpha_2^T R_x \alpha_2 + \lambda_2 \left(\alpha_2^T \alpha_2 - 1\right) + u \alpha_2^T \alpha_1 \tag{5.26}$$

Differentiating the functional with respect to $\alpha_2$ gives

$$\frac{\partial}{\partial \alpha_2} L(\alpha_2, \lambda_2, u) = 2(R_x - \lambda_2 I)\alpha_2 + u\alpha_1 \tag{5.27}$$

The necessary condition for the extrema is to let the right side of the above equation be equal to zero

$$2(R_x - \lambda_2 I)\alpha_2 + u\alpha_1 = 0 \tag{5.28}$$

Premultiplying both sides of Equation (5.28) by $\alpha_1^T$ gives

$$2\alpha_1^T (R_x - \lambda_2 I)\alpha_2 + u = 0 \tag{5.29}$$

or

$$2\alpha_1^T R_x \alpha_2 + u = 0 \tag{5.30}$$

The symmetry of $R_x$ and the fact that $\alpha_1$ is an eigenvector of $R_x$ ensure

$$2\lambda_1 \alpha_1^T \alpha_2 + u = 0 \tag{5.31}$$

hence $u = 0$ and Equation (5.29) reduces to the following eigenvalue problem

$$R_x \alpha_2 = \lambda_2 \alpha_2 \tag{5.32}$$

where $\alpha_2$ is the eigenvector of $R_x$. Due to the same reason that the variance of $y_2$ is expressed as $\sigma_{y_2}^2 = \mathrm{Var}(y_2) = \alpha_2^T R_x \alpha_2 = \lambda_2$, in order to obtain the maximum variation of $y_2$, $\alpha_2$ can only be taken as the eigenvector corresponding to the second largest eigenvalue of $R_x$.

The remaining principal components can be found in a similar manner. In general, the $i-$th principal component of $x$ is $y_i = \alpha_i^T x$ and the variance of $y_i$ is $\sigma_{y_i}^2 = \mathrm{Var}(y_i) = \lambda_i$, where $\lambda_i$ is the $i-$th largest eigenvalue of $R_x$, and $\alpha_i$ is its corresponding eigenvector. As stated above, it can be shown that for the third, fourth,…, and $l-$th principal components, the vectors of coefficients $\alpha_3, \alpha_4, \ldots, \alpha_l$ are the eigenvectors of $R_x$ corresponding to $\lambda_3, \lambda_4, \ldots, \lambda_l$ which are the third, fourth,…, and $l-$th largest eigenvalues, respectively.

In summary, the objective function for finding the optimal basis vectors in PCA is equivalent to

$$\max_{\alpha_i} \sum_{i=1}^{l} \sigma_{y_i}^2 = \sum_{i=1}^{l} \alpha_i^T R_x \alpha_i \tag{5.33}$$

$$\text{subject to} \quad \alpha_i^T \alpha_j = \delta_{ij}$$

If the original random vector is approximated in terms of the first $l$ principal components, the mean square error is

$$\varepsilon^2(l) = E\left[\|x - x(l)\|^2\right] = E\left[\left\|\sum_{i=l+1}^{m} y_i \alpha_i\right\|^2\right] = \sum_{i=l+1}^{m} E\left[y_i^2\right] \tag{5.34}$$

where

$$x = \sum_{i=1}^{m} y_i \alpha_i, \quad x(l) = \sum_{i=1}^{l} y_i \alpha_i \tag{5.35}$$

Noting that

$$E[y_i] = E[\alpha_i^T x] = \alpha_i^T E[x] = 0 \tag{5.36}$$

thus

$$E[y_i^2] = E[(y_i - E[y_i])^2] = \sigma_{y_i}^2 \tag{5.37}$$

and the mean square error is

$$\varepsilon^2(l) = \sum_{i=l+1}^{m} \sigma_{y_i}^2 = \sum_{i=l+1}^{m} \lambda_i \tag{5.38}$$

In fact, the original random variables can be expressed exactly by all principal components. Supposing that all the principal components $y_i$ $(i = 1,2,\ldots,m)$ are found and given as

$$y_i = \alpha_i^T x, \quad (i = 1, 2, \ldots, m) \tag{5.39}$$

Premultiplying both sides of the above equation by $\alpha_i$ gives

$$y_i \alpha_i = \alpha_i \alpha_i^T x, \quad (i = 1, 2, \ldots, m) \tag{5.40}$$

Summation of the equation on both sides from 1 to $m$ yields

$$\left( \sum_{i=1}^{m} \alpha_i \alpha_i^T \right) x = \sum_{i=1}^{m} y_i \alpha_i \tag{5.41}$$

where $\alpha_i \alpha_i^T$ is a $m \times m$ matrix. Let

$$B^{(k)} = \alpha_k \alpha_k^T, \quad (k = 1, 2, \ldots, m) \tag{5.42}$$

where the element of $B^{(k)}$ is given by

$$b_{ij}^{(k)} = \alpha_{ik} \alpha_{jk} \tag{5.43}$$

Let $B = \sum_{k=1}^{m} B^{(k)}$, then the element of $B$ is

$$b_{ij} = \sum_{k=1}^{m} \alpha_{ik} \alpha_{jk} = \delta_{ij} \tag{5.44}$$

hence

$$B = I \tag{5.45}$$

In fact, from

$$I = (\alpha_1, \alpha_2, \ldots, \alpha_m)(\alpha_1, \alpha_2, \ldots, \alpha_m)^T = \sum_{k=1}^{m} \alpha_k \alpha_k^T \tag{5.46}$$

it can be shown that

$$b_{ij} = \sum_{k=1}^{m} \alpha_{ik} \alpha_{jk} = \delta_{ij} . \tag{5.47}$$

Thus

$$x = \sum_{i=1}^{m} y_i \alpha_i \tag{5.48}$$

where $\alpha_i$, $(i = 1, 2, \cdots, m)$ are the eigenvectors of $R_x$ corresponding to the eigenvalues of $R_x$ with descending order.

The proper orthogonal decomposition of the sampled vector is completed using PCA technique at this stage. The orthonormal basis vectors and the mean square error of the approximate expression for the original random data have been established.

## 5.3 DISCRETE KARHUNEN-LOÈVE DECOMPOSITION

The procedure of KLD as optimal series expansion for representation of continuous time stochastic process has been briefly introduced in Section 3.1. It can be considered as the extension of PCA to the problem of the infinite-dimensional spaces, such as the space of continuous time functions. KLD for discrete time process is described in this section for the purpose of establishing its equivalence to PCA. In terms of optimality, KLD is found to have the same optimal properties of least square reconstruction and variance maximization as PCA. In the following paragraphs, the discrete KLD is stated in detail according to Fukunaga (1990).

Assuming that $x \in R^m$ is a random vector, and $\{\phi_i\}_{i=1}^m$ is a set of orthonormal basis vectors in $R^m$, there exists

$$y_i = \phi_i^T x \tag{5.49}$$

so that $x$ can be represented without error by linear combination of $m$ independent vectors

$$x = \sum_{i=1}^{m} y_i \phi_i = \Phi y \tag{5.50}$$

Let

$$x(l) = \sum_{i=1}^{l} y_i \phi_i + \sum_{i=l+1}^{m} b_i \phi_i, \quad (l \le m) \tag{5.51}$$

where $b_i$, $(i = l+1, l+2, \ldots, m)$ are constants. Without losing the generality, assuming that only the first $l$ terms are calculated, the truncation error is found to be

$$\Delta x(l) = x - x(l) = \sum_{i=l+1}^{m} (y_i - b_i)\phi_i \tag{5.52}$$

where $x$ and $x(l)$ are random vectors, thus $\Delta x(l)$ is also a random vector. The mean square error is chosen as a measure to indicate the quality of the expression of $x$

$$\varepsilon^2(l) = E\left[\|\Delta x(l)\|^2\right] = E\left[\left\|\sum_{i=l+1}^{m} (y_i - b_i)\phi_i\right\|^2\right] = E\left[\sum_{i=l+1}^{m} (y_i - b_i)^2\right] \tag{5.53}$$

and the derivative of $\varepsilon^2(l)$ with respect to $b_i, (i = l+1, l+2, \ldots, m)$ is

$$\frac{\partial}{\partial b_i} \varepsilon^2(l) = -2E[y_i - b_i] \tag{5.54}$$

The necessary condition for optimum choice of $b_i$ is obtained by setting the right-hand side of the above equation to zero. Then

$$b_i = E[y_i] = \phi_i^T E[x], \; (i = l+1, l+2, \ldots, m) \tag{5.55}$$

It is noted that $b_i = 0$ if the mean value is subtracted from $x$.

Substituting Equation (5.55) into Equation (5.53) yields

$$\varepsilon^2(l) = \sum_{i=l+1}^{m} E[y_i - E[y_i]]^2 = \sum_{i=1+1}^{m} \phi_i^T E[(x - E[x])(x - E[x])^T]\phi_i$$
$$= \sum_{i=l+1}^{m} \phi_i^T R_x \phi_i = tr(\Phi^T{}_{m-l} R_x \Phi_{m-l}) \tag{5.56}$$

where $R_x$ is the covariance matrix of $x$ and $\Phi_{m-l}$ is defined as

$$\Phi_{m-l} = (\phi_{l+1}, \phi_{l+2}, \ldots, \phi_m) \in R^{m\times(m-l)} \tag{5.57}$$

Hence, KLD problem is transformed into a constrained extreme value problem

$$\min_{\phi_i} \ \varepsilon^2(l) = \sum_{i=l+1}^{m} \phi_i^T R_x \phi$$
$$\text{subject to} \quad \phi_i^T \phi_j = \delta_{ij}, \qquad (i, j = l+1, l+2, \ldots, m) \tag{5.58}$$

Introducing the Lagrangian multipliers $u_{ij}, (i = l+1, l+2, \ldots, m)$ gives

$$L = \sum_{i=l+1}^{m} \phi_i^T R_x \phi_i - \sum_{i=l+1}^{m} \sum_{j=l+1}^{m} u_{ij} (\phi_i^T \phi_j - \delta_{ij}) \tag{5.59}$$

Differentiating both sides of the above equation with respect to $\phi_i$ yields

$$\frac{\partial L}{\partial \phi_i} = 2(R_x \phi_i - \Phi_{m-l} u_i) \tag{5.60}$$

where $u_i = (u_{l+1i}, u_{l+2i}, \cdots, u_{mi})^T, (i = l+1, l+2, \ldots, m)$. Rewriting the above equation in a matrix form gives

$$\frac{\partial L}{\partial \Phi_{m-l}} = 2(R_x \Phi_{m-l} - \Phi_{m-l} U_{m-l}) \tag{5.61}$$

where $U_{m-l} = (u_{l+1}, u_{l+2}, \ldots, u_m)$. The necessary condition for an extremum of (5.59) is then obtained by setting the right hand side of the above equation to be zero

$$R_x \Phi_{m-l} = \Phi_{m-l} U_{m-l} \tag{5.62}$$

Multiplying both sides of the above equation by $\Phi_{m-l}^T$ gives

$$U_{m-l} = \Phi_{m-l}^T R_x \Phi_{m-l} \tag{5.63}$$

Since $y_i = \phi_i^T x$, $U_{m-l}$ in Equation (5.63) is the covariance matrix of the vector formed by the last $m-l$ elements of the random vector $y$ after the transformation $y = \Phi^T x$. Thus $U_{m-l}$ is a semi-definite matrix with dimension of $(m-l)\times(m-l)$. Denoting the diagonal matrix formed by the eigenvalues of $U_{m-l}$ as $\Lambda_{m-l}$, and the square matrix formed by the corresponding eigenvectors be $\Psi_{m-l}$ and performing the transformation $z = \Psi_{m-l}^T y$, the following is obtained

$$\Lambda_{m-l} = \Psi_{m-l}^T U_{m-l} \Psi_{m-l} \tag{5.64}$$

Substituting Equation (5.63) into Equation (5.64) yields

$$\Lambda_{m-l} = \left(\Phi_{m-l}\Psi_{m-l}\right)^T R_x \left(\Phi_{m-l}\Psi_{m-l}\right) \tag{5.65}$$

It can be seen that the diagonal elements of $\Lambda_{m-l}$ are the $m-l$ eigenvalues of $R_x$, and the eigenvectors corresponding to the eigenvalues form $\left(\Phi_{m-l}\Psi_{m-l}\right)_{m\times(m-l)}$. Denote the eigenvector matrix as $\Phi_{m-l}^*$ gives

$$\Phi_{m-l} = \left(\Phi_{m-l}^* \Psi_{m-l}^T\right)_{m\times(m-l)} \tag{5.66}$$

and the mean square error is obtained as

$$\begin{aligned} \varepsilon^2(l) &= tr\left(\Phi_{m-l}^T R_x \Phi_{m-l}\right) = tr\left(\Psi_{m-l}\Phi_{m-l}^{*T} R_x \Phi_{m-l}^* \Psi_{m-l}^T\right) = tr\left(\Phi_{m-l}^{*T} R_x \Phi_{m-l}^* \Psi_{m-l}^T \Psi_{m-l}\right) \\ &= tr\left(\Phi_{m-l}^{*T} R_x \Phi_{m-l}^*\right) = \sum_{s=1}^{m-l} \lambda_{k_s} \end{aligned} \tag{5.67}$$

where $\lambda_{k_s}, (s = 1, 2, \ldots, m-l)$ are the eigenvalues corresponding to the columns of $\Phi_{m-l}^*$. Once $x$ is mapped onto the $(m-l)-$dimensional subspace spanned by $m-l$ eigenvectors of $R_x$, further application of an orthonormal transformation will not change the mean square error. Therefore, $\Phi_{m-l}$ and $U_{m-l}$ in Equation (5.62) can be

chosen simply as the matrices formed by the eigenvectors and eigenvalues of $R_x$, respectively. In general, the eigenvectors $\phi_1, \phi_2, \ldots, \phi_m$ associated with eigenvalues $\lambda_1, \lambda_2, \ldots, \lambda_m$ of $R_x$ can be arranged in descending order. It can be seen that in order to enable the minimum value problem of (5.58) to hold, the orthonormal basis vectors can be selected as the eigenvectors of $R_x$, and the mean square error to measure the quality of the approximation of $x$ by using the first $l$ basis vectors is expressed as

$$\varepsilon^2(l) = \sum_{i=l+1}^{m} \lambda_i \tag{5.68}$$

## 5.4 SINGULAR VALUE DECOMOPSITION

Klema and Laub (1980) indicated that SVD was established for real square matrices in the 1870's by Beltrami and Jordan, for complex square matrices in 1902 by Autonne, and for general rectangular matrices in 1939 by Eckart and Young. SVD can be viewed as an extension of the eigenvalue decomposition for nonsquare matrices. As far as the proper orthogonal decomposition is concerned, SVD can also be seen as an extension for nonsymmetric matrices. Because SVD is much more general than the eigenvalue decomposition and intimately related to the matrix rank and reduced-rank least-squares approximation, it becomes a very important and fundamental tool in many areas such as matrix theory, linear systems, statistics and signal analysis (Lawson and Hanson, 1974; Forsythe et al., 1977; Marple, 1987; Biglieri and Yao, 1989).

The process for realizing the POD by using SVD is stated below. The basic concept is the same as those that appear in some literatures (Lawson and Hanson, 1974; Forsythe

et al., 1977; Klema and Laub, 1980; Marple, 1987) but described in the way to keep the description for the three POD methods consistent in this chapter.

Suppose that there are $n$ samples $x_1, x_2, \ldots, x_n$ where $x_i \in R^m$. Consider the samples are more than enough such that $n > m$ and define

$$X = (x_1, x_2, \ldots, x_n) \tag{5.69}$$

then $X \in R^{m\times n}$, and $XX^T \in R^{m\times m}$ is a $m \times m$ semi-definite matrix. Let the eigenvalues of $XX^T$ be arranged in decreasing order

$$\lambda_1 \ge \lambda_2 \ge \ldots \ge \lambda_r > \lambda_{r+1} = \ldots = \lambda_m = 0 \tag{5.70}$$

In SVD, $\sigma_i = \sqrt{\lambda_i}, (i = 1, 2, \ldots, m)$ are called the singular values of matrix $X^T$. Let the eigenvectors of $XX^T$ associated with eigenvalues $\lambda_1, \lambda_2, \ldots, \lambda_m$ be $v_1, v_2, \ldots, v_m$.

Define $V = [V_1, V_2]$ where $V_1 = (v_1, v_2 \ldots, v_r)$, $V_2 = (v_{r+1}, v_{r+2} \ldots, v_m)$, and denote the subscript $r$ as the index of the smallest positive eigenvalue of $XX^T$, then the matrix $V$ is a $m \times m$ orthonormal matrix and the following is given

$$XX^T V = V\begin{pmatrix} \lambda_1 & & & \\ & \lambda_2 & & \\ & & \ddots & \\ & & & \lambda_m \end{pmatrix} = V\begin{pmatrix} \sigma_1^2 & & & \\ & \sigma_2^2 & & \\ & & \ddots & \\ & & & \sigma_m^2 \end{pmatrix} \tag{5.71}$$

Premultiplying the both sides of the above equation by $V^T$ yields

$$[V_1, V_2]^T XX^T [V_1, V_2] = \begin{pmatrix} R_r^2 & 0 \\ 0 & 0 \end{pmatrix} \tag{5.72}$$

where

$$R_r^2 = \mathrm{diag}(\sigma_1^2, \sigma_2^2, \ldots, \sigma_r^2) \tag{5.73}$$

Let

$$U_1 = X^T V_1 R_r^{-1} \tag{5.74}$$

where

$$R_r^{-1} = \text{diag}\left(\sigma_1^{-1}, \sigma_2^{-1}, \ldots, \sigma_r^{-1}\right) \tag{5.75}$$

the following is obtained

$$U_1^T U_1 = \left(X^T V_1 R_r^{-1}\right)^T X^T V_1 R_r^{-1} = R_r^{-1} R_r^2 R_r^{-1} = I_r \tag{5.76}$$

From the above equation, it can be seen that the columns of the matrix $U_1$ are mutually orthogonal. Denote

$$U_1 = \left(u_1, u_2, \ldots, u_r\right) \tag{5.77}$$

according to the basis extension theorem in vector space, there exist $n-r$ orthonormal vectors in $R^n$ and they are orthogonal to the columns of $U_1$. Let the $n-r$ orthonormal vectors be $u_{r+1}, u_{r+2}, \ldots, u_n$. In the singular value decomposition, $u_1, u_2, \ldots, u_m$ and $v_1, v_2, \ldots, v_m$ are called left and right singular vectors of $X^T$ corresponding to eigenvalues $\sigma_1, \sigma_2, \cdots, \sigma_m$, respectively. Let $U = \left[U_1, U_2\right]$ where $U_2 = \left(u_{r+1}, u_{r+2}, \ldots, u_n\right)$, then $U$ is a $n \times n$ orthonormal matrix and the following equation is derived

$$U^T X^T V = \left[U_1, U_2\right]^T X^T \left[V_1, V_2\right] = \begin{pmatrix} U_1^T X^T V_1 & U_1^T X^T V_2 \\ U_2^T X^T V_1 & U_2^T X^T V_2 \end{pmatrix} \tag{5.78}$$

where

$$\begin{aligned} U_1^T X^T V_1 &= R_r^{-1} V_1^T X X^T V_1 = R_r \\ U_1^T X^T V_2 &= R_r^{-1} V_1^T X X^T V_2 = 0 \\ U_2^T X^T V_1 &= U_2^T (X^T V_1 R_r^{-1}) R_r = U_2^T U_1 R_r = 0 \end{aligned} \tag{5.79}$$

Note that

$$X X^T V_2 = 0 \tag{5.80}$$

Premultiplying both sides of the above equation by $V_2^T$ gives

$$V_2^T X X^T V_2 = \left(X^T V_2\right)^T X^T V_2 = 0 \tag{5.81}$$

From the above equation, it is obvious that

$$tr\left(\left(X^T V_2\right)^T \left(X^T V_2\right)\right) = 0 \,. \tag{5.82}$$

Thus

$$X^T V_2 = 0 \tag{5.83}$$

and the following is obtained

$$U_2^T X^T V_2 = 0 \,. \tag{5.84}$$

Hence Equation (5.78) can then be rewritten as

$$U^T X^T V = \left[U_1, U_2\right]^T X^T \left[V_1, V_2\right] = \begin{pmatrix} U_1^T X^T V_1 & U_1^T X^T V_2 \\ U_2^T X^T V_1 & U_2^T X^T V_2 \end{pmatrix} = \begin{pmatrix} R_r & 0 \\ 0 & 0 \end{pmatrix} \tag{5.85}$$

Premultiplying both sides of the above equation by $U$ and postmultiplying the result by $V^T$ give

$$X^T = U \begin{pmatrix} R_r & 0 \\ 0 & 0 \end{pmatrix} V^T \tag{5.86}$$

Transposing the above equation yields

$$\left[x_1, x_2, \ldots, x_n\right] = V \begin{pmatrix} R_r & 0 \\ 0 & 0 \end{pmatrix} U^T \tag{5.87}$$

Denote the columns of the matrix $\begin{pmatrix} R_r & 0 \\ 0 & 0 \end{pmatrix} U^T$ as $d_1, d_2, \ldots, d_n$. From Equation (5.87) it follows that

$$x_i = V d_i, \quad \left(i = 1, 2, \ldots, n\right) \tag{5.88}$$

Now the description of the proper orthogonal decomposition for the sampled vectors is completed. From Equations (5.87) and (5.88), it can be seen that the components $d_{r+1,i}, d_{r+2,i}, \ldots, d_{m,i}$ of $d_i$, $\left(i = 1, 2, \ldots, n\right)$ are equal to zero when the singular values

$\sigma_{r+1}, \sigma_{r+2}, \ldots, \sigma_m$ of $X^T$ are equal to zero. Then it needs only $r$ right singular vectors as basis to represent the samples $x_i, (i = 1, 2, \ldots, n)$ in space $R^m$.

Suppose a set of orthonormal basis vectors $\phi_1, \phi_2, \ldots, \phi_m$ is chosen arbitrarily in $R^m$ to represent $n$ samples, then

$$x_i = c_{1i}\phi_1 + c_{2i}\phi_2 + \ldots + c_{mi}\phi_m \tag{5.89}$$

where $c_{ji} = \phi_j^T x_i$. When the first $l$ basis vectors are selected to approximate the samples, it gives

$$x_i(l) = c_{1i}\phi_1 + c_{2i}\phi_2 + \cdots + c_{li}\phi_l \tag{5.90}$$

The criterion to measure the approximation is the error of the entire samples instead of the error of an individual sample. Hence, the following error function is considered as

$$\begin{aligned}\varepsilon^2(l) &= \sum_{i=1}^{n} \left\| x_i - x_i(l) \right\|^2 = \sum_{i=1}^{n} \left\| \sum_{j=l+1}^{m} c_{ji}\phi_j \right\|^2 = \sum_{i=1}^{n} \sum_{j=l+1}^{m} c_{ji}^2 = \sum_{i=1}^{n} \sum_{j=l+1}^{m} \phi_j^T x_i x_i^T \phi_j \\ &= \sum_{j=l+1}^{m} \phi_j^T X X^T \phi_j = \left\| X^T \Phi_{m-l} \right\|_F^2\end{aligned} \tag{5.91}$$

where $\Phi_{m-l} = (\phi_{l+1}, \phi_{l+2}, \ldots, \phi_m)$. Hence the problem of finding the optimal basis vectors is transformed to the following extreme value problem

$$\begin{aligned}&\min_{\phi_j} \quad \varepsilon^2(l) = \sum_{j=l+1}^{m} \phi_j^T X X^T \phi_j \\ &\text{subject to.} \quad \phi_i^T \phi_j = \delta_{ij}\end{aligned} \tag{5.92}$$

Introducing the Lagrangian multipliers $u_{ij}, (i, j = l+1, l+2, \ldots, m)$, the corresponding functional for this constrained extreme value problem can be written as

$$L(\phi_i, u_{ij}) = \sum_{j=l+1}^{m} \phi_j^T X X^T \phi_j - \sum_{i=l+1}^{m} \sum_{j=l+1}^{m} u_{ij} \left( \phi_i^T \phi_j - \delta_{ij} \right) \tag{5.93}$$

Differentiating the above with respect to $\phi_j$ yields

$$\frac{\partial L}{\partial \phi_j} = 2\left( XX^T\phi_j - u_{ij}\sum_{i=l+1}^{m}\phi_i \right) = 2XX^T\phi_j - 2\Phi_{m-l}u_j, \quad (j = l+1, l+2, \ldots, m) \tag{5.94}$$

where $u_j = \left(u_{l+1j}, u_{l+2j}, \ldots, u_{mj}\right)^T$. The above equation can be rewritten in a matrix form as

$$\frac{\partial L}{\partial \Phi_{m-l}} = 2XX^T\Phi_{m-l} - 2\Phi_{m-l}U_{m-l} \tag{5.95}$$

where $U_{m-l} = \left(u_{l+1}, u_{l+2}, \ldots, u_m\right)$.

The necessary condition for extreme is that the functional first derivative vanishes. Thus equating $\partial L/\partial \Phi_{m-l}$ to zero gives

$$XX^T\Phi_{m-l} = \Phi_{m-l}U_{m-l} \tag{5.96}$$

Premultiplying both sides of the equation by $\Phi_{m-l}^T$ yields

$$U_{m-l} = \Phi_{m-l}^T XX^T \Phi_{m-l} \tag{5.97}$$

Note that $U_{m-l}$ is a semi-definite matrix. Then there exist an orthogonal matrix $P$ such that

$$\Lambda = P^T U_{m-l} P = P^T \Phi_{m-l}^T XX^T \Phi_{m-l} P \tag{5.98}$$

where $\Lambda$ is a diagonal matrix. Postmultiplying both sides of Equation (5.96) by $P$ gives

$$XX^T\Phi_{m-l}P = \Phi_{m-l}PP^TU_{m-l}P \tag{5.99}$$

hence

$$XX^T\Phi_{m-l}P = \Phi_{m-l}P\Lambda \tag{5.100}$$

From the above equation, it can be seen that the diagonal elements of the matrix $\Lambda$ are the eigenvalues $\lambda_i$ of the matrix $XX^T$, and the matrix $\Phi_{m-l}P$ consists of the eigenvectors corresponding to $\lambda_i$. That is, the diagonal elements of the matrix $\Lambda$ are

the squares of the singular values $\sigma_i$ of the matrix $X^T$, and $\Phi_{m-l}P$ consists of the right singular vectors corresponding to $\sigma_i$ .

The following theorem (Golub and Loan, 1989) is given without proof as the preparation for the further description of the POD.

Theorem: Let $A \in R^{n\times m}$, $Q \in R^{m\times m}$ be an orthogonal matrix, and $\|\bullet\|_F$ be the Frobenius norm, then $\|A\|_F = \|AQ\|_F$.

Considering the Equation (5.91) and the above theorem, it indicates that

$$\varepsilon^2(l) = \left\|X^T\Phi_{m-l}\right\|_F^2 = \left\|X^T\Phi_{m-l}P\right\|_F^2 = tr\left(\left(X^T\Phi_{m-l}P\right)^T X^T\Phi_{m-l}P\right) = tr(\Lambda) \tag{5.101}$$

Note that $\Lambda$ is a diagonal matrix and its diagonal elements are the squares of the singular values $\sigma_i$ of the matrix $X^T$. In order to attain the minimum error, the diagonal elements of $\Lambda$ can only be the last $m-l$ singular values of the matrix $X^T$. Thus

$$\varepsilon^2(l) = tr\left(\left(X^T\Phi_{m-l}P\right)^T X^T\Phi_{m-l}P\right) = tr(\Lambda) = \sum_{j=l+1}^{m}\sigma_j^2 \tag{5.102}$$

Hence it is proved not only that the optimality is attained when the right singular vectors of $X^T$ are taken as basis vectors but also that the minimum error is simply the square summation of the last $m-l$ singular values of the matrix $X^T$.

## 5.5 THE EQUIVALENCE OF THREE PROPER ORTHOGONAL DECOMPOSITION METHODS

From the above discussion it can be seen that there exist close relations among the three POD methods: PCA, KLD, and SVD, although their derivations are different. The existing equivalence relations among them are understood by researchers. Some

of the equivalence relationships pointed out by the previous researchers are summarized as follows:

i) Mees et al. (1987) pointed out that the relationship between KLD and PCA was first noticed by Watanabe in 1965. Diamantaras and Kung (1996) and Ravindra (1999) indicated that the difference between KLD and PCA was that KLD was typically referred to stochastic processes, whereas PCA referred to random vectors. If the time parameter $t$ was a discrete variable and one had a finite collection of random variables, then KLD reduced to PCA.

ii) Diamantaras and Kung (1996) pointed out that there was an asymptotic connection between PCA and SVD.

iii) Kunisch and Volkwein (1999) described the relationship between KLD and SVD within the context of its relevance to the application to optimal control problems.

iv) Chatterjee (2000) indicated the correspondence with the expression of SVD and the finite sum of KLD.

It is important and useful for researchers to understand the equivalence relationships among these three methods in the studies and applications of the POD methods. There exists neither complete description nor systematic and theoretical proof on the equivalence of the three methods in the literature. In this section, the equivalence of the three methods is discussed from different point of view and the proofs on the equivalence of the three methods are derived. The aim of the work is to demonstrate the close connections among the three methods. It should be pointed out that in practice, the applications of the three methods may not be always the same. If the methods are actually applied the same way, they may lead to exactly the same basis functions. If the methods are applied slightly differently, yet in equivalent ways, then the equivalence is more hidden, or implicitly rather than explicitly (Cao and Levin,

1995).

The main results on the equivalence relationships of the three methods obtained through the POD derivations mentioned in the above section are summarized as follows

### 5.5.1 THE EQUIVALENCE OF PRINCIPAL COMPONENT ANALYSIS AND KARHUNEN-LOÈVE DECOMPOSITION

i) The same matrices for processing

Both PCA and discrete KLD handle the problems of random vectors. For a random vector $x$ with dimension $m$, the matrices used for finding basis vectors derived from the two methods are the same. The matrix is a $m \times m$ covariance matrix corresponding to the random vector and expressed as in Equation (5.9).

ii) The same objective functions for finding the optimal basis vectors

In PCA the objective for finding the optimal basis vectors is to maximize the variance summation of the first $l$ $(1 \leq l < m)$ principal components, i.e.

$$\max_{\alpha_i} \sum_{i=1}^{l} s_{y_i}^2 = \sum_{i=1}^{l} \alpha_i^T R_x \alpha_i \tag{5.103}$$

Obviously, the above equation is equivalent to minimizing the variance summation of the last $m-l$ principal components, i.e.

$$\min_{\alpha_i} \sum_{i=l+1}^{m} s_{y_i}^2 = \sum_{i=l+1}^{m} \alpha_i^T R_x \alpha_i \tag{5.104}$$

In KLD the objective for finding the optimal basis vectors is that is minimizing the error after truncating the last $m-l$ basis vectors, i.e.

$$\min_{\phi_i} \varepsilon^2(l) = \sum_{i=l+1}^{m} \phi_i^T R_x \phi_i \tag{5.105}$$

Comparing Equation (5.104) with (5.105), it can be seen that the objective functions for finding the optimal basis vectors by using the two methods have the same form.

iii) The same or equivalent optimal basis vectors

The basis vectors found using the two methods are the eigenvectors of a covariance matrix corresponding to the same random vector. In fact, the covariance matrix $R_x$ is a $m \times m$ linear transformation in a real field. Let the linear transformation be $\sigma$. Because $R_x$ is semi-definite, it has $m$ non-negative real eigenvalues. Denote the eigenvalues of $R_x$ as $\lambda_1, \lambda_2, \ldots, \lambda_m$ and let them be arranged in decreasing order.

If all $\lambda_i, (i = 1, 2, \ldots, m)$ are distinct, then each eigen-subspace of $\sigma$: $\sigma(\lambda_1)$, $\sigma(\lambda_2), \ldots, \sigma(\lambda_m)$ has only one basis vector, respectively, which is denoted as $v_1, v_2, \ldots, v_m$. The difference among the elements in each subspace $\sigma(\lambda_1)$, $\sigma(\lambda_2), \ldots, \sigma(\lambda_m)$ is only a constant factor, i.e., if $v_i^{(1)}$ and $v_i^{(2)}$ are the elements of the eigen-subspace $\sigma(\lambda_i)$ of $\sigma$, then there exists a real number $\alpha$ such that $v_i^{(1)} = \alpha v_i^{(2)}$. Because the basis vectors are required to be normal, the basis vectors belonging to the $\lambda_i$ obtained by using PCA and KLD are the same after normalization.

If some eigenvalues are multiple, without loss of generality, let $\lambda_1$ have multiplicity $n_1$. Then in the eigen-subspace $\sigma(\lambda_1)$, there exit $n_1$ orthonormal vectors that can be selected as basis vectors. The basis vector $\alpha_1$ associated with the $\lambda_1$ selected by using PCA may not be the same as the basis vector $\phi_1$ corresponding to the $\lambda_1$ selected by using KLD. But both of them are basis vectors of the eigen-subspace $\sigma(\lambda_1)$ of $\sigma$. If $n_1$ optimal basis vectors are selected by using PCA and KLD, respectively, to approximate the original random vector $x$, they may be two different basis vectors of the eigen-subspace $\sigma(\lambda_1)$. However, they are obviously equivalent. In fact, they can

be expressed mutually, i.e., there exist constants $\beta_{ij}$ such that $\alpha_i = \sum_{j=1}^{n_1} \beta_{ij}\phi_j$, $(i = 1, 2, \ldots, n_1)$. Because the $n_1$ basis vectors selected by PCA and KLD, respectively, satisfy the orthonormal condition, it only needs an orthogonal transformation to enable the orthonormal basis vectors selected by using PCA and KLD to be completely the same.

iv) The same approximate matrices processed in practical calculation

Because the variables such as the probability and the expectation associated with the covariance matrix are not known *a priori*, the estimate of the covariance matrix is needed in order to obtain the approximate covariance matrix. In PCA and KLD, $(1/n)(X - \overline{X})(X - \overline{X})^T$ is used as the approximation of $R_x$. In general the data are centralized before the proper orthogonal decomposition is performed, i.e. $\overline{X} = 0$. Therefore in the two methods the approximate matrix processed in practical calculation is $(1/n)XX^T$, where $X$ is a matrix whose columns are formed by the given samples.

### 5.5.2 THE EQUIVALENCE OF PRINCIPAL COMPONENT ANALYSIS (KARHUNEN-LOÈVE DECOMPOSITION) AND SINGULAR VALUE DECOMPOSITION

i) The equivalence of the eigenvalue problems of PCA (KLD) and SVD

From the above discussion it can be seen that SVD is to perform the singular value decomposition to the transposed matrix $X^T$ of the matrix $X$. The singular values obtained are the arithmetic square roots of the eigenvalues of the matrix $XX^T$ and the right singular vectors selected as the basis vectors are the eigenvectors of the $XX^T$.

Thus if the transformation $\tilde{X} = \left(1/\sqrt{n}\right)X$ is made, performing the singular value decomposition to the matrix $\tilde{X}^T$ is equivalent to searching the eigenvalues and eigenvectors of the matrix $(1/n)XX^T$. Since both the matrices $XX^T$ and $(1/n)XX^T$ have the same eigenvectors, the basis vectors obtained using SVD to $X^T$ are the same as those obtained using PCA (KLD) to $(1/n)XX^T$.

ii) The asymptotic connection between PCA (KLD) and SVD

The asymptotic relationship between PCA (KLD) and SVD can be obtained directly by using the eigenvalue problems of SVD and PCA (KLD), and the asymptotic relationship between the matrices $(1/n)XX^T$ and $R_x$. The detail of this asymptotic relationship is derived as follows.

Denote the elements of the covariance matrix $R_x$ as $\sigma_{ij}$. From the definition of the covariance matrix of Equation (5.9), it is derived that

$$\sigma_{ij} = \mathrm{Cov}(x_i, x_j) = E\left[\left(x_i - E[x_i]\right)\left(x_j - E[x_j]\right)\right] \tag{5.106}$$

Denote the values of the $i-\text{th}$ component $x_i$ of the random vector $x$ as $x_i^1, x_i^2, \ldots, (i = 1,\ 2, \ldots, m)$ which represent some events of the component $x_i$. Let the expectation of the $x_i$ be $E[x_i] = u_i$, $(i = 1,\ 2, \ldots, m)$ and the probability of the event $\left(x_i^p - u_i\right)\left(x_j^q - u_j\right)$ be $P_{ij}^{pq}$, then

$$\sigma_{ij} = \sum_{p,q}\left(x_i^p - u_i\right)\left(x_j^q - u_j\right)P_{ij}^{pq} \tag{5.107}$$

Because in most cases the values of expectation $u_i$ and probability $P_{ij}^{pq}$ of a random variable are not known *a priori*, rather, they can only be obtained approximately from a large number of samples.

Assume that $n$ samples of a random vector $x$ are selected, which are defined as

$x^{(1)}, x^{(2)}, \ldots, x^{(n)} \in R^m$, $(n > m)$. Let

$$X = \left(x^{(1)}, x^{(2)}, \ldots, x^{(n)}\right) \in R^{m \times n} \tag{5.108}$$

Firstly, the number of the events of $x_i$ is counted, i.e., counting the number of times that different values of the $i-$th components of all $n$ samples appear. Denote the number as $n_i$, $(i = 1, 2, \ldots, m)$ and the expectation of $x_i$ as

$$u_i = \frac{1}{n}\sum_{j=1}^{n} x_i^{(j)}, \quad (i = 1, 2, \ldots, m) \tag{5.109}$$

Then the number of the events of $\left(x_i^p - u_i\right)\left(x_j^q - u_j\right)$, $(i, j = 1, 2, \ldots, m$, $p = 1, 2, \ldots, n_i$, $q = 1, 2, \ldots, n_j)$ is counted, where $x_i^p$ and $x_j^q$ represent the $p$ and $q$ kinds of values for the $i-$th and $j-$th components of the random vector $x$, respectively. Let the number of the appearance of $\left(x_i^p - u_i\right)\left(x_j^q - u_j\right)$ in the $n$ samples be $n_{ij}^{pq}$. Define the probability as

$$\tilde{P}_{ij}^{pq} = \frac{n_{ij}^{pq}}{n} \tag{5.110}$$

where $\sum_{p,q} n_{ij}^{pq} = n$ as both $x_i^p$ and $x_j^q$ are in the same sample merely appear in the $i-$th and $j-$th places, respectively.

It is noted that the larger the number $n$ of the samples is, the closer the probability $\tilde{P}_{ij}^{pq}$ defined by Equation (5.110) will tend to the true probability $P_{ij}^{pq}$ of the random event $\left(x_i^p - u_i\right)\left(x_j^q - u_j\right)$, i.e.

$$\lim_{n \to \infty} \tilde{P}_{ij}^{pq} = P_{ij}^{pq} \tag{5.111}$$

Let

$$\tilde{R}_x = \frac{1}{n}\left(X - \overline{X}\right)\left(X - \overline{X}\right)^T = \frac{1}{n}\sum_{i=1}^{n}\left(x^{(i)} - u\right)\left(x^{(i)} - u\right)^T \tag{5.112}$$

where $u = (u_1, u_2, \cdots, u_m)^T = 1/n \sum_{i=1}^{n} x^{(i)}$ and $\overline{X} = \underbrace{(u, u, \cdots, u)}_{n}$. Let the elements of $\tilde{R}_x$ be $\tilde{\sigma}_{ij}$, then

$$\tilde{\sigma}_{ij} = \frac{1}{n} \sum_{l=1}^{n} \left(x_i^{(l)} - u_i\right)\left(x_j^{(l)} - u_j\right) = \sum_{p,q} \frac{n_{ij}^{pq}}{n} \left(x_i^p - u_i\right)\left(x_j^q - u_j\right) \tag{5.113}$$

From Equations (5.106) and (5.113), it is derived that $\lim_{n\to\infty} \tilde{\sigma}_{ij} = \sigma_{ij}$. Then the limitation $\lim_{n\to\infty} \tilde{R}_x = R_x$ holds. In general, the centralization for the samples is performed after the $n$ samples are obtained, i.e., the expectation of $(1/n)\sum_{i=1}^{n} x^{(i)}$ is subtracted from each sample. Hence $\tilde{R}_x = (1/n) X X^T$ and we have

$$R_x = \lim_{n\to\infty} \tilde{R}_x = \lim_{n\to\infty} \frac{1}{n} X X^T \tag{5.114}$$

Equation (5.114) shows the asymptotic relationship between the covariance matrix (or the correlation matrix because the expectation of samples is set to zero) $R_x$ in PCA (KLD) and its approximate matrix $(1/n) X X^T$. The asymptotic relationship of PCA (KLD) and SVD can be obtained theoretically from the combination of Equation (5.114) with the equivalence of the eigenvalue problems of SVD and PCA (KLD) mentioned above.

Hence the equivalence relationships among the three POD methods have been given. The above derivation of the equivalence is performed for the discrete cases. It should be noted that KLD can also be used to handle the problem of continuous random variables, whereas PCA and SVD can only be used to deal with discrete random variables.

## 5.6 CONCLUSION

In this chapter, the derivation and the performance of the three POD methods, PCA, KLD and SVD are summarised when they are used to handle the discrete random vectors. Proofs on their equivalence are presented through the theoretical comparison of the matrices for processing, the objective functions in optimization to extract the optimal basis vectors and the expression of mean square errors as well as the asymptotic connections among them. In Chapter 4, it is noted that the principal eigenvectors extracted by using GHA of PCA is identical to KLMs extracted by KLD numerically, this identity is thus proved in this chapter theoretically.

# CHAPTER 6

# COMPUTATION IMPROVMENT IN THE MACROMODEL DYNAMIC SIMULATION

A doubly-clamped microbeam actuated by electrostatic force with squeezed gas-film damping is a well-known standard micro-device in microelectromechanical system for many researchers to demonstrate how reduced-order dynamic macromodel as an effective way to faithfully capture the device behaviours. It has been demonstrated in the preceding Chapters 3, 4 and Hung and Senturia (1999) how the macromodels are generated by extracting the global basis functions from a few fully meshed model computations to parameterize a model with far fewer degrees-of-freedom and how accurate and flexible the macromodel simulations are. It is however found in real numerical experiments that much of computer time is spent on the re-computation of the time-dependant nonlinear terms at every time step during the numerical integration thus results in relatively low efficiency in these macromodels simulation. Two methods to improve the computation are developed in this chapter to further enhance the efficiency of macromodel simulations. In the first method, the computation improvement is achieved based on the pre-computation concept, i.e. the nonlinear terms are firstly expressed explicitly in the time-dependant generalized modal coordinates and their coefficients are then pre-computed prior to numerical time integration once the basis for macromodel is obtained. The second method is to use cubic splines approximation to interpolate the basis functions and their first and second derivatives, and apply the Gaussian quadrature to scale down the spatial integration of the macromodel so as to improve the macromodel simulation efficiency. The

numerical experiments demonstrate that both methods can enhance the efficiency of the macromodel simulation compared with the previous computation results.

## 6.1 MACROMODEL

For the MEMS device idealized as doubly-clamped microbeam as shown in Figure 3.8, it has been described in the Chapters 3 and 4 that the ensembles of deflection and back pressure obtained by FDM solutions are used as the snapshots, i.e. the ensemble of signals for KLD or as the inputs to the GHA of neural network-based PCA to generate the eigenvectors (or modes). The Galerkin procedure employing these eigenvectors as basis functions is then applied to the original nonlinear governing PDEs (3.44) and (3.45) to convert them to low-dimensional macromodels with a smaller number of ODEs. It has been proved in Chapter 5 that the eigenvectors extracted by either KLD or GHA from the same system or the same ensembles of signals are identical because both numerical techniques process the same random vector and the same correlation matrix, and both techniques have the same objective function for finding the optimal basis vector. As such, the eigenvectors extracted by KLD or GHA with respect to deflection are denoted as $\phi_i^w(x)$ and those with respect to the back pressure as $\phi_j^p(x, y)$, respectively. The microbeam deflection $w(x,t)$ and back pressure $p(x,y,t)$ due to squeezed gas-film damping can then be represented as a linear combination of the eigenvector as described by Equations (3.50) and (3.51) which are rewritten as

$$w(x,t) - w_0 = \sum_{i=1}^{I} a_i^w(t)\phi_i^w(x) = \tilde{w} \tag{6.1}$$

$$p(x,y,t) - p_a = \sum_{j=1}^{J} a_j^p(t)\phi_j^p(x,y) = \tilde{p} \tag{6.2}$$

where $w_0$ is the initial gap between the deformable microbeam and the substrate, $p_a$ is the gap air ambient pressure, $a_i^w(t)$ and $a_j^p(t)$ are the time-dependant generalized modal coordinates to be determined, and $I$ and $J$ are the number of basis functions for deflection and back pressure representation in macromodel, respectively.

Substituting Equations (6.1) and (6.2) into the governing PDEs (3.44) and (3.45), and applying the Galerkin procedure, a set of ODEs of Equations (3.54) and (3.55) is obtained which is re-listed in this chapter as follows

$$M_j \frac{d^2 a_j^w}{dt^2} + \sum_{i=1}^{I} K_{ji} a_i^w + f_j = 0, \quad (j = 1, 2, \cdots, I) \tag{6.3}$$

$$\sum_{i=1}^{J} H_{ji} \frac{da_i^p}{dt} + \sum_{i=1}^{J} S_{ji} a_i^p + c_j = 0, \quad (j = 1, 2, \cdots, J) \tag{6.4}$$

where

$$M_j = \int_L \rho \left(\phi_j^w\right)^2 dx \tag{6.5}$$

$$K_{ji} = K_{ij} = \int_L \left( EI \frac{\partial^2 \phi_j^w}{\partial x^2} \frac{\partial^2 \phi_i^w}{\partial x^2} + T \frac{\partial \phi_j^w}{\partial x} \frac{\partial \phi_i^w}{\partial x} \right) dx \tag{6.6}$$

$$f_j = \int_L \left( \frac{\varepsilon_0 b V^2}{2w^2} - \int_0^b (p - p_a)\, dy \right) \phi_j^w \, dx \tag{6.7}$$

$$H_{ji} = H_{ij} = \int_A \frac{12\mu}{1 + 6K_n} w \phi_j^p \phi_i^p dxdy \tag{6.8}$$

$$S_{ji} = S_{ij} = \int_A \left[ w^3 p \left( \frac{\partial \phi_j^p}{\partial x} \frac{\partial \phi_i^p}{\partial x} + \frac{\partial \phi_j^p}{\partial y} \frac{\partial \phi_i^p}{\partial y} + \frac{12\mu}{1 + 6K_n} \phi_j^p \phi_i^p \frac{\partial w}{\partial t} \right) \right] dxdy \tag{6.9}$$

$$c_j = \int_A \frac{12\mu}{1 + 6K_n} p_a \phi_j^p \frac{\partial w}{\partial t} \, dxdy \tag{6.10}$$

The smaller set of coupled ODEs (6.3) and (6.4) constitutes the macromodel with global basis functions $\phi_i^w(x)$ and $\phi_j^p(x, y)$, which is the low-order representation of

the original nonlinear PDEs (3.44) and (3.45). The macromodel can be integrated numerically in time by Runge-Kutta method to simulate the dynamics of the system when an input voltage is applied. Examining the terms expressed in Equations (6.5)-(6.10) for the unknown time-dependant generalized modal coordinates $a_i^w(t)$ and $a_j^p(t)$ in (6.3) and (6.4) reveals that some terms can be pre-computed without difficulties once the basis functions $\phi_i^w(x)$ and $\phi_j^p(x,y)$ are known; for example, $M_j$ in (6.5) and $K_{ji}$ in (6.6) if the bending induced tension effect $t_b$ is ignored. However, the terms, $H_{ji}$, $S_{ji}$, $c_j$ and $f_i$, which are related to the microbeam flexural deflection, electrostatic force, squeezed gas-film damping and bending induced tension cannot be expressed directly in the generalized coordinates or modal coordinates $a_i^w(t)$ and $a_j^p(t)$. Since $w$, $p$ and $T$ in these equations are time-dependent, much of the computation time is thus spent on re-computation of these elements at every time step during the numerical integration of Equations (6.3) and (6.4). Gabbay and Senturia (2000) proposed a method of pre-computation technique in the Galerkin procedure by rational function approach to approximate the nonlinear electrostatic force directly in terms of modal coordinates to achieve very good computation efficiency if both nonlinear bending induced stress and squeezed gas-film damping are ignored. However, this approach requires many tedious simulations and rational function fitting. Moreover, it cannot handle the system with dissipation, such as the squeezed gas-film damping.

It is also noted that every step of re-computation of the terms expressed in Equations (6.7)-(6.10) is performed as the spatial integration in the original Cartesian coordinate system. The most direct method to perform this spatial integration numerically is to use the classical formulas for equally spaced abscissas, for example, the trapezoidal

rule since the values of the basis functions on every discrete grid point, as shown in Figure 3.9, have been obtained. It has been demonstrated in the preceding Chapter 3 that by doing so the macromodel simulation of pull-in dynamics can be improved by around 11 times than the full model FDM simulation when the device shown in Figure 3.8 is applied with an input step voltage of 10.25 V. However, it is expected that this direct numerical integration cannot achieve the best computation efficiency because much of the computation time is spent on the re-computation of time-dependant terms at every time step. The computation efficiency will be harmed further especially when the number of grid points for integration is very large. In order to improve the macromodel simulation but retain the simulation accuracy, two methods to enhance the computation efficiency of the macromodel simulation have been developed. These two methods are described in the following sections. The improvement of the macromodel computation efficiency is demonstrated by some numerical experiments.

## 6.2 PRE-COMPUTATION

It is impractical to fully pre-compute the nonlinear time-dependant terms expressed in Equations (6.7)-(6.10). However, these equations could be expressed explicitly in the time-dependant generalized modal coordinates $a_i^w(t)$ and $a_j^p(t)$. The coefficients of $a_i^w(t)$ and $a_j^p(t)$ are the known spatial integration after the basis functions are obtained, hence can be pre-computed to avoid re-computations at every time step during numerical time integration of the macromodel so as to improve the macromodel simulation efficiency. This procedure is called the ‘pre-computation’ method in this section and the details are described below.

It is noted that, once the number of the deflection basis functions $I$ and back pressure basis functions $J$ are chosen for macromodel simulation, $H_{ji}$, $S_{ji}$ and $c_j$ of Equations (6.8)-(6.10) can be explicitly expressed in time-dependant modal coordinates $a_i^w(t)$ and $a_j^p(t)$ as follows by making use of the multinomial theorem

$$H_{ji} = h_{ji,0}^{(0)} + \sum_{k=1}^{I} h_{ji,k}^{(1)} a_k^w(t) \tag{6.11}$$

$$\begin{aligned} S_{ji} = {} & s_{ji,0}^{(0)} + \sum_{k=1}^{I} s_{ji,k}^{(1)} a_k^w(t) + \sum_{k=1}^{J} s_{ji,k}^{(2)} a_k^p(t) + \sum_{k=1}^{I}\sum_{l=1}^{J} s_{ji,kl}^{(3)} a_k^w(t) a_l^p(t) \\ & + \sum_{k_1+\ldots+k_I=2} s_{ji,k_1+\ldots+k_I}^{(4)} \left(a_1^w(t)\right)^{k_1} \ldots \left(a_I^w(t)\right)^{k_I} \\ & + \sum_{k_1+\ldots+k_I=2} \sum_{l}^{J} s_{ji,k_1+\ldots+k_I}^{(5)} \left(a_1^w(t)\right)^{k_1} \ldots \left(a_I^w(t)\right)^{k_I} a_l^p(t) \\ & + \sum_{k_1+\ldots+k_I=3} s_{ji,k_1+\ldots+k_I}^{(6)} \left(a_1^w(t)\right)^{k_1} \ldots \left(a_I^w(t)\right)^{k_I} \\ & + \sum_{k_1+\ldots+k_I=3} \sum_{l}^{J} s_{ji,k_1+\ldots+k_I}^{(7)} \left(a_1^w(t)\right)^{k_1} \ldots \left(a_I^w(t)\right)^{k_I} a_l^p(t) + \sum_{k=1}^{I} s_{ji,k}^{(8)} \frac{da_k^w(t)}{dt} \end{aligned} \tag{6.12}$$

$$c_j = \sum_{k=1}^{I} c_{j,k} \frac{da_k^w(t)}{dt} \tag{6.13}$$

where $h_{ji,k}^{(m)}$, $s_{ji,\bullet}^{(m)}$ and $c_{j,k}$ are constants that are the known spatial integration once the $\phi_i^w(x)$ and $\phi_j^p(x,y)$ are obtained. Special attention needs to be paid on the term related to electrostatic force $\left(\varepsilon_0 bV^2\right)/\left(2w^2\right)$ in $f_j$ of Equation (6.7) because the time-dependant flexural deflection $w(x,t)$ is the denominator. It tends to zero and induces singularity when pull-in occurs. In order to express $f_j$ explicitly in time-dependant

modal coordinates $a_i^w(t)$ and $a_j^p(t)$, a fourth order polynomial function is used to approximate $1/w^2$ with the microbeam deflection ratio $\tilde{w}/w_0$ ranging from $-0.7$ to 0

$$\frac{1}{w^2} = \frac{1}{w_0^2(1+\tilde{w}/w_0)^2} \approx \frac{1}{w_0^2}\Big[p_4(\tilde{w}/w_0)^4 + p_3(\tilde{w}/w_0)^3 + p_2(\tilde{w}/w_0)^2 + p_1(\tilde{w}/w_0) + p_0\Big] \tag{6.14}$$

Where $p_0 = 1.1095$, $p_1 = 2.6136$, $p_2 = 43.4482$, $p_3 = 117.8236$ and $p_4 = 127.9959$ are obtained by MatLab® simulation. Since the maximum stable deflection of the microbeam is about 67% of the original gap $w_0$ in the quasi-static case (Tilmans, 1996), the above lower order polynomial function for approximation of nonlinear term $1/w^2$ is sufficient for the deflection range of 0.0 to 0.7 which counts for 70% of the original gap $w_0$. The trade off is that it could not be used to simulate the system closed to the pull-in region when $\tilde{w}/w_0$ approaches $-1$. Using the multinomial theorem, Equation (6.7) can be re-written in terms of $a_i^w(t)$ and $a_j^p(t)$ as

$$f_j = f_{j,0}^{(0)} + \sum_{k=1}^{4} \sum_{k_1+\ldots+k_I=k} f_{j,k_1+\ldots+k_I=k}^{(1)} \left(a_1^w(t)\right)^{k_1} \ldots \left(a_I^w(t)\right)^{k_I} + \sum_{l=1}^{J} f_{j,l}^{(2)} a_l^p(t). \tag{6.15}$$

Similarly, the values of $f_j^{(m)}$ are the constants in the form of spatial integration that can be computed once the basis functions are known.

## 6.3 CUBIC SPLINES APPROXIMATION AND GAUSSIAN QUADRATURE

It is expected that, in general, the Gaussian quadrature is simpler, accurate and more effective compared with the traditional quadrature formulas for equally spaced abscissas, e.g. trapezoidal rule, in numerical integration. Recalling the procedure for the snapshots generation described in Chapter 3, the snapshots are obtained from the

numerical simulations of the continuous range of $x$ values on the domain $\Omega$ by FDM, hence the basis functions are only available on a discrete set of point in the domain. Azeez and Vakakis (2001) had demonstrated that smooth interpolations can be performed to evaluate the integral accurately and efficiently by the Gaussian quadrature. As such, it is expected that the macromodel performance and efficiency can be improved by computing the Equations (6.5)-(6.10) using the following Gaussian quadrature for spatial integration in the numerical time integration of the macromodel simulation

$$M_j = \sum_{k=1}^{m} v_k \rho \left(\phi_j^w (x_k)\right)^2 \tag{6.16}$$

$$K_{ji} = \sum_{k=1}^{m} v_k \left[ EI \frac{\partial^2 \phi_j^w (x_k)}{\partial x^2} \frac{\partial^2 \phi_i^w (x_k)}{\partial x^2} + T \frac{\partial \phi_j^w (x_k)}{\partial x} \frac{\partial \phi_i^w (x_k)}{\partial x} \right] \tag{6.17}$$

$$f_j = \sum_{k=1}^{m} v_k \frac{\varepsilon_0 b V^2}{2w^2 (x_k, t)} \phi_j^w (x_k) - \sum_{k=1}^{m} \sum_{l=1}^{n} v_k v_l \left[ p(x_k, y_l, t) - p_a \right] \phi_j^w (x_k) \tag{6.18}$$

$$H_{ji} = \frac{12\mu}{1 + 6K_n} \sum_{k=1}^{m} \sum_{l=1}^{n} v_k v_l \, w(x_k, t) \phi_j^p (x_k, y_l) \phi_i^p (x_k, y_l) \tag{6.19}$$

$$\begin{aligned} S_{ji} = {} & \sum_{k=1}^{m} \sum_{l=1}^{n} v_k v_l \, w^3 (x_k, t) p_{kl} (x_k, y_l, t) \left[ \frac{\partial \phi_j^p (x_k, y_l)}{\partial x} \frac{\partial \phi_i^p (x_k, y_l)}{\partial x} \right. \\ & \left. + \frac{\partial \phi_j^p (x_k, y_l)}{\partial y} \frac{\partial \phi_i^p (x_k, y_l)}{\partial y} \right] \\ & + \frac{12\mu}{1 + 6K_n} \sum_{k=1}^{m} \sum_{l=1}^{n} v_k v_l \, \phi_j^p (x_k, y_l) \phi_i^p (x_k, y_l) \frac{\partial w(x_k, t)}{\partial t} \end{aligned} \tag{6.20}$$

$$c_j = \frac{12\mu}{1 + 6K_n} p_a \sum_{k=1}^{m} \sum_{l=1}^{n} v_k v_l \, \phi_j^p (x_k, y_l) \frac{\partial w(x_k, y_l)}{\partial t} \tag{6.21}$$

where $m$ and $n$ are the numbers of the Gaussian integration points, and $v_k$ and $v_l$ are the associated weighting factors, respectively. In this method, once the discrete basis

functions are obtained, the natural cubic splines approximation, in which the second derivative on both boundaries of the basis function will be set to zero, is used to interpolate the values of basis functions. Their first and second order derivatives at the $k-$th Gaussian integration point are computed by generalised differential quadrature. The Gaussian quadrature is used to perform the spatial integration of (6.16)-(6.21) in the macromodel simulation.

## 6.4 NUMERICAL RESULTS

In order to validate the above methods, simulation based on the MEMS device shown in Figure 3.8 with material properties and geometric parameters listed in Table 3.1 are carried out. Similar to the procedure described in Chapter 3, snapshots are obtained from the solution of Equations (3.44) and (3.45) by using FDM for an ensemble of input step voltages of $V_1 = 10\,\text{V}$ and $V_2 = 16\,\text{V}$, which are assumed to be the device operating voltage under consideration. Two sets of eigenvectors can then be obtained by applying KLD or the GHA neural network to these snapshots, respectively, and are employed as basis functions in the Galerkin procedure to the original nonlinear PDEs (3.44) and (3.45) to generate the macromodel. The two sets of the eigenvectors obtained independently by KLD and GHA are shown to be the same as indicated in the Chapters 4 and 5. The number of the basis for deflection and back pressure chosen in the macromodel for system simulation can be determined by the system energy level captured by these eigenvectors. It has been shown in Chapter 3 that, for microbeam deflection simulation, the first eigenvector $\phi_1^w(x)$ can capture 99.99% of the system energy while it takes at least four eigenvectors $\phi_j^p(x,y)$ for the back pressure to capture the same level of energy in the back pressure simulation. As such, one

deflection basis and four back pressure basis are employed in the macromodel simulation to ensure sufficient accuracy.

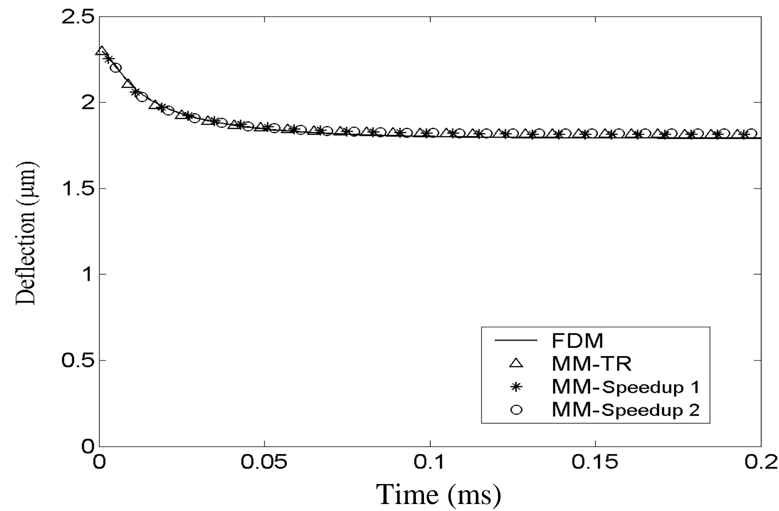


Figure 6.1 Comparison of the microbeam pull-in dynamics for an input step voltage of 8 V.

Figure 6.1 shows the comparison of the deflection of the centre point of microbeam between the FDM solution of the original nonlinear PDEs (3.44) and (3.45) and the macromodel simulations when the system is applied with an input step voltage of 8 V. Macromodel simulations are carried out by numerical integration of ODEs (6.3) and (6.4) with

i) the direct classical formulas for equally spaced abscissas, e.g. the trapezoidal rule (TR) for spatial integration,

ii) pre-computation (speedup 1) of the known coefficients of the generalized modal coordinates and

iii) cubic splines approximation and the simplified Gaussian quadrature with 7×7 Gaussian integration grid size (speedup 2) for spatial integration.

It is noted that the minimum step pull-in voltage for this device is calculated at 8.87 V by FDM. Thus, pull-in does not happen when the input step voltage is less than the system pull-in voltage. The macromodel performance with respect to FDM is listed in

Table 6.1 for the simulation period from 0 to 200 $\mu$s where the mean square error (MSE) between the results using the macromodel and those using the FDM is defined by Equation (4.40). Table 6.1 indicates that the speed for the macromodel simulation with speedup 1 and speedup 2 techniques can be improved by up to 85 and 5 times, respectively, compared with the macromodel simulation with TR method which has already achieved 7 times faster than FDM simulation. The errors of macromodel simulations are small compared with FDM simulation. It is clear from this numerical example that when the applied input step voltage is less than the minimum pull-in voltage, macromodel simulation with speedup 1 or speedup 2 are very attractive as both methods are accurate and the computation effort required are much less compared with TR and FDM simulations.

Table 6.1 Performance of macromodels with respect to FDM simulation for an input step voltage of 8 V.

| Method for simulation | Number of ODEs | Mean square error | Computer system time (seconds) | Speed up factor |
|---|---|---|---|---|
| FDM | 819 | 0 | 1048 | 1 |
| Macromodel (TR) | 6 | $2.1\times10^{-4}$ | 145 | 7 (1)* |
| Macromodel (Speedup 1) | 6 | $2.85\times10^{-4}$ | 1.7 | 616 (85)* |
| Macromodel (Speedup 2) | 6 | $3.95\times10^{-4}$ | 27.3 | 38 (5)* |

Figure 6.2 plots the comparison of the deflection of the centre point of microbeam simulations when the system is applied with an input step voltage of 10.25 V which is larger than the minimum pull-in voltage. As expected, macromodel simulation with speedup 1 could not provide accurate results near pull-in area because $w$ approaching zero is not counted for in the approximation of $1/w^2$ expressed in Equation (6.14).

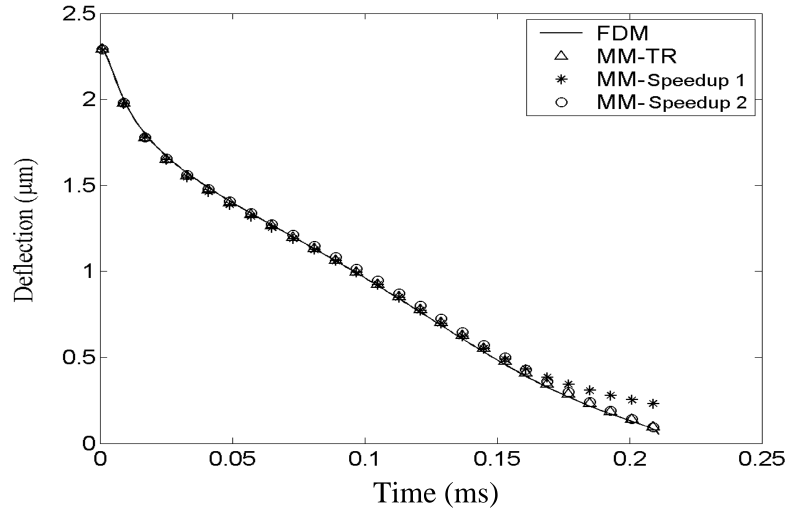


Figure 6.2 Comparison of the microbeam pull-in dynamics for an input step voltage of 10.25 V.

Table 6.2 Performance of macromodels with respect to FDM simulation for an input step voltage of 10.25 V.

| Method for simulation | Number of ODEs | Mean square error | Computer system time (seconds) | Speed up factor |
|---|---|---|---|---|
| FDM | 819 | 0 | 1952 | 1 |
| Macromodel (TR) | 6 | $2.27\times10^{-4}$ | 182 | 11 (1)* |
| Macromodel (Speedup 1) | 6 | $7.06\times10^{-4}$ | 1.4 | 1394 (130)* |
| Macromodel (Speedup 2) | 6 | $6.87\times10^{-4}$ | 20.5 | 95 (9)* |

* The figure in the bracket stands for the macromodel speed up factor comparison with respect to macromodel simulation by using trapezoidal rule (TR).

Table 6.2 shows that the macromodel simulation with speedup 2 method has smaller error compared with FDM but the error of speedup 1 is relatively large, the computation efficiency of speedup 1 method is much better in the sense that it can achieve 1394 times faster than FDM and 130 times faster than macromodel simulation with TR method, while speedup 2 method achieves 95 times and 9 times accordingly. Hence when the input voltage is less than the minimum pull-in voltage, macromodel

with speedup 1 method is attractive to be used. However, the macromodel with speedup 2 simulation is the choice for system designer when the applied voltage is larger than the minimum pull-in voltage.

## 6.5 CONCLUSION

Two methods to enhance the computation efficiency of the macromodels which are generated by the eigenvectors obtained either from KLD or the GHA neural network-based method together with the Galerkin procedure are presented in this chapter. It has been demonstrated in numerical experiments that both methods can enhance the computation efficiency of the macromodel simulation for MEMS device. Although the pre-computation method does not deliver favourite results near pull-in, however, it can still give satisfied results for non pull-in dynamics analysis.

# CHAPTER 7

# MACROMODEL GENERATION AND SIMULATION FOR COMPLEX MEMS DEVICES

Most of the macromodels which have been developed over the past few years in MEMS community focused only on single structure MEMS devices, for instance, single microbeam or plate structure. Many MEMS devices, such as comb drives and some optical switches are however structurally complex, hence efficient model order reduction techniques for such connected structurally complex MEMS devices are needed for system design and optimisation. There are no available methods to generate macromodels for complex MEMS device dynamic simulation in the literature to date other than to treat them as single structure. A novel method for macromodel generation for dynamic simulation and analysis of structurally complex MEMS device is developed by making use of Karhunen-Loève decomposition (KLD), and the classical component mode synthesis (CMS). The CMS is a classical model order reduction method whereby a complex structure is regarded as an assembly of substructures or components (Hurty, 1965; Craig and Bampton, 1968). The idea of CMS is to model each component independently using a number of lower "component modes" and then to impose constraints at interconnections of various components to force these components to act as a single structure. The key advantage of using the CMS is that there is no need to redo or regenerate the governing equations for the entire structure if there are design changes in a particular component so long as the changes do not affect the structural behaviours of that component. In present work, the complex MEMS device is modelled as an assemblage of interacting components, KLD

is used to extract Karhunen-Loève modes (KLMs) and their corresponding Karhunen-Loève values (KLVs) for each component from an ensemble of data obtained by selective runs of the full model simulation. These KLMs for each component are similar to "components modes" and used as basis functions in Galerkin projection to formulate the equations of motion for each component expressed in terms of a set of generalized component coordinates. When the continuity conditions at the interfaces are imposed, a set of constraint equations is obtained which relates the component generalized coordinates to the system generalized coordinates through a transformation matrix. Finally, a macromodel, presented by a set of equations of motion expressed in terms of a set of system generalized coordinates, is formulated to determine the system dynamic responses. The effectiveness and flexibility of the proposed model order reduction methodology are demonstrated with the simulations of the pull-in dynamics of a complex micro-optical device modelled as non-uniform microbeam and a micro-mirror device modelled as rigid square mirror plate with four clamped-guided parallel microbeams along each side of the plate subjected to electrostatic actuation force with squeezed gas-film damping effect.

## 7.1 MACROMODEL FOR A MICRO-OPTICAL DEVICE

### 7.1.1 MODEL DESCRIPTION

A micro-optical switch designed as a non-uniform microbeam with two ends clamped as shown in Figure 7.1 is used as a structurally complex MEMS device for the macromodel development and generation. This MEMS device is idealised as three connected uniform microbeams. Input voltage is applied on the top structure and the

substrate. The squeezed gas-film damping effect is only considered between the wider microbeam 2 and the substrate, while it is neglected on the two relatively narrow microbeams 1 and 3.

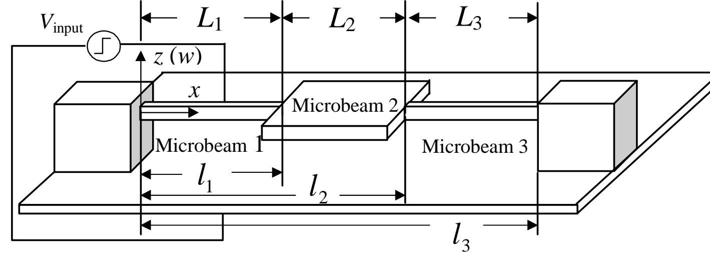


Figure 7.1 An idealized micro-optical switch device.

The microbeam configuration is modelled using Euler-Bernoulli beam theory, and the squeezed gas-film damping is modelled with nonlinear Reynold's equation. The governing equations, which are expressed by nonlinear partial differential equations (PDEs) for the three microbeams are as follows

$$EI_1 \frac{\partial^4 w_1}{\partial x^4} - T_1 \frac{\partial^2 w_1}{\partial x^2} = -\frac{\varepsilon_0 b_1 V^2}{2{w_1}^2} - \rho_1 \frac{\partial^2 w_1}{\partial t^2}, \qquad (0 \le x \le l_1) \tag{7.1}$$

$$\begin{cases} EI_2 \dfrac{\partial^4 w_2}{\partial x^4} - T_2 \dfrac{\partial^2 w_2}{\partial x^2} = -\dfrac{\varepsilon_0 b_2 V^2}{2{w_2}^2} + \displaystyle\int_0^{b_2} (p - p_a) dy - \rho_2 \dfrac{\partial^2 w_2}{\partial t^2} \\ \nabla \cdot ({w_2}^3 p \nabla p) = \dfrac{12\mu}{1 + 6K_n} \dfrac{\partial (p w_2)}{\partial t}, \qquad (l_1 \le x \le l_2,\ 0 \le y \le b_2) \end{cases} \tag{7.2}$$

$$EI_3 \frac{\partial^4 w_3}{\partial x^4} - T_3 \frac{\partial^2 w_3}{\partial x^2} = -\frac{\varepsilon_0 b_3 V^2}{2{w_3}^2} - \rho_3 \frac{\partial^2 w_3}{\partial t^2}, \qquad (l_2 \le x \le l_3) \tag{7.3}$$

where $E$ is Young's modulus, $I_i = b_i h_i^3 / 12$ is the second moment of area where $b_i$ is the width and $h_i$ is the thickness of the microbeam $i$, $\rho_i$ is the density, $\mu$ is the air viscosity, $w_i(x,t)$ is the height of the microbeam above the substrate, $K_n(x,t) = \lambda / w_i$ is the Knudsen number where $\lambda$ is the mean-free path of the air, $V$ is the applied voltage, $\varepsilon_0$ is the permittivity of free space, $p(x, y, t)$ is the back pressure acting on

microbeam 2 due to the squeezed gas-film in which an isothermal process is assumed, $p_a$ is the ambient pressure and $T_i/(b_i h_i)$ is the sum of residual stress $t_{r,i}$ and the bending induced stress $t_{b,i}$ due to large deflection, which can be expressed as

$$\frac{T_i}{b_i h_i} = t_{r,i} + t_{b,i} = t_{r,i} + E\,\Delta L_i / L_i \approx t_{r,i} + \frac{E}{2L_i}\int_{L_i}\left(\frac{dw_i}{dx}\right)^2 dx\,, \quad i = 1, 2, 3 \tag{7.4}$$

where $L_i$ is the length of microbeam $i$.

### 7.1.2 KARHUNEN-LOÈVE MODES FOR COMPONENTS

The procedure of KLD method in extracting KLMs and the corresponding KLVs from a set of time series data (signals) available on a domain has been described in Chapter 3. To obtain the ensemble of numerical data, the full model FDM is used to simulate the system response in Equations (7.1)-(7.3) subjected to the applied voltage beyond the dynamic pull-in voltage. Based on numerical experiments, a mesh size of 40×1 for microbeams 1 and 3, and 40×40 for microbeam 2 in the FDM simulation of the original non-linear equations (7.1)-(7.3) is able to generate sufficient accuracy. Following KLD procedure, the KLMs and the corresponding KLVs for each component are obtained. Figure 7.2 shows the first normalized deflection KLM for microbeams 1, 2 and 3 with the material properties and geometric dimensions listed in Table 7.1 when the microbeams are subjected to an input step voltage of $25\,\text{V}$. The second normalized deflection KLM for each microbeam is plotted in Figure 7.3. It is noted that these deflection KLMs include values at two imaginary nodes on each side of the interface, which are introduced in the central FDM after imposing the geometric and force continuity conditions which state that the deflection, slope, bending moment and shear force are continuous across the interface. These two nodes to the right of the

interface represent an imaginary extension of the left microbeam while the other two nodes to the left of the interface represent an imaginary extension of the right microbeam beyond the interface of two connected microbeams. The values of KLMs at imaginary nodes are useful in constructing a set of constraint equations. The first three normalized back pressure KLMs along the centre of the microbeam 2 are plotted in Figure 7.4.

Table 7.1 Properties and geometric dimensions of microbeams.

| Microbeam $i$ | Young's modulus $E$ (GPa) | Density $\rho_i/(b_i h_i)$ (kg m$^{-3}$) | Residual Stress $t_{r,i}$ (MPa) | Knudsen's Number $K_n = \lambda/w_i$ |
|---|---|---|---|---|
| 1 | | | | |
| 2 | 149 | 2330 | -3.7 | ≈0.028 |
| 3 | | | | |

| Microbeam $i$ | Initial gap $w_0$ ($\mu$m) | Thickness $h_i$ ($\mu$m) | Length $L_i$ ($\mu$m) | Width $b_i$ ($\mu$m) |
|---|---|---|---|---|
| 1 | | | 180 | 10 |
| 2 | 2.3 | 2.2 | 90 | 90 |
| 3 | | | 160 | 10 |

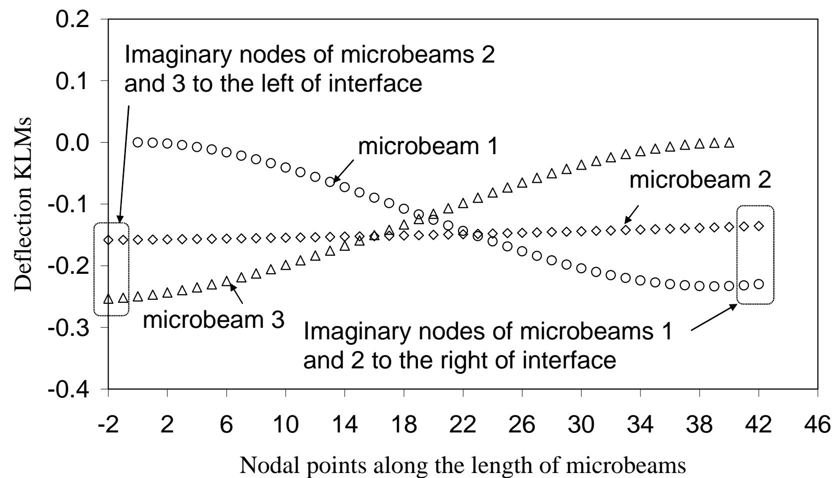


Figure 7.2 The first KLM for deflection of microbeams.

Table 7.2 and Table 7.3 list the normalized KLVs and accumulative normalized KLVs with respect to the number of deflection and back pressure KLMs for each component where the total sum of the KLVs is normalized to one. The magnitude of accumulative normalized KLVs represents the percentage of system characteristics, or energy captured by the corresponding number of the KLMs.

Table 7.2 Normalized accumulative KLVs corresponding to the number of deflection KLMs.

| Number of KLMs | Microbeam 1 | | Microbeam 2 | |
|---|---|---|---|---|
| | Normalized KLVs $\bar{\lambda}_i = \lambda_i \Big/ \sum_{i=1}^{N} \lambda_i$ | Accumulative normalized KLVs $S_{N_i} = \sum_{i=1}^{N_i} \bar{\lambda}_i$ | Normalized KLVs $\bar{\lambda}_i = \lambda_i \Big/ \sum_{i=1}^{N} \lambda_i$ | Accumulative normalized KLVs $S_{N_i} = \sum_{i=1}^{N_i} \bar{\lambda}_i$ |
| 1 | $\bar{\lambda}_1 = 0.9998537200$ | $S_1 = 0.9998537200$ | $\bar{\lambda}_1 = 0.9998014300$ | $S_1 = 0.9998014300$ |
| 2 | $\bar{\lambda}_2 = 0.0001452977$ | $S_2 = 0.9999990177$ | $\bar{\lambda}_2 = 0.0001985024$ | $S_2 = 0.9999999324$ |
| 3 | $\bar{\lambda}_3 = 0.0000008469$ | $S_3 = 0.9999998646$ | $\bar{\lambda}_3 = 0.0000000667$ | $S_3 = 0.9999999991$ |
| 4 | $\bar{\lambda}_4 = 0.0000001313$ | $S_4 = 0.9999999959$ | – | – |

| Number of KLMs | Microbeam 3 | |
|---|---|---|
| | Normalized KLVs $\bar{\lambda}_i = \lambda_i \Big/ \sum_{i=1}^{N} \lambda_i$ | Accumulative normalized KLVs $S_{N_i} = \sum_{i=1}^{N_i} \bar{\lambda}_i$ |
| 1 | $\bar{\lambda}_1 = 0.9999522036$ | $S_1 = 0.9999522036$ |
| 2 | $\bar{\lambda}_2 = 0.0000471248$ | $S_2 = 0.9999993284$ |
| 3 | $\bar{\lambda}_3 = 0.0000006268$ | $S_3 = 0.9999999552$ |
| 4 | $\bar{\lambda}_4 = 0.0000000402$ | $S_4 = 0.9999999954$ |

Table 7.3 Normalized accumulative KLVs corresponding to the number of back pressure KLMs for microbeam 2.

| Number of KLMs | Normalized KLVs $\bar{\lambda}_i = \lambda_i \Big/ \sum_{i=1}^{N} \lambda_i$ | Accumulative normalized KLVs $S_{N_i} = \sum_{i=1}^{N_i} \bar{\lambda}_i$ |
|---|---|---|
| 1 | $\bar{\lambda}_1 = 0.9677175500$ | $S_1 = 0.9677175500$ |
| 2 | $\bar{\lambda}_2 = 0.0320025360$ | $S_2 = 0.9997200860$ |
| 3 | $\bar{\lambda}_3 = 0.0002777716$ | $S_3 = 0.9999978576$ |
| 4 | $\bar{\lambda}_4 = 0.0000020734$ | $S_4 = 0.9999999310$ |

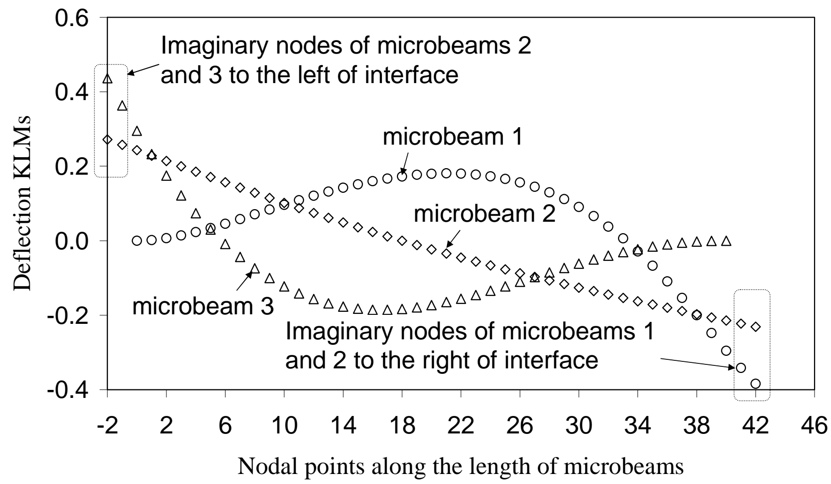


Figure 7.3 The second KLM for deflection of microbeams.

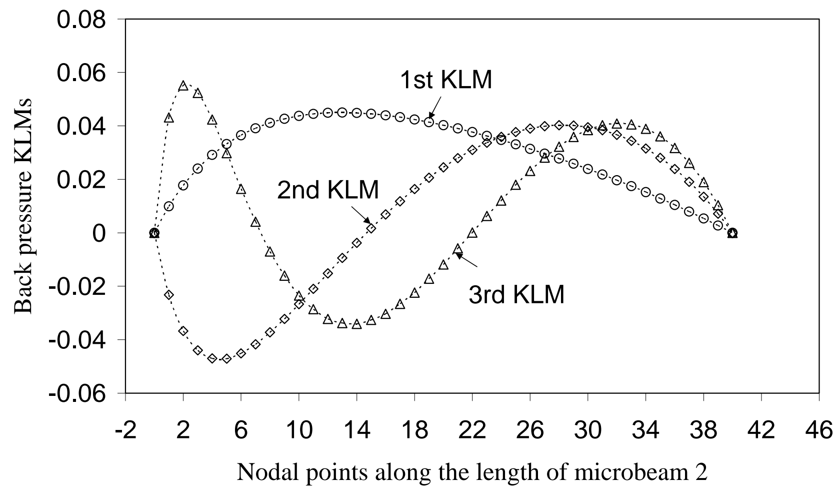


Figure 7.4 First three KLMs for back pressure of microbeam 2.

### 7.1.3 COMPONENT MODE SYNTHESIS AND MACROMODEL GENERATION

A low-order model for the system shown in Figure 7.1 is constructed using the KLMs for each component obtained from the above procedure. The flexural deflection of the microbeams and the back pressure due to the squeezed gas-film damping effect can be represented as a linear combination of the KLMs of each individual component as follows

$$w_1(x,t) - w_0 = \sum_{i=1}^{I_1} a_i^{w_1}(t)\phi_i^{w_1}(x), \qquad (0 \le x \le l_1) \tag{7.5}$$

$$\begin{cases} w_2(x,t) - w_0 = \sum_{i=1}^{I_2} a_i^{w_2}(t)\phi_i^{w_2}(x) \\ \\ p(x,y,t) - p_a = \sum_{j=1}^{J_2} a_j^{p}(t)\phi_j^{p}(x,y), \qquad (l_1 \le x \le l_2,\ 0 \le y \le b_2) \end{cases} \tag{7.6}$$

$$w_3(x,t) - w_0 = \sum_{i=1}^{I_3} a_i^{w_3}(t)\phi_i^{w_3}(x), \qquad (l_2 \le x \le l_3) \tag{7.7}$$

Here $w_0$ is the initial gap between the microbeams and the substrate, $\phi_i^{w_1}$, $\phi_i^{w_2}$ and $\phi_i^{w_3}$ are the deflection KLMs for microbeams 1, 2 and 3, respectively, $\phi_j^{p}$ is the back pressure KLMs for microbeam 2. $I_1$, $I_2$ and $I_3$ are the number of deflection KLMs, and $J_2$ is the number of back pressure KLMs. The coefficients $a_i^{w_1}$, $a_i^{w_2}$ and $a_i^{w_3}$ as well as $a_j^{p}$ are the amplitudes of the KLMs and the component generalized coordinates (or modal coordinates) in modal decomposition. Substituting Equations (7.5)-(7.7) into the governing equations (7.1)-(7.3) and applying the Galerkin procedure using the above KLMs as the basis functions, the following ordinary differential equations are obtained in terms of the component generalized coordinates of $a_i^{w_1}$, $a_i^{w_2}$, $a_i^{w_3}$ and $a_j^{p}$

$$M_1 \ddot{a}^{w_1} + K_1 a^{w_1} + f_1 = 0 \tag{7.8}$$

$$\begin{cases} M_2 \ddot{a}^{w_2} + K_2 a^{w_2} + f_2 = 0 \\ H_2 \dot{a}^p + S_2 a^p + c_2 = 0 \end{cases} \tag{7.9}$$

$$M_3 \ddot{a}^{w_3} + K_3 a^{w_3} + f_3 = 0 \tag{7.10}$$

Here $a^{w_i}$ and $a^p$ are the vectors whose elements $a_i^{w_1}$, $a_i^{w_2}$, $a_i^{w_3}$ and $a_j^p$ are to be determined, $f_i$ is the genelarized forces. The elements in matrix $M_i$ can be obtained once the KLMs are known, the elements in matrixes $K_i$, $H_2$ and $S_2$ and vectors $c_2$ , $f_i$ are expressed as

$$M_{kl,i} = \int_{L_i} \rho_i \phi_k^{w_i} \phi_l^{w_i} dx \ , \quad (k,l = 1,2,\ldots,I_i,\ i = 1,2,3) \tag{7.11}$$

$$\begin{aligned} K_{kl,i} = EI_i \Bigg\{ & \frac{\partial^3 \phi_k^{w_i}}{\partial x^3} \phi_l^{w_i} \bigg|_{x=L_i} - \frac{\partial^3 \phi_k^{w_i}}{\partial x^3} \phi_l^{w_i} \bigg|_{x=0} - \frac{\partial^2 \phi_k^{w_i}}{\partial x^2} \frac{\partial \phi_l^{w_i}}{\partial x} \bigg|_{x=L_i} + \frac{\partial^2 \phi_k^{w_i}}{\partial x^2} \frac{\partial \phi_l^{w_i}}{\partial x} \bigg|_{x=0} \\ & + \int_{L_i} \frac{\partial^2 \phi_k^{w_i}}{\partial x^2} \frac{\partial^2 \phi_l^{w_i}}{\partial x^2} dx \Bigg\} - T_i \Bigg\{ \frac{\partial \phi_k^{w_i}}{\partial x} \phi_l^{w_i} \bigg|_{x=L_i} - \frac{\partial \phi_k^{w_i}}{\partial x} \phi_l^{w_i} \bigg|_{x=0} \\ & - \int_{L_i} \frac{\partial \phi_k^{w_i}}{\partial x} \frac{\partial \phi_l^{w_i}}{\partial x} dx \Bigg\}, \quad (k,l = 1,2,\ldots,I_i,\ i = 1,2,3) \end{aligned} \tag{7.12}$$

$$f_{l,i} = \int_{L_i} \frac{\varepsilon_0 b_i V^2}{2 w_i^2} \phi_l^{w_i} dx, \quad (k,l = 1,2,\ldots,I_i,\ i = 1,3) \tag{7.13}$$

$$f_{l,2} = \int_{L_2} \frac{\varepsilon_0 b_2 V^2}{2 w_2^2} \phi_l^{w_2} dx - \int_A (p - p_a) \phi_l^{w_2} dxdy, \quad (l = 1,2,\ldots,I_2) \tag{7.14}$$

and

$$H_{kl} = \int_A \frac{12\mu}{1+6K_n} w_2 \phi_k^p \phi_l^p dxdy\ , \quad (k,l = 1,2,\ldots,J_2) \tag{7.15}$$

$$S_{kl} = \int_A \left\{ w_2^3 p \left( \frac{\partial \phi_k^p}{\partial x} \frac{\partial \phi_l^p}{\partial x} + \frac{\partial \phi_k^p}{\partial y} \frac{\partial \phi_l^p}{\partial y} \right) + \frac{12\mu}{1+6K_n} \phi_k^p \phi_l^p \frac{\partial w_2}{\partial t} \right\} dxdy, \quad (k, l = 1, 2, \ldots, J_2) \tag{7.16}$$

$$c_l = \int_A \frac{12\mu}{1+6K_n} p_a \phi_l^p \frac{\partial w_2}{\partial t} dxdy, \quad (l = 1, 2, \ldots, J_2) \tag{7.17}$$

where $\int_{L_i}$ indicates the integration along the length of microbeams 1, 2 and 3, and $\int_A$ is the integration over the area of microbeam 2. It is noted that the elements $K_{kl,i}$, $f_{l,i}, H_{kl}, S_{kl}$ and $c_l$ are corresponding to the nonlinear terms related to deflection, electrostatic force, squeezed gas-film damping and bending induced stress in the original PDEs described by Equations (7.1)-(7.3) and cannot be expressed directly in the generalized coordinates or modal coordinates.

Equation (7.8), the first of Equation (7.9) and Equation (7.10) for all the components of the system in terms of component generalized coordinates $a_i^{w_1}$, $a_i^{w_2}$ and $a_i^{w_3}$ can be rewritten as

$$M\ddot{a} + Ka + f = 0 \tag{7.18}$$

where the generalized coordinates and the forces for the components are grouped as

$$a = \begin{Bmatrix} a^{w_1} \\ a^{w_2} \\ a^{w_3} \end{Bmatrix}, \quad f = \begin{Bmatrix} f_1 \\ f_2 \\ f_3 \end{Bmatrix} \tag{7.19}$$

and the matrixes in Equation (7.18) have the form

$$M = \begin{bmatrix} M_1 & 0 & 0 \\ 0 & M_2 & 0 \\ 0 & 0 & M_3 \end{bmatrix}, \quad K = \begin{bmatrix} K_1 & 0 & 0 \\ 0 & K_2 & 0 \\ 0 & 0 & K_3 \end{bmatrix} \tag{7.20}$$

Physically, Equation (7.18) can be interpreted as a set of equations of motion for the group of components not connected together. Using the concept of the classical component mode synthesis (CMS) as described by Hurty (1965), the process of connecting these results in a set of constraint equations between the elements of the generalized coordinate vector $a$. If there are $m$ elements in vector $a$ and $k$ constraint equations relating them, the number of independent generalized coordinates in a vector $q$ for the system is $n = m - k$. Hence there exists a transformation which relates the vector $a$ to $q$ as follows

$$\underset{m\times 1}{a} = \underset{m\times n}{C}\,\underset{n\times 1}{q} \tag{7.21}$$

The construction of transformation matrix $C$ requires the knowledge of constraints imposed on all components by the system of connections. For the system shown in Figure 7.1, there are four continuity conditions each at the interfaces of microbeams 1 and 2 as well as microbeams 2 and 3. These continuity conditions are the contraints which require that the deflection, slope, bending moment and shear force are continuous across the interfaces. Thus, at the interface between microbeams 1 and 2,

$$\sum_{i=1}^{I_1} a_i^{w_1}(t)\phi_i^{w_1}(l_1) = \sum_{i=1}^{I_2} a_i^{w_2}(t)\phi_i^{w_2}(l_1) \tag{7.22}$$

$$\sum_{i=1}^{I_1} a_i^{w_1}(t)\frac{\partial\phi_i^{w_1}(l_1)}{\partial x} = \sum_{i=1}^{I_2} a_i^{w_2}(t)\frac{\partial\phi_i^{w_2}(l_1)}{\partial x} \tag{7.23}$$

$$EI_1\sum_{i=1}^{I_1} a_i^{w_1}(t)\frac{\partial^2\phi_i^{w_1}(l_1)}{\partial x^2} = EI_2\sum_{i=1}^{I_2} a_i^{w_2}(t)\frac{\partial^2\phi_i^{w_2}(l_1)}{\partial x^2} \tag{7.24}$$

$$EI_1\sum_{i=1}^{I_1} a_i^{w_1}(t)\frac{\partial^3\phi_i^{w_1}(l_1)}{\partial x^3} = EI_2\sum_{i=1}^{I_2} a_i^{w_2}(t)\frac{\partial^3\phi_i^{w_2}(l_1)}{\partial x^3} \tag{7.25}$$

At the interface between microbeams 2 and 3, it follows that

$$\sum_{i=1}^{I_2} a_i^{w_2}(t)\phi_i^{w_2}(l_2) = \sum_{i=1}^{I_3} a_i^{w_3}(t)\phi_i^{w_3}(l_2) \tag{7.26}$$

$$\sum_{i=1}^{I_2} a_i^{w_2}(t)\frac{\partial \phi_i^{w_2}(l_2)}{\partial x} = \sum_{i=1}^{I_3} a_i^{w_3}(t)\frac{\partial \phi_i^{w_3}(l_2)}{\partial x} \tag{7.27}$$

$$EI_2\sum_{i=1}^{I_2} a_i^{w_2}(t)\frac{\partial^2 \phi_i^{w_2}(l_2)}{\partial x^2} = EI_3\sum_{i=1}^{I_3} a_i^{w_3}(t)\frac{\partial^2 \phi_i^{w_3}(l_2)}{\partial x^2} \tag{7.28}$$

$$EI_2\sum_{i=1}^{I_2} a_i^{w_2}(t)\frac{\partial^3 \phi_i^{w_2}(l_2)}{\partial x^3} = EI_3\sum_{i=1}^{I_3} a_i^{w_3}(t)\frac{\partial^3 \phi_i^{w_3}(l_2)}{\partial x^3} \tag{7.29}$$

Using standard central finite difference to approximate the derivatives in Equations (7.22)-(7.29) requires the KLMs value at imaginary nodes as shown in Figure 7.2 and Figure 7.3.

The matrix $C$ is of the order $m \times n$ where $m > n = m - k = m - 8$. Substituting for $a$ of Equation (7.18) in terms of $q$ from Equation (7.21) and premultiplying by the transpose $C^T$, Equation (7.18) can be rewritten as

$$C^T MC\ddot{q} + C^T KCq + C^T f = 0 \tag{7.30}$$

Comparing Equations (7.18) and (7.30), the size of the system is reduced from $m \times m$ to $n \times n$ in addition to the model order reduction techniques performed in the previous KLD procedure.

Grouping Equation (7.30) and the second of Equation (7.9), the low-order model or macromodel is obtained in terms of ODEs for the idealised complex MEMS device of Figure 7.1

$$\begin{bmatrix} C^T MC & 0 \\ 0 & H_2 \end{bmatrix}\begin{Bmatrix} \ddot{q} \\ \dot{a}^p \end{Bmatrix} + \begin{bmatrix} C^T KC & 0 \\ 0 & S_2 \end{bmatrix}\begin{Bmatrix} q \\ a^p \end{Bmatrix} + \begin{Bmatrix} C^T f \\ c_2 \end{Bmatrix} = 0 \tag{7.31}$$

Sovling for $q$ and $a^p$, the complete structural system dynamic response is obtained. Making use of Equations (7.19) and (7.21), the component dynamic responses, expressed in Equations (7.5)-(7.7) are then determined.

### 7.1.4 NUMERICAL RESULTS AND DISCUSSION

In order to validate the present macromodel generation method for structurally complex MEMS device dynamic simulation, a simulation of the MEMS device as shown in Figure 7.1 is carried out. The material properties and geometric dimensions for the microbeams are listed in Table 7.1.

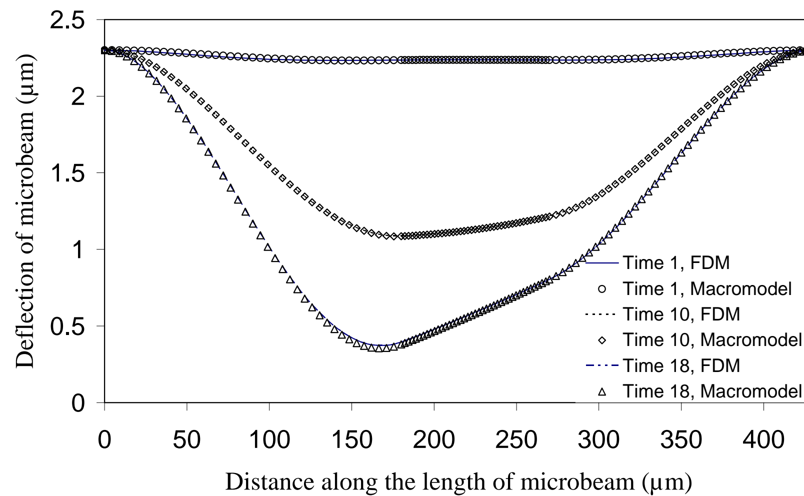


Figure 7.5 Comparison of the pull-in dynamics for an input step voltage of $30\,\mathrm{V}$.

Figure 7.5 shows a comparison of the deflection response of the microbeam at different time instants of 1, 10 and 18 $\mu$s between the macromodel approximation and the full FDM simulation of the original nonlinear PDEs (7.1)-(7.3) when the microbeam is subjected to an input step voltage of $30\,\mathrm{V}$. Figure 7.6 shows a comparison of the deflection response when the microbeam is subjected to an input step voltage of $50\,\mathrm{V}$. The KLMs for each component are generated for deflection and back pressure based on a finite difference code for an input step voltage of $25\,\mathrm{V}$, which is beyond the minimum pull-in voltage of $13.6\,\mathrm{V}$. The number of 25 snapshots, which is able to capture sufficient accuracy in KLMs and KLVs generation based on

numerical experiments, are taken at a fixed time interval from the moment when input step voltage is applied until the pull-in occurs.

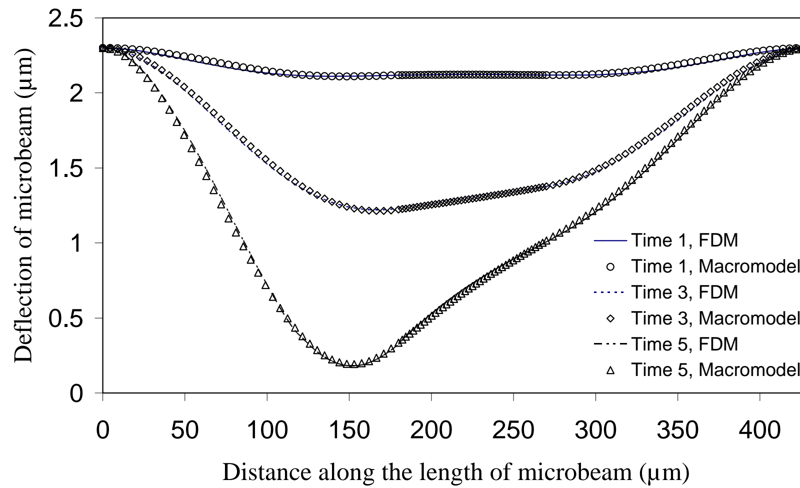


Figure 7.6 Comparison of the pull-in dynamics for an input step voltage of 50 V .

Four deflection KLMs for microbeams 1 and 3 ($I_1 = I_3 = 4$ in Equations (7.5) and (7.7)) and three deflection KLMs for microbeam 2 ($I_2 = 3$ in Equation (7.6), thus $m = I_1 + I_2 + I_3 = 11$ in Equation (7.21)) as well as three back pressure KLMs for microbeam 2 ($J_2 = 3$ in Equation (7.6)) are used. Numerical results show that $m = 11$ could deliver sufficient accuracy for macromodel simulation and it is also the minimum number of the total deflection KLMs for simulation since there are eight constraint equations needed to be satisfied. At least one independent component generalized coordinate corresponding to deflection KLM from each component is required in Equations (7.19), (7.21) and (7.22)-(7.29). Table 7.2 indicates that each four ($I_1 = I_3 = 4$) deflection KLMs for microbeams 1 and 3, and 3 ($I_2 = 3$) deflection KLMs for microbeam 2 can capture almost 100% of the system characteristics or energy. Based on numerical experiments and previous expirences which have been described and explained in Chapters 3, if the accumulative normalized KLVs can

capture 99.99% of the system energy (Equation (3.64)), then the low order models which are generated using these KLMs will represent the original system almost exactly. It is shown in Table 7.3 that it needs at lease three back pressure KLMs to capture this 99.99% energy level in the back pressure simulation. Figure 7.7 shows the error between the macromodel and FDM simulations for the midponit of microbeam 2, where the error is defined as

$$\text{error} = \frac{w_{2,\text{MM}}(x_c, t) - w_{2,\text{FDM}}(x_c, t)}{w_0} \times 100\% \tag{7.32}$$

here $w_{2,\text{MM}}$ denotes the midpoint deflection of the microbeam 2 from the macromodel, and $w_{2,\text{FDM}}$ denotes the finite difference solution of the original nonlinear PDEs (7.1)-(7.3). It is noted that the error is very small ($\leq 0.3\%$) when $I_1 = I_3 = 4$, $I_2 = 3$ and $J_2 = 3$. Figure 7.6 also indicates that flexibility of the macromodel to simulate an input step voltage of $50\,\text{V}$ which is far away from the voltage of $25\,\text{V}$ used to generate the KLMs and the accuray of macromodel simulation with respect to FDM is better than $0.8\%$ as shown in Figure 7.7.

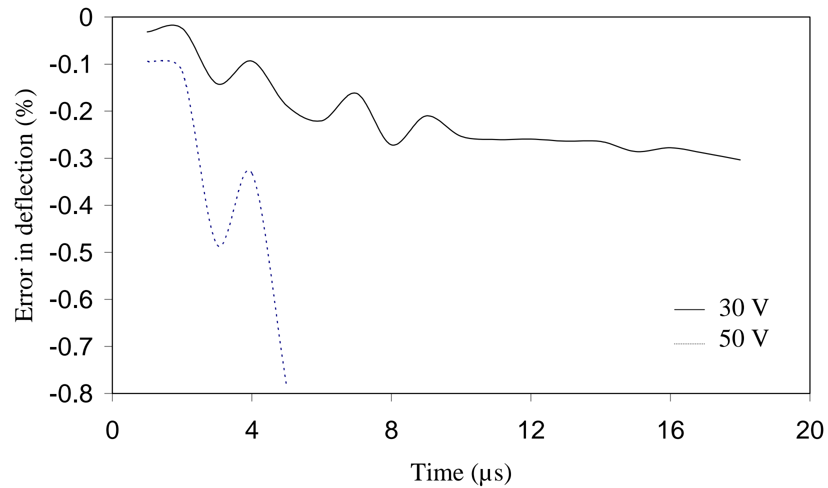


Figure 7.7 Error in midpoint deflection of microbeam 2 from macromodel simulations with respect to FDM results for input step voltages of $30\,\text{V}$ and $50\,\text{V}$.

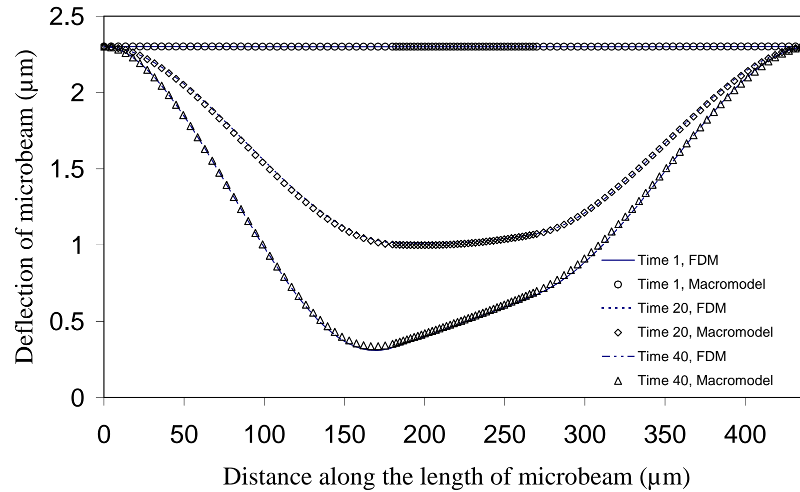


Figure 7.8 Comparison of pull-in dynamics for an input sinusoidal voltage of $30\,\mathrm{V}$ at a frequency of $20\,\mathrm{kHz}$.

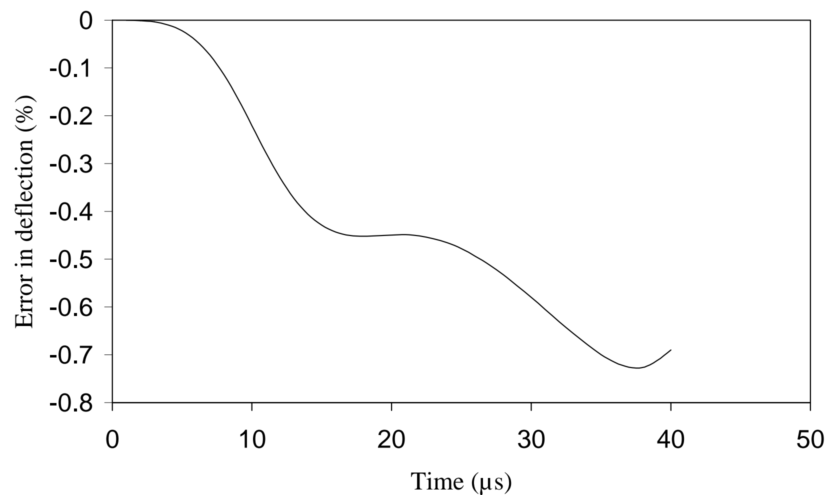


Figure 7.9 Error in midpoint deflection of microbeam 2 from macromodel simulation with respect to FDM results for an input sinusoidal voltage of $30\,\mathrm{V}$ at a frequency of $20\,\mathrm{kHz}$.

It is noted that KLD has additional distinctive advantage. In most cases, the KLMs obtained from KLD for a set of system parameters and inputs can be used to represent of the system whose parameters and inputs are slightly different from the original system without regenerating the KLMs. This is important because a primary motivation for the development of macromodel techniques for MEMS devices is that a

single macromodel maybe used to run many simulations without having to reconstruct KLMs should some parameters or inputs change in the system design and optimization stages. A few numerical experiment studies have validated this advantage in the application of KLD for low-order models for the mechanical structural systems (Azeez and Vakakis, 2001). To test this in the present study, the same macromodel described above, which is generated using the KLMs from an input step voltage of $25\,\text{V}$ applied on the complex MEMS device with geometric dimensions and mechanical properties listed in Table 7.1, is used to simulate the system responses to an input sinusoidal voltage with a magnitude of $30\,\text{V}$ at a frequency of 20 kHz. The length of microbeam 3 is also modified to $L_3 = 170\ \mu\text{m}$ from the original length of $L_3 = 160\ \mu\text{m}$. The results plotted in Figure 7.8 shows that, at different time instants of 1, 20 and 40 $\mu\text{s}$, the macromodel simulation employing $I_1 = I_3 = 4$, $I_2 = 3$ and $J_2 = 3$ can capture the system dynamics accurately and the error shown in Figure 7.9 for midpoint deflection of the microbeam 2 is very small $(\leq 0.73\%)$ compared with FDM solutions. The results demonstrate that the macromodel is flexible to simulate the system response well with different input voltage spectra and some parameter modifications without regenerating the KLMs. In order to understand this macromdel flexibility characteristics qualitatively, the KLMs for the system with this input sinusoidal voltage and the modified length of microbeam 3 are extracted independently following KLD procedure, and compared with the KLMs extracted for the original system with input step voltage and original length of microbeam 3.

The comparisons of the first and the second deflection KLMs for each microbeam plotted in Figure 7.10 and Figure 7.11 show that the mode shape difference between these two different input voltages and lengths of microbeam are neglegible.

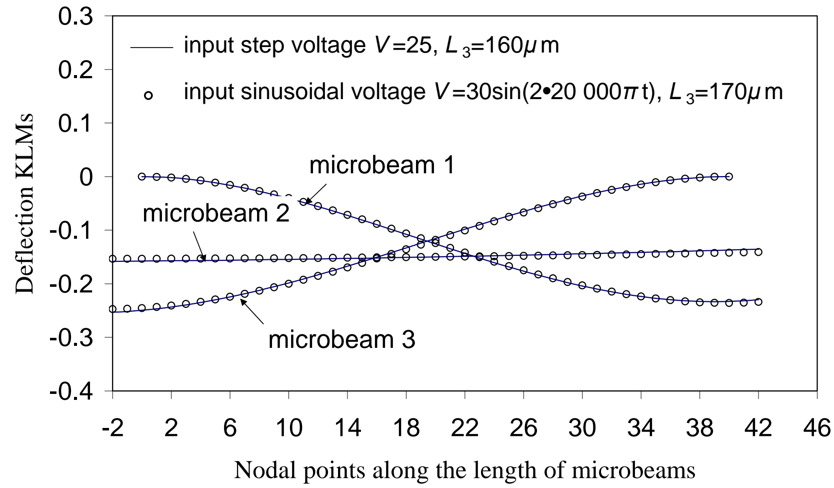


Figure 7.10 Comparison of the first KLM for deflection of microbeams with different input voltage spectrum and length of microbeam 3.

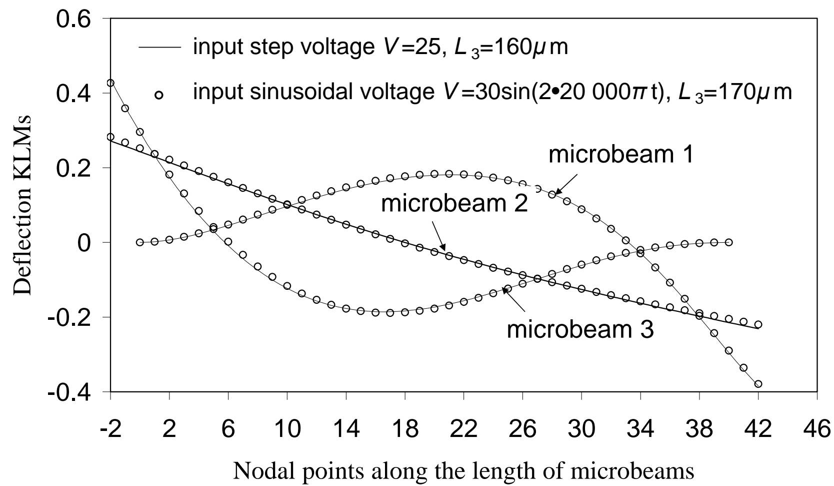


Figure 7.11 Comparison of the second KLM for deflection of microbeams with different input voltage spectrum and length of microbeam 3.

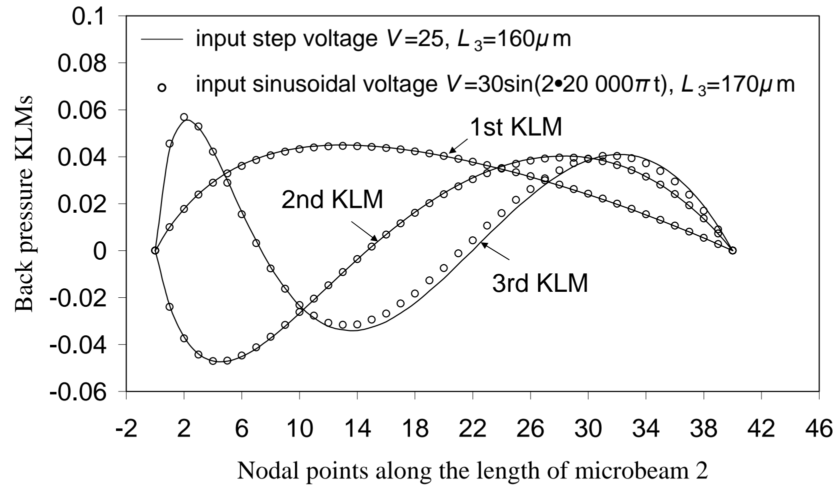


Figure 7.12 Comparison of first three KLMs for back pressure of microbeam 2 with different input voltage spectrum and length of microbeam 3.

Figure 7.12 shows the comparison for the first three back pressure KLMs for microbeam 2 between these two system configurations. It is shown in Figure 7.12 that the first two back pressure KLMs are almost identical while there is some noticeable difference betweem the third KLM, but this difference does not cause significant accuracy drop in the macromodel simulation as indicated in Figure 7.8 and Figure 7.9 due to the system energy lever captured by the third KLM (0.03% as indicated in Table 7.3) is much lower that those captured by the first (96.77%) KLM and the second KLM (3.2%) which are obviously the dominant modes. Again, the above observations are based on the qualitatively numerical experimental results, the accuracy limits on quantitatively measure or scaling of parameter changes, over the parameter space in which the KLMs can still be used, needs to be studied further. For the present system as shown in Figure 7.1, one issue is also raised on what are the advantages to separate the microbeams into each individual component and obtain the KLMs and KLVs locally for each component compared with treating the original system as a single beam structure and obtain its KLMs and KLVs globally. Except for the above-mentioned advantages, that KLMs for each component can be treated as component

modes in the CMS procedure for complex structure order reduction (Equation (7.21)), numerically. If the problems encountered are with large data sets consisting of irregularly distributed points with high dimensions, the local methods for such data sets are more appealing to achieve improved order reduction when compared with global methods. Moreover, quite often the local modelling can be computed in parallel so as to enhance the computation efficiency. Here, the proceeding process of extraction KLMs for each component is similar to address local approaches for representing large data set. This approach is referred as Local Karhunen-Loève Decomposition in Kirby (2001). The local approach to extract the KLMs and KLVs for each component is also appealing for the system with complex geometry such as a micro-mirror that is designed as a square plate with four clamped-guided parallel microbeams along each side of the plate (Min and Kim, 1999) since it is computationally inefficient to treat this system as a single structure to obtain the global KLMs and KLVs for model order reduction. As an example of comparison, Figure 7.13 plots the system pull-in dynamics results for an input step voltage of $30\,\text{V}$ simulated by the macromodel using two global deflection KLMs, and three global back pressure KLMs obtained by treating the system as single structure for an input step voltage of $25\,\text{V}$ with material properties and geometric dimensions of microbeam listed in Table 7.1. Both numbers of KLMs used in macromodel capture more than 99.99% of the system energy. The error between the macromodel and FDM simulations for the midpoint of microbeam 2 plotted in Figure 7.14 shows that its simulation accuracy (max error at 0.65%) is lower than the results (max error at 0.3% as shown in Figure 7.7) simulated by macromodel using the local KLMs by treating the system as separate components.

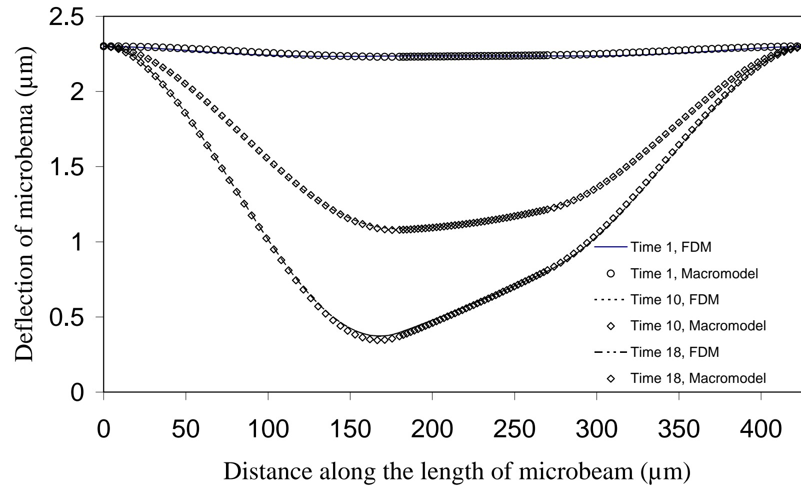


Figure 7.13 Comparison of the pull-in dynamics for an input step voltage of $30\,\mathrm{V}$ when treating the system as a single structure.

The computation efficiency comparison run on Silicon Graphics Origin 2000 indicates that it takes 106.82 min to generate global KLMs and KLVs for an input step voltage of $25\,\mathrm{V}$ and 3.57 min for macromodel simulation of system pull-in dynamics for an input step voltage of $30\,\mathrm{V}$ by treating the system as a single structure. However, it takes only 77.65 min to generate local KLMs and KLVs and 3.65 min for macromodel simulation for the same system by treating the system as an assemblage of separate components. Although the computation efficiency for both macromodel simulations is almost the same, the results demonstrate that it is more efficient to generate the KLMs and KLVs locally for each component than globally for the whole system if the whole system is treated as a single structure.

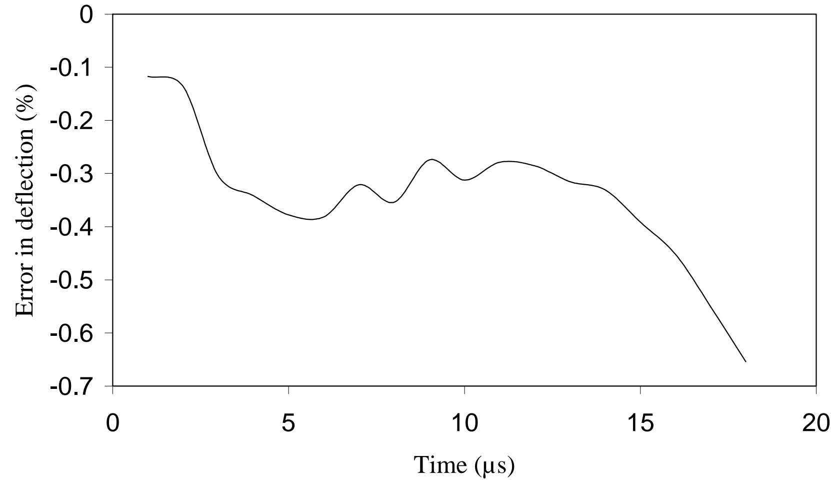


Figure 7.14 Error in midpoint deflection of microbeam 2 from macromodel simulation with respect to FDM results for an input step voltage of 30 V when treating the system as a single structure.

## 7.2 MACROMODEL FOR A MICRO-MIRROR DEVICE

### 7.2.1 MODEL DESCRIPTION

A structural complex structure designed as micro-mirror for the optical phase modulation (Min and Kim, 1999) or lightwave switching is shown in Figure 7.15. It consists of a square micro-mirror plate and four suspension microbeams. This structure has also been applied as micro-accelerometer (Gianchandani and Crary, 1998) and voltage-controlled oscillator for frequency tuning (Young and Boser, 1997) due to its excellent high frequency quality and potential large bandwidth. Using the techniques developed above, macromodel for dynamic simulation of this MEMS device is presented in this section. The device is modelled as a rigid mirror plate with four clamped-guided parallel microbeams along each side of the plate. The input voltages are applied between each component and the substrate, respectively, and the

squeezed gas-film damping effect is considered between the mirror and the substrate but neglected on four relatively narrow microbeams. Similar to the preceding section, the microbeam is modelled by Euler beam, and the squeezed gas-film damping is governed by nonlinear Reynold's equation. Assuming that the rigid mirror plate undergoes only three motions, these are, the translational movement in the vertical $Z$ direction and the rotations about the global axes $X$ and $Y$ which are fixed and coincide with the principal axes centred at the centre of mass of the rigid plate $C$ at the initial state.

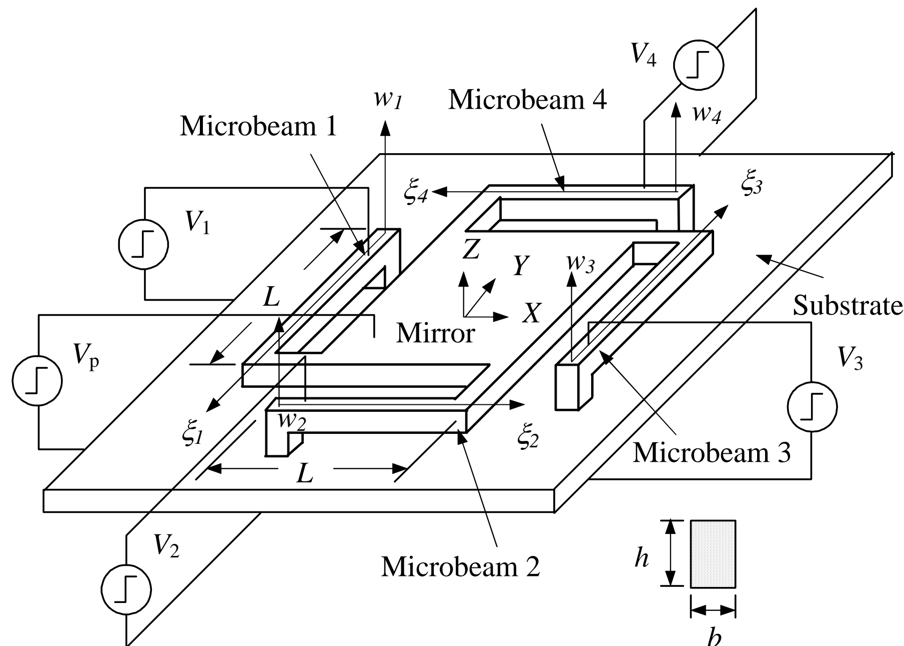


Figure 7.15 A micro-mirror structure.

Figure 7.16 illustrates the coordinate for mirror plate rotations around $X$ and $Y$ axes. In this case of space-fixed rotations, the new coordinate measured in $x_1 y_1 z_1$ after the rotation around $X$ axis by $\theta_X$ is given as (Ginsberg, 1995)

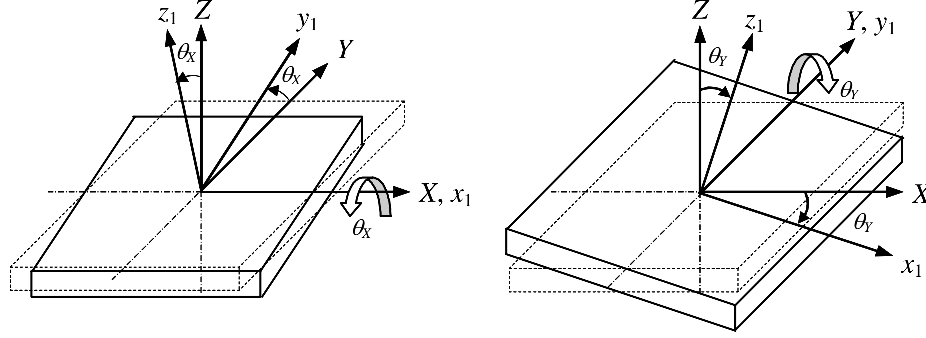


Figure 7.16 Mirror plate rotations.

$$\begin{Bmatrix} x_1 \\ y_1 \\ z_1 \end{Bmatrix} = R_X \begin{Bmatrix} X \\ Y \\ Z \end{Bmatrix}, \quad R_X = \begin{bmatrix} 1 & 0 & 0 \\ 0 & \cos\theta_X & \sin\theta_X \\ 0 & -\sin\theta_X & \cos\theta_X \end{bmatrix} \tag{7.33}$$

where $R_X$ is the transfer matrix. Similarly, the new coordinate after the rotation around $Y$ axis by $\theta_Y$ is expressed as

$$\begin{Bmatrix} x_1 \\ y_1 \\ z_1 \end{Bmatrix} = R_Y \begin{Bmatrix} X \\ Y \\ Z \end{Bmatrix}, \quad R_Y = \begin{bmatrix} \cos\theta_Y & 0 & -\sin\theta_Y \\ 0 & 1 & 0 \\ \sin\theta_Y & 0 & \cos\theta_Y \end{bmatrix} \tag{7.34}$$

If the mirror undergoes a sequence of rotations of $\theta_X$ followed by $\theta_Y$, the transformation from $XYZ$ to the final $xyz$ components is obtained as

$$\begin{Bmatrix} x \\ y \\ z \end{Bmatrix} = R \begin{Bmatrix} X \\ Y \\ Z \end{Bmatrix}, \quad R = R_X R_Y = \begin{bmatrix} \cos\theta_Y & 0 & -\sin\theta_Y \\ \sin\theta_X \sin\theta_Y & \cos\theta_X & \sin\theta_X \cos\theta_Y \\ \cos\theta_X \sin\theta_Y & -\sin\theta_X & \cos\theta_X \cos\theta_Y \end{bmatrix} \tag{7.35}$$

Similarly, a sequence of rotations of $\theta_Y$ followed by $\theta_X$ would lead to

$$\begin{Bmatrix} x \\ y \\ z \end{Bmatrix} = R \begin{Bmatrix} X \\ Y \\ Z \end{Bmatrix}, \quad R = R_Y R_X = \begin{bmatrix} \cos\theta_Y & \sin\theta_Y \sin\theta_X & -\sin\theta_Y \cos\theta_X \\ 0 & \cos\theta_X & \sin\theta_X \\ \sin\theta_Y & -\cos\theta_Y \sin\theta_X & \cos\theta_Y \cos\theta_X \end{bmatrix} \tag{7.36}$$

For simplicity without losing generality, consideration of the small magnitude of the angles of rotation in this structure leads to the following approximations

$$\cos\theta_x \approx 1,\ \sin\theta_x \approx \theta_x \ \text{ and } \ \cos\theta_y \approx 1,\ \sin\theta_y \approx \theta_y \tag{7.37}$$

Neglecting the higher order terms, Equation (7.35) is simplified as

$$\begin{Bmatrix} x \\ y \\ z \end{Bmatrix} = R \begin{Bmatrix} X \\ Y \\ Z \end{Bmatrix}, \ R = R_X R_Y = \begin{bmatrix} 1 & 0 & -\theta_Y \\ 0 & 1 & \theta_X \\ \theta_Y & -\theta_X & 1 \end{bmatrix} \tag{7.38}$$

Similarly, Equation (7.36) becomes

$$\begin{Bmatrix} x \\ y \\ z \end{Bmatrix} = R \begin{Bmatrix} X \\ Y \\ Z \end{Bmatrix}, \ R = R_Y R_X = \begin{bmatrix} 1 & 0 & -\theta_Y \\ 0 & 1 & \theta_X \\ \theta_Y & -\theta_X & 1 \end{bmatrix} \tag{7.39}$$

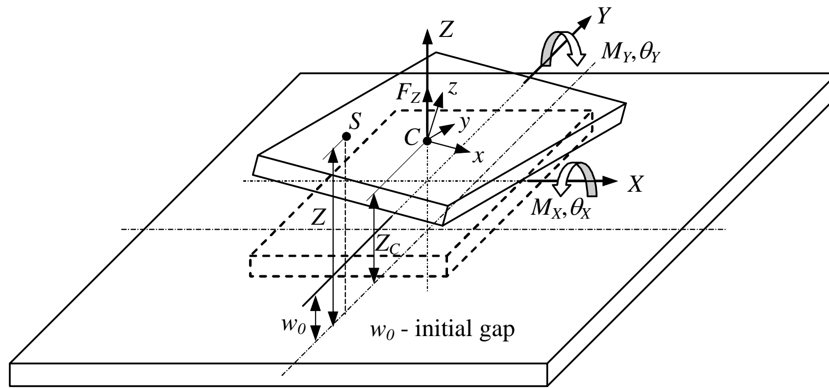


Figure 7.17 Mirror plate position after vertical translational movement and two rotations.

Comparing Equation (7.38) with (7.39), it is noted that the transfer matrix $R$ for both sequences of rotations are the same. In order words, the final position of the mirror plate after rotations does not depend on the sequence of rotations. The distance between a point $S$ on the mirror plate and the substrate as shown in Figure 7.17 is approximated as

$$Z = Z_C - x\theta_Y + y\theta_X \tag{7.40}$$

where $Z_C$ is the tanslational movement of the center of mass of the mirror plate which is $w_0$ initially.

The governing equations for the four microbeams and plate are expressed as follows

i) for microbeams

$$EI_i \frac{\partial^4 w_i}{\partial \xi_i^4} - T_i \frac{\partial^2 w_i}{\partial \xi_i^2} = -\frac{\varepsilon_0 b_i V_i^2}{2 w_i^2} - \rho_i \frac{\partial^2 w_i}{\partial t^2}, \qquad \left(0 \le \xi_i \le L,\ i = 1, 2, 3, 4\right) \tag{7.41}$$

where $E$ is Young's modulus, $I_i = b_i h_i^3 / 12$ is the second moment of area where $b_i$ is the width and $h_i$ is the thickness of the microbeam $i$, $\rho_i$ is the density, $\xi_i$ is the local variable along the length of microbeam as shown in Figure 7.15, $w_i(\xi_i, t)$ is the height of the microbeam above the substrate, $V_i$ is the applied voltage between microbeam $i$ and substrate, $\varepsilon_0$ is the permittivity of free space and $T_i/(b_i h_i)$ is the sum of residual stress $t_{r,i}$ and the bending induced stress $t_{b,i}$ due to large deflection which can be expressed as

$$\frac{T_i}{b_i h_i} = t_{r,i} + t_{b,i} = t_{r,i} + E\,\Delta L / L \approx t_{r,i} + \frac{E}{2L}\int_L \left(\frac{dw_i}{d\xi_i}\right)^2 d\xi_i\,, \quad \left(i = 1, 2, 3, 4\right) \tag{7.42}$$

where $L$ is the length of the microbeam.

ii) for micro-mirror plate

$$\sum F_Z = m\ddot{Z}_C \tag{7.43}$$

$$\sum M_X = I_{XX}\ddot{\theta}_X \tag{7.44}$$

$$\sum M_Y = I_{YY}\ddot{\theta}_Y \tag{7.45}$$

$$\nabla \cdot (Z^3 p \nabla p) = \frac{12\mu}{1 + 6K_n}\frac{\partial (pZ)}{\partial t} \tag{7.46}$$

where $\sum F_Z$ denotes the sum of external forces acting on the rigid mirror plate in $Z$ direction, $Z_C$ is the tanslational movement of the center of mass of the plate, $m$ is the mass of the plate, $\sum M_X$ and $\sum M_Y$ represent the sum of the moments of the external

forces, $I_{XX}$ and $I_{YY}$ are the second moment of area, and $\theta_X$ and $\theta_Y$ are the angles of rotation about the axes $X$ and $Y$ whose original is the centre of mass of the plate, $\mu$ is the air viscosity, $Z(x, y, t)$ is the height of the mirror plate above the substrate expressed by Equation (7.40), $p(x, y, t)$ is the back pressure force acting on plate due to the squeezed gas-film damping in which an isothermal process is assumed, $p_a$ is the ambient pressure.

The electrostatic and back pressure forces and their moments exerted on the plate can be expressed in detail as follows

$$F_Z^E = -\frac{\varepsilon_0 V_p^{\ 2}}{2}\int_A \frac{1}{(Z_C - x\theta_Y + y\theta_X)^2} dxdy \tag{7.47}$$

$$M_X^E = \frac{\varepsilon_0 V_p^{\ 2}}{2}\int_A (-y)\frac{1}{(Z_C - x\theta_Y + y\theta_X)^2} dxdy \tag{7.48}$$

$$M_Y^E = \frac{\varepsilon_0 V_p^{\ 2}}{2}\int_A x\frac{1}{(Z_C - x\theta_Y + y\theta_X)^2} dxdy \tag{7.49}$$

and

$$F_Z^P = \int_A (p - p_a) dxdy \tag{7.50}$$

$$M_X^P = \int_A y(p - p_a) dxdy \tag{7.51}$$

$$M_Y^P = \int_A (-x)(p - p_a) dxdy \tag{7.52}$$

$V_p$ is the applied voltage between mirror plate and substrate. Substituting Equations (7.47)-(7.52) into Equations (7.43)-(7.46), the equations of motion for the mirror plate can be rewritten as

$$m\ddot{Z}_C - F_Z^p - F_Z^E + \sum_{i=1}^{4} Q_i = 0 \tag{7.53}$$

$$I_{XX}\ddot{\theta}_X - M_X^p - M_X^E - \frac{L}{2}(Q_1 + Q_2 - Q_3 - Q_4) - M_3 + M_1 = 0 \tag{7.54}$$

$$I_{YY}\ddot{\theta}_Y - M_Y^p - M_Y^E - \frac{L}{2}(Q_2 + Q_3 - Q_1 - Q_4) - M_4 + M_2 = 0 \tag{7.55}$$

where

$$\overline{Z}_C = Z_C - w_0 \tag{7.56}$$

and $Q_i$ and $M_i$ are the mechanical restoring shear forces and moments exerted by the microbeams on the mirror plate.

### 7.2.2 KARHUNEN-LOÈVE MODES FOR COMPONENTS

FDM is used to simulate the system dynamic responses described by Equations (7.41) and (7.43)-(7.46), when the system is subjected to an ensemble of applied voltages. It generates the ensemble of 25 snapshots taken at fixed time step from the beginning till pull-in for KLD to extract the KLMs and KLVs for each component. The microbeams are considered to have clamped-guided ends with the following boundary conditions.

At $\xi_i = 0$

$$w_i = 0, \quad \frac{\partial w_i}{\partial \xi_i} = 0, \quad (i = 1, 2, 3, 4) \tag{7.57}$$

At $\xi_i = L$

$$\frac{\partial w_i}{\partial \xi_i} = 0, \quad -\frac{\partial}{\partial \xi_i}\left(EI_i \frac{\partial w_i^2}{\partial \xi_i^2}\right) + T_i \frac{\partial w_i}{\partial \xi_i} = Q_i, \quad -EI_i \frac{\partial w_i^2}{\partial \xi_i^2} = M_i, \quad (i = 1, 2, 3, 4). \tag{7.58}$$

The properties and geometric dimensions of the micro-mirror structure are listed in Table 7.4. Similarly, a mesh size of 40×1 for microbeams 1 to 4, and 40×40 for plate in the FDM simulations of the original non-linear PDEs (7.41) and (7.43)-(7.46) are able to generate sufficient accuracy. Following KLD procedure, the KLMs and the corresponding KLVs for each component are obtained.

Table 7.4 Properties and geometric dimensions of microbeams and mirror plate.

| Microbeam $i$ | Young's modulus $E$ (GPa) | Density $\rho_i/(b_i h_i)$ (kg/m$^3$) | Residual Stress $t_{r,i}$ (MPa) | Knudsen's Number $K_n = \lambda/Z_i$ |
|---|---|---|---|---|
| 1 | | | | |
| 2 | | | -4.03 | – |
| 3 | 149 | 2330 | | |
| 4 | | | | |
| Mirror plate | | | – | ≈0.021 |

| Microbeam $i$ | Initial gap $w_0$ ($\mu$m) | Thickness $h_i$ ($\mu$m) | Length $L$ ($\mu$m) | Width $b_i$ ($\mu$m) |
|---|---|---|---|---|
| 1 | | | | |
| 2 | | | | 5 |
| 3 | 3 | 3.7 | 173 | |
| 4 | | | | |
| Mirror plate | | | | 173 |

### 7.2.3 COMPONENT MODE SYNTHESIS AND MACROMODEL GENERATION

Once the KLMs for each component are obtained, the flexural deflection of the microbeams and the back pressure due to the squeezed gas-film damping effect can be represented as a linear combination of the KLMs as follows

$$w_i(\xi_i, t) - w_0 = \sum_{j=1}^{I_i} a_j^{w_i}(t)\phi_j^{w_i}(\xi_i), \quad (0 \le \xi_i \le L,\ i = 1, 2, 3, 4) \tag{7.59}$$

$$p(x, y, t) - p_a = \sum_{j=1}^{J} a_j^p(t)\phi_j^p(x, y), \quad (0 \le x, y \le L) \tag{7.60}$$

Here $w_0$ is the initial gap between the microbeams and the substrate, $\phi_j^{w_i}$ is the deflection KLMs for microbeams 1, 2, 3 and 4, respectively, $\phi_j^p$ is the back pressure

KLMs for mirror plate, $I_i$ is the number of deflection KLMs, and $J$ is the number of back pressure KLMs employed in the macromodel, $a_j^{w_i}$ and $a_j^p$ are the amplitudes of the KLMs and are also the component generalized coordinates in modal decomposition. Substituting Equations (7.59) and (7.60) into the governing equations (7.41) and (7.46) and applying the Galerkin procedure by using the above KLMs as the basis functions, the following ordinary differential equations are obtained in terms of the component generalized coordinates of $a_j^{w_i}$ and $a_j^p$;

$$M_i^w \ddot{a}^{w_i} + K_i^w a^{w_i} + f_i^w = 0, \quad (i = 1, 2, 3, 4) \tag{7.61}$$

$$H^p \dot{a}^p + S^p a^p + c^p = 0 \tag{7.62}$$

where $a^{w_i}$ and $a^p$ are the vectors whose elements $a_j^{w_1}$, $a_j^{w_2}$, $a_j^{w_3}$, $a_j^{w_4}$ and $a_j^p$ are to be determined. The elements in matrix $M_i^w$ can be obtained once the KLMs for each component are known, the elements in matrixes $K_i^w$, $H^p$ and $S^p$ and vectors $f_i^w$, $c^p$ are expressed as follows

$$M_{kl,i}^w = \int_L \rho_i \phi_k^{w_i} \phi_l^{w_i} d\xi_i, \quad (k, l = 1, 2, \ldots, I_i,\ i = 1, 2, 3, 4) \tag{7.63}$$

$$\begin{aligned} K_{kl,i}^w = EI_i \left( \frac{\partial^3 \phi_k^{w_i}}{\partial \xi_i^3} \phi_l^{w_i} \bigg|_{\xi_i = L} + \int_L \frac{\partial^2 \phi_k^{w_i}}{\partial \xi_i^2} \frac{\partial^2 \phi_l^{w_i}}{\partial \xi_i^2} d\xi_i \right) \\ + T_i \int_L \frac{\partial \phi_k^{w_i}}{\partial \xi_i} \frac{\partial \phi_l^{w_i}}{\partial \xi_i} d\xi_i, \quad (k, l = 1, 2, \ldots, I_i,\ i = 1, 2, 3, 4) \end{aligned} \tag{7.64}$$

$$f_{l,i}^w = \int_L \frac{\varepsilon_0 b_i V_i^2}{2 w_i^2} \phi_l^{w_i} d\xi_i, \quad (l = 1, 2, \ldots, I_i,\ i = 1, 2, 3, 4) \tag{7.65}$$

and

$$H_{kl}^p = \int_A \frac{12\mu}{1 + 6K_n} Z \phi_k^p \phi_l^p dxdy, \quad (k, l = 1, 2 \ldots, J) \tag{7.66}$$

$$S_{kl}^{p} = \int_A \left\{ Z^3 p \left( \frac{\partial \phi_k^p}{\partial x} \frac{\partial \phi_l^p}{\partial x} + \frac{\partial \phi_k^p}{\partial y} \frac{\partial \phi_l^p}{\partial y} \right) \right.$$

$$\left. + \frac{12\mu}{1+6K_n} \phi_k^p \phi_l^p \frac{\partial Z}{\partial t} \right\} dxdy, \quad (k, l = 1, 2\ldots, J) \tag{7.67}$$

$$c_l^p = \int_A \frac{12\mu}{1+6K_n} p_a \phi_l^p \frac{\partial Z}{\partial t} dxdy, \quad (l = 1, 2\ldots, J) \tag{7.68}$$

Substituting Equations (7.59) and (7.60) into Equations (7.53)-(7.55), the equations of motion for the mirror plate can be rewritten as

$$M^{w_p} \ddot{a}^{w_p} + f^{w_p} = 0 \tag{7.69}$$

where $a^{w_p}$ is the vector for the unknown tanslational movement and angles of rotation of the mirror plate

$$a^{w_p} = \begin{Bmatrix} \bar{Z}_C \\ \theta_X \\ \theta_Y \end{Bmatrix} \tag{7.70}$$

$f^{w_p}$ is the vector of generalized forces, and matrix $M^{w_p}$ is given as

$$M^{w_p} = \begin{bmatrix} m & 0 & 0 \\ 0 & I_{XX} & 0 \\ 0 & 0 & I_{YY} \end{bmatrix} \tag{7.71}$$

Grouping Equations (7.61) and (7.69) gives the equations of motion for the group of components which are not connected together

$$M \ddot{a} + K a + f = 0 \tag{7.72}$$

where the generalized coordinates and the generalized forces for the components are grouped as

$$\underset{m\times 1}{a} = \begin{Bmatrix} a^{w_1} \\ a^{w_2} \\ a^{w_3} \\ a^{w_4} \\ a^{w_p} \end{Bmatrix}, \quad \underset{m\times 1}{f} = \begin{Bmatrix} f_1^{w} \\ f_2^{w} \\ f_3^{w} \\ f_4^{w} \\ f^{w_p} \end{Bmatrix}, \quad m = \sum_{i=1}^{4} I_i + 3 \tag{7.73}$$

The matrices are given as follows

$$M = \begin{bmatrix} M_1^w & 0 & 0 & 0 & 0 \\ 0 & M_2^w & 0 & 0 & 0 \\ 0 & 0 & M_3^w & 0 & 0 \\ 0 & 0 & 0 & M_4^w & 0 \\ 0 & 0 & 0 & 0 & M^{w_p} \end{bmatrix}, \quad K = \begin{bmatrix} K_1^w & 0 & 0 & 0 & 0 \\ 0 & K_2^w & 0 & 0 & 0 \\ 0 & 0 & K_3^w & 0 & 0 \\ 0 & 0 & 0 & K_4^w & 0 \\ 0 & 0 & 0 & 0 & 0 \end{bmatrix} \tag{7.74}$$

For the system shown in Figure 7.15, the deflection continuity condition at the interface of each microbeam and the mirror plate forms four constraint equations as follows

$$\sum_{j=1}^{I_1} a_j^{w_1}(t)\phi_j^{w_1}(L) = \overline{Z}_C + \frac{L}{2}\theta_Y - \frac{L}{2}\theta_X, \quad \text{at interface of microbeam 1 and plate} \tag{7.75}$$

$$\sum_{j=1}^{I_2} a_j^{w_2}(t)\phi_j^{w_2}(L) = \overline{Z}_C - \frac{L}{2}\theta_Y - \frac{L}{2}\theta_X, \quad \text{at interface of microbeam 2 and plate} \tag{7.76}$$

$$\sum_{j=1}^{I_3} a_j^{w_3}(t)\phi_j^{w_3}(L) = \overline{Z}_C - \frac{L}{2}\theta_Y + \frac{L}{2}\theta_X, \quad \text{at interface of microbeam 3 and plate} \tag{7.77}$$

$$\sum_{j=1}^{I_4} a_j^{w_4}(t)\phi_j^{w_4}(L) = \overline{Z}_C + \frac{L}{2}\theta_Y + \frac{L}{2}\theta_X, \quad \text{at interface of microbeam 4 and plate} \tag{7.78}$$

Following the procedure of the classical component mode synthesis, the transfromation matrix $C$ with dimensions of $m \times n$ is obtained. Here $m$ is the number of elements in vector $a$ and $n = m - 4$ is the number of independent generalized coordinates in vector $q$. Substituting for $a$ in terms of $q$ through transformation matrix and premultiplying by the transpose $C^T$, Equation (7.72) is rewritten as

$$C^T MC\ddot{q} + C^T KCq + C^T f = 0 \tag{7.79}$$

Grouping Equation (7.79) and Equation (7.62), the macromodel is formed in terms of ODEs

$$\begin{bmatrix} C^T MC & 0 \\ 0 & H^p \end{bmatrix} \begin{Bmatrix} \ddot{q} \\ \dot{a}^p \end{Bmatrix} + \begin{bmatrix} C^T KC & 0 \\ 0 & S^p \end{bmatrix} \begin{Bmatrix} q \\ a^p \end{Bmatrix} + \begin{Bmatrix} C^T f \\ c^p \end{Bmatrix} = 0 \tag{7.80}$$

After solving for $q$ and $a^p$, the complete structural system dynamic response is obtained. The component dynamic responses expressed in Equations (7.59) and (7.60) can also be determined by making use of Equations (7.21) and (7.73).

### 7.2.4 NUMERICAL RESULTS AND DISCUSSION

The following two combinations of applied voltages resulting in two types of structural dynamical responses are considered.

i) Applied equal voltage between each microbeam and substrate

In this case, the input voltage applied on each microbeam and the substrate is equal, i.e.

$$V_1 = V_2 = V_3 = V_4 \tag{7.81}$$

In this case the mirror undergoes vertical translational movement only. The device is used as an optical phase modulator in Min and Kim (1999) under such combination of input voltages. Figure 7.18 plots the first three normalized deflection KLMs for microbeams 1-4 when the microbeams and mirror are subjected to an input step voltage of $60\,\text{V}$. Figure 7.19-Figure 7.21 show the first three normalized back pressure KLMs for mirror plate. Table 7.5 and Table 7.6 list the normalized KLVs and accumulative normalized KLVs with respect to the number of deflection and back pressure KLMs for each component.

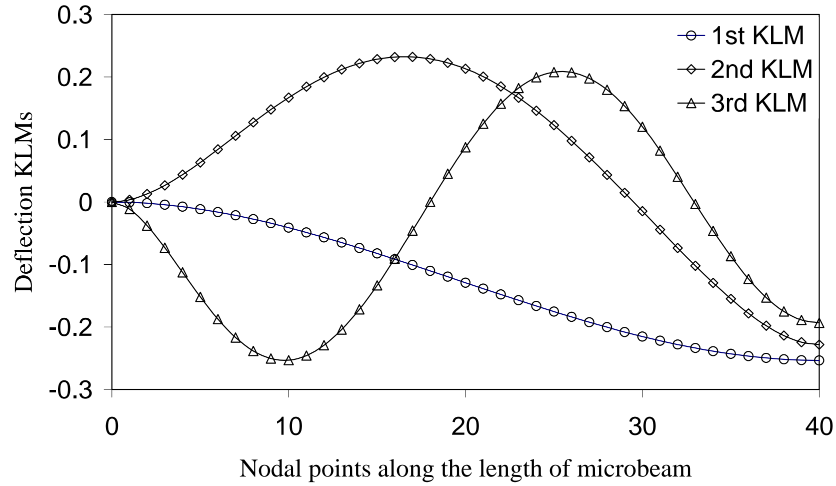


Figure 7.18 First three KLMs for deflection of microbeams 1, 2, 3 and 4.

Table 7.5 Normalized accumulative KLVs corresponding to the number of deflection KLMs.

| Number of KLMs | Microbeams 1, 2, 3 and 4 | |
|---|---|---|
| | Normalized KLVs $\bar{\lambda}_i = \lambda_i \Big/ \sum_{i=1}^{N} \lambda_i$ | Accumulative normalized KLVs $S_{N_i} = \sum_{i=1}^{N_i} \bar{\lambda}_i$ |
| 1 | $\bar{\lambda}_1 = 0.9999977296$ | $S_1 = 0.9999977296$ |
| 2 | $\bar{\lambda}_2 = 0.0000021273$ | $S_2 = 0.9999998569$ |
| 3 | $\bar{\lambda}_3 = 0.0000001379$ | $S_3 = 0.9999999948$ |
| 4 | $\bar{\lambda}_4 = 0.0000000052$ | $S_4 = 1.0000000000$ |

Table 7.6 Normalized accumulative KLVs corresponding to the number of back pressure KLMs.

| Number of KLMs | Mirror plate | |
|---|---|---|
| | Normalized KLVs $\bar{\lambda}_i = \lambda_i \Big/ \sum_{i=1}^{N} \lambda_i$ | Accumulative normalized KLVs $S_{N_i} = \sum_{i=1}^{N_i} \bar{\lambda}_i$ |
| 1 | $\bar{\lambda}_1 = 0.9984900488$ | $S_1 = 0.9984900488$ |
| 2 | $\bar{\lambda}_2 = 0.0015042097$ | $S_2 = 0.9999942585$ |
| 3 | $\bar{\lambda}_3 = 0.0000056977$ | $S_3 = 0.9999999562$ |
| 4 | $\bar{\lambda}_4 = 0.0000000257$ | $S_4 = 0.9999999819$ |

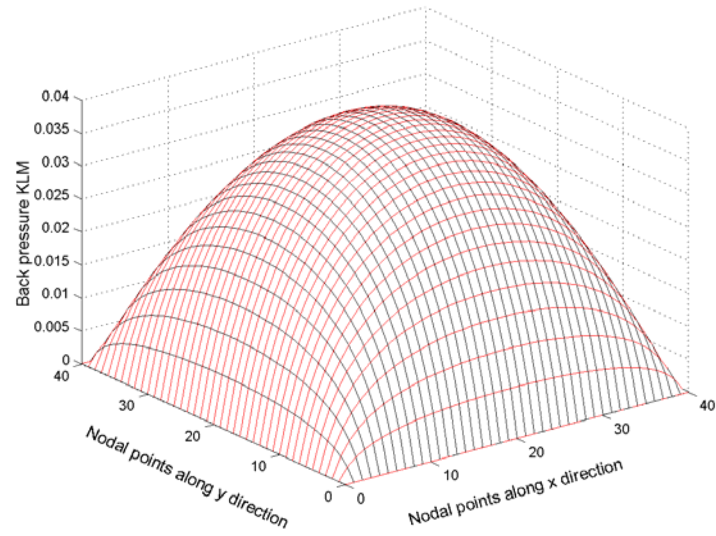


Figure 7.19 The first KLM for back pressure of mirror plate.

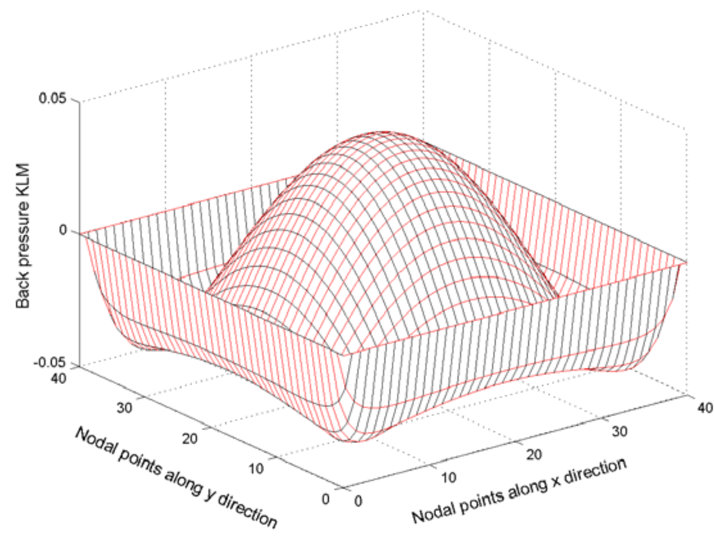


Figure 7.20 The second KLM for back pressure of mirror plate.

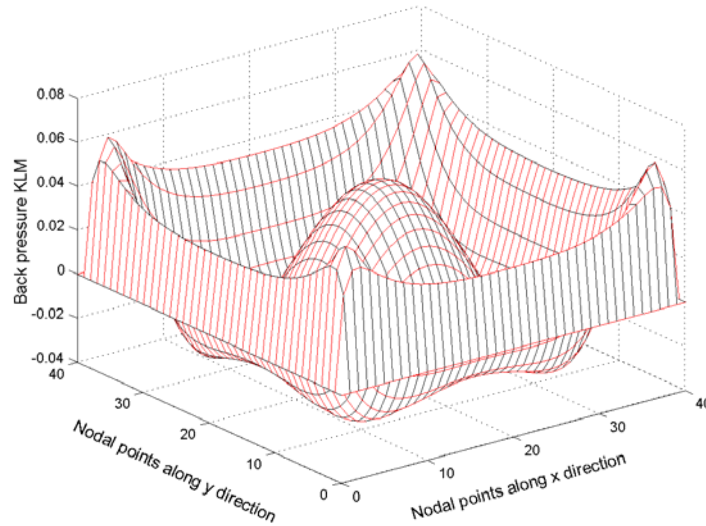


Figure 7.21 The third KLM for back pressure of mirror plate.

Figure 7.22 illustrates the comparison of the deflection response of the microbeam at 1, 15 and 34 $\mu$s (pull-in) between the macromodel approximation and the full FDM simulations of the original nonlinear PDEs (7.41)-(7.46) when the microbeams and mirror plate are subjected to an input step voltage of $50\,\mathrm{V}$. Two deflection KLMs for each microbeam ($I_1 = I_2 = I_3 = I_4 = 2$ in Equations (7.59) and two back pressure KLMs for mirror plate ($J = 2$ in Equation (7.60)) are used in the macromodel simulation. Similarly, numerical experiment results indicate that $m = 2 \times 4 + 3 = 11$, where 3 refers to the number of one translation mode and two angles of rotation modes of the mirror, can deliver sufficient accuracy for macromodel simulation and it is also the minimum number of the total deflection KLMs for simulation since there are four constraint equations to be satisfied and at least one independent component generalized coordinate corresponding to deflection KLM from each component is required in Equations (7.21), (7.73) and (7.75)-(7.78).

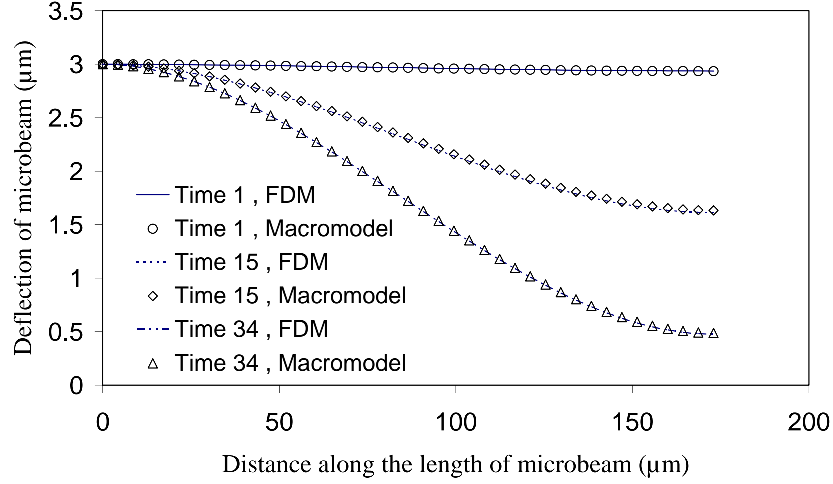


Figure 7.22 Comparison of pull-in dynamics of microbeams 1-4 for input step voltages of $V_1 = V_2 = V_3 = V_4 = V_p = 50$ V .

Table 7.5 indicates that two deflection KLMs for microbeams 1-4 can capture more than 99.99% of the system characteristics or energy. It is shown in Table 7.6 that two back pressure KLMs can also capture up to 99.99% energy level in the back pressure simulation. Figure 7.23 shows the error between the macromodel and FDM simulations for the end ponit of microbeam, where the error is defined as

$$\text{error} = \frac{w_{i,\text{MM}}(L,t) - w_{i,\text{FDM}}(L,t)}{w_0} \times 100\% , \quad (i = 1, 2, 3, 4). \tag{7.82}$$

$w_{i,\text{MM}}$ denotes the end point deflection of the microbeam from the macromodel, and $w_{i,\text{FDM}}$ denotes the finite difference solution of the original nonlinear PDEs. It is clear that the error is very small ($\leq$0.67%) when $I_1 = I_2 = I_3 = I_4 = 2$ and $J = 2$. Computation effciciency study making use of Silicon Graphics Origin 2000 indicates that it needs 105.43 min to obtain the pull-in time for the system from FDM simulaton of the original PDEs, however, it takes only 1.19 min to simulate the same dynamics by macromodel. Although an initial effort of 41.87 min is needed to extract the KLMs

and KLVs, the macromodel can achieve a 88.6 fold improvement in speed compared with full model FDM simulation while capturing the system accurately.

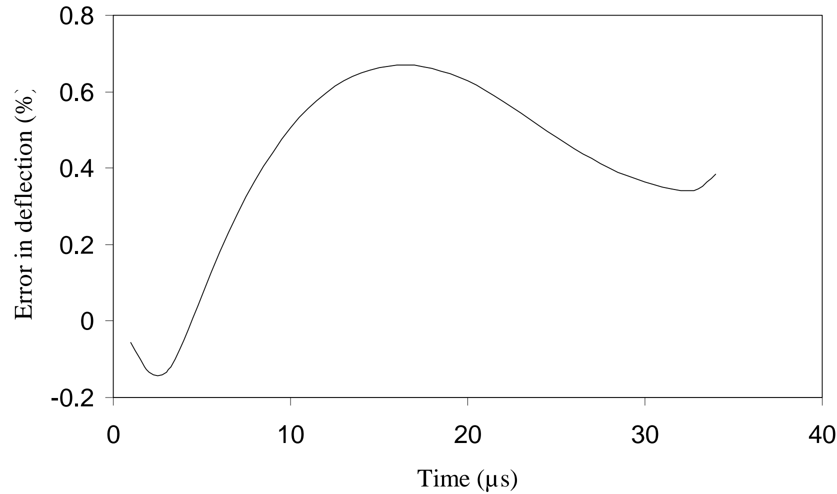


Figure 7.23 Error in end point deflection of microbeams 1-4 from macromodel simulation with respect to FDM results for input step voltages of $V_1 = V_2 = V_3 = V_4 = V_p = 50\ \text{V}$ .

ii) Applied equal voltage between a pair of microbeams and the substrate

In this combination, the input voltage applied on one pair of adjacent microbeams and the substrate is equal but differs from the other pairs. Assuming that the applied voltages applied on two pairs of microbeams are

$$V_1 = V_2, \quad V_3 = V_4$$
$$V_1 \neq V_3 \tag{7.83}$$

The mirror plate would undergo translational movement and rotational motion around $X$ under this combination of applied voltages. Figure 7.24 and Figure 7.25 illustrate the first three normalized deflection KLMs for microbeams 1, 2 and 3, 4, respectively, with a combination of input step voltages of $90\ \text{V}$ applied on the pair of microbeams 1 and 2, and $60\ \text{V}$ on pair of microbeams 3 and 4 as well as the mirror plate. Figure 7.26-Figure 7.28 plot the first three normalized back pressure KLMs for mirror plate.

The normalized KLVs and accumulative normalized KLVs with respect to the number of deflection and back pressure KLMs for each component are given in Table 7.7 and Table 7.8.

Table 7.7 Normalized accumulative KLVs corresponding to the number of deflection KLMs.

| Number of KLMs | Microbeams 1, 2 | | Microbeams 3, 4 | |
|---|---|---|---|---|
| | Normalized KLVs $\bar{\lambda}_i = \lambda_i \Big/ \sum_{i=1}^{N} \lambda_i$ | Accumulative normalized KLVs $S_{N_i} = \sum_{i=1}^{N_i} \bar{\lambda}_i$ | Normalized KLVs $\bar{\lambda}_i = \lambda_i \Big/ \sum_{i=1}^{N} \lambda_i$ | Accumulative normalized KLVs $S_{N_i} = \sum_{i=1}^{N_i} \bar{\lambda}_i$ |
| 1 | $\bar{\lambda}_1 = 0.9999768526$ | $S_1 = 0.9999977296$ | $\bar{\lambda}_1 = 0.9999863737$ | $S_1 = 0.9999863737$ |
| 2 | $\bar{\lambda}_2 = 0.0000229729$ | $S_2 = 0.9999998255$ | $\bar{\lambda}_2 = 0.0000135616$ | $S_2 = 0.9999999353$ |
| 3 | $\bar{\lambda}_3 = 0.0000000967$ | $S_3 = 0.9999999222$ | $\bar{\lambda}_3 = 0.0000000560$ | $S_3 = 0.9999999913$ |
| 4 | $\bar{\lambda}_4 = 0.0000000318$ | $S_4 = 0.9999999540$ | $\bar{\lambda}_4 = 0.0000000044$ | $S_4 = 0.9999999957$ |

Table 7.8 Normalized accumulative KLVs corresponding to the number of back pressure KLMs.

| Number of KLMs | Mirror plate | |
|---|---|---|
| | Normalized KLVs $\bar{\lambda}_i = \lambda_i \Big/ \sum_{i=1}^{N} \lambda_i$ | Accumulative normalized KLVs $S_{N_i} = \sum_{i=1}^{N_i} \bar{\lambda}_i$ |
| 1 | $\bar{\lambda}_1 = 0.9487936663$ | $S_1 = 0.9487936663$ |
| 2 | $\bar{\lambda}_2 = 0.0503111010$ | $S_2 = 0.9991047673$ |
| 3 | $\bar{\lambda}_3 = 0.0008851364$ | $S_3 = 0.9999899037$ |
| 4 | $\bar{\lambda}_4 = 0.0000089365$ | $S_4 = 0.9999988402$ |

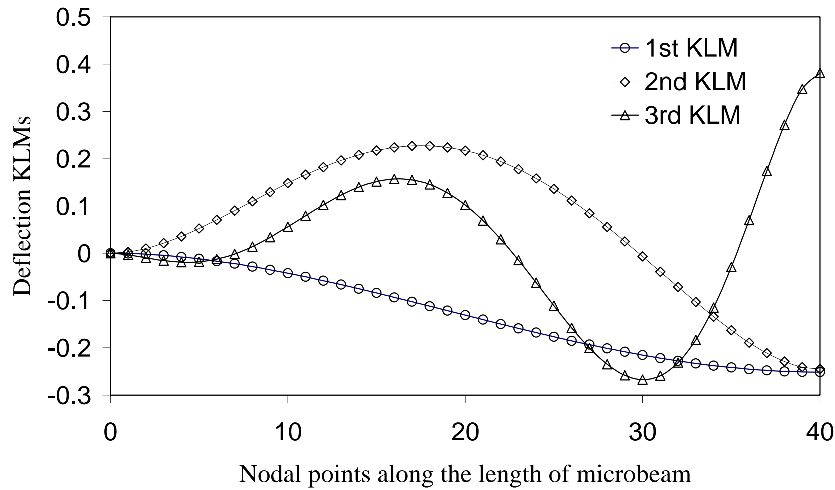


Figure 7.24 First three KLMs for deflection of microbeams 1 and 2.

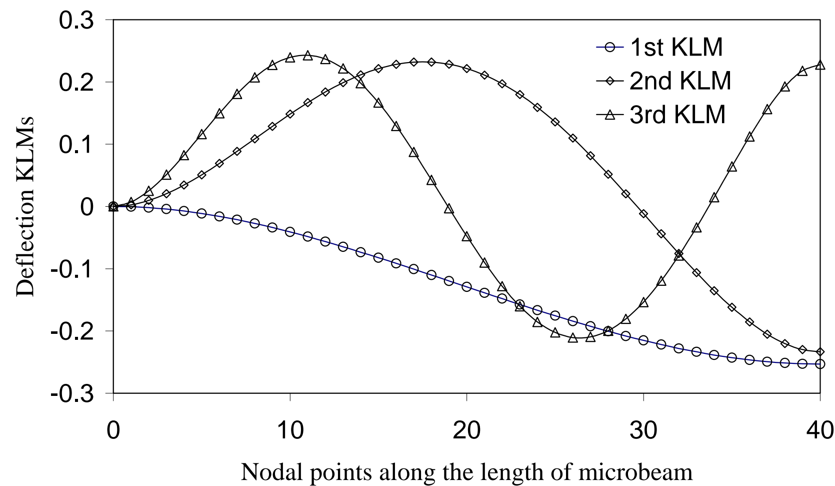


Figure 7.25 First three KLMs for deflection of microbeams 3 and 4.

With a combination of input step voltages of $V_1 = V_2 = 80\,\text{V}$, $V_3 = V_4 = V_p = 60\,\text{V}$. The dynamic response of the microbeam obtained by the macromodel approximation at 1, 5 and 14 $\mu$s and the full FDM simulations of the original nonlinear PDEs is plotted in Figure 7.29. Figure 7.30 shows the comparison of deflection response for microbeams 3 and 4. Two deflection KLMs each for microbeams 1-4 are used but three back pressure KLMs for mirror plate ($J = 3$ in Equation (7.60)) are employed in the macromodel simulation. This is because it needs at least three back pressure KLMs to

capture 99.99% of the energy as indicated in Table 7.8. The dynamic response for the angle of rotation of mirror plate about the $X$ axis simulated by macromodel and FDM is shown in Figure 7.31, the error in angle from macromodel simulation compared with FDM results is plotted in Figure 7.32, where the error is defined as

$$\text{error} = \frac{\theta_{X,\text{MM}} - \theta_{X,\text{FDM}}}{\theta_{X,\text{FDM}}} \times 100\% \quad . \tag{7.84}$$

$\theta_{X,\text{MM}}$ is the angle of rotation from the macromodel simulation, $\theta_{X,\text{FDM}}$ is from FDM solution. Figure 7.32 shows that the error is oscillatory and tends to increase with time due to the relatively less accurate approximation near pull-in.

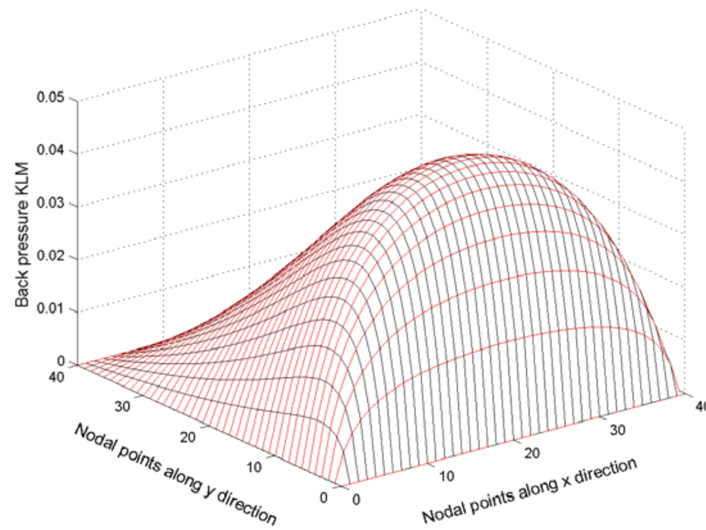


Figure 7.26 The first KLM for back pressure of mirror plate.

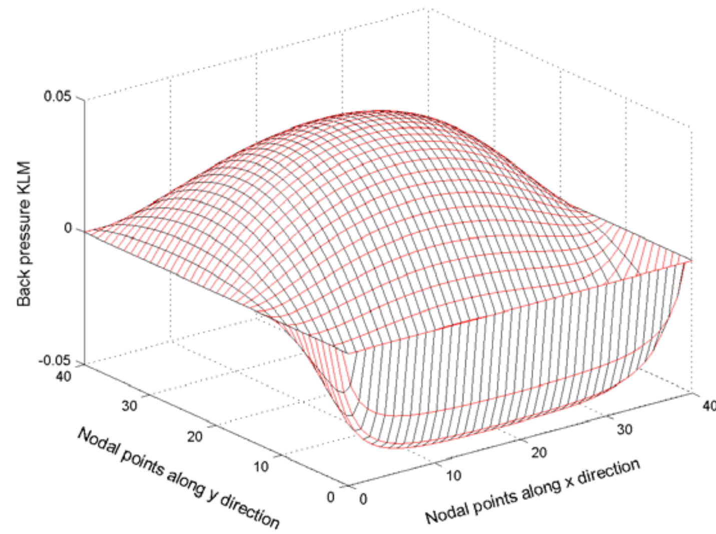


Figure 7.27 The second KLM for back pressure of mirror plate.

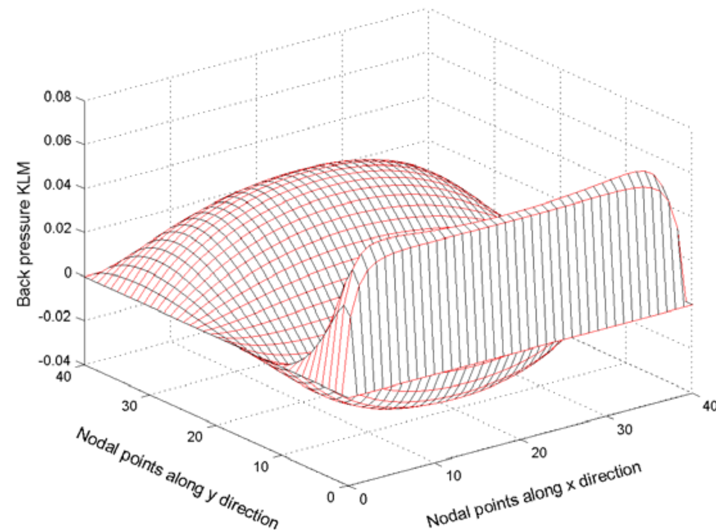


Figure 7.28 The third KLM for back pressure of mirror plate.

The calculation of computational efficiency of macromodel simulation indicates that it needs 25.34 min to obtain the pull-in time for the system from FDM simulaton of the original PDEs, while it takes only 1.41 min to simulate the same dynamics using macromodel. Initial overhead of 31.04 min is needed to extract the KLMs and KLVs in KLD procedure. Hence the macromodel can achieve 17.97 times faster in

simulation compared with full model FDM solutions in this pattern of micromirror dymanics.

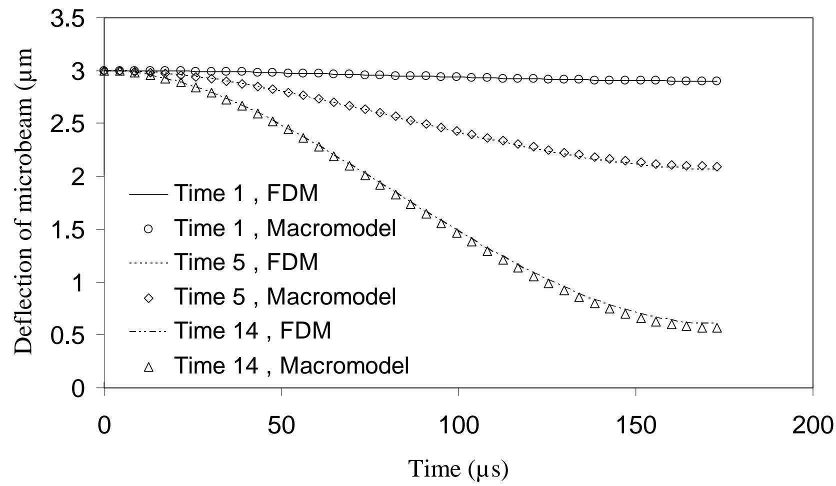


Figure 7.29 Comparison of pull-in dynamics of microbeams 1 and 2 for the combination of input step voltages of $V_1 = V_2 = 80\text{ V}$, $V_3 = V_4 = V_p = 60\text{ V}$.

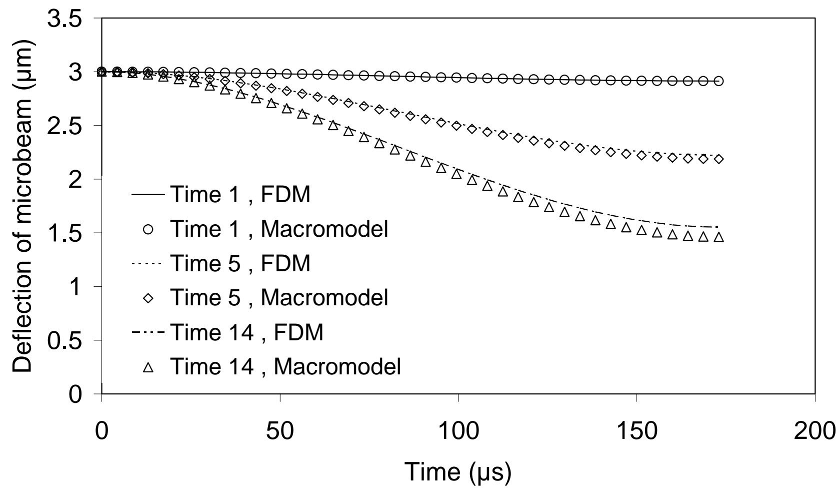


Figure 7.30 Comparison of pull-in dynamics of microbeams 3 and 4 for the combination of input step voltages of $V_1 = V_2 = 80\text{ V}$, $V_3 = V_4 = V_p = 60\text{ V}$.

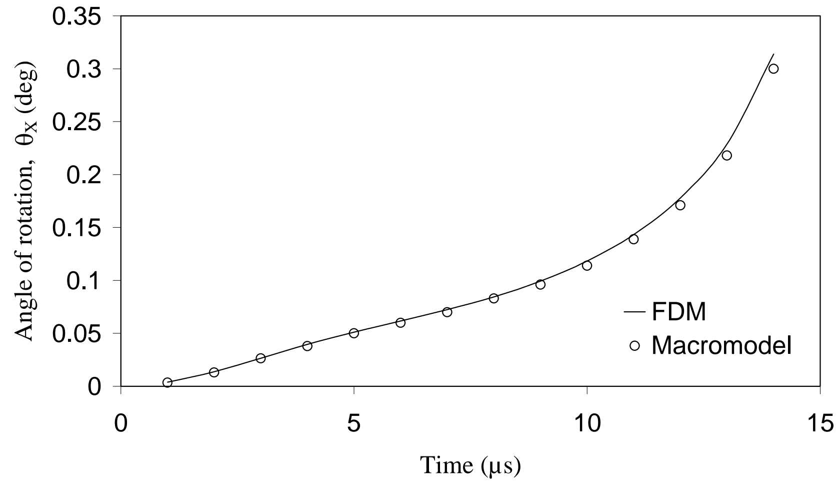


Figure 7.31 Comparison of angle of rotation of mirror plate for the combination of input step voltages of $V_1 = V_2 = 80\,\mathrm{V}$, $V_3 = V_4 = V_p = 60\,\mathrm{V}$.

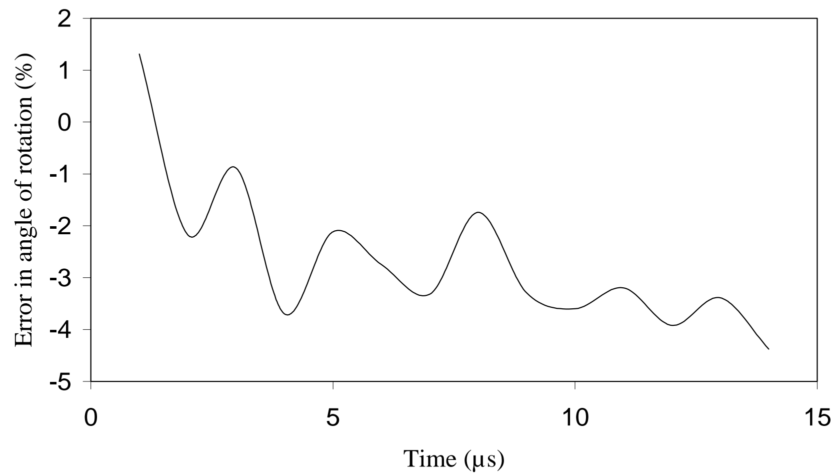


Figure 7.32 Error in angle of rotation of mirror plate from macromodel simulation with respect to FDM results for the combination of input step voltages of $V_1 = V_2 = 80\,\mathrm{V}$, $V_3 = V_4 = V_p = 60\,\mathrm{V}$.

## 7.3 CONCLUSION

A new approach of model order reduction by combination KLD and CMS for dynamic simulation of complex MEMS device has been presented in this chapter. It has demonstrated that it is efficient to divide the structurally complex MEMS device into substructures or components to obtain the KLMs as "component modes" for each individual component in the modal decomposition process. Using the CMS technique, the original nonlinear PDEs can be represented by a macromodel with a smaller number of degrees-of-freedom, and the macromodel can perform the simulation for the complete system accurately. As an indication of computational efficiency, when Silicon Graphics Origin 2000 is used, it takes 82.40 mins to obtain the pull-in time for the system in Figure 7.1 from FDM simulation of original nonlinear PDEs whilst it needs only 3.65 mins to simulate the same pull-in dynamics by using the macromodel. Although it needs an initial process of 77.65 mins for extraction of KLMs and KLVs for each component in KLD procedure, numerical experimental results demonstrate that the macromodel is flexible to achieve good simulation accuracy without regenerating KLMs for different input voltage spectra and some dimension changes in a particular component provided the changes do not affect the structural behaviour of that component. The present way of macromodel generation provides an efficient tool for structurally complex MEMS device dynamic analysis.

# CHAPTER 8

# CONCLUDINS

## 8.1 CONCLUSIONS

For quasi-static simulation of MEMS devices, the approximate solutions for the nonlinear differential equations through the use of variational principle and Rayleigh-Ritz method can provide an accurate and efficient tool for electrostatic actuators simulation and analysis. It has demonstrated in Chapter 2 that, for a MEMS device idealized as doubly-clamped microbeam, the global admissible trial functions obtained from the deflection profile of the uniformly distributed load can be used to generate macromodels to simulate accurate static pull-in and electromechanical hysteresis comparable with those obtained from finite element method (FEM) and boundary element method (BEM)-based commercial CoSolve-EM and other numerical techniques, such as meshless and shooting methods.

The model order reduction techniques used in the present work for dynamic simulation of the MEMS devices are based on the principle of proper orthogonal decomposition (POD) which consists of three equivalent methods, i.e., Karhunen-Loève decomposition (KLD), principal component analysis (PCA) and singular value decomposition (SVD). Macromodels are generated by the Galerkin projection which employs the eigenfunctions (eigenvectors) extracted by POD as basis to convert the original PDEs to a set of ordinary differential equations (ODEs) with much smaller number of degrees-of-freedom.

Numerical experiment results obtained in Chapter 3 have demonstrated that the macromodels based on KLD are accurate, efficient and flexible in the representation of the original system compared with the results obtained from the full model based on finite difference method (FDM). The macromodel simulation carried out in supercomputer, Silicon Graphics Original 2000, for dynamic pull-in response of a doubly-clamped microbeam shows that macromodel can achieve up to 11 times faster speed with less than 1.2% error in computation compared with FDM results. However, the nonlinear time-dependent terms presented in the macromodels cannot be expressed directly in the generalised coordinates or modal coordinates. This leads to inefficient re-computation of these nonlinear terms at every time step during the numerical integration. Moreover, in the macromodel flexibility aspect, the accuracy limits on quantitatively measure or scaling of parameter changes, over the parameter space in which the basis functions for macromodels can still be used without re-generation, remains opens and needs to be studied further.

Chapter 4 has demonstrated that neural network-based GHA algorithm for PCA has its computation advantages in extracting the basis functions, especially when the measured data as input signals are large. It needs only to find very few basis functions obtained through a step by step network training rather than explicit computation of the correlation matrix of the input signals which has to be done in KLD and other existing PCA methods. The shortcoming in GHA, however, is the lack of the indication on the least number of the basis needed in the macromodels in order to achieve sufficient accuracy comparable with KLD, in which the accumulative normalized Karhunen-Loève values (KLVs) provide the guideline for the required number of the Karhunen-Loève modes (KLMs) required in the macromodels. Chapter 4 also shows that the robust GHA algorithm provides a stable and robust tool in

extracting the basis functions for macromodel generation when noise is presented in the ensemble of data for PCA processing.

The relationship and the equivalency between each of the three POD methods, KLD, PCA and SVD, are clearly described in Chapter 5. When these three methods are used to handle discrete random vectors, the normalized optimal basis vectors obtained by each of them are identical. It has also been shown that there also exist asymptotic relationships among the three methods. This clears the ambiguity in the description of POD and the relationship between KLD, PCA and SVD in literature.

In order to enhance the computation efficiency of macromodels based on POD, Chapter 6 demonstartes that if the applied input voltages are less than the minimum pull-in voltage, the pre-computation, in which the nonlinear terms in macromodels are expressed explicitly in the time-dependant generalized modal coordinates and their coefficients are pre-computed prior to numerical time integration once the basis for macromodel is obtained, can achieve much better computation efficiency. However, the pre-computation method fails at the pull-in. The technique of using cubic splines to interpolate the basis functions, and the Gaussian quadrature to scale down the spatial integration of the macromodels has the advantages of faster computation and being able to provide accurate results near or at the pull-in zone. However, it is a tedious work which needs the numerical processes of the basis functions prior to macromodel simulations.

A novel macromodel generation for dynamic simulations of structurally complex MEMS devices is presented in Chapter 7. It demonstrates the computation efficiency of dividing the complex MEMS device into substructures or components to obtain the local KLMs as "component modes" for each individual component in the modal decomposition process. Using the component mode synthesis (CMS) technique, the

original nonlinear PDEs can be accurately represented by a macromodel with a smaller number of degrees-of-freedom. The advantages of the local KLMs with CMS over the global KLMs, which are obtained when treating the complex system as a single structure, are discussed through the comparison of numerical results. Obviously, if the structurally complex system is fully nonlinear, the macromodel generated by using the technique of local KLMs with CMS has lower number of computation and higher computation efficiency compared with macromodel generated by global KLMs. Numerical experiments carried out on a micro-switch and a micro-mirror have also validated that the macromodels are flexible to able to achieve good simulation accuracy without regenerating KLMs for the parameters change in the system.

In conclusion, it can be said that the present model order reduction techniques, including the global admissible trial functions and the principle of minimum potential energy; proper orthogonal decomposition (POD), including Karhunen-Loève decomposition (KLD), principal component analysis (PCA), and the Galerkin procedure; KLD and classical component mode synthesis (CMS) in macromodel generations developed in this thesis have provided accurate, efficient and flexible solutions for simulating the quasi-static and dynamic behaviours of single and complex MEMS devices. It is thus a viable and useful tool for use in design and optimization of the MEMS devices and systems.

## 8.2 SCOPE FOR FUTURE RESEARCH

This thesis provides the model order reduction techniques for fast simulations of MEMS devices and systems. In MEMS community, much more work is necessary to create the viable macromodels that meet the needs of the system designers.

Macromodels considering the effects of electrostatic fringing fields and anchor compliance can improve the simulation accuracy for real world MEMS devices.

As mentioned earlier in this chapter, macromodels generation based in POD have shown the flexibility qualitatively in numerical experiments, the parametric studies on the accuracy limits or scaling of the system parameter changes over the parameter space in which the same macromodels can still be used without re-generation of the basis functions needs to be explored further in future research.

Eventually, it will be possible to automatically incorporate and insert the macromodels developed in this thesis into the existing system-level simulators for system designers to design and analyze the behaviours of MEMS devices and systems.

# REFERENCES


ABAQUS, ABAQUS Inc., 1080 Main Street, Pawtucket, RI 02860-4847, USA.

Aluru, N.R. A Reproducing Kernel Particle Method for Meshless Analysis of Microelectromechanical Systems, Computational Mechanics, 23, pp. 324-338. 1999.

Alvin, K.F., Peterson, L.D. and Park, K.C. Consistent Model Reduction of Experimental Modal Parameters for Reduced-Order Control, Journal of Guidance, Control, and Dynamics, 18, pp. 748-755. 1995.

Anathasuresh, G.K., Gupta, R.K. and Senturia, S.D. An Approach to Macromodeling of MEMS for Nonlinear Dynamic Simulation, Microelectromechanical Systems (MEMS), ASME, DSC, 59, pp. 401-407. 1996.

Archer, R.R (ed). An Introduction to the Mechanics of Solids, New York: McGraw-Hill, 1978.

Arian, E., Fahl, M. and Sachs, E.W. Trust-Region Proper Orthogonal Decomposition for Flow Control, NASA/CR-2000-210124, ICASE Report N0. 2000-25. 2000.

Azeez, M.F.A. and Vakakis, A.F. Proper Orthogonal Decomposition (POD) of A Class of Vibroimpact Oscillations, Journal of Sound and vibration, 240, pp.859-889. 2001.

Baker, J. and Christofides, P.D. Finite-Dimensional Approximation and Control of Non-Linear Parabolic PDE Systems, International Journal of Control, 73, pp. 439-456. 2000.

Banks, H.T., Joyner, M.L., Wincheski, B. and Winfree, W.P. Nondestructive Evaluation Using a Reduced-Order Computational Methodology, Inverse Problem, 16, pp.929-945. 2000.

Bellman, R.E. and Roth, R.S. Methods in Approximation: Techniques for Mathematical Modelling, Dordrecht: D. Reidel Pub. Co. 1986.

Berkooz, G., Holms, P. and Lumley, J.L. The Proper Orthogonal Decomposition in the Analysis of Turbulent Flows, Annual Review of Fluid Mechanics, 25, pp. 539-575. 1993.

Bermúdez, A. and Fernández, J. Solving Unilateral Problems for Beams by Finite Element Methods, Computer Methods in Applied Mechanics and Engineering, 54, pp. 67-73. 1986.

Biglieri, E. and Yao, K. Some Properties of Singular Value Decomposition and Their Applications to Digital Signal Processing, Signal Processing, 18, pp. 277-289. 1989.

Blech, J.J. On Isothermal Squeeze Films, Journal of Lubrication Technology, 105, pp. 615-620. 1983.

Buser, R. A., Crary, S. B. and Juma, O.S. Integration of the Anisotropic Silicon Etching Program ASEP within the CAEMEMS CAD/CAE Framework, In MEMS'92, February 1992, Travemtinde, Gerrnany, pp. 133-138.

Cao, Y. and Levin, D.N. On the Relationship between Feature-Recognizing MRI Encoded by Singular Value Decomposition, Magnetic Resonance in Medicine, 33, pp. 140-142. 1995.

Chang, K.M., Lee, S.C. and Li, S.H. Squeeze Film Damping Effect on A MEMS Torsion Mirror, Journal of Micromechanics and Microengineering, 12, pp. 556-561. 2002.

Chatterjee, A. An Introduction to the Proper Orthogonal Decomposition, Current Science, 78, pp. 808-817. 2000.

Chen, Y. Model Order Reduction for Nonlinear Systems, Master Thesis, Massachusetts Institute of Technology. 1999.

Choi, B. and Lovell, E.G. Improved Analysis of Microbeams under Mechanical and Electrostatic Loads, Journal of Micromechanics and Microengineering, 7, pp. 24-29. 1997.

CoventorWare™, Coventor, Inc., 4001 Weston Parkway, Cary, NC 27513, USA.

Craig, R.R.Jr. and Bampton, M.C.C. Coupling of Substructures for Dynamic Analyses, AIAA, 6, pp. 1313-1319, 1968.

Craig, R.R.Jr. Methods of Component Mode Synthesis, Shock and Vibration Digest, 9, pp. 3-10. 1977.

Craig, R.R.Jr. A Review of Time-Domain and Frequency-Domain Component-Mode Synthesis Methods, Journal of Modal Analysis, pp. 59-72. 1987.

Craig, R.R.Jr. and Hale, A.L. Block-Krylov Component Synthesis Method for Structural Model Reduction, J. Guidance, 11, pp. 562-570. 1988.

Craig, R.R.Jr. and Ni, Z.H. Component Mode Synthesis for Model Order Reduction of Nonclassically Damped Systems, J. Guidance, 12, pp.577-584. 1989.

Crary, S. and Zhang, Y. CAEMEMS: An Integrated Computer-Aided Engineering Workbench for Micro-Electro-Mechanical Systems, In Proceedings IEEE Micro Electro Mechanical Systems, February 1990, Napa Valley, CA, USA, pp 113-114.

Curnier, A. On three Modal Synthesis Variants, Journal of Sound and Vibration, 90, pp. 527-540. 1983.

Cusumano, J.P., Sharkady, M.T. and Kimble, B.W. Experimental Measurements of Dimensionality and Spatial Coherence in the Dynamics of A Flexible-Beam

Impact Oscillator, Philosophical Transactions of the Royal Society of London, Physical Sciences and Engineering, 347, pp.421-438. 1994.

Davis, P.J. and Rabinowitz, P. Numerical Integration, Mass.: Blaisdell Pub. Co. 1967.

Diamantaras, K.I. and Kung, S.Y. Principal Component Neural Networks: Theory and Applications, John Wiley & Sons, Inc. 1996.

Eisley, J.G. Nonlinear Vibration of Beams and Rectangular Plates, ZAMP, 15, pp.167-175, 1964.

Essenburg, F. On Surface Constraints in Plate Problems, Journal of Applied Mechanics, pp.340-344, 1962.

Essenburg, F. On the Significance of the Inclusion of the Effect of Transverse Normal Strain in Problems with Surface Constraints, Journal of Applied Mechanics, pp.127-132, 1975.

Fedder, G.K. Simulation of Microelectromechanical Systems. Ph.D Thesis, University of California at Berkeley. 1994.

Feldmann, U., Kreuzer, E. and Pinto, F. Dynamic Diagnosis of Railway Tracks by Means of the Karhunen-Loève Transformation, Nonlinear Dynamics, 22, pp. 193-203. 2000.

Feeny, B.F. and Kappagantu, R. On the Physical Interpretation of Proper Orthogonal Modes in Vibrations, Journal of Sound and Vibration, 211, pp.607-616. 1998.

Feeny, B.F. On Proper Orthogonal Co-ordinates as Indicators of Modal Activity, Journal of Sound and Vibration, 255, pp. 805-817. 2002.

Feldmann, U., Kreuzer, E. and Pinto, F. Dynamic Diagnosis of Railway Tracks by Means of the Karhunen-Loève transformation, Nonlinear Dynamics, 22, pp. 193-203. 2000.

Fernando, K.V.M. and Nicholson, H. Discrete Double-Sided Karhunen-Loève Expansion, IEE Proc., 127, pp. 155-160. 1980.

Fernando, K.V.M. and Nicholson, H. Karhunen-Loève Expansion with Reference to Singular-Value Decomposition and Separation of Variables, IEE Proc., 127, pp. 204-206. 1980.

Fiori, S. An Experimental Comparison of Three PCA Neural Networks, Neural Processing, 11, pp.209-218. 2000.

Forsythe, G.E., Malcolm, M.A. and Moler, C.B. Computer Methods for Mathematical Computations, New Jersey: Prentice-Hall Inc. 1977.

Friswell, M.I., Penny, J.E.T. and Garvey, S.D. Using Linear Model Reduction to Investigate the Dynamics of Structures with Local Non-Linearities, Mechanical Systems and Signal Processing, 9, pp. 317-328. 1995.

Friswell, M.I., Penny, J.E.T. and Garvey, S.D. The Application of the IRS and Balanced Realization Methods to Obtain Reduced Models of Structures with Local Non-Linearities, Journal of Sound and Vibration, 196, pp. 453-468. 1996.

Fujita, H. Microactuators and Micromachines, Proceedings of the IEEE, 86, pp. 1721-1732. 1998.

Fukunaga, K. Introduction to Statistical Pattern Recognition, Boston: Academic Press. 1990.

Funk, J.M., Korvink, J.G., Bühler, J., Bächtold, M. and Baltes, H. SOLIDIS: A Tool for Microactuator Simulation in 3-D, Journal of Microelectromechanical Systems, 6, pp. 70-82. 1997.

Gabbay, L.D. Computer Aided Macromodelling for MEMS, Ph.D Thesis, Dept of Electrical Engineering and Computer Science, Massachusetts Institute of Technology, 1998.

Gabbay, L.D., Mehner, J.E. and Senturia, S.D. Computer-Aided Generation of Nonlinear Reduced-Order Dynamic Macromodels - I: Non-Stress-Stiffened Case. Journal of Microelectromechanical Systems, 9, pp. 262-269. 2000.

Gallina, P. Neural Network Painting Defect Classification Using Karhunen-Loève Transformation, Optics and Lasers in Engineering, 32, pp. 29-40. 1999.

Ginsberg, J.H. Advanced Engineering Dynamics, New York: Cambridge University Press, 1995.

Georgiou, I.T., Schwartz, I.B., Emaci, E. and Vakakis, A.F Interaction between Slow and Fast Oscillations in an Infinite Degree-of-Freedom Linear System Coupled to A Nonlinear Subsystem: Theory and Experiment, Journal of Applied Mechanics, Transactions of the ASME, 66, pp.448-459. 1999.

Georgiou, I.T. and Schwartz, I.B. Dynamics of Large Scale Coupled Structural Mechanical Systems: A Singular Perturbation Proper Orthogonal Decomposition Approach. SIAM Journal on Applied Mathematics, 59, pp.1178-1207. 1999.

Gianchandani, Y.B. and Crary, S.B. Parametric Modeling of A Microaccelerometer: Comparing I- and D-Optimal Design of Experiments for Finite-Element Analysis, Journal of Microelectromechanical Systems, 7, pp. 274-282. 1998.

Gilbert, J.R., Legtenberg, R. and Senturia, S.D. 3D Coupled Electro-Mechanics for MEMS: Application of Cosolve-EM, In Proc. MEMS'95, February 1995, Ft. Lauderdale, FL, USA. pp. 122-127.

Gilbert, J.R., Ananthasuresh, G.K. and Senturia, S.D. 3D Modeling of Contact Problems and Hysteresis in Coupled Electro-Mechanics, The Ninth Annual International Workshop on Micro Electro Mechanical Systems, IEEE, pp.127-132. 1996.

Ginsberg, J.H. Advanced Engineering Dynamics, New York : Cambridge University Press. 1995.

Golub, G.H. and Loan, C.F.V. Matrix Computations, Baltimore, MD: Johns Hopkins University Press. 1989.

Graham, M.D. and Kevrekidis, I.G. Alternative Approaches to the Karhunen-Loève Decomposition for Model Reduction and Data Analysis, Computers Chem. Engrg, 20, pp. 495-506. 1996.

Greywall, D.S., Busch, P.A. and Walker, J.A. Phenomenological Model for Gas-Damping of Micromechanical Structure, Sensors and Actuators, 72, pp. 49-70. 1999.

Griffin, W.S., Richardson, H.H. and Yamanami, S. A Study of Fluid Squeeze-Film Damping, Journal of Basic Engineering, pp.451-456. 1966.

Grimme, E.J. Krylov Projection Methods for Model Reduction, Ph.D Thesis, University of Illinois at Urbana-Champaign. 1997.

Gupta, R.K. and Senturia, S.D. Pull-in Time Dynamics as A Measure of Absolute Pressure, In Proc. MEMS, 1997, pp.290-294.

Hale, A.L. and Meirovitch, L. A General Substructure Synthesis Method for the Dynamic Simulation of Complex Structures, Journal of Sound and Vibration, 69, pp. 309-326, 1980.

Hamrock, B.J. Fundamentals of Fluid Lubrication, New York: McGraw-Hill, 1994.

Haykin, S. Neural Networks: A Comprehensive Foundation, Upper Saddle River: Prentice Hall. 1999.

Hickin, J. and Sinha, N.K. Model Reduction for Linear Multivariable Systems, IEEE Transactions on Automatic Control, AC-25, pp. 1121-1127. 1980.

Hintz, R.M. Analytical Methods in Component Modal Synthesis, AIAA Journal, 13, pp. 1007-1016. 1975.

Hodges, D.H. and Bless, R.R. Analysis of Beam Contact Problems via Optimal Control Theory, AIAA Journal, 3, pp.551-556. 1995.

Holmes, P. Lumley, J.L. and Berkooz, G. Turbulence, Coherent Structures, Dynamical Systems and Symmetry. Cambridge: Cambridge University Press. 1996.

Hotteling, H. Analysis of a Complex of Statistical Variables into Principal Components, Journal of Educational Psychology, 24, pp. 417-441, 498-520. 1933.

Hou, S.N. Review of Modal Synthesis Techniques and A New Approach, Shock and Vibration Bulletin, 40, pp.25-39. 1969.

Huang, K.Y. Neural Networks for Seismic Principal Components Analysis, IEEE Transactions on Geoscience and Remote Sensing, 37, pp.297-311. 1999.

Hung, E.S. and Senturia, S.D. Generating Efficient Dynamical Models For Microelectromechanical Systems from A Few Finite-Element Simulation Runs, J. of Microelectromechanical Systems, 8, pp. 280-289. 1999.

Hung, E.S. and Senturia, S.D. Extending the Traval Range of Analog-Tuned Electrostatic Actuators, J. of Microelectromechanical Systems, 8, pp. 497-505. 1999.

Hurty, W.C. Dynamic Analysis of Structural Systems Using Components Modes, AIAA, 3, pp. 678-685, 1965.

IntelliSuite™, Corning IntelliSense 36 Jonspin Rd., Wilmington, MA 01887, USA.

Jacobson, J.D., Goodwin-Johansson, S.H., Bobbip, S.M., Bartlett, C.A. and Yadon, L.N. Integrated Force Arrays: Theory and Modeling of Static Operation, Journal of Microelectromechanical Systems, 4, pp. 139-150. 1995.

Kappagantu, R. and Feeny, B.F. An “Optimal” Modal Reduction of a System with Frictional Excitation. Journal of Sound and Vibration, 224, pp.863-877. 1999.

Kappagantu, R. and Feeny, B.F. Part 1: Dynamical Characterization of a Frictionally Excited Beam. Nonlinear Dynamics, 22, pp.317-333. 2000.

Kappagantu, R. and Feeny, B.F. Part 2: Proper Orthogonal Modal Modeling of A Frictionally Excited Beam. Nonlinear Dynamics, 23, pp.1-11. 2000.

Karhunen, J. and Joutsensalo, J. Generalizations of Principal Component Analysis, Optimization Problems, and Neural Networks. J. Neural Networks, 8, pp. 549-562. 1995.

Kerhunen, K. Uer Lineare Methoden in der Wahrscheinlichkeitsrechnumg, Annals of Academic Science Fennicae Series A1, Mathematical Physics 37. 1946.

Kirby, M. Geometric Data Analysis: An Empirical Approach to Dimensionality Reduction and the Study of Patterns. New York : Wiley. 2001.

Klema, V.C. and Laub, A.J. The Singular Value Decomposition: Its Computation and Some Applications, IEEE Transactions on Automatic Control, 25, pp. 164-176. 1980.

Koppelman, G.M. OYSTER, A 3-Dimensional Structural Simulator for Microelectromechanical Design, Sensors and Actuators, 20, pp. 179-185. 1989.

Korvink, J., Funk, J., Roos, M., Wachutka, G. and Baltes, H. SESES: A Comprehensive MEMS Modelling System. In Proc. 7th IEEE Int. Workshop on Microelectromechanical Systems, 1994, Kanagawa, Japan, pp. 22-27.

Kosambi, K.K. Statistics in Function Space, J. Indian Math. Soc., 7, pp. 76-88. 1943.

Krysl, P., Lall, S. and Marsden, J.E. Dimensional Model Reduction in Non-Linear Finite Element Dynamics of Solids and Structures, International Journal for Numerical Methods in Engineering, 51, pp. 479-504. 2001.

Kunisch, K. and Volkwein, S. Control of the Burgers Equation by a Reduced-Order Approach Using Proper Orthogonal Decomposition, Journal of Optimization Theory and Applications, 102, pp. 345-371. 1999.

Kunisch, K. and Volkwein, S. Galerkin Proper Orthogonal Decomposition Methods for a General Equation in Fluid Dynamics, SIAM Journal on Numerical Analysis, 40 pp. 492-515. 2002.

Lahme, B. and Miranda, R. Karhunen-Loève Decomposition in the Presence of Symmetry – Part I, IEEE Transactions on Image Processing, 8, pp. 1183-1190. 1999.

Langlois, W.E. Isothermal Squeeze Films, Quarterly of Applied Mathematics, XX, pp.131-150. 1962.

Lawson, C.L. and Hanson, R.J. Solving Least Squares Problems, New Jersey: Prentice-Hall Inc. 1974.

Lee, A.Y. and Tsuha, W.S. Model Reduction Methodology for Articulated, Multiflexible Body Structures, Journal of Guidance, Control, and Dynamics, 17, pp. 69-75. 1994.

Lee, G.B. and Kwak, B.M. Formulation and Implementation of Beam Contact Problems under Large Displacement by A Mathematical Programming, Computers and Structures, 31, pp.365-376. 1989.

LeGresley, P.A. and Alonso, J.J. Investigation of Non-Linear Projection for POD Based Reduce Order Models for Aerodynamics. AIAA 2001-0926. 2001.

Legtenberg, R., Gilbert, J., Senturia, S.D., and Elwenspoek, M. Electrostatic Curved Electrode Actuators, Journal of Microelectromechanical Systems, 6, pp.257-265, 1997.

Liang, Y.C., Lin, W.Z., Lee, H.P., Lim, S.P., Lee, K.H. and Feng, D.P. A Neural-Network-Based Method of Model Reduction for the Dynamic Simulation of MEMS, Journal of Micromechanics and Microengineering, 11, pp.226-233, 2001.

Liang, Y.C., Lee, H.P., Lim, S.P., Lin, W.Z., Lee, K.H. and Wu, C.G. Proper Orthogonal Decomposition And Its Applications - Part I: Theory, Journal Sound And Vibration, 252, pp. 527-544. 2002.

Liang, Y.C., Lin, W.Z., Lee, H.P., Lim, S.P., Lee, K.H. and Sun, H. Proper Orthogonal Decomposition And Its Applications - Part II: Model Reduction for MEMS Dynamical Analysis, Journal Sound And Vibration, 256, pp. 515-532. 2002.

Lin, W.Z., Lee, K.H., Lim, S.P. and Lu, P. A Method of Model Reduction for Dynamic Simulation of Microelectromechanical Systems, Dynamics, Acoustics and Simulations ASME, DSC 68, pp.155-162. 2000.

Lin, W.Z., Lee, K.H., Lim, S.P. and Lu, P. A Model Reduction Method for the Dynamic Analysis of Microelectromechanical Systems, International Journal of Nonlinear Sciences and Numerical Simulation, 2, pp. 89-100. 2001.

Lin, W.Z., Lee, K.H., Lim, S.P., Lu, P. and Liang, Y.C. The Relationship between Eigenfunctions of Karhunen-Loève Decomposition and The Modes of Distributed Parameter Vibration System, Journal of Sound and Vibration, 256, pp. 791-799. 2002.

Lin, W.Z., Lee, K.H. and Lim, S.P. Computation Speedup of Macromodels for Dynamic Simulation of Microsystem, In International Conference on Modeling and Simulation of Microsystems, MSM2002, April 2002, Puerto Rico, USA, pp. 368-371.

Lin, W.Z., Lee, K.H. and Lim, S.P. Proper Orthogonal Modes for Macromodel Generation for Complex MEMS Devices, Nanotech 2003, February 2003, San Francisco, California, USA, pp. 542-545.

Lin, W.Z., Liang, Y.C., Lee, K.H., Lim, S.P. and Lee, H.P. Computation Speedup in the Dynamic Simulation of MEMS by Macromodel, Progress in Natural Science, 13, pp. 219-227, 2003.

Lin, W.Z., Lee, K.H., Lim, S.P. and Liang, Y.C. Proper Orthogonal Decomposition and Component Mode Synthesis in Macromodel Generation for the Dynamic Simulation of a Complex MEMS Device, Journal of Micromechanics and Microengineering, 13, pp. 646-654. 2003.

Loève, M.M. Probability Theory, Princeton NJ: Von Nostrand, 1955.

Lumley, J.L. Stochastic Tools in Turbulence. New York: Academic Press. 1970.

Luo, F.L. and Unbehauen, R. Applied Neural Networks for Signal Processing, Cambridge University Press. 1997.

Ma, X.H. and Vakakis, A.F. Karhunen-Loève Decomposition of the Transient Dynamics of a Multibay Truss. AIAA Journal, 37, pp.939-946. 1999.

Ma, X., Azeez, M.F.A. and Vakakis, A.F. Non-Linear Normal Modes and Non-parametric System Identification of Non-linear Oscillators, Mechanical Systems and Signal Processing, 14, pp.37-48. 2000.

Ma, X.H., Vakakis, A.F. and Bergman, L.A. Karhunen-Loève Modes of a Truss: Transient Response Reconstruction and Experimental Verification, AIAA Journal, 39, pp.687-696. 2001.

Ma, X.H. and Vakakis, A.F. Nonlinear Transient Localization and Beat Phenomena Due to Backlash in a Coupled Flexible System, Journal of Vibration and Acoustics-Transactions of the ASME, 123, pp.36-44. 2001.

MacMeal, R.H. A Hybrid method of Component Mode Synthesis, 1, pp. 581-601. 1971.

Marple, S.L. Jr. Digital Spectral Analysis with Applications, New Jersey: Prentice-Hall Inc. 1987.

McCarthy, B., Adams, G.G., McGruer, N.E. and Potter, D. A Dynamic Model, Including Contact Bounce, of An Electrostatically Actuated Microswitch, Journal of Microelectromechanical Systems, 11, pp. 276-283. 2002.

Mees, A.I., Rapp, P.E. and Jennings, L.S. Singular Value Decomposition and Embedding Dimension, Physical Review A, 36, pp. 340-346. 1987.

Meirovitch, L. Principles and Techniques of Vibrations, N.J.: Prentice Hall. 1997.

Meirovitch, L. and Hale, A.L. On the Substructure Synthesis Method, AIAA, 19, pp. 940-947, 1981.

Meirovitch, L. and Kwak, M.K. Rayleigh-Ritz Based Substructure Synthesis for Flexible Multibody Systems, AIAA, 29, pp. 1709-1719, 1991.

Meirovitch, L. and Kwak, M.K. Inclusion Principal for the Rayleigh-Ritz Based Substructure Synthesis, AIAA Journal, 30, pp. 1344-1351, 1992.

Min, Y.H. and Kim, Y.K. Modeling, Design, Fabrication and Measurement of a Single Layer Polysilicon Micromirror with Initial Curvature Compensation, Sensors and Actuators, 78, pp. 8-17. 1999.

Minami, K., Matsunaga, T. and Esashi, M. Simple Modeling and Simulation of the Squeeze Film Effect and Transient Response of the MEMS Device, In Proc. of IEEE International Workshop on Micro Electro Mechanical Systems, 1999, pp.338-343.

Moore, B.C. Principal Component Analysis in Linear Systems: Controllability, Observability, and Model Reduction, IEEE Trans. Automat. Contr., AC-26, pp.17-32. 1981.

Mrcarica, Z., Litovski, V.B. and Detter, H. Modelling and Simulation of Microsystems Using Hardware Description Language, Microsystem Technologies, 3, pp. 80-85. 1997.

Murdoch, D. C. Linear Algebra. New York: John Wiley & Sons Inc. 1970.

Mukherjee, T., Fedder, G.K., Ramaswamy, D. and White, J. Emerging Simulation Approaches for Micromachined Devices, IEEE Transactions on Computer-Aided Design of Integrated Circuits and Systems, 19, pp. 1572-1589. 2000.

Nabors, K. and White, J. FastCap: A Multipole Accelerated 3-D Capacitance Extraction Program, IEEE Transactions on Computer-Aided Design, 10, pp.1447-1459. 1991.

Nabors, K. Kim, S. and White, J. Fast Capacitance Extraction of General Three-Dimensional Structures, IEEE Transactions on Theory and Techniques, 40, pp. 1496-1506. 1992.

Nabors, K. and White, J. Multipole-Accelerated Capacitance Extraction Algorithms for 3-D Structures with Multiple Dielectrics, IEEE Transactions on Circuits and Systems–I: Fundamental Theory and Applications, 39, pp. 946-954. 1992.

Naghdi, P.M. and Rubin, M.B. On the Significance of Normal Cross-Sectional Extension in Beam Theory with Application to Contact Problems, Int. J. Solids Structures, 25, pp.249-265, 1989.

Ngiam, L.N. Quasistatic and Dynamic Analyses of Electrostatic Microactuators Using the Shooting Method, Master Thesis, National University of Singapore. 2000.

Nguyen, C.T.C., Katehi, L.P.B. and Rebeiz, G.M. Micromachined Devices for Wireless Communications, Proceedings of the IEEE, 86, pp. 1756-1768. 1998.

Noor, A.K. Reduced Basis Technique for Nonlinear Analysis of Structures, AIAA Journal, 18, pp. 455-462. 1980.

Noor, A.K. Recent Advances in Reduction Methods for Nonlinear Problems, Computers and Structures, 13, pp. 31-44. 1981.

Noor, A.K. and Peters, J.M. Mixed Models and Reduction Techniques for Large-Rotation Nonlinear Problems, Computer Methods in Applied Mechanics and Engineering, 44, pp. 67-89. 1984.

Noor, A.K. Recent Advance and Applications of Reduction Methods, Appl Mech Rev, 47, pp.125-146. 1994.

Obukhov, A.M. Statistical Description of Continuous Fields, Trudy Geophys. Int. Aked. Nauk. SSSR, 24 pp. 3-42. 1954.

Oja, E. A Simplified Neuron Model as a Principal Component Analyzer, Journal of Mathematics and Biology 15, pp.267-273. 1982.

Osterberg, P.M. and Senturia, S.D. M-TEST: A Test Chip for MEMS Material Property Measurement Using Electrostatically Actuated Test Structures, Journal of Micromechanics and Microengineering, 6, pp. 107-118, 1997.

Pamidighantam, S., Puers, R., Baert, K. and Tilmans, H.A.C., Pull-in Voltage Analysis of Electrostatically Actuated Beam Structures with Fixed-Fixed and Fixed-Free End Conditions, Journal of Micromechanics and Microengineering, 12, pp. 458-464. 2002.

Park, H.M. and Cho, D.H. The Use of the Karhunen-Loève Decomposition for the Modeling of Distributed Parameter Systems, Chemical Engineering Science, 51, pp.81-98. 1996.

Pearson, K. On Lines and Planes of Closest Fit to Systems of Points in Space, Philosophical Magazine, 2, pp.559-572. 1901.

Pilkey, D.F., Ribbens, C.J. and Inman, D.J. High Performance Computing Issues for Model Reduction/Expansion, Advances in Engineering Software, 29, pp. 389-393. 1998.

Pougachev, V.S. General Theory of the Correlations of Random Functions, Izv. Akad, Nauk. SSSR. Math. Ser., 17, pp. 401-402. 1953.

Prasad, R. Pade Type Model Order Reduction for Multivariable Systems Using Routh Approximation, Computers and Electrical Engineering, 26, pp. 445-459. 2000.

Press, W.H., Teukolsky, S.A., Vetterling, W.T. and Flannery, B.P. Numerical Recipes in Fortran: The Art of Scientific Computing, Cambridge: Cambridge University Press. 1992.

Rajan, J.J. and Rayner, P.J.W. Model Order Selection for the Singular Value Decomposition and the Discrete Karhunen-Loève Transform Using A Bayesian Approach, IEE Proc., 144, pp.116-123. 1997.

Ravindra, B. Comments on “On the Physical Interpretation of Proper Orthogonal Modes in Vibrations”, Journal of Sound and Vibration, 219, pp.189-192. 1999.

Ravindran, S.S. Reduced-Order Adaptive Controllers for Fluids Using Proper Orthogonal Decomposition, AIAA2001-0925. 2001.

Reed, I.S. and Lan, L.S. A Fast Approximate Karhunen-Loève Transform (AKLT) for Data Compression, Journal of Visual Communication and Image Representation, 5, pp. 304-316. 1994.

Reissner, E. On One-Dimensional Finite-Strain Beam Theory: the Plane Problem, Journal of Applied Mechanics and Physics (ZAMP), 33, pp.795-804. 1972.

Rewienski, M. and White, J. Generating Macromodels for System Design with Micromachined Devices, In SMA 1st Annual Symposium, January 2001, Singapore, pp. C12-1-C12.6.

Rewienski, M. and White, J. A Trajectory Piecewise-Linear Approach to Model Order Reduction and Fast Simulation of Nonlinear Circuits and Micromachined Devices, In IEEE/ACM International Conference on Computer Aided Design, ICCAD 2001, pp. 252-257.

Robertson, G.A. and Cameron, I.T. Analysis of Dynamic Process Models for Structural Insight and Model Reduction - Part 1. Structural Identification Measures, Computers and Chemical Engineering, 21, pp. 455-473. 1997.

Robertson, G.A. and Cameron, I.T. Analysis of Dynamic Models for Structural Insight and Model Reduction - Part 2. A Multi-Stage Compressor Shutdown Case-Study, Computers and Chemical Engineering, 21, pp. 475-488. 1997.

Rocha, M.M., Cabral, S.V.S. and Riera, J.D. A Comparison of Proper Orthogonal Decomposition and Monte Carlo Simulation of Wind Pressure Data, Journal of Wind Engineering and Industrial Aerodynamics, 84, pp. 329-344. 2000.

Romanowicz, B.F. Methodology for the Modeling and Simulation of Microsystems, Boston: Kluwer Academic Publishers, 1998.

Rowley, C.W. and Marsden, J.E. Reconstruction Equation and the Karhunen-Loève Expansion for Systems with Symmetry, Physica D, 142, pp.1-19. 2000.

Rubin, S. Improved Component-Mode Representation for Structural Dynamic Analysis, AIAA Journal, 13, pp. 995-1006. 1975.

Saad, Y. and Schultz, M.H. GMRES: A Generalized Minimal Residual Algorithm for Solving Nonsymmetric Linear Systems, SIAM J. Sci. Stat. Comput. 7, pp. 856-869. 1986.

Sanger, T.D. Optimal Unsupervised Learning in a Single-Layer Linear Feedforward Neural Network, Neural Networks, 2, pp.459-473. 1989.

Schroth, A., Blochwitz, T. and Gerlach, G. Simulation of A Complex Sensor System Using Coupled Simulation Programs, Sensors and Actuators A-Physical, 54, pp. 632-635. 1996.

Senturia, S.D., Harris, R.M., Johnson, B.P., Kim, S., Nabors, K., Shulman, M.A. and White, J. A Computer-Aided Design System for Microelectromechanical Systems (MEMCAD), Journal of Microelectromechanical Systems, 1, pp. 3-13. 1992.

Senturia, S.D., Aluru, N. and White, J. Simulating the Behavior of MEMS Devices: Computational Methods and Needs, IEEE Computational Science and Engineering, 2, pp. 30-43. 1997.

Senturia, S.D. CAD Challenges for Microsensors, Microactuators, and Microsystems, Proc. IEEE, 86, pp. 1611-1626. 1998.

Senturia, S.D. Microsystem Design, Boston: Kluwer Academic Publishers, 2001.

Seshu, P. Substructuring and Component Modes Synthesis, Shock and Vibration, 4, pp,199-210, 1997.

Shvartsman, S.Y. and Kevrekidis, I.G. Nonlinear Model Reduction for Control of Distributed Systems: A Computer-Assisted Study, AIChE Journal, 44, pp. 1579-1595. 1998.

Shvartsman, S.Y., Theodoropoulos, C., Rico-Martinez, R., Kevrekidis, I.G., Titi, E.S. and Mountziaris, T.J. Order Reduction for Nonlinear Dynamic Models of Distributed Reacting Systems, Journal of Process Control, 10, pp. 177-184. 2000.

Sirovich, L. Turbulence and The Dynamics of Coherent Structures Part I: Coherent Structures, Quarterly of Applied Mathematics, XLV, pp. 561-571. 1987.

Sirovich, L. Turbulence and The Dynamics of Coherent Structures Part II: Symmetries and Transformations, Quarterly of Applied Mathematics, XLV, pp. 573-582. 1987.

Sirovich, L. Turbulence and The Dynamics of Coherent Structures Part III: Dynamics and Scaling, Quarterly of Applied Mathematics, XLV, pp. 583-590. 1987.

Sirovich, L. and Park, H. Turbulent Thermal Convection in A Finite Domain: Part I. Theory, Physics of Fluids A – Fluid Dynamics, 2, pp.1649-1658. 1990.

Sirovich, L. and Park, H. Turbulent Thermal Convection in A Finite Domain: Part II. Numerical Results, Physics of Fluids A – Fluid Dynamics, 2, pp. 1659-1668. 1990.

Sirovich, L., Knight, B.W. and Rodriguez, J.D. Optimal Low-Dimensional Dynamical Approximations, Quarterly of Applied Mathematics, XLVIII, pp.535-548. 1990.

Skoogh, D. Krylov Subspace Methods for Linear Systems, Eigenvalues and Model Order Reduction, Ph.D Thesis, University of Göteborg. 1998.

Slaats, P.M.A., Jongh, J.D. and Sauren, A.A.H.J. Model Reduction Tools for Nonlinear Structural Dynamics, Computers and Structures, 54, pp. 1155-1171. 1995.

Starr, J.B. Squeeze-Film Damping in Solid-State Accelerometers, In Technical Digest, IEEE Solid-State Sensor and Actuator Workshop, June 1990, Hilton Head Island, South Carolina, USA, pp. 44-47.

Stroud, A. H. and Secrest, D. Gaussian Quadrature Formulas, N.J.: Prentice-Hall. 1966.

Stroud, A. H. Approximate Calculation of Multiple Integrals, N.J.: Prentice-Hall. 1971.

Swart, N.R., Bart, S.F., Zaman, M.H., Mariappan, M., Gilbert, J.R. and Murphy, D. AutoMM: Automatic Generation of Dynamic Macromodels for MEMS Devices, In Proc. SPIE, IEEE MEMS Workshop, January 1998, Heidelberg, Germany, pp. 178-183.

Tamura, Y., Suganuma, S., Kikuchi, H. and Hibi, K. Proper Orthogonal Decomposition of Random Pressure Field, Journal of Fluids and Structure, 13, pp. 1069-1095. 1999.

Thomson, W.T. and Dahleh, M.D. Theory of Vibration with Applications, 5th edition, New Jersey: Prentice Hall. 1998.

Tilmans, H.A.C. Micro-Mechanical Sensors Using Encapsulated Built-in Resonant Strain Gauges, Ph.D Thesis, University of Twente. 1993.

Tilmans, H.A.C. and Legtenberg, R. Electrostatically Driven Vacuum-Encapsulated Polysilicon Resonators, Part II. Theory and Performance, Sensors and Actuators A, 45, pp.67-84, 1994.

Tilmans, H.A.C. Equivalent Circuit Representation of Electromechanical Transducers: I. Lumped-Parameter Systems (Micromechanical Systems), Journal of Micromechanics and Microengineering, 6, pp.157-176. 1996.

Timoshenko, S. Strength of Materials, 3rd edition, Part II, Van Nostrand, Princeton, 1956.

Toshiyoshi, H., Piyawattanametha, W., Chan, C.T. and Wu, M.C. Linearization of Electrostatically Actuated Surface Micromachined 2-D Optical Scanner, Journal of Microelectromechanical Systems, 10, pp. 205-214. 2001.

Vandemeer, J.E., Kranz, M.S. and Fedder, G. Hierarchical Representation and Simulation of Micromachined Inertial Sensors, In Technical Proceedings of the 1998 International Conference on Modeling and Simulation of Microsystems, April 1998, Santa Clara, California, USA, pp. 540-545.

Varghese, M., Amantea, R., Sauer, D. and Senturia, S.D. Resistive Damping of Pulse-Sensed Capacitive Position Sensors, In Transducers ’97, International Conference on Solid-State Sensors and Actuators, June 1997, Chicago, USA, pp.1121-1124.

Veijola, T. Kuisma, H., Lahdenperä, J. and Ryhänen, T. Equivalent-Circuit Model of the Squeezed Gas Film in A Silicon Accelerometer, Sensors and Actuators A, 48, pp.239-248. 1995.

Veijola, T., Kuisma, H. and Lahdenperä, J. The Influence of Gas-Surface Interaction on Gas-Film Damping in A Silicon Accelerometer, Sensors and Actuators A, 66, pp. 83-92. 1998.

Vellemagne, C.D. and Skelton, R.E. Model Reduction Using A Projection Formulation, Int. J. Control, 46, pp. 2141-2169. 1987.

Washizu, K. Variational Methods in Elasticity and Plasticity. Oxford: Pergamon Press. 1982.

Wang, F. and White, J. Automatic Model Order Reduction of A Microdevice Using The Arnoldi Approach, Microelectromechanical Systems (MEMS), ASME, DSC, 66, pp.527-530. 1998.

Westbrook, D.R. Contact Problems for the Elastic Beam, Computers and Structures, 15, pp. 473-479, 1982.

Willcox, K. and Peraire, J. Balanced Model Reduction via the Proper Orthogonal Decomposition, AIAA 2001-2611, 2001.

Yang, Y.J., Gretillat, M.A. and Senturia, S.D. Effect of Air Damping on the Dynamics of Nonuniform Deformation of Microstructures, In Transducers '97, International Conference on Solid-State Sensors and Actuators, June 1997, Chicago, USA, pp.1093-1096.

Young, D.J. and Boser, B.E. A Micromachine-Based RF Low-Noise Voltage-Controlled Oscillator, In Custom Integrated Circuits Conference, May 1997, Santa Clara, CA, USA, pp. 431-434.

Zaman, M.H., Bart, S.F., Gilbert, J.R. Swart, N.R., and Mariappan, M. An Environment for Design and Modeling of Electromechanical Micro-Systems, Journal of Modeling and Simulation of Microsystems, 1, pp. 65-76. 1999.

Zhang, Y.W. and Ma, Y,L. CGHA for Principal Component Extraction in the Complex Domain, IEEE Transactions on Neural Networks, 8, pp.1031-1036. 1997.

Zou, Q., Li, Z. and Liu, L. New Method for Measuring Mechanical Properties of Thin Films in Micromachining: Beam Pull-in Voltage (VPI) Method and Load Beam Deflection (LBD) Method, Sensors and Actuators A, 48, pp.137-143, 1995.

Zhou, G.Y., Tay, F.E.H. and Chau, F.S. Macro-modelling of a Double-Gimballed Electrostatic Torsional Micromirror, Journal of Micromechanics and Microengineering, 13, pp. 532-547. 2003.

Zhou, M., Schonberg, W.P. and Alabama, H. Rotation Effects in the Global/Local Analysis of Cantilever Beam Contact Problem, Acta Mechanica, 108, pp. 49-62. 1995.

Zhou, N., Clark, J.V. and Pister, K.S.J. Nodal Simulation for MEMS Design Using SUGAR v0.5. In International Conference on Modeling and Simulation of Microsystems Semiconductors, Sensors and Actuators, April 1998, Santa Clara, CA, USA, pp. 308-313.